MICROSCOPIC APPLICATIONS OF HOLOGRAPHIC BEAM SHAPING AND STUDIES OF OPTICALLY TRAPPED AEROSOLS

Daniel Richard Burnham

A Thesis Submitted for the Degree of PhD
at the
University of St. Andrews

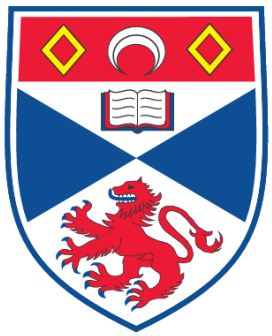

2009

Microscopic Applications of Holographic Beam Shaping and Studies of Optically Trapped Aerosols

Daniel Richard Burnham

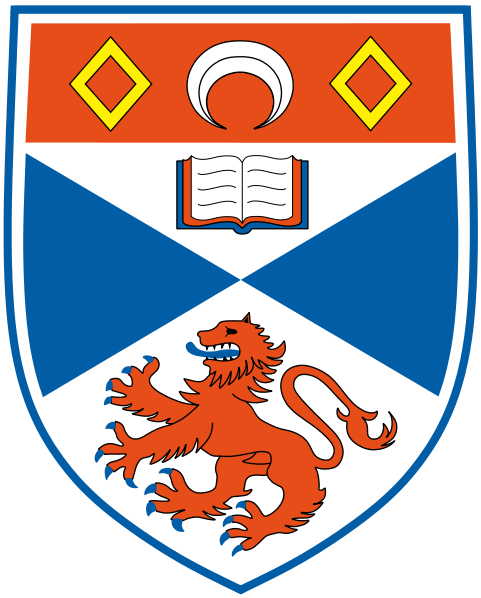

Thesis submitted for the degree of Doctor of Philosophy
of the University of St Andrews

March 2009

Abstract

This thesis has two themes. Firstly, it concerns the original application of holographic beam shaping, employed through the methods associated with optical manipulation, to three microscopic fields of research. Secondly, it studies the optical trapping of aerosol droplets through experimentation and computational modelling.

The aims are to not only provide an account of the work carried out but also a base for future researchers and students.

Chapter 1 provides an intoduction to the field of optical manipulation and the relevance of my studies. Chapter 2 outlines the construction of an optical tweezers which is the basis of advanced experimental work described in later chapters. It also overviews how optical tweezers operate and are quantified.

In chapter 3 I describe how beam shaping is implemented for my investigations with a spatial light modulator and phase-only holograms. I detail the algorithms and software written before discussing their performance and finally the optimisation of the apparatus.

Chapter 4 describes three original applications of beam shaping, including the trapping and coagulation of multiple aerosols, the manipulation of filamentous fungi hyphal tips and novel digital microfluidic operations using thermocapillary forces. I also lay down preliminary results for observing orbital angular acceleration using beams carrying orbital angular momentum.

To study single optically trapped aerosols I use two methods. Firstly, their Brownian motion is investigated through sub diffraction limit position detection. Unique results in optical tweezers are shown with liquid droplets behaving as under-damped Brownian oscillators. Through these studies I demonstrate a new technique for sizing trapped aerosols, with significant advantages over current methods. I also show the droplets can be be parametrically excited which can result in trap failure.

Secondly, in chapter 6, I use a theoretical model to describe the forces imparted to a trapped droplet. I extend current theories to include the effects of a three medium focal region to accurately describe airborne optical traps. The work qualitatively explains the phenomena observed experimentally.

The work contained here leaves much scope for future investigations, for which I provide an overview in chapter 7.

Declaration

I, Daniel Richard Burnham, hereby certify that this thesis, which is approximately 60,000 words in length, has been written by me, that it is the record of work carried out by me and that it has not been submitted in any previous application for a higher degree.

I was admitted as a research student in October 2005 and as a candidate for the degree of Doctor of Philosophy in October 2006; the higher study for which this is a record was carried out in the University of St Andrews between 2005 and 2009.

Signature of Candidate:..... **Date:** .....

I hereby certify that the candidate has fulfilled the conditions of the Resolution and Regulations appropriate for the degree of Doctor of Philosophy in the University of St Andrews and that the candidate is qualified to submit this thesis in application for that degree.

Signature of Supervisor:..... **Date:** .....

In submitting this thesis to the University of St Andrews we understand that we are giving permission for it to be made available for use in accordance with the regulations of the University Library for the time being in force, subject to any copyright vested in the work not being affected thereby. I also understand that the title and abstract will be published, and that a copy of the work may be made and supplied to any bona fide library or research worker, that my thesis will be electronically accessible for personal or research use unless exempt by award of an embargo as requested below, and that the library has the right to migrate my thesis into new electronic forms as required to ensure continued access to the thesis. We have obtained any third-party copyright permissions that may be required in order to allow such access and migration, or have requested the appropriate embargo below.

The following is an agreed request by candidate and supervisor regarding the electronic publication of this thesis:

Access to Printed copy and electronic publication of thesis through the University of St Andrews.

Signature of Candidate:..... **Signature of Supervisor:**.....
Date: .....

Acknowledgements

I have been fortunate during studying for my PhD to have met dozens of researchers who have played helpful parts in my studies and without whom this thesis would not be as complete.

Firstly, a big thank you to the Aerosol Dynamics group in Bristol. My visits have always been fun and productive, and everyone has always taken the time to assist me with solving problems and answering questions.

Secondly, I would like to thank Graham Wright and Nick Read from the Fungal Cell Biology group at Edinburgh University whom with I collaborated to study the optical manipulation of filamentous fungus. Without Graham watching fungus grow could potentially be quite dull, and no doubt their expertise made the studies far more successful.

Thirdly, I want to thank the Glasgow University Optics group for all their assistance and hospitality and, by extension, Roberto di Leonardo for answering my questions and useful comments.

Next I would like to thank Maria-Luisa and Charles Baroud from l'École Polytechnique in Paris for the microfluidic fun and the nice results we obtained, again adding depth to my thesis.

Finally I want to thank the Optical Trapping group at the University of St Andrews and more generally colleagues and staff for putting up with my continuous questions. A big thanks to Peter for his patience and determination in making the QPD system work, David G for always taking the time to help me find things and James for his TeX support.

The thank yous must continue to include those that have passed through our group, Dan, Graham, Marc, Carlos and Michael who have made the whole experience far more enjoyable. I also cannot forget my supervisor, David McGloin, for always taking the time to discuss topics, correct documents, answer stupid questions, spending what must amount to days to finding missing $2\pi s$ and generally being available.

Finally I must thank my parents for their unquestioning support and enthusiasm, my brother for emergency tech support, and Sammi, without whom I think the completion of this work would not have been possible.

"Dans les champs de l'observation le hasard ne favorise que les esprits préparés."

"In the fields of observation chance favours only the prepared mind"

Louis Pasteur (1854)

Peer-Reviewed Publications

"Brownian dynamics of optically trapped liquid droplets", *D. R. Burnham*, P. Reece and D. McGloin, In preparation (2009)

"Mixing via thermocapillary generation of flow patterns inside a microfluidic drop", M. Cordero, H. O. Rolfsnes, *D. R. Burnham*, P. A. Campbell, David McGloin and C. N. Baroud, Submitted (2009)

"Underdamped modes in a hydrodynamically coupled microparticle system", A. M. Yao, S. A. J. Keen, *D. R. Burnham*, J. Leach, R. Di Leonardo, D. McGloin and M. J. Padgett, Submitted (2009)

"Radius measurements of optically trapped aerosols through Brownian motion", *D. R. Burnham* and D. McGloin, Submitted (2008)

"Spectroscopic characterisation and manipulation of arrays of sub-picolitre aerosol droplets", J. R. Butler, J. B. Wills, L. Mitchem, *D. R. Burnham*, D. McGloin and J. P. Reid, Lab Chip, 9, 521-528 (2009)

"Thermocapillary manipulation of droplets using holographic beam shaping: Microfluidic pin-ball", M. Cordero, *D. R. Burnham*, C. N. Baroud and D. McGloin, APL 93, 034107 (2008)

"Phase dynamics of continuous topological upconversion in vortex beams", C. Lopez-Mariscal, *D. R. Burnham*, D. Rudd, D. McGloin and J. Gutierrez-Vega, Optics Express 16, 11411-11422 (2008)

"Trapping solid aerosol with optical tweezers: A comparison between liquid and gas phase optical traps", M. D. Summers, *D. R. Burnham* and D. McGloin, Optics Express 16, 7739-7747 (2008)

"Optical manipulation of airborne particles: techniques and applications", D. McGloin, *D. R. Burnham*, M. D. Summers, D. Rudd, N. Dewar and S. Anand, Faraday Discussions, 137, 335-350 (2008)

"Holographic and single beam optical manipulation of hyphal growth in filamentous fungi", *D. R. Burnham*, G. D. Wright, N. D. Read and D. McGloin, J. Opt. A: Pure and Applied Optics, 9, S172-S179 (2007)

"Parametric resonance of optically trapped aerosols", R. Di Leonardo, G. Ruocco, J. Leach, M. J. Padgett, A. J. Wright, J. M. Girkin, *D. R. Burnham* and D. McGloin, Phys. Rev. Lett. 99, 010601 (2007)

"Colloidal interactions and transport in nematic liquid crystals", S. A. Tatarkova, *D. R. Burnham*, A. K. Kirby, G. D. Love and E. M. Terentjev, Phys. Rev. Lett. 98, 157801 (2007)

"Holographic optical trapping of aerosol droplets", *D. R. Burnham* and D. McGloin, Opt. Express 14, 4175-4181 (2006)

List of symbols

δ	phase retardation
$\Delta\epsilon$	dielectric anisotropy
Δh	water layer thickness
γ_0	viscous drag in bulk
γ	f/w
Γ	viscous damping
$\hat{\boldsymbol{\epsilon}}$	rotation by Euler angles
η	dynamic viscosity
κ	trap stiffness
λ_0	wavelength of light in vacuum
μ_0	permeability
ψ_n	aberration function
ρ_{medium}	density of medium
$\rho_{particle}$	density of particle
$\boldsymbol{\rho}$	vector describing position in back focal, Fourier, or image plane of lens
θ_0	opening angle of objective lens with NA $= n_m sin\theta_0$
θ_1	angle of incidence (geometrical optics regime)
θ_2	angle of refraction (geometrical optics regime)
θ_g	angle in glass
θ_w	angle in water
θ_a	angle in air
ν	kinematic viscosity
ω	natural frequency
ξ	size parameter

a_n, b_n	Mie coefficients
A	amplitude of electromagnetic wave
c	speed of light
d	distance of modulation plane from lens
$\boldsymbol{d}$, $d_\perp$, z_d, ρ_d	vector, magnitude and coordinates of sphere position
$\boldsymbol{E}, E$	electric field
f	focal length of lens
f_p	paraxial focal position
F_{drag}	viscous drag force
F_{grad}	gradient force
F_{scat}	scattering force
g	acceleration due to gravity
H	Heaviside step function
I_0	incident intensity
J	Bessel function
k_B	Boltzmann's constant
$\boldsymbol{k}$	wavevector
$\hat{\boldsymbol{k}}$	unit vector of incident light ray
$\hat{\boldsymbol{l}}$	unit vector of incident light ray
L_1	Height of paraxial focus above coverslip
L_2	Height of paraxial focus above water layer
m	relative refractive index of particle and suspending medium
NA	numerical aperture
Δn	birefringence
n_a	refractive index of air
n_g	refractive index of glass
n_m	refractive index of suspending medium
n_p	refractive index of particle
n_w	refractive index of water
N_1	n_w/n_g
N_2	n_a/n_w

P	laser power
Q	efficiency of momentum transfer
Q_z	axial efficiency of momentum transfer
Q_ρ	lateral efficiency of momentum transfer
r	Fresnel reflection coefficient
R	sphere radius
$\boldsymbol{r}$	vector describing position in front focal or hologram plane of lens
$\hat{\boldsymbol{r}}$	vector along ray propagation direction
r_{ap}	radius of lens aperture
r_f	objective lens focus position without interfaces
r_s, r_p	Fresnel reflection coefficient, and specifically for s and p polarised light
t, t_s, t_p	Fresnel transmission coefficient, and specifically for s and p polarised light
T	temperature
T_{obj}	transmission of objective lens
E_{obj}	filed magnitude at back aperture of objective lens
$\boldsymbol{T}$	Maxwell's stress tensor
v	relative velocity of sphere and fluid
v_{max}	velocity of sphere 'just' after fall from trap
V_{sphere}	volume of sphere
w	beam waist
w_0	beam waist at focus
x	position
X	objective axial displacement
z	sphere axial position
z_1	position of first interface
z_2	position of second interface
z_{eq}	axial equilibrium position
ρ_{eq}	lateral equilibrium position

List of acronyms

AOD	Acousto-Optic Deflector
CCD	Charge-Coupled Device
CERS	Cavity Enhanced Raman Spectroscopy
DOE	Diffractive Optical Element
EOD	Electro-Optic Deflector
GO	Geometrical Optics
HOTs	Holographic Optical Tweezers
LCoS	Liquid Crystal over Silicon
LUT	Look Up Table
LWD	Long Working Distance
NA	Numerical Aperture
OAM	Orbital Angular Momentum
PDMS	Polydimethylsiloxane
QPD	Quadrant Photodiode
SAM	Spin Angular Momentum
SLM	Spatial Light Modulator
μTAS	Micro Total Analysis System

Contents

Contents **i**

1 Introduction **1**

1.1 Optical Tweezers 2

1.1.1 Arthur Ashkin 3

1.2 State of the art of optical optical manipulation 5

1.3 Aerosols 7

1.4 Holographic Optical Tweezers (HOTs) 10

1.5 Further topics 11

1.6 Aims and outline 11

2 Optical Tweezers Basics **13**

2.1 How are optical tweezers built? 14

2.2 How does it work? 18

2.2.1 Rayleigh scattering limit $R \ll \lambda$ 20

2.2.2 Geometrical Optics (GO) limit$R \gg \lambda$ 21

2.3 How are optical tweezers quantified? 26

2.4 Conclusion 27

3 Beam Shaping **29**

3.1 Static methods 30

3.2 Dynamic methods 31

3.2.1 Spatial Light Modulators (SLMs) 32

3.3 Beam shaping for optical tweezers 35

3.3.1 Holography 38

3.3.2 Algorithms 41

3.3.3 Algorithm performance 48

3.3.4 More complex tweezers and continuous patterns 49
3.4 How to implement SLMs in optical manipulation systems 50
3.4.1 Generating software 53
3.5 Optimisation 56
3.5.1 Phase characterisation 56
3.5.2 Aberration correction 59
3.5.3 Problems 61
3.6 Conclusion 62

4 Applications of Holographic Beam Shaping 63
4.1 Quantities relevant to experiments 64
4.2 Aerosols 67
4.2.1 Apparatus specific to the manipulation of aerosols 67
4.2.2 Holographic optical trapping of aerosol droplets 68
4.3 Orbital Angular Momentum (OAM) 75
4.4 Fungi 76
4.4.1 Apparatus and experimental procedure specific to fungi 79
4.4.2 Results 80
4.4.3 Discussion 85
4.4.4 Conclusion 87
4.5 Thermocapillary digital microfluidics 87
4.5.1 How it works 89
4.5.2 Apparatus and experimental specific to microfluidics 89
4.5.3 Results 90
4.5.4 Discussion 94
4.5.5 Conclusion 95
4.6 Outlook 96
4.7 Conclusion 96

5 Single Beam Studies of Trapped Aerosol Dynamics 97
5.1 Brownian motion 97
5.2 Theory 98
5.2.1 How can the parameters be measured experimentally? 102
5.2.2 Why should the dynamics of optically trapped aerosols be studied? . 104
5.2.3 Theory for power spectrum of harmonically trapped microspheres . 105

5.3 Experimental . . . 109
5.3.1 Data analysis . . . 113
5.4 Results . . . 114
5.4.1 Langevin dynamics . . . 114
5.4.2 Sizing . . . 118
5.5 Discussion . . . 122
5.6 Parametric oscillation . . . 126
5.7 Conclusion . . . 128

6 Optical Trap Modelling 129
6.1 More rigorous Geometrical Optics (GO) . . . 133
6.2 Mie scattering and Richards and Wolf theory . . . 137
6.2.1 Richards and Wolf theory . . . 137
6.2.2 Mie scattering . . . 140
6.2.3 Force calculation . . . 141
6.3 Results and discussion . . . 144
6.3.1 Comparison of geometrical optics and Mie scattering . . . 145
6.3.2 Predicting experimental observations . . . 149
6.3.3 Limits of techniques . . . 153
6.3.4 Optimisation and extension of limits . . . 157
6.3.5 Capture volume . . . 159
6.4 Shortcomings of theory . . . 159
6.5 Conclusion . . . 160

7 Conclusion and Outlook 161
7.1 Outlook . . . 161
7.1.1 Single beam studies . . . 161
7.1.2 Fungi . . . 162
7.1.3 Sizing . . . 162
7.1.4 Hydrodynamics . . . 162
7.1.5 Spherical aberration correction . . . 163
7.2 Conclusion . . . 164

References 167

Chapter 1

Introduction

Light's interaction with matter has long been a fascination of man. Trying to understand its nature has driven people to dangerous experiments; Newton stared at the sun for hours on end and placed bobkin needles around the back of his eye. It was in the late 19^{th} and early 20^{th} century when its wave and quantum nature was described in full. I cannot say light is "fully understood" as it still throws up surprises and indeed there are still controversies in its interpretation[1].

Without these descriptions of the nature of light, microscopy could not have reached its full potential as a tool for scientists. The ability to observe and study microscopic pieces of matter including crystals, plant cells, liquid crystals, pollen grains, animal cells and their infrastructure, chromosomes and nuclei, to name but a few, has lead to major advances in the understanding of our world. The evolution of normal brightfield microscopy into confocal, phase contrast, darkfield and fluorescence microscopy for example, is constantly improving the tools at our disposal hence improving our understanding further still.

Microscopy techniques have used the shaping of matter, in the form of lenses and mirrors, to manipulate light for specific purposes. In the latter half of the 20^{th} century the opposite began to occur with the advent of the laser, light began to 'shape matter'. It is well known that light can be used to control the cooling of matter at the atomic level, even so far as to create a new state of matter, the Bose-Einstein condensate. Perhaps less well known is the work which lead up, and evolved parallel, to it; the application of light to mechanically manipulate microscopic objects. Starting in the early 1970s this topic has matured considerably and shows no sign of slowing down. Now, not only can objects be observed through microscopes, they can also be repositioned, ablated, cut, probed, stimulated and isolated, amongst much more. Just as microscopy lead to advances in many diverse disciplines through providing new research tools, optical manipulation will

extend our limits of knowledge even further.

The fact that the manipulated objects are visible through microscopes means the field of research is visual and thus easily appreciated on a basic level by the general public. The ability to observe with ones own eyes the mechanical forces imparted by something as ethereal as light is not only exciting upon first introduction but remains so for years to come. The research raises more questions as it progresses and the answers found provide interesting and beautiful demonstrations of physical principles from the undergraduate level to in-depth high level academic discussions. However, the simplicity of these visual experiments should not overshadow some of the awesome abilities optical manipulation can provide. The boundaries of optical manipulation are constantly being pushed forward and this thesis should be regarded as a snapshot in time of the state of the art.

In this thesis I not only develop, but also apply optical manipulation tools for specific applications that have not been considered before. A large portion of this thesis delves deep into the understanding of the physics behind one particular application and covers a broad range of topics including hydrodynamic interactions, fluid flow, Brownian motion, light scattering, beam aberrations, harmonic potentials, stochastic processes, parametric oscillation and computational approaches. The number of topics touched on demonstrates the diverse nature of this field of research.

As the main tool used to manipulate microscopic matter with light is the optical tweezers this will be covered first.

1.1 Optical Tweezers

Optical tweezers use tightly focussed laser beams to manipulate microscopic objects. The techniques of optical manipulation have matured considerably in the four decades since Ashkin first demonstrated the acceleration of particles using radiation pressure[2]. Tight focusing however is now no longer a necessity although it is still the tool of choice. The leap forward that firmly established the field was the demonstration of a *single beam gradient force trap*, christened *optical tweezers*, by Ashkin *et al.*[3]. These tweezers have developed into a tool that is routinely used to probe biological function[4,5], colloidal dynamics[6,7], properties of light beams[8,9] as well as to facilitate stable trapping and manipulation of particles at the micron scale in further, wide ranging, disciplines. In recent years the field has started to revisit Ashkin's early experiments in the form of dual beam traps delivered through fibre optics[10] and the more precise manipulation of objects in air[11,12]. The history and understanding of the early experiments is not only interesting but provides a good starting point for our discussion.

1.1.1 Arthur Ashkin

In 1969 with a "back of the envelope" [13] calculation Arthur Ashkin gave birth to the field of optical manipulation. He simply considered the force created by the reflection of electromagnetic radiation from a perfect mirror, termed radiation pressure. Incident light with power P will have $P\lambda/hc$ photons striking the mirror per second, each carrying a momentum h/λ. Assuming each photon reflects back to its source the total momentum change of the light, and hence mirror, per second is $(2P\lambda/hc)(h/\lambda) = 2P/c$. Equivalently the mirror will experience a force $F_{mirror} = 2P/c$ in the propagation direction of the incident light. A power of 10 mW produces a very small force, $F_{mirror} = 70$ pN, but Ashkin realised its potential by considering the possibility of focusing the incident light onto a particle $\simeq 1$ μm in diameter. Continuing the poor assumption of 100% reflectivity, particles with a density $\simeq 1$ gcm^{-3} would receive an acceleration of $a_{particle} = F_{mirror}/m_{particle} \simeq 10^4$ ms^{-2} $\simeq 10^3$g. Even with the approximations made this should be easily observable.

Using a Gaussian laser beam as his source of momentum Ashkin performed the first radiation pressure experiments in late 1969 and observed, as expected, particle motion in the propagation direction of the laser. Unexpectedly, an additional force was seen that drew particles toward the higher intensity beam centre. "Particles stayed there...even if the entire beam was slewed back and forth within the chamber. Particles were being guided by the light!" [13].

During the 1970s and 1980s Ashkin published three seminal papers describing four experiments; acceleration, dual beam trapping, levitation in air and vacuum, and single beam gradient force trapping of microscopic particles. The study of these themes has recently been returned to and some are detailed in this thesis. Reviewing their history and evolution assists in appreciating the nature of this field and will therefore be briefly outlined here.

Figure 1.1 shows the apparatus used by Ashkin to observe the "acceleration of freely suspended particles by the forces of radiation pressure from...laser light" [2]. It uses a relatively simple setup with a focussed laser beam propagating horizontally through a sample containing an aqueous suspension of latex spheres. The light, having been focussed to dimensions similar to that of the particles, provides enough momentum transfer to produce observable displacement. In this setup the motion will continue until the particle reaches the sample cell wall.

Having proved the principle of acceleration via radiation pressure Ashkin performed another experiment using two counter-propagating laser beams constructed as shown in figure 1.2. A particle placed in an arbitrary position in either beam travels along its

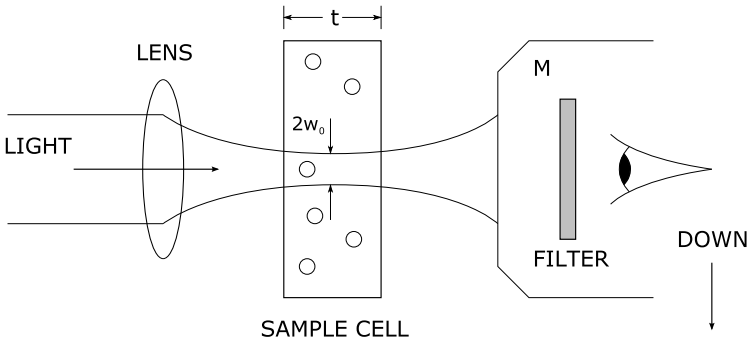

Figure 1.1: The geometry of Ashkin's first experiment in 1970 which demonstrated the acceleration of microscopic particles along the propagation direction of a tightly focused laser beam with waist w_0. The small circles represent either 0.59, 1.31 or 2.38 μm diameter particles in aqueous suspension contained in a cell with $t = 120$ μm. The sample is observed down beam through a microscope M. (Diagram adapted from Ashkin[2]).

propagation direction but no longer reaches the sample cell wall. Instead the second beam provides an equal but opposite force creating, effectively, an 'optical potential well' equidistant from each beam waist. Any displacement from the centre of this well results in a restoring force and so the particle is said to be in an 'optical trap'.

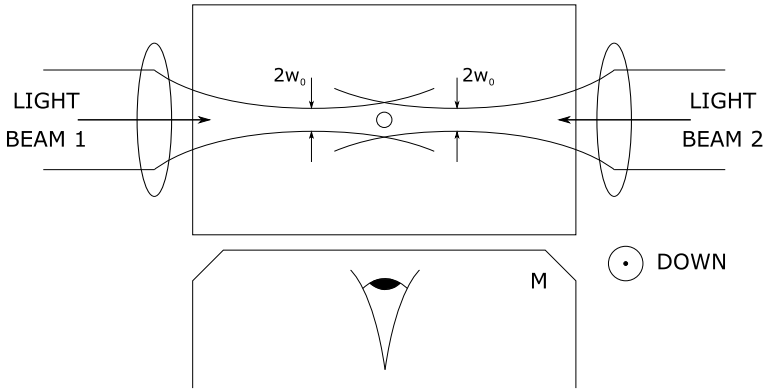

Figure 1.2: The set-up used by Ashkin to create the first 'optical trap'. Two focussed counter-propagating laser beams, with waist w_0, enter an open cell containing an aqueous suspension of micrometer size spheres. The light scattered by the particles was observed through a microscope M. (Diagram adapted from Ashkin[2]).

A further experiment in 1971 used the force produced by radiation pressure from a vertically propagating laser beam to balance a particle's weight, resulting in an equilibrium position just above the beam waist[14]. The apparatus is shown in figure 1.3 and remains similar to those previous.

An observation common to all the experiments was the microscopic particle's tendency to move into the beam centre, when viewed perpendicular from the direction of propagation. It was this 'gradient force', named after the lateral intensity gradient in a Gaussian beam,

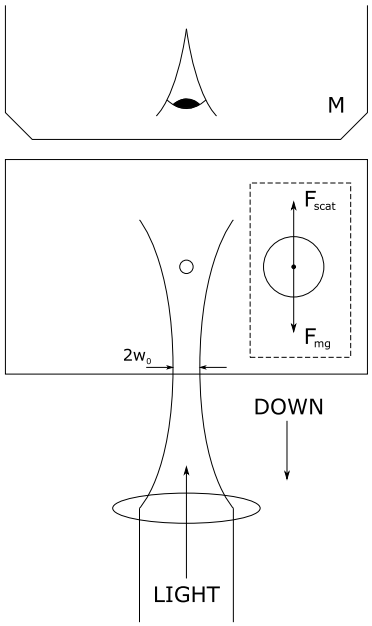

Figure 1.3: The levitation apparatus used by Ashkin. A focussed Gaussian laser beam, with waist w_0, is directed vertically upwards, against gravity, into a sealed vessel containing spheres $\simeq 15 - 25$ μm in diameter in either air or vacuum. The levitating spheres are viewed through the microscope M. Inset in the dashed box is a free force diagram of the levitating sphere. At the point of equilibrium the scattering force F_{scat} equals the spheres weight F_{mg} and thus moves neither up nor down. (Diagram adapted from Ashkin and Dziedzic[14]).

that in 1986 Ashkin and colleagues realised could be used to produce a single beam gradient force optical trap[3]. Shown in figure 1.4 is the relatively simple apparatus used by Ashkin *et al.*[3] to demonstrate the first *optical tweezers*. It is important to note that the experiment used neither counter propagating beams nor a balance of forces with gravity to produce an optical potential well and hence a stable optical trap.

1.2 State of the art of optical optical manipulation

Since its early development by Ashkin optical manipulation has mainly been applied to colloidal[6,15–20] and biological[21–25] studies in the micron size regime, situated in a liquid medium[26–28]. Many of these results are not only technologically impressive but are also of great scientific importance. The Block group directly observed the transcription of DNA into mRNA, a vital step in the synthesis of proteins, with a resolution of the order of the Bohr radius[29]. Dual beam fibre traps also demonstrated cells in the human retina have evolved to behave as optical fibres, thus solving the mystery as to why photoreceptive cells in the retina are positioned well below the surface on which light is incident. The

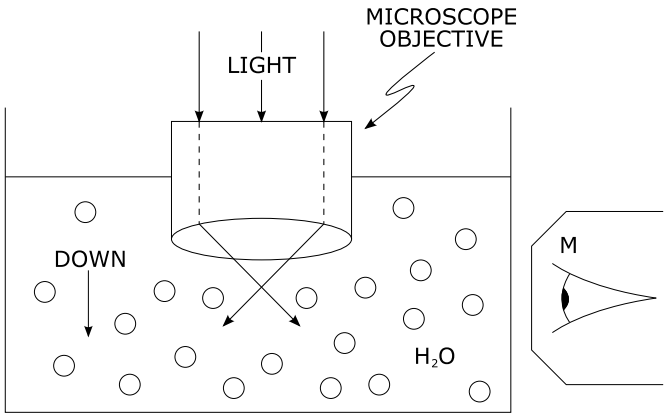

Figure 1.4: Diagram of the first 'Optical Tweezers' apparatus. An argon ($\lambda =$ 514.5 nm) laser beam is focussed down into an open cell using a high numerical aperture water immersion microscope objective lens. The cell contains an aqueous suspension of micron sized particles. The sample is viewed from the side through the microscope M. (Diagram adapted from Ashkin and Dziedzic[14]).

experiments even showed that the nucleus of cells occupy a specific position to increase forward light scattering[30]. The understanding of the transfer of spin and orbital angular momentum has advanced due to its direct observation on microscopic objects with many fundamental results[9,31–33]. More esoteric applications come in the form of optical matter[34]; the interaction or 'binding' between scattering objects meaning perturbations to one particle affects all others[35]. This 'optical matter' created through scattering can itself manipulate light[34,36].

One major advancement is the ability to manipulate multiple particles simultaneously using several different techniques[37–41]. Applications of these methods have been few but with the availability of commercial systems they are finding more uses in different disciplines[42,43]. Similar methods have allowed the shaping of beams beyond single Gaussians enabling for example applications in the sorting of biological samples[22,44] and cellular transfection[45].

The beginnings of optical manipulation mostly began with studying solid particles but its use was quickly applied to objects of similar dimensions such as bacteria[46] and mammalian cells[47]. They are now also applied in the world of chemistry to study liquid in liquid systems[48]. This interdisciplinary use continues and is where the technology really comes to fruition.

One area that has fallen behind is airborne manipulation. Through combinations of techniques, incredible results are possible with measurements of radii precise to $< 2\%$[49], and the detection of 0.1 mK temperature changes[50], all *in situ* and non-destructive.

One main group[51] has picked up the reins of airborne tweezing with the aim of furthering the understanding of atmospheric chemistry. The advances in optical manipulation have not been brought to bear on this field and is one of the aims of this thesis. Next I shall discuss the importance and interest in aerosols and hence why they should be studied.

1.3 Aerosols

An aerosol is a multiphase system composed of a suspension of fine solid particles or liquid droplets in a gas. They occur in a broad range of subject fields directly important to people's everyday lives.

Toxic airborne particles from industry and individuals' lifestyles can penetrate deep within the lungs where the body is designed with superb efficiency to exchange gas with the blood stream[52]. There is also strong evidence suggesting delivery of medication via the lungs has advantages over conventional oral delivery[53]. Clearly, understanding aerosol behaviour in the lungs and how they enter and interact with the body is relevant for both the effects of pollution on the human population and the efficacy of medicinal drugs.

Furthermore, understanding their creation can help design techniques for removal of aerosol after combustion, for example the removal of particulate non-combusted material in coal fired power stations by electrostatic precipitators.

The current interest in climate change highlights the need for confidence in scientists' explanations and predictions of how the atmosphere affects the climate. Aerosols are a massive constituent of the atmosphere and a major factor in determining its chemical balance, for example the ozone hole and acid rain[54]. They also impair visibility and contribute to radiative balance[52]. Clearly, their precise understanding is key to predicting future trends and interpreting current data and hence form part of large efforts to improve the understanding of how aerosols affect climate from the 'bottom up'[55]. When determining the effects of all the necessary factors that can change Earth's temperature the largest error on known values is from aerosols, due to lack of their understanding, as can be seen in one of many reports from the Intergovernmental Panel on Climate Change[56]. These uncertainties have not really improved since the report six years earlier[57] again highlighting the need for new tools for use in the study of aerosols.

The reasons I have given are brief but clearly the continued advancement of our understanding of aerosols is paramount.

Aerosols can be grouped into three main categories or modes. The nucleation mode consists of small emitted or newly nucleated particles with a mean radius less than 0.05 μm.

Upon growth and coagulation these particles move into the accumulation mode with radii between 0.05 μm and 1 μm. Finally the coarse mode of aerosols consists of particles with radii greater than 1 μm[52].

In terms of surface area to volume ratio, accumulation mode aerosol constitutes the largest proportion of atmospheric aerosol and therefore dominates atmospheric aerosol chemistry[54]. This mode is also able to penetrate deep into the lungs playing a major role in the interaction of aerosol with the human body. Its near wavelength size also affects visibility[52]. My work concentrates on coarse mode liquid phase aerosols, particularly relevant in drug delivery and atmospheric chemistry. However, the questions that can be answered with current techniques are limited so they will need to be altered to allow accumulation mode aerosol to be studied. Analysis of the limits and how to push them is discussed in chapters 5 and 6.

In general aerosol systems, the droplet and gas phases are coupled; changes in composition or temperature of the gas will affect the properties of the droplets and vice versa. The composition at the droplet surface can vary significantly from the bulk aerosol system[58] thus quantification of the chemistry involved cannot be determined through studying the bulk system. Instead one must analyse individual aerosol droplets.

The majority of techniques to study aerosols to date have used ensemble averaging of data over a distribution of particle sizes to infer information about the properties of single aerosols. They include methods such as impactors and cyclones for size fractionation, fibrous and porous filters for particle collection, and optical and electrostatic methods for sizing; a more thorough review is given by Reid[54]. These techniques are often destructive so evaluation of particle parameters and composition can only be followed as an average over many independent experiments. Additionally, droplet lifetime within real world samples, such as clouds, is unkown which again impacts on the precision of the properties extracted[59].

To study without ensemble averaging and destroying the object under study one must look towards methods of isolating the aerosol of interest from its surroundings. To do so the object must, ideally, be trapped at a single location indefinitely by overcoming its weight, Brownian motion if significant, and any other forces, for example, occurring from external air flows.

Several approaches have been undertaken with this aim. Sonic levitation uses the nodes within a longitudinal standing pressure wave to trap not only liquid droplets but also solid particles with radii and density in the ranges of 22 μm to 2.5 mm and $0.5 - 8 \times 10^3$ kgm^{-3} respectively, hence are generally limited to the coarse mode of aerosol[60–62]. Electrostatic levitation uses the interaction of an electric field with a charged particle to overcome grav-

ity as in Millikan's classic oil drop experiment, but is obviously limited to particles with additional charge[63]. Magnetic levitation has many tight constraints including requiring diamagnetic materials and large fields. The final method allows particles from 100 nm to 0.1 mm to be trapped; this method is the topic of my thesis; optical manipulation.

Since the early experiments of Ashkin optical manipulation studies have concentrated on experiments within liquid environments. This is understandable with the large range of interesting questions that can be answered by studying such systems. Perhaps another reason is the complexity of trapping in different environments. In particular there may have been the belief that there is not sufficient damping in air to remove energy from the object's Brownian motion to keep it trapped in a single beam gradient force trap.

However, in recent years a resurgence of interest in the ability to trap and localise particles via optical methods has lead to a 'boom' in research. Initial radiation pressure experiments looked at levitation in air, as described, with later studies on airborne liquid droplets[64]. The field has since intermittently explored more levitation experiments including the levitation of non-spherical solid particles[65], solid[66] and liquid[67,68] particles for further analysis by Raman spectroscopy, and frozen droplets[69,70].

Levitation has its problems as the particles are not necessarily very stable nor well localised and their imaging is often difficult leading to mis-interpretation of results[71,72]. Although some stabilisation of levitated particles was achieved[73], a true single beam gradient force trap would improve particle localisation, control, movement and observation. Also it would allow for better integration with the wide range of powerful analysis techniques developed for optical tweezers and enable the sampling of smaller particle sizes. Only a few studies using the optical tweezing of aerosols have been described in literature. Firstly Omori *et al.*[11] used a piezoelectric transducer to 'shake' a coverslip with microparticles resting on it until one 'jumped' into the optical tweezers created above by a specialised air microscope objective lens. Magome *et al.*[74] demonstrated that water droplets could be stably tweezed by creating them in a supersaturated environment with a nucleation site resulting from a reaction between hydrochloric acid and ammonia, and subsequently studied their growth.

The piezoelectric method has been attempted several times in my group and others with no success as the van der Waals forces between coverslip and particle are too great. One method that has not been tested to enable the tweezing of airborne particles is the use of a high power pulsed laser to break the bond between coverslip and sphere as has been done for levitation experiments[75]. This method however could be difficult due to the high peak powers and carefully constructed microscope objective lenses needed for tweezing.

The first meaningful forays into the optical tweezing of liquid aerosols were performed by

Hopkins *et al.*[12] and King *et al.*[76]. Hopkins *et al.* successfully trapped $2-7$ μm radius water or decane droplets over a range of powers and with various microscope objective lenses. Of great benefit when studying airborne droplets is their obvious preference to forming spherical bodies, due to their high surface tension. These spheres act as very good optical cavities and so coupling their tweezers with a technique called cavity enhanced Raman spectroscopy (CERS)[77], dependent on the morphology of the illuminated object[68], enables their radius to be measured incredibly precisely, to within $< 2\%$[49]. The same spectroscopy can be used to study composition allowing systematic studies of processes on and within aerosols to be carried out with the atmospheric sciences being the main beneficiaries[58] as demonstrated by King *et al.*

Only a handful of researchers and groups have studied or used airborne tweezing since with none considering solid particles. The localisation of droplets in this way has mainly allowed their use as atmospheric probes. For example, they have been used to probe the Raman spectra of a trapped seawater droplet[76], have helped the characterisation of organic layers on the surface of inorganic aqueous aerosols[78] and many others performed by the Reid group in Bristol.

There has been little development of techniques and methods for the trapping of airborne particles until recent years[79–82]. Also no investigation of the physics that governs them has been carried out, although some of their potential in accessing interesting physics has been realised with experiments in optical binding[71] and Brownian oscillators[83].

The further development, exploration of parameter space, and understanding of optical manipulation techniques for airborne particles is a major theme of this thesis. It is the first time a detailed study of the properties and parameters has been carried out not only resulting in its detailed understanding and explanation, but also in novel applications for the field of airborne trapping. There are clear advantages to increasing the number of particles that can be trapped and the method chosen, holographic optical manipulation, forms the second theme of this thesis.

1.4 Holographic Optical Tweezers (HOTs)

In the ten years since diffractive optical elements were first used for optical tweezers[84] and the seven years since the first holographic optical tweezers[85] a large number of journal articles have been published on the subject. For example, improvements in algorithms have been developed[41,85–88], slightly different implementations have been described[88–93], improvements in computation hardware have been demonstrated[94,95], novel user interaction techniques explored[96–98] and detailed studies of precision and limits undertaken[99–101].

However, only relatively few applications have been found with the majority centered on tweezing objects of various different geometries and morphology[102–105]. There has been a slow increase in the past two to three years of truly novel applications; they have been used to assist in the microscopy of cells[106], studying objects at an air-water interface[107], creating microfluidic pumps and flow sensors[108], studying two dimensional fluids[109,110], and are starting to be used as multipoint force transducers[111]. In chapter 3 I shall discuss three new areas of application of HOTs extending the disciplines over which they are used and moving away from the manipulation of simple aqueous suspensions of various sphere like objects.

1.5 Further topics

Aerosols and holographic optical tweezers are the underlying themes of this thesis, however, as mentioned, three novel applications of HOTs will also be discussed. Each have their own subtleties which will be introduced and discussed later within their dedicated chapters and sections.

1.6 Aims and outline

One aim of this thesis is to document the information necessary to perform the experiments described hence benefit future researchers wishing to investigate similar topics. So, in chapter 2 I will describe the building of a basic optical tweezers, how to understand their principle of operation, and some ways to quantify and measure their parameters.

Another aim is to improve the versatility of holographic optical tweezers and apply them to diverse research fields outwith physics. Before being able to do this one must understand how they operate and are constructed. In chapter 3 I will introduce the various methods available to beam shape before going on to describe how my choice of device, the spatial light modulator, operates. I will describe the best methods for kinoform generation in holographic optical tweezers and discuss their performance in the context of optical traps. The integration of spatial light modulators in optical manipulation will be explained along with the generation software I have created. Finally, I will consider methods of optimisation in order to maximise the quality of the beam shaping performed.

Having described how optical manipulation is performed on both simple single beam and complex holographic levels I will, in chapter 4, demonstrate three original applications of holographic optical tweezers.

It has been described how the development of optical tweezing techniques can improve tools for many different areas of research. Pushing these tools toward improving aerosol investigation is another aim of this thesis, but to really push the limits one must understand the physics that governs the system. To this end I investigate, in chapter 5, the mechanical parameters of liquid aerosols trapped in optical tweezers.

One piece of physics that cannot be easily inferred through the techniques of chapter 5 is the optical forces acting on the objects due to the momentum of light. So, in chapter 6 I consider the computational modelling of optical tweezers in an attempt to understand the remaining physics of the system.

Finally, in chapter 7, I discuss where the work of this thesis leaves the field of research and what should be done in future.

Chapter 2

Optical Tweezers Basics

The field of optical tweezers is full of terminology unfamiliar to the uninitiated. Before tackling the main body of the thesis I shall begin by describing how a simple optical tweezers is constructed and operates, thus setting a background for the reader. A large amount of variation is found in the literature but only a basic optical tweezers will be described here which is the starting point for any laboratory.

In this chapter I neglect both gravity and buoyancy, unless otherwise stated, to simplify the discussion without loss of generality. Indeed for the majority of work this is a reasonable approximation with the objects under study having approximately the same density as their surrounding environment.

Common terms throughout this thesis are the two directions axial and lateral; referring to the directions parallel and perpendicular to the beam propagation direction and also gravity where applicable, respectively. These definitions are shown in figure 2.1.

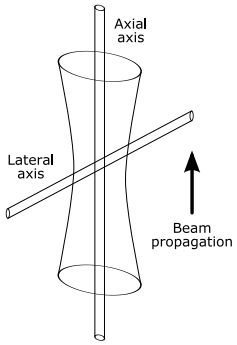

Figure 2.1: Definition of the axes used in this thesis. The axial axis is along the beam propagation direction and centred on the beam axis. The lateral axis is perpendicular to the beam propagation direction and crosses the axial axis.

2.1 How are optical tweezers built?

For the simplest optical tweezers the equipment does not need to be of the highest standard. However, as one wishes to improve the nature of experiments then specialised equipment is necessary, which will be discussed in later chapters. There are eight main components used to construct an optical tweezers. A source of trapping light, namely a laser, a microscope objective lens, a sample of interest, an illumination source, steering mirrors, a dichroic mirror, a camera, and finally an application specific set of optics between laser and objective lens. The two most commonplace designs are 'inverted' and 'non-inverted' where the laser propagates toward the laboratory ceiling or floor respectively. A simple schematic of an entry level optical tweezers in the inverted geometry is shown in figure 2.2 along with the eight main components.

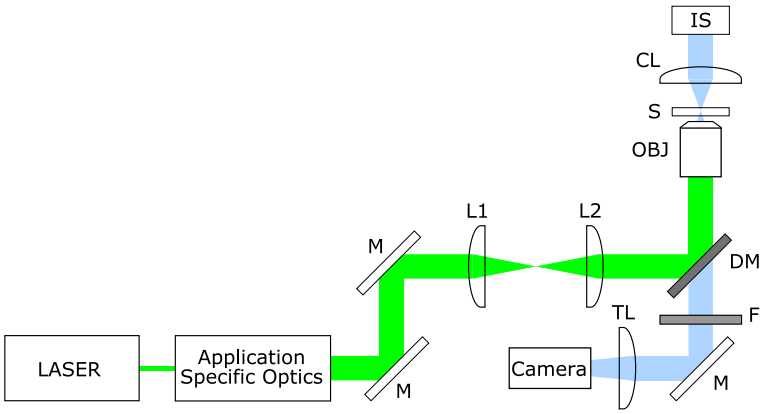

Figure 2.2: A basic optical tweezers. A laser beam passes through a set of application specific optics and is then steered into the back aperture of a microscope objective lens (OBJ) via steering mirrors (M) and lenses (L1 and L2). The dichroic mirror (DM) allows the transmission of the image light but reflects the trapping laser light. The image light is passed through a filter (F) to remove any unwanted laser light and imaged onto a camera via a tube lens (TL). The objective focusses the trapping light into a sample (S) which is illuminated via a condenser lens (CL) and illumination source (IS).

The most common arrangement I have observed is the inverted geometry and hence I will tackle the subject from this perspective. The choice between the two can be crucial when wanting to perform the experiments described within this thesis, as will become obvious in chapter 6. Horizontally propagating beams are feasible and practiced in certain applications[112] but I prefer to propagate the beam with or against gravity as this can keep the experiment cylindrically symmetric thus simplifying certain aspects of analysis.

The detailed specifications of the components required can vary greatly with application and I will not outline what is necessary for each as there are many review articles that provide an introduction[19,20,24–28,77,113], but, I will look at each component's purpose and

how it fits into the apparatus.

The ***laser*** produces a collimated, monochromatic, and coherent Gaussian beam to enable focussing to a diffraction limited waist at the focussing lens' back focal plane. This produces highly convergent light propagating through an area comparable in size to objects in the microscopic size regime. The focussing ability of an objective is characterised by its numerical aperture, $\mathrm{NA} = n_m \sin\theta$ where θ is the cone of focus half angle. The larger this NA the tighter the focussing.

The ***microscope objective*** lens serves three purposes in most optical tweezers. It is used to image the sample in exactly the same manner as when used in a commercial microscope. It also focusses the beam from the aforementioned laser to a diffraction limited waist approximately the same order of magnitude in size as the object under study. Finally, it produces highly convergent light with some rays considered to be travelling near perpendicular to the beam propagation direction. Microscope objective lenses used in the context of optical tweezers are usually oil immersion. The aim is to refractive index match the glass objective to the microscope slide by using viscous liquids of specific refractive index.

The ***sample*** is perhaps the most simple of elements. Most objects to be trapped are suspended in fluid media, namely water, and their refractive index n_p must be higher than the surrounding medium's. This produces forces in the correct direction as I will show later. It is possible to trap objects with lower refractive indices but this requires a slightly more sophisticated approach. The sample normally consists of a shallow well above a microscope coverslip that allows transmission of the focussed beam to just inside the well. A second coverslip is placed on top of the sample to enclose the system and allow illumination from above. Mounting the sample on an x, y, and z translation stage enables control over the position of the tweezer in the sample plane without any beam movement.

The ***illumination source*** and the manner in which it is conveyed to the sample is of great importance. The simplest method is to place the source directly above the sample; slightly more efficacious is critical illumination where the source is focussed on the sample using a lens. Finally, a far superior method is Köhler illumination, where the source is relayed to the sample via multiple lenses and controlled with adjustable diaphragms, which I shall discuss specifically in the next section.

Although feasible without ***steering mirrors*** they are a helpful addition to optical tweezers and must be used if two dimensional manipulation is required without translation stages. The optimum location for these mirrors is discussed in detail in the following pages.

In their simplest form the ***application specific optics*** are two lenses designed to expand or reduce the incident laser beam before entering the microscope objective. This expansion is again a critical part of an optical tweezers as we shall see later. In more complex systems the optics can take the form of holographic elements, steerable mirrors, gratings, spatial filters, special glass optics, and much more.

Traditionally optical tweezers take the form of a classic microscope arrangement with an imaging objective and condenser lens for illumination. To create an optical tweezers an extra light path must be inserted for the laser which can practically only be via the condenser or microscope objective lens. As objective lenses are designed to output a collimated beam of light producing an image at infinity they are perfectly suited to focussing collimated input beams to diffraction limited waists. This, along with the appropriate field of views normally obtained, makes the imaging objective the ideal tweezers lens. However, this still poses the problem of placing the laser and image paths coincident. To enable this a ***dichroic mirror*** is used that only reflects the laser's wavelength of light and transmits the remaining illumination light. As such the beam can be reflected into the objective whilst still allowing the image to propagate onto the camera (via appropriate tube lenses). The mirror also helps to remove any scattered laser light from being imaged on the camera which are often sensitive to wavelengths other than those in the illumination source. Sometimes a filter is also needed to completely remove any unwanted scattered light. It is also possible to use the imaging and trapping objective as the illumination condenser but this choice is really down to the type of sample being imaged or trapped.

Finally the last element is the ***camera***. In this thesis a Firewire CMOS camera is used that through adjustment of its area of interest allows videos to be taken at speeds up to 1000 frames per second. For basic tweezers a simple 30 frames per second analogue CCD is sufficient. The quality of the camera can be important when the images produced are used to extract data for quantitative analysis.

I will now look in detail at Köhler illumination and steering mirrors as they convey important messages that are necessary when building an optical tweezers.

Köhler illumination

It is hard to overestimate the importance of good illumination and in many setups this is the limiting factor in image quality. There is no point in having a high NA microscope objective lens to image samples if the light being used to illuminate the sample does not also converge with high NA. Köhler illumination is illustrated in figure 2.3; it provides a uniform field of illumination across the sample field of view and allows control over

contrast and resolution.

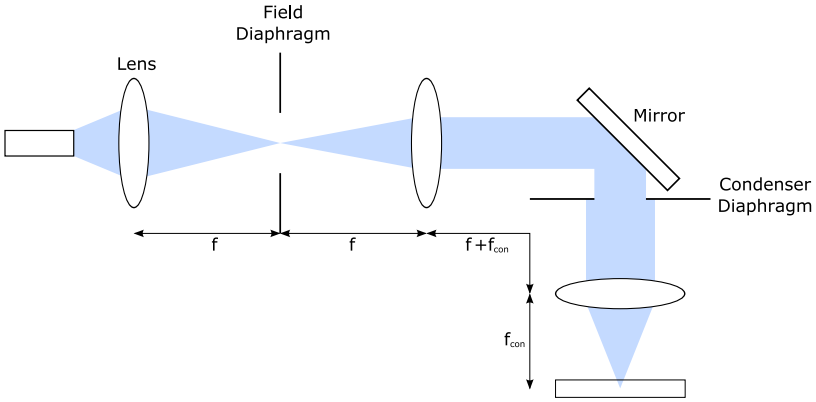

Figure 2.3: Köhler illumination. The light path shows the path of the imaging rays. The lens system is arranged to image the illumination source onto the condenser diaphragm which is then imaged into the sample by the condenser lens to provide a uniform illumination. The lens system also images the field diaphragm into the sample plane to reduce glare and hence increase image contrast. Adjusting the condenser diaphragm alters the resolution and contrast of the image, which at the correct balance improves image quality.

A 4f imaging system is used to image the lamp structure, whether it be a filament or fibre bundle, onto the condenser diaphragm. A second 4f imaging system, using the condenser and penultimate lens in the optical train images the field diaphragm into the sample plane.

Adjustment of the field diaphragm reduces glare and hence increases contrast, however, adjustment of the condenser diaphragm alters both the contrast and resolution of the image. A balance between contrast and resolution has to be determined depending on the optical properties of the sample under study.

Steering mirrors and conjugate planes

In order to manipulate objects in two dimensions the beam needs to move laterally in the focal plane of the trapping objective lens. Simple ray optics allows one to clearly see that collimated beams entering a lens at an angle produces this lateral shift of focus in the focal plane. This could be simply achieved by displacing an additional lens off-axis or placing a tiltable mirror before the focussing objective lens. However, the first option will induce additional aberrations and both options will shift the beam so it is no longer centred on the back aperture of the lens, thus deforming the focus, creating an asymmetric focus and trap.

The solution is to place the objective at one end of a 4f imaging system, with a tiltable mirror at the other, as illustrated in figure 2.4. This illustrates several conjugate planes

which are defined as planes whose intensity distribution is an image of the intensity distribution across a corresponding plane[114]. When set up in this way an angular displacement at the mirror has a matching angular displacement at the objective back aperture, without any lateral movement, thus creating a symmetric focus and trap. This is the ideal steering mirror configuration but in reality other constraints may prevent it from being possible and less precision in the relative locations of the lenses and mirrors can be tolerated.

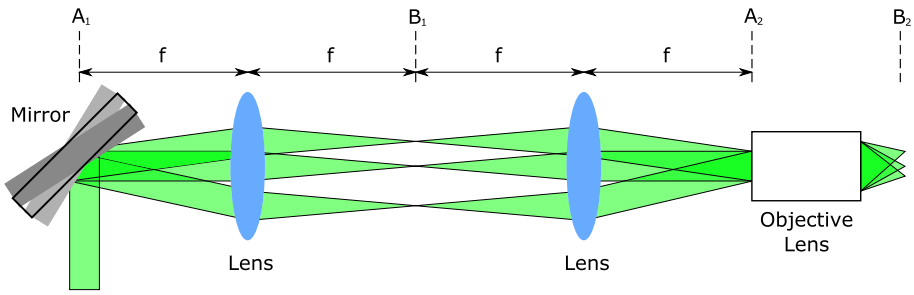

Figure 2.4: A steering mirror and objective setup in the ideal manner to achieve lateral control of foci in the sample plane. Planes A_1 and A_2, and B_1 and B_2 are conjugate to each other. Angular displacement of the mirror results in angular deviation of the laser beam. As the planes are conjugate this angular deviation also occurs as it enters the back aperture of the objective lens. An angular deviation into the back aperture of the objective lens results in a lateral displacement of the focus in the sample plane. The device can also be thought of as imaging plane B_1 to its conjugate B_2. The rear of the objective in this case coincides with its front focal plane. f is the focal length of the lenes.

2.2 How does it work?

A rigorous description of how the forces in optical tweezers arise is complex and be will discussed in chapter 6. Here I shall give a somewhat hand waving description that will allow the reader to appreciate the principles of optical tweezers which can be very helpful from day to day in the laboratory. These ideas can accurately explain the phenomena observed when looking in detail at colloidal systems but the ideas begin to break down when considering some of the experiments contained within this thesis and new extensions to the more rigorous theories must be developed.

Following tradition[115] the force created by the interaction of incident radiation with dielectric particles in optical tweezers is resolved into two separate components. One is the scattering force, which causes acceleration of particles in the light's propagation direction, the other is the gradient force, which draws particles into regions of higher intensity.

As stated earlier, in order to observe these two forces the laser beam is focussed to a size similar in dimensions to the particle. This allows the majority of the light to be incident

upon the particle while also creating a high spatial intensity gradient. Focussing the light to pass through an area ~ 1 μm in diameter increases the spatial intensity gradient $\simeq 10^6$ times, thus providing a highly inhomogeneous electric field.

Consider the effect of the two force components individually on a dielectric particle. The scattering force can be understood by simply extending Ashkin's back of the envelope calculation (see section 1.1.1). In reality a particle is not a perfect mirror and light is scattered in various directions and also partially absorbed. Both processes still cause a momentum change between incident and scattered light, and hence the particle. If one would like to trap an object with a single beam then the scattering force must be overcome with an equal but opposite force acting back along the beam propagation direction, as Ashkin showed[3]. If the particle is spherical and centred about the axial axis the scattering and absorption will be symmetric and all force components perpendicular to the beam will cancel each other out resulting in a force along the propagation direction alone.

Normally the scattering component will dominate, as demonstrated and taken advantage of in acceleration and levitation experiments. However, a tightly focussed laser beam creates a region of high intensity gradient where, as basic electrodynamics show, a point dipole placed in an inhomogeneous electric field will experience a force along the field gradient[116]. The laser induces fluctuating dipoles in the dielectric particle and their interaction with the highly inhomogeneous electric field at the beam focus gives rise to the gradient force. This force is proportional to both the dielectric's polarisability and the magnitude of the intensity gradient[28].

This simple view using point dipoles is clearly inappropriate for a large number of objects studied. Their finite extent complicates matters such that the calculation of forces created in an optical tweezers falls into three categories depending on the sizes of the objects under study relative to the wavelength of trapping light.

Each category, or regime, is shown schematically in figure 2.5. Firstly, the Rayleigh regime is appropriate where the particle's radius is far below the wavelength of trapping light, $R \ll \lambda$. Secondly, the geometrical optics regime is suitable where the radius is far greater than the wavelength, $R \gg \lambda$. Finally, the third regime encompasses the parameter space in between, where the radius is approximately that of the trapping wavelength, $R \simeq \lambda$.

I shall now briefly discuss the former two limits but will leave the latter for chapter 6 as it is far more complex.

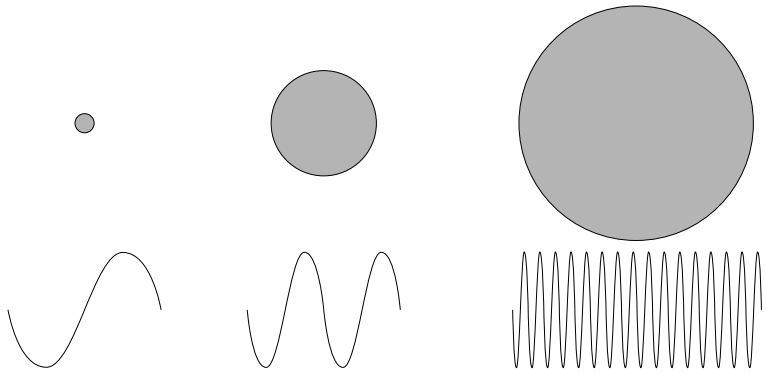

Figure 2.5: Illustration showing the relative dimensions of trapping laser wavelength and particle for three different limiting regimes over which the forces on particles can be calculated. Left) Rayleigh regime; $R \ll \lambda$. Centre) Mie regime; $R \simeq \lambda$. Right) Geometrical optics regime; $R \gg \lambda$.

2.2.1 Rayleigh scattering limit $R \ll \lambda$

Spherical particles in this limit are treated as point dipoles allowing the force to be separated into two components. The scattering force, F_{scat}, is due to the absorption and re-radiation of light by the dipole[28], directed along the axis of incident light. It is given by[3]

$$F_{scat} = \frac{I_0}{c}\frac{128\pi^5 R^6}{3\lambda_0^4}\left(\frac{m^2-1}{m^2+2}\right)^2 n_m, \tag{2.1}$$

where I_0 is the intensity of incident light, R is the radius of the sphere, c is the speed of light in vacuum, λ_0 is the wavelength of the light, n_m is the suspending mediums refractive index, and $m = n_p/n_m$, the ratio of the refractive indices of the particle and medium. The second component, the gradient force, F_{grad}, is directed with the intensity gradient at the beam focus and given by[3]

$$F_{grad} = -\frac{n_m}{2}\alpha\nabla E^2 = -\frac{n_m^3 R^3}{2}\left(\frac{m^2-1}{m^2+2}\right)^2 \nabla E^2, \tag{2.2}$$

where E is the electric field, α is the particle's polarisability and the remaining symbols retain their same meaning.

The two forces are opposed in direction so to achieve a stable axial trap, against the lasers propagation direction, the ratio of F_{grad} to F_{scat} must be greater than unity[3]. F_{scat} is directly proportional to intensity while F_{grad} scales with intensity gradient so simply adjusting the laser power is insufficient to form the stable state. Instead the intensity gradient of the focussed laser beam must be increased to change F_{grad} alone. In most standard optical tweezers this is accomplished by focussing the laser with a high numerical aperture and high magnification immersion microscope objective lens which gives a small

and highly converging focal point in the sample plane.

Outside the Rayleigh regime the optical force no longer naturally splits into the scattering and gradient components but the nomenclature is kept throughout.

2.2.2 Geometrical Optics (GO) limit $R \gg \lambda$

When the radius of light scattering particles is much larger than the wavelength of the trapping light the scattering becomes independent of the wavelength and ray optics can be used to calculate the optical forces on the particles. Although the ray optics regime's quantitative results may not always apply, its qualitative results remain appropriate and useful for understanding optical tweezers.

Consider a silica sphere, suspended in a medium with a lower refractive index, placed near a tightly focussed Gaussian laser beam, as depicted in figure 2.6. Due to the intensity gradient in the focussed beam more intense light passes through the left of the sphere than the right, indicated by the larger arrows. The higher refractive index sphere acts as a small positive lens, refracting the rays toward each other.

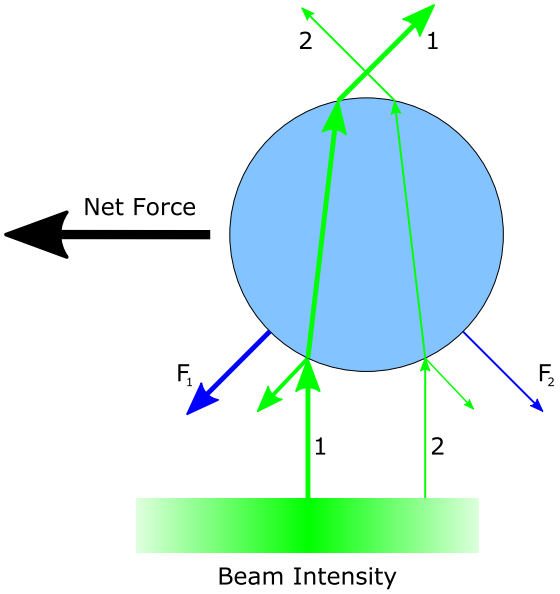

Figure 2.6: Lateral Trapping. The larger the arrow the higher the light intensity and the larger the forces. The sphere pushes more light to the right than to the left so by Newton's third law the light pushes the sphere to the left.

The best way to understand the forces qualitatively is as follows. As more intense light enters the left of the sphere, the sphere pushes more light to the right than the left, thus by Newton's third law the light pushes the sphere more to the left than the right. Overall

the sphere is drawn towards the beam centre.

At the beam centre the sphere exists at a lateral equilibrium position where any displacement from the centre results in a restoring force. This simple thought experiment shows how particles are trapped laterally but how does the gradient force overcome the scattering force to create a stable axial trap? There are two cases to consider; where the sphere is either above or below the beam focus. If the sphere centre is above the beam focus, represented by the black spot in figure 2.7, it will push the light in a more upward direction than when incident and thus the light pushes the sphere downwards. In the second case the sphere centre is below the beam focus, figure 2.8, and directs the refracted light in a less upwardly direction than when incident so the sphere is forced upwards. In both cases the sphere is drawn toward the beam focus.

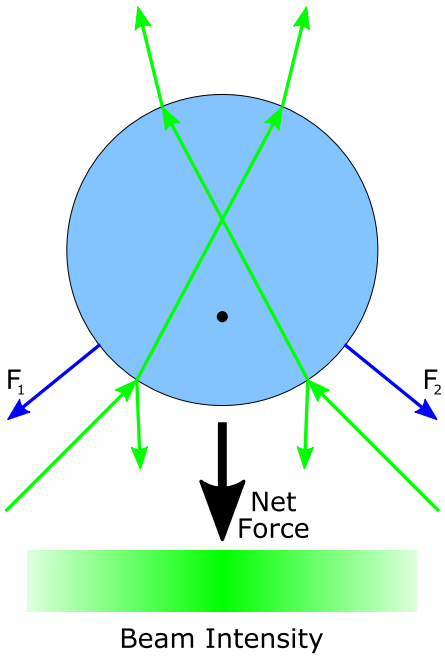

Figure 2.7: Axial Trapping. With the sphere above the focus (black spot) the rays are refracted upward. From Newton's third law the effect of light being pushed up is to push the sphere down.

The more quantitative approach to the forces created in the ray optic regime on which the preceeding is based was developed by Roosen[117–120] and applied to single beam gradient force traps by Ashkin[115]. It begins with a known distribution of parallel rays entering the back aperture of an objective lens assumed to focus to a point. The lights reflection and refraction at the surface of a sphere which contribute to the force is calculated for a single ray together with all the internally reflected and refracted rays. The exact geometry of the system is detailed in figure 2.9.

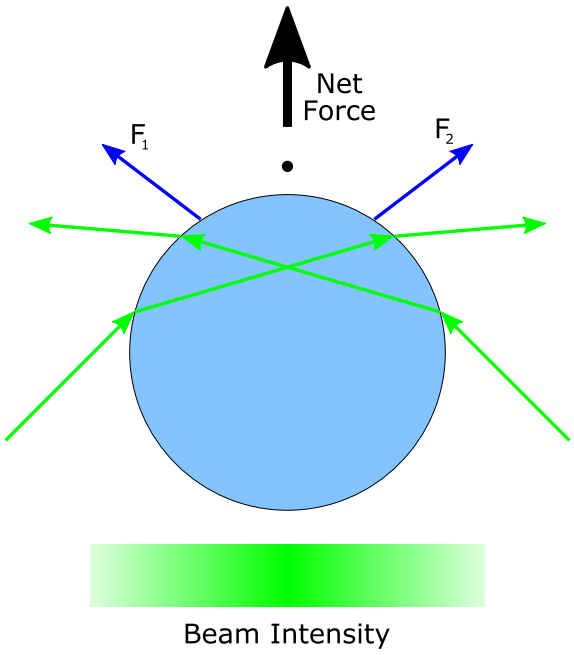

Figure 2.8: Axial trapping. With the sphere below the focus (black spot) the rays are refracted more obliquely. From Newton's third law the effect of light is to push the sphere up.

The force, F, due to a single ray of power P, on a transparent sphere in this geometry is then[24,115]

$$\boldsymbol{F} = \boldsymbol{F}_{scat} + \boldsymbol{F}_{grad} = \frac{n_m P}{c}\left[\left(1 + r\cos 2\theta_1 - \frac{t^2\left[\cos\left(2\theta_1 - 2\theta_2\right) + r\cos 2\theta_1\right]}{1 + r^2 + 2r\cos 2\theta_2}\right)\hat{\boldsymbol{k}} + \left(r\sin 2\theta_1 - \frac{t^2\left[\sin\left(2\theta_1 - 2\theta_2\right) + r\sin 2\theta_1\right]}{1 + r^2 + 2r\cos 2\theta_2}\right)\hat{\boldsymbol{l}}\right] \tag{2.3}$$

where θ_1 is the angle of incidence, θ_2 is the angle of refraction, $\hat{\boldsymbol{k}}$ and $\hat{\boldsymbol{l}}$ are unit vectors parallel and perpendicular to the direction of the incident ray, r and t are the Fresnel reflection and transmission coefficients respectively, and the remaining symbols retain their previous meaning. The total force acting on the sphere is just the sum of the vector $\boldsymbol{F}$ for each constituent ray of the beam that originally entered the objective lens' back aperture.

Using figure 2.9 and equation 2.3 it is clear the smallest forces occur back along the beam propagation direction and to achieve a good trap all efforts must be made to maximise the forces in this direction. Increasing the laser power alone will not do this, the two unit vectors $\hat{\boldsymbol{k}}$ and $\hat{\boldsymbol{l}}$ must be rotated. As the two unit vectors are parallel and perpendicular to the incident ray the rotation is simply achieved with an increase in angle of incidence, θ_1. This leads to a most significant conclusion; a highly convergent laser beam must be used

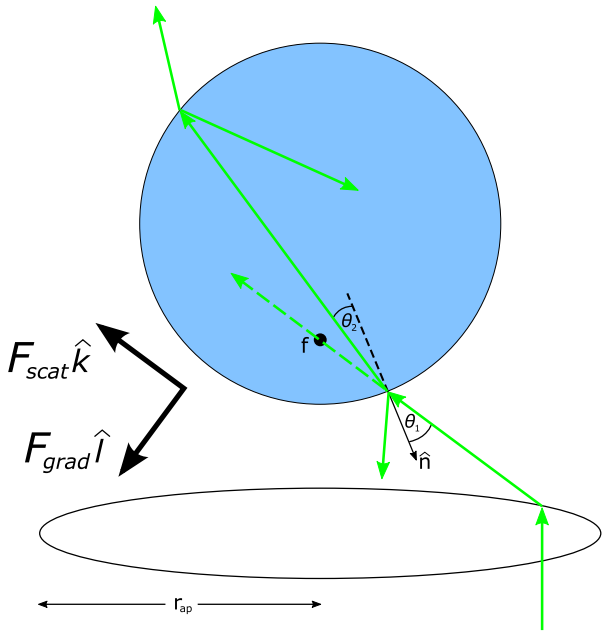

Figure 2.9: Geometry of the system considered when calculating the force on a dielectric sphere in the ray optic regime. θ_1 is the angle of incidence, θ_2 is the angle of refraction, $\hat{\boldsymbol{k}}$ and $\hat{\boldsymbol{l}}$ are unit vectors parallel and perpendicular to the direction of the incident ray, $\hat{\boldsymbol{n}}$ is the unit normal vector, f is the focal point, r_{ap} is the radius of the objective back aperture, and F_{scat} and F_{grad} are the scattering and gradient forces respectively (adapted from Svoboda and Block[24]).

to increase the number of rays incident at large angles and hence increase trap stability.

The forces calculated in the two regimes described are exact and very good when studying objects well within their limits. Unfortunately the particles normally trapped within optical tweezers have a radius that falls within an order of magnitude of the trapping wavelength and cannot be accurately described by either Rayleigh scattering or geometrical optics theory. I will discuss in chapter 6 how these descriptions fair against more realistic ones. In the meantime it should be re-iterated that the ideas presented in the previous two sections do provide some interesting insights into the different parameters that affect optical tweezers and the things one must consider when designing them which I shall now briefly discuss.

Both theories imply simply increasing the laser power will not help form a stable optical trap. The magnitude of the vector in the negative axial direction must be increased. Using the geometrical optics model Ashkin showed the ratio of the beam waist incident on the lens to the lens aperture is an important parameter in governing the maximum axial restoring trapping efficiency[115]. The larger this ratio the stronger the axial trap due to an increase in gradient component of the optical forces. This is because the external rays

in the focussed beam effectively have a greater relative intensity now that the Gaussian beam's rays at the extremities are not entering the back aperture of the objective lens. This is an important criterion for optical tweezers; the back aperture of the objective lens should be slightly overfilled to optimise the trap efficiency and stability in the axial direction.

Another way to improve the performance is to increase the converging angle, NA, of the focussed beam which in turn creates rays of light with larger angles of incidence on the sphere. These 'new' rays have a larger component of force acting in the negative axial direction than the previously most external rays which helps to create a more stable trap.

Along with an increase in NA a decrease in wavelength allows focussing to a smaller diffraction limited volume. If wishing to trap sufficiently small particles this becomes important to ensure the external rays (the ones that have a large gradient relative to scattering vector) are incident on the particle. These two effects are nicely summarised by the beam waist after focussing by a lens, given by

$$w = \frac{\lambda}{\pi \mathrm{NA}}, \tag{2.4}$$

where w is the beam waist and the other symbols retain their same meaning.

Although more complex the effect of changing the relative refractive index between particle and medium can be considered as follows; an increase in the relative refractive index between sphere and medium will increase Fresnel's reflection coefficient for both polarisations and hence the scattering force, in turn increasing the force in the positive axial direction. However, there will be an associated increase in the gradient force due to the light being refracted more at the medium to particle interface. The interplay between these two points is complex and can only really be elucidated through numerical modelling.

If the refractive index of the particle is less than that of the surrounding medium, $n_p < n_m$, then one effect would be immediately noticeable. Considering the lens analogy of geometrical optics, the light rays would be refracted in the opposite sense creating forces in the opposite direction to those previously considered. This will result in the particle being repelled from regions of high intensity gradient. Clearly, it is important that the relative refractive index, $m = n_p/n_m > 1$ to enable trapping in a Gaussian beam. There are ways to circumvent this requirement but they are not of concern to this thesis.

It is also clear that removal of the central core of the beam will decrease the scattering to gradient force ratio. Ashkin used a doughnut mode (TEM_{01}) rather than a Gaussian beam in his calculations to show this is true because the highly scattering centre rays do not exist[115]. This has also been shown to be the case experimentally [121].

Finally it is important to consider an obvious problem with geometrical optics theory. The theory is size-independent, but, as any experimenter will quickly observe there are certain particle sizes that trap far better than others and can withstand larger external forces before falling from their trap (even with the drag difference due to size taken into account). This is a problem with the limiting regime in which the theory operates and to obtain a more realistic explanation of observations more complex theories are used, as is done in chapter 6.

2.3 How are optical tweezers quantified?

There are several parameters that quantify the performance of an optical tweezers and I shall briefly describe the most basic ones here. There is the efficiency with which light momentum is transferred to a force, the stiffness with which the particle is retained in the trap, and the potential well the trap forms.

I provide the easiest method to measure the trap efficiency but an explanation of how the others are determined is more complex and is more suitably discussed in later chapters.

Efficiency

Following tradition[115] the magnitude of trapping forces is given by

$$F = Q\frac{n_m P}{c}, \tag{2.5}$$

where P is the power in the incident laser beam, n_m is the suspending medium's refractive index, c is the speed of light in vacuum, and Q is a dimensionless parameter describing the efficiency with which the power is transferred to a force[27]. Q depends upon physical parameters of the tweezing system which are the numerical aperture of the focussing objective lens, the laser wavelength and mode structure, the light polarisation state, the geometry of the trapped particle, and the ratio of the particle's refractive index to the surrounding medium's[24].

I define both an axial and lateral efficiency, Q_z and Q_ρ respectively. To experimentally determine Q_z, for a given power, a particle is trapped and the power reduced until it falls away in the axial direction. This gives the power needed, P_{min}, to just overcome the weight of the particle and hence, taking into account buoyancy, the axial efficiency is given by

$$Q_z = \frac{(\rho_{sphere} - \rho_{medium})\, V_{sphere} g c}{n_m P_{min}}, \tag{2.6}$$

where ρ_{sphere} and ρ_{medium} are the particle and medium density respectively, V_{sphere} is the sphere volume and g is the acceleration due to gravity. The simplest method to find Q_ρ is to laterally displace the trapped sphere at increasing velocity until it falls from the trap. Equivalently the sphere can remain stationary while the fluid is moved. The increasing velocity, v, increases the drag force F_{stokes} acting on the sphere, given by Stokes' law,

$$F_{stokes} = -6\pi\eta R v, \tag{2.7}$$

where η is the dynamic viscosity of the medium and R is the sphere radius, with the maximum force occurring just before the particle falls from the trap[†]. Thus it is simple to calculate Q_ρ through

$$Q_\rho = \frac{6\pi\eta R v_{max} c}{n_m P}, \tag{2.8}$$

where v_{max} is the sphere velocity just after release from the trap. This method's principle still applies for non-spherical objects as long as its associated drag is correctly determined, which can be very complex.

Stiffness

The force exerted by the light on a particle is usually considered to be Hookean thus giving a restoring force $F = -\kappa x$. Its measurement is slightly more complex and will be discussed in chapter 5 but simplistically it is related to the gradient of the force on the particle as a function of displacement.

Potential

Finding the potential is relatively straightforward if the force versus displacement is known by using $U_r = -\int F dr$, except one must be careful to define the correct value of the potential at infinity. If the full force curve is unknown more complex experiments need to be carried out to determine the shape and size of the potential well[123,124].

2.4 Conclusion

An outline of how to build, understand and quantify a simple single beam optical tweezers has been described. Should one wish to improve the apparatus, develop a more advanced

[†]It should be noted that this treatment is rather simplistic with any lateral movement also resulting in axial displacement [122].

understanding or provide more precise physical explanations, the basics covered in this chapter are a useful background.

In the next chapter I delve into my first more advanced optical technique; holographic beam shaping.

Chapter 3

Beam Shaping

In the preceding chapters I have discussed the development of optical manipulation based around the use of Gaussian laser beams. Altering the beam's shape, in terms of amplitude and phase, will help to increase the versatility of optical manipulation.

Only beams that are solutions to the wave equation can propagate through space by imaging themselves and so can be manipulated after creation. Beam shaping is essential to produce multiple beams or patterns of light with their creation being a clear advantage to technology. One could, for example, carry out multiple processes in parallel, investigate the effects of non 'normal' beams on matter[125], project images of objects in space[126] or use non-diffracting beams for optical interconnections[127].

This thesis mainly concerns directional alterations to laser beams using optical elements that sometimes evolve through time. This does not involve changing the temporal shape of laser pulses, as seen in ultrafast studies, but rather directional changes over a time span of seconds. As well as changing the direction occasionally the beam's amplitude, phase, or both, are varied.

There are numerous techniques for beam shaping which I shall outline in the context of optical manipulation before detailing how the method of choice is implemented. The techniques can be coarsely grouped into three categories, complex modulation, amplitude-only modulation and phase-only modulation. Complex modulation devices alter both phase and amplitude but these are relatively hard to produce especially if time varying beam shaping is required.

Amplitude-only modulation is possible[128] but the efficiency of such modulators is low (they work by removing sections of the beams) and their production or purchase is relatively difficult. With this in mind I turn to phase-only modulation which is far more efficient

and the devices are easier to produce and come by. They can be coupled with further elements such as polarisers[128] or phase contrast filters[93] to effectively create amplitude modulation devices.

Within optical manipulation the power reaching the sample is of great concern therefore so is the efficiency with which the methods of beam shaping work. Another concern is the ease with which techniques can be implemented. So, although amplitude modulating methods have roles at which they excel, it is for ease of implementation and efficiency reasons that most optical tweezers laboratories choose phase modulation devices, as I do here.

Within phase modulating techniques there are two main areas; static or dynamic methods, which will now be discussed.

3.1 Static methods

Methods which produce beams that do not alter their shape over time are considered static and for many purposes are the best choice, allowing for simplicity and cost efficiency. However, they are generally limited to a specific application and are not very versatile.

The majority of optical elements such as lenses, mirrors, prisms and gratings can be considered static methods of beam shaping. However, only the more complex diffractive optical elements will be discussed here as they challenge the boundaries of propagating beams.

Diffractive optical elements (DOEs) are commonly either amplitude or phase only objects. It is well known that variations in transmission within an object can cause diffraction and with the aid of computing can allow complicated patterns of light to be formed[129,130].

By controlling the 'optical depth' and hence phase retardation, across a DOE, phase only 'masks' can be created that vary the phase profile of a transmitted beam. In the context of optical manipulation DOEs have allowed the creation of three dimensional interference patterns to sort particles[17], create multiple trapping sites[131], and create crystal like lattices of colloid[132].

There are many ways to understand how diffractive optical elements work, they can be thought of, for example, as retarding the phase of a single wavefront, as splitting a single wavefront into many, as a blazed grating, or simply as a collection of prisms and lenses. The calculation of the correct phase profile is the same as when dealing with dynamic methods and therefore will be discussed later in section 3.3.

3.2 Dynamic methods

Dynamic methods are those deemed to be easily changeable over time but tend to be more expensive than static methods. Yet they hold a great advantage to the experimenter in the quick and easy ability to test and evaluate ideas and designs, without the need to undertake complex production processes.

There are two main methods of approach for dynamic beam shaping; either a single beam is re-positioned continuously and is 'shared' between desired directions or the single beam is 'split' between all directions simultaneously.

In this thesis I design holograms to work with spatial light modulators that distribute the incident beam simultaneously into multiple beams. Next I will place this work in context by considering a number of alternate time-sharing techniques.

Deformable mirrors

Deformable mirrors provide wavefront modulation by physically altering the optical path length the light takes. The path length is usually modulated by some form of actuator placed behind the mirror to deform it. Either multiple actuators support a whole single mirror or the mirror is made from multiple segments each supported by an individual actuator.

When dealing with optical tweezers, beams more complex than a simple Gaussian are often desired, for example Laguerre-Gaussian, Bessel, or Matthieu beams. These, however, require a discontinuity in the phase wavefront of the beam which deformable mirrors cannot achieve unless they are segmented[133].

Although the mirrors have reasonably high speeds ~ 1 kHz[134], their magnitude of beam deflection is small putting limits on their usefulness. However, they are ideally suited to correction of aberrations within optical tweezers[135].

Scanning mirrors

Galvanometer and piezo-electric driven mirror techniques are relatively low cost with negligible optical power loss and allow large beam deflection angles at quite high speeds of ~ 2 kHz, but they do suffer from wobble and jitter stability problems[38]. They have been easily integrated into optical tweezers enabling the spatial patterning of particles[136–138]. They also enable the trapping of particles where the ratio of medium and particle refractive

indices is opposite to that required for trapping in a normal Gaussian beam[139,140].

Acousto- and Electro-Optic Deflectors (AODs and EODs)

AODs have a reasonable optical transmission of $\sim 80\%$ but for both x and y deflection this decreases to $\sim 64\%$. In the context of optical tweezers where the time duration of the potential is important their high speed, ~ 20 kHz, allows the time sharing of more traps. One disadvantage is the variation of diffraction efficiency over the acoustic bandwidth of the device resulting in variation in powers of $\sim 10 - 15\%$ for different diffraction angles.

EODs can perform at much higher speeds, ~ 10 MHz, have a higher optical transmission of $\sim 90\%$ ($\sim 81\%$ for x and y together), a far more uniform diffraction efficiency as a function of angle and increased accuracy[38,141].

AODs and EODs have been used to perform some of the most stunning experiments with optical tweezers such as studying certain biomolecular processes at the single molecule level with no ensemble averaging[142].

3.2.1 Spatial Light Modulators (SLMs)

Spatial light modulators (SLMs) are relatively slow in comparison to the previous techniques operating at ~ 75 Hz but have the major advantage of diffracting beams into multiple directions simultaneously although this does decrease the peak power per beam. There are ferro-electric SLMs available capable of speeds of tens of kilohertz but these can only produce two levels of phase retardation, significantly reducing their efficiency[90].

Nematic spatial light modulators can achieve efficiencies of $\sim 50\%$[143], significantly below that of its competitors. However, two more major advantages contribute to making them useful versatile devices. Firstly, they can perform mode conversion on propagating beams, for example they can convert a Gaussian into a Laguerre-Gaussian beam. Secondly, they can also change the phase profile of a beam along its axial direction enabling the focussing of beams with no physical optical element.

Finally, at the time of purchase, the cost and ease with which the device could be plugged in and up and running (its 'plug and play nature') was far superior to its then competitors. At the time of writing other methods are becoming more user friendly but there are still challenges to overcome such as limits on resolution set by digital to analogue conversion on computer hardware[144].

Although in this thesis I will concentrate on SLMs, the techniques are applicable to all

phase-only diffractive optical elements. Within the literature there are slight variations on the apparatus and design, for example it is possible to use Fresnel based systems[91], amplitude modulation[145,146] and ferroelectric SLMs[90,147].

Having established my use of SLMs a background of their operation will now be given.

How the phase is modulated

Rather than varying the thickness of a glass substrate, as for phase-only DOEs, materials can be used that alter their retardation properties without changing size, namely liquid crystals. Liquid crystals are an additional state of matter lying between liquid and solid such that they do not possess positional order but do exhibit orientational order. On average, over time, the elongated liquid crystal molecules tend to point in a given direction called the director, $\boldsymbol{n}$, of the liquid crystal as shown in figure 3.1.

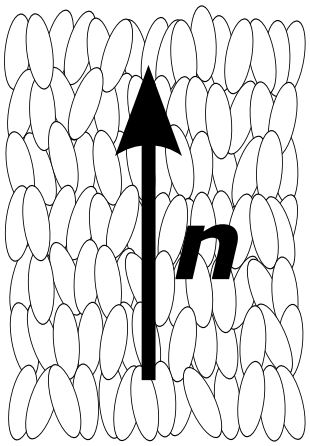

Figure 3.1: Image showing the elongated nature of liquid crystal molecules along with their orientational, but not positional, order. The arrow and vector $\boldsymbol{n}$ indicate the director which on a time average points along the direction of orientation of the molecules.

The basic design of all spatial light modulators is similar; they consist of a thin layer of liquid crystal between either two transparent electrodes or one reflective and one transparent electrode as shown in figure 3.2.

The nematic phase possesses a dielectric anisotropy, $\Delta\epsilon$, governing its response to an electric field, defined as

$$\Delta\epsilon = \epsilon_{\parallel} - \epsilon_{\perp}, \tag{3.1}$$

where $\epsilon_{\parallel}$ and $\epsilon_{\perp}$ are the dielectric permittivity measured parallel and perpendicular to the director respectively. Under an applied electric field the molecules will try and minimise their electric energy density by aligning perpendicular or parallel to the electric field given

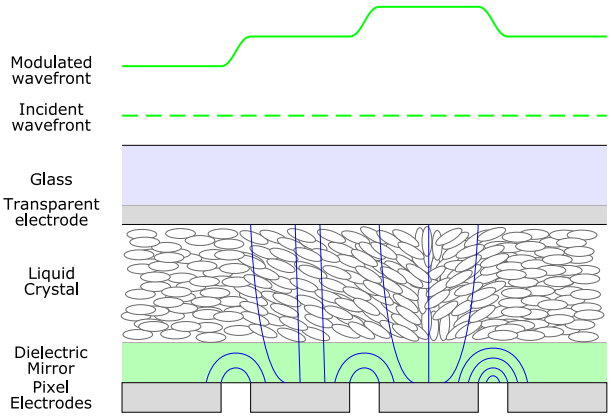

Figure 3.2: A Liquid Crystal over Silicon (LCoS) spatial light modulator. The individually addressed pixels, which act as one electrical contact are shown at the bottom and a transparent second electrical contact layer is placed above the liquid crystal. When an electric field is applied the liquid crystal molecules, hence director, rotate and change the local extraordinary refractive index, thus altering the retardation imparted to the wavefront in that pixels area.

that the dielectric anisotropy is either negative or positive respectively. They also compete against an opposing force due to the elasticity of the liquid crystal, hence the molecules also attempt to minimise their elastic energy density[148].

As an electric field is applied across individual pixels the molecules, wishing to align with the electric field, begin to rotate until they reach an equilibrium with the elastic energy density (figure 3.2). With larger fields the molecules, hence local director, will rotate further. With no voltage applied across the liquid crystal polarized light entering along the extraordinary axis, will experience a refractive index n_e. As a voltage is applied and the director rotates through an angle, θ_d, the light will experience a modified extraordinary refractive index $n_e(\theta_d)$ giving an effective birefringence

$$\Delta n = n_e(\theta_d) - n_o, \tag{3.2}$$

where n_o is the refractive index along the optical axis. Therefore the phase of the light incident on a specific pixel area is retarded by

$$\delta = \frac{2\pi}{\lambda_o} d \left|\Delta n\right|, \tag{3.3}$$

where d is the thickness of the liquid crystal layer and λ_0 is the wavelength of light. So, increasing the electric field across a nematic liquid crystal varies the extraordinary refractive index of the material, hence produces a shift in the phase of the incident light.

The fact that the voltage alters the refractive index along the extraordinary axis of the material means the amount of retardation is polarisation sensitive and it must be ensured

that the incident light's polarisation is aligned with this axis. Either a rotatable polariser or half-wave plate can be used.

3.3 Beam shaping for optical tweezers

It is only appropriate to discuss a brief history of the type of instrument I am trying to build before going into the detailed discussion of how my specific system is implemented.

In the two decades since Ashkin's first single beam optical trap many techniques have been developed to produce multiple trapping sites with user interactivity. The first step beyond single beam tweezers are dual beam traps[149] allowing two traps to be created with easy control over their position. These can be simply created with everyday optics without need for complex apparatus.

The majority of multi-beam techniques involve utilising the beam shaping technologies discussed in sections 3.1 and 3.2 to create multiple (> 2) beams for multiple traps by focussing them through the normal microscope objective. The details are slightly more subtle but for now this will suffice. As alluded to previously, the methods can coarsely be placed into two categories; those techniques that 'share' a single beam between multiple beams like computer controlled galvonometer or piezo actuated mirrors[138] or acousto-optic deflectors[38] and allowing the beam to be 'stationary' at certain points. Or, those that 'split' a single beam between spatially separate locations like diffractive optics[131] or SLMs[85]. The choice of method can be critical to the operation of certain experiments[44,144] as is the case here and will be demonstrated in section 5.6.

Before attempting to explain how SLMs can create multiple beams and traps with complex algorithms I will begin by considering the simplest case of how a phase altering optical element can be used to 'deflect' a single beam. A simple glass prism can perform such a task but let us see why. Figure 3.3 shows a plane wave incident on and transmitted by such a prism.

Ideally the prism does not alter the wave's amplitude but does its phase, as a function of x or y position. This is because its 'optical depth' varies due to the thickness variation but constant refractive index. Delaying the phase in this manner results in an angular shift of the plane wave and hence change in beam propagation direction.

Stepping into the third dimension it is realised that to obtain an axial displacement of the objective lens' focus, the beam's collimation as it enters the lens must be altered. A diverging or converging beam will be focussed past or before the lens' 'true' focus respectively, and to obtain such a beam a simple concave or convex lens can be placed

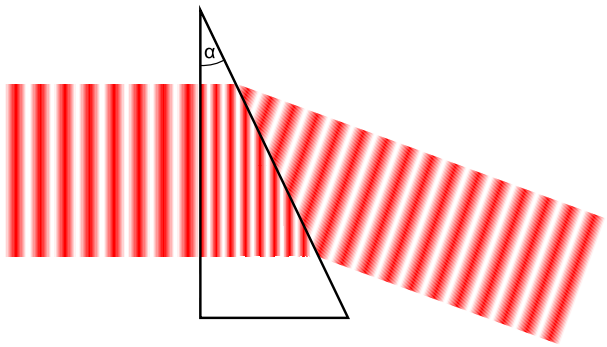

Figure 3.3: Plane waves incident on a prism are slowed down within the glass, with a change in λ. The portion of the wave to emerge first increases in speed thus giving it a 'head start' over the wavefront remaining in the prism. As this continues an inclined wavefront is produced. α is the prism angle in the x-plane and not shown is the y-plane prism angle β.

in the incident beam's path. Again, the lens works by delaying the phase of the incident plane wavefront via its varying optical depth but this time the result is a curved wavefront as shown in figure 3.4.

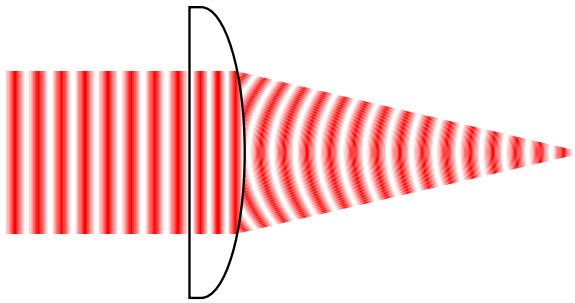

Figure 3.4: Plane wavefronts entering a convex lens are 'held up' more in the centre of the lens due to the slower speed of light within glass and the larger thickness than at the edge. Therefore, upon emerging the wavefronts are spherically shaped. The same occurs for a concave lens except the waves are more held up at the edges and hence the spherical waves diverge as they propagate away.

These two optical elements are described by the prism and lens *phase profiles*, ϕ_{prism} and ϕ_{lens} respectively, given by

$$\phi^{prism} = \frac{2\pi}{\lambda}(sin\alpha + sin\beta), \tag{3.4}$$

and

$$\phi^{lens} = \frac{2\pi}{\lambda f}p^2, \tag{3.5}$$

where α and β are the prism angles and $p = \sqrt{x^2 + y^2}$, the position of a point on the lens.

Knowing the phase profiles they can be programmed onto an SLM to emulate the physical optical elements. When using the SLM as a device to shift angular deviation, it is apparent that it can replace the mirror in figure 2.4. This setup is shown in figure 3.5 where the ability to axially shift foci is also illustrated. It must be ensured that the angle of incidence of the incoming beam is as small as possible (preferably $< 10°$) which makes sure the maximum amount of light exits each pixel and also that the light interacts with the liquid crystal in the correct orientation.

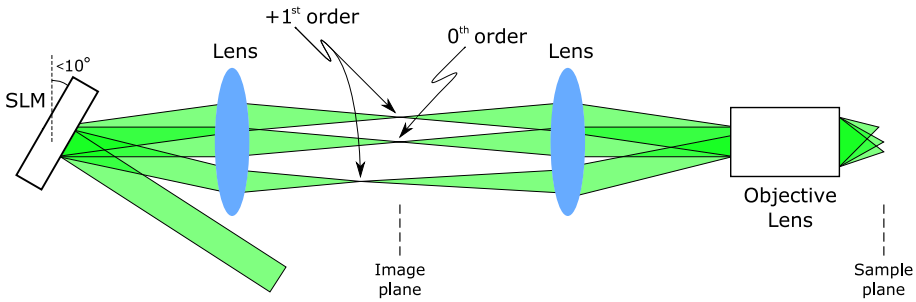

Figure 3.5: Multiple beams are diffracted at varying angles from an SLM placed in the plane conjugate to the objective's back aperture so that each beam is entering the objective with an angular deviation. The foci of light are laterally displaced in the objective focus without incurring any additional aberration. Ideally the SLM should be angled at $< 10°$ to ensure the light interacts with the liquid crystal molecules in the correct orientation. Also a lens function can now be added to axially shift a focus in the first image plane and hence the conjugate sample plane. The rear of the objective in this case coincides with its front focal plane.

Included in figure 3.5 is a *zeroth order*. This is a consequence of the non-perfect nature of the diffraction optics, for example the pixellated construction and polarisation sensitivity, causing no phase modulation on a significant fraction, $\simeq 40\%$, of the incident light. This can significantly affect the distribution of desired light in the sample plane and so should be removed before reaching it. The method I use and others are discussed later on.

So, it can be seen how, for a monochromatic wave, a single beam and hence focus can be laterally and axially displaced by applying simple optical elements to an SLM. Varying the deflection angle in a simple time-sharing manner will achieve my goal of multiple foci[105]. However, the programming of the SLM to emulate these optical elements and the production of multiple beams simultaneously is more subtle and will be explained next.

3.3.1 Holography

Clearly, splitting into multiple beams produces multiple foci, but this picture is really only suitable when looking at discrete points of light. If one wishes to create a continuous pattern of light in a sample plane it is hard to understand how this is created when considering that diffraction from SLMs consists of multiple beams. Therefore an alternate method of analysing the problem must be found, hence I turn to holography.

Most people are familiar with the term 'hologram' and associate it with the little one on their credit cards or possibly interactive three dimensional ones from the world of science fiction. These holograms are generally a piece of material that contains both the phase and amplitude information about a particular three dimensional object and are called *complex* holograms. It is also possible to produce *amplitude-* and *phase*-only holograms that influence only the amplitude or phase of the incident light respectively. Having decided on SLMs as the beam shaping method of choice (section 3.2.1) with their forté being phase modulation, it is to the computation of phase-only holograms that I dedicate a large portion of what remains in this chapter.

Ideally I would like to create a particular distribution of phase and amplitude in a specific three dimensional volume; this can be achieved experimentally with holography. It happens that the basic premise of optical tweezers, the focussing of a collimated beam by a lens, is ideally suited to the task. To see why, let me construct the problem and solution in what follows. Consider the most basic lens system in figure 3.6. Using Fourier optics[114] it is possible, given the field of complex intensity and phase incident on the lens, to calculate the field in the back focal plane of said lens.

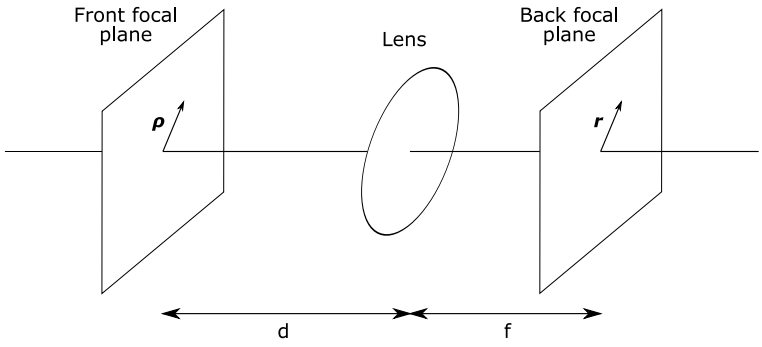

Figure 3.6: Planes in a simple lens system. Positions in the front and back focal planes of a lens are described by the vectors $\boldsymbol{\rho}$ and $\boldsymbol{r}$ respectively. Here f is the lens' focal length and d is the distance in front of a lens at which we know the complex field.

Considering a collimated, monochromatic wave incident upon a lens with amplitude $u(\boldsymbol{\rho})$ and phase $\varphi(\boldsymbol{\rho})$ that has been modulated by a hologram in the front focal plane of a lens

at position d, as shown in figure 3.6, then the complex field in the back focal plane is

$$E(\boldsymbol{r}) = \frac{e^{\left(i\frac{\pi}{\lambda f}\left(1-\frac{d}{f}\right)\boldsymbol{r}\cdot\boldsymbol{r}\right)}}{i\lambda f}\int\int u(\boldsymbol{\rho})e^{i\varphi(\boldsymbol{\rho})}e^{-i\frac{2\pi\boldsymbol{r}\cdot\boldsymbol{\rho}}{\lambda f}}d^2\boldsymbol{\rho}. \tag{3.6}$$

where λ is the wavelength of light, f is the focal length of the lens, d is the distance to the wavefront modifying element, the vector $\boldsymbol{r}$ describes position in the back focal plane of the lens, and the vector $\boldsymbol{\rho}$ describes position in the front focal plane. Of particular interest is the quadratic phase prefactor and will become important later.

Knowing the amplitude and phase modulation imparted to the beam from an SLM, equation 3.6 can be used to calculate the field distribution in the back focal plane of the lens. Unfortunately it would be far more useful to start with the field distribution desired and calculate the phase modulation needed to impart onto the beam. However, inverting equation 3.6 is non-trivial and the challenge presented is a classic 'inverse problem'[150].

Several solutions exist that allow the discovery of the answer to this inverse problem depending on the exact form of the output field desired. In the following section I will discuss these in detail, but first I will start with a brief review of the history of the relevant topic.

The solution to this problem is through computer generated holography[151], a sub-category of holography. Conventional holography creates a hologram by interfering a reference wave with one scattered from a three-dimensional object[152]. Conversely, in computer generated holography no object needs to exist. Also, as already stated, rather than knowing the diffracting object and calculating the resulting image, the desired image is known and the diffracting object, or hologram, calculated[129]. The earliest forms of computer generated holograms consisted of an opaque mask with transparent areas that represent the desired image's Fourier transform. The lateral shift in the transparent areas gave rise to the name detour phase holograms while they were also referred to as binary holograms due to the transmittance value of either 0 or 1[129]. A more detailed account of the earliest forms of computer generated holograms can be found in Tricoles[151] with an extensive bibliography relevant to the subject.

These detour phase or binary holograms are inefficient[84] but by creating true phase-only holograms, or ***kinoforms***, this efficiency can be greatly improved, along with a decrease in computation time[153]. As discussed the spatial light modulator is my device of choice so it is the kinoform approach that I have taken.

Having found a solution to the problem of constructing a desired three dimensional pattern of light the next challenge was to discover an algorithm that provided quick kinoform

computation with reconstruction producing efficient and uniform results. This has been a major direction in research since inception.

An important early development in the field of computer generated holography was the Fourier transform hologram which uses a simple lens to perform an optical Fourier transform[154] and is the basis of the techniques used in this thesis. The idea was further developed to take advantage of the Gerchberg-Saxton algorithm[155], an iterative Fourier transform algorithm for phase retrieval, to reduce the error in the optical reconstruction of the kinoform[156].

An additional method that produces high quality kinoforms at the expense of computation time is the direct search algorithm. This is nicely exemplified for phase only holograms by Clark and Smith[157] who design binary holograms to produce simple geometric shapes and discuss the appropriate use of cost function, pixel selection, and their effects. The method can be further extended to produce high quality three dimensional greyscale continuous patterns of light[158].

To my knowledge the first use of diffractive elements combined with optical tweezers was performed by He *et al.* by producing 'vortex' beams with a blazed spiral phase computer generated hologram and passing it into a microscope[84]. The next major step was taken by Reicherter *et al.*[159] where the kinoforms were displayed on a liquid crystal display to enable dynamic lateral control of the 'vortex' tweezers and was soon developed to control the axial displacement too[160].

The previous three studies used analytical solutions to calculate their computer generated holograms. The first experiment to use a true algorithm to design the kinoform used in optical tweezers started life as the 'hexadeca-tweezer'[131] which used a commercially available diffractive 4×4 square array generator. The diffracted beams were collimated and then imaged into the focal plane of the optical tweezers. A few years later this was extended to more complex patterns of tweezers[85] and the computation of diffractive optical elements, or more specifically, kinoforms, became important. To calculate the kinoforms the adaptive-additive algorithm was employed[161], an extension of the iterative Gerchberg-Saxton algorithm, that converges to a solution for the desired output of tweezers.

Having discussed the use of kinoforms in optical tweezers I will now only discuss the algorithms in this context. A definitive discussion of the algorithms currently in use for holographic optical tweezers is discussed in di Leonardo *et al.*[87] with a heavy mathematical basis which should be used for reference. Here I will discuss the algorithms from a more practical and concise perspective.

3.3.2 Algorithms

As one may expect the most commonly desired field of light in optical micromanipulation is multiple foci[†], leading to multiple tweezers. It is to this topic I will dedicate most time but I will also diverge into creating continuous fields of light although this has not been investigated as fully. The differences between the kinoforms generated by each algorithm is subtle and to appreciate them I shall consider three important metrics relating to their optical reconstruction. Firstly, the efficiency

$$\epsilon = \frac{\sum_m I_m}{I_0} = \frac{\sum_m A_m^2}{A_0^2}, \tag{3.7}$$

where I_m and A_m are the intensity and amplitude of each foci respectively, I_0 and A_0 are the incident intensity and amplitude respectively and the efficiency, ϵ, is defined to be the ratio of the theoretically predicted total intensity to the incident intensity. Other definitions of efficiency can be defined as the ratio of light in the first diffracted order to that in the zeroth order or the ratio of light in the first diffracted order to that incident on the SLM.

Secondly, the uniformity is defined as

$$u = 1 - \frac{I_m^{max} - I_m^{min}}{I_m^{max} + I_m^{min}}, \tag{3.8}$$

were I_{max} and I_{min} are the maximum and minimum intensities in the image plane respectively.

Finally the standard deviation is defined as

$$\sigma = 100\frac{\sqrt{\langle (I - \langle I \rangle_m^2) \rangle_m}}{\langle I \rangle_m}. \tag{3.9}$$

One major effect that inhibits all three parameters from reaching their optimum value is the production of *ghost tweezers* which arise due to constructive interference from the higher order modes of diffraction[99]. It is often an aim of the algorithms to remove these unwanted traps.

I will start with the simplest of algorithms that takes the idea of prisms and lenses and applies them to SLMs, as illustrated in figure 3.5, but now will be more rigorous in the description of how a three dimensional object can be placed on an, effectively, two dimensional device.

[†]Here the term foci refers to more than one focus that can exist anywhere within a volume in image space.

Superposition of prisms and lenses

Only two things need to be changed in equations 3.4 and 3.5 to implement prisms and lenses on SLMs in optical manipulation. Firstly, the obvious problem is the 'flat' nature of SLMs and the physical extent of the optical elements. This is quickly resolved by borrowing the idea of Fresnel lenses, just as is done in lighthouses. These effectively remove redundant volumes of phase retarding material from a lens and then place what remains all on the same plane, as shown in figure 3.7(a).

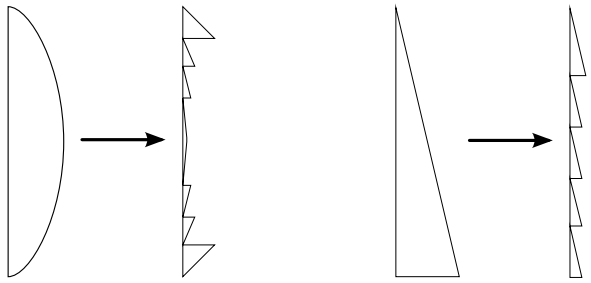

(a) (b)

Figure 3.7: A simple lens (a) or prism (b), that relies on phase modulation alone, can be 'flattened' by removing redundant volumes of retarding material so the relative modulation between areas is the same but the absolute difference has been removed. The same idea is used in lighthouses to reduce the mass of the very large lenses and is based on Fresnel lenses.

The amount of material removed is an integer multiple of the wavelength of light because only the relative phase between positions on the wavefront contribute to the new wavefront. The same can be done with the prism optical component as shown in figure 3.7(b) and for both is mathematically equivalent to taking the phase profile modulo 2π.

The second fact to be considered is the mathematical relationship between the position of a focus and the phase profile incident on what I now call the transform lens. If the optical element is placed in the front focal plane of the transform lens (I will show why this is a bit later) its phase retardation is

$$\varphi^{prism} = \frac{2\pi}{\lambda f} (\boldsymbol{r} \cdot \boldsymbol{\rho}) \bmod 2\pi, \tag{3.10}$$

and

$$\varphi^{lens} = \frac{2\pi z}{\lambda f^2} (\boldsymbol{\rho} \cdot \boldsymbol{\rho}) \bmod 2\pi. \tag{3.11}$$

where z is the axial displacement required and f is the transform lens focal length. To obtain a phase profile, φ^{3D}, that displaces a focus laterally and axially simultaneously these two functions are summed modulo 2π;

$$\varphi^{3D} = \left(\varphi^{prism} + \varphi^{lens}\right) \bmod 2\pi. \tag{3.12}$$

As these functions alter the phase only, they can be referred to as kinoforms. To extend the principle into multiple foci the argument of the sum of the complex functions of the individual kinoforms is found;

$$\varphi^{S} = arg\left(\sum_{m} e^{i\varphi_m^{3D}}\right) \bmod 2\pi, \tag{3.13}$$

where there are m desired individual foci, hence kinoforms. The relative merits of this technique are discussed in section 3.3.3 along with the other methods still to describe for ease of comparison.

This prisms and lenses technique is usually referred to as 'gratings and lenses' or 'superposition'[160] and is the basic starting point for everything that follows. Having established these basic principles, I will next discuss two small extensions to this 'algorithm' that provide a different route to the answer required.

Random Superposition

The same procedure as before is followed except before following equation 3.13 an additional random phase is added to each individual kinoform such that the superposition is now

$$\varphi^{RS} = arg\left(\sum_{m} e^{i\left(\varphi_m^{3D}+\psi\right)}\right) \bmod 2\pi, \tag{3.14}$$

where ψ is a random number in the set $[0, 2\pi]$. Considering the phase retardation analogy this basically means the beam creating each individual focus is placed randomly out of phase relative to the rest. This small modification can, for many configurations of trap locations, reduce the number of ghost traps, improve the efficiency metric and decrease the standard deviation metric[99].

Random phase mask

To understand this method it is appropriate to note that although I have been considering the hologram to be continuous, in reality they are designed for a pixellated device with

finite extent. As such each pixel, j, out of the N^2 total pixels, for an $N \times N$ device, must be assigned a discrete phase value. For m desired individual trap sites there are m initial kinoforms each with N^2 pixels; a given pixel in a given kinoform is denoted ϕ_j^m.

The random phase mask is found through;

$$\varphi_j^{RM} = \phi_j^b, \tag{3.15}$$

where b is a random number from the set representing the individual kinoforms, [0, m]. Qualitatively this algorithm goes through every pixel in the final kinoform and places a phase value from a randomly chosen individual kinoform.

The algorithm can be altered slightly to drastically decrease the number of ghost tweezers present in the focal plane[162]. To do this m random binary phase masks are calculated such that each one contains N^2/m 'transparent' pixels while ensuring that if summed the total mask would be a transmission function of unity. Each phase mask is then multiplied by an individual kinoform used to make one of the foci desired and the results summed to obtain the final kinoform. Figure 3.8 explains this more clearly.

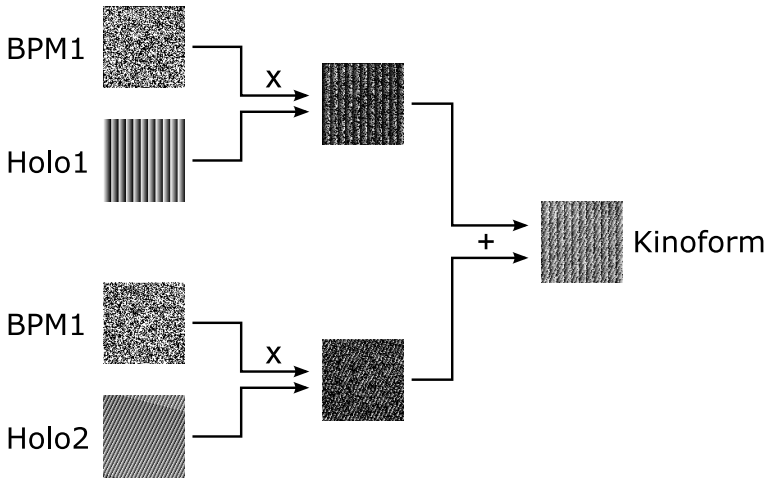

Figure 3.8: Diagram describing the random binary phase mask (RBPM) algorithm. In this example only two foci are desired. The kinoforms for both individual foci desired, Holo1 and Holo2, are multiplied by BPM1 and BPM2 respectively, which are random binary phase masks each with $N^2/m = N^2/2$ pixels but making sure that if summed the total mask would be a transmission function of unity. Finally the results are summed to obtain the final kinoform.

So far all the algorithms have been analytical. The kinoforms used to produce the individual foci are combined and manipulated in some way to produce a kinoform that will create all the foci simultaneously. The remaining algorithms are all iterative in nature and need a starting estimate for the answer which can take the form of a constant or random

phase distribution across the kinoform. However, a more intelligent guess is to use one of the previous analytical methods as the starting point.

Direct Search

In this simplest of iterative algorithms the correct kinoform is found by directly searching through as many choices as possible as explained in the flow chart of figure 3.9.

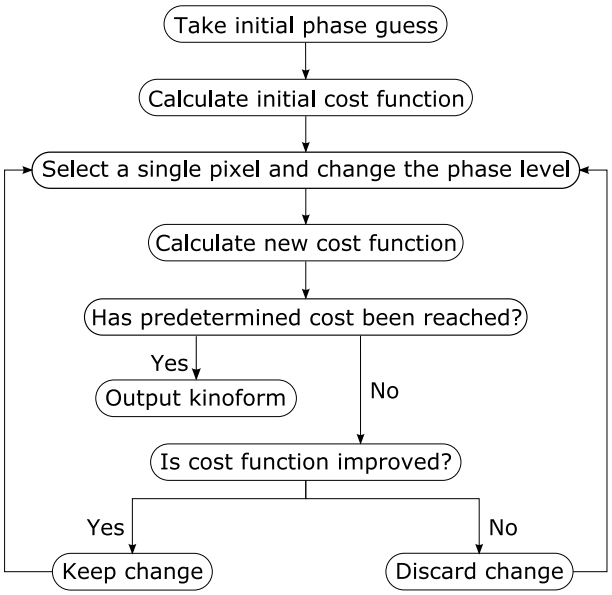

Figure 3.9: Flow chart describing the simple but computationally heavy direct search method of kinoform generation.

The choice of cost function is important and within this thesis is

$$C = \langle A^2 \rangle - f\sigma, \tag{3.16}$$

where σ is standard deviation, A is the amplitude of a focus, and f is a number between 0 and 1 that governs the balance between efficiency and uniformity. The manner in which the pixels are cycled through has a significant impact on the computation time but not the overall efficiency of the kinoform (see figure 9 in Clark and Smith[157]). A random exhaustive pixel selection has the quickest computation time, for a given end cost, compared to a simply random or sequential selection.

Gerchberg-Saxton

For the following I return to equation 3.6 noting with interest the quadratic phase prefactor, associated with the distance, d, between a hologram and a simple lens. If this distance is equal to the focal length of the lens, $d = f$, a very important result is realised, and equation 3.6 becomes

$$E(\boldsymbol{r}) = \frac{1}{i\lambda f}\int\int u(\boldsymbol{\rho})e^{i\varphi(\boldsymbol{\rho})}e^{-i\frac{2\pi \boldsymbol{r}\cdot\boldsymbol{\rho}}{\lambda f}}d^2\boldsymbol{\rho}, \tag{3.17}$$

where the symbols retain their same meaning.

In this special case the field at the back focal plane of the lens is an exact Fourier transform of the field at the hologram (front focal plane) with spatial frequencies $u/\lambda f$ and $v/\lambda f$. Here u and v are the spatial coordinates in the hologram plane and $\rho^2 = u^2 + v^2$. It is now clear that the simple lens in figure 3.6 becomes a Fourier transform lens when $d = f$. This is an amazing result and provides a superb route to calculating holograms.

Unfortunately the inverse problem still remains. This can be simplified as the input amplitude is known and this is not altered with phase-only holograms, hence $u(\boldsymbol{\rho})$ is simply a Gaussian (or equal to unity if the calculation is to be simplified still further). Also the phase distribution at the focus is not a concern, only the amplitude. The way to solve the inverse problem is to use an iterative scheme. The reasonable guess from the analytical methods is Fourier transformed to give the field distribution in the focal plane. The next step is to keep the phase information but discard the amplitude and replace it with some other function. This is conveyed in figure 3.10.

Having calculated a 'corrected' field, it is inverse Fourier transformed resulting in the field in the hologram plane. Discarding the amplitude leaves the phase required to be imparted to the beam, the new kinoform estimate. This phase, although not perfect, will be a more accurate estimate of the true answer. The procedure is repeated until a predetermined error function reaches a given threshold.

In the classic Gerchberg-Saxton algorithm the discarded amplitude in the image plane is replaced with the desired intensity distribution. For example, should the desired pattern be a grid of sixteen foci the amplitudes at these points are replaced by $A = \sqrt{I} = \sqrt{1/16}$, while all other areas have zero amplitude. The mixing formula in figure 3.10 for a Gerchberg-Saxton algorithm is simply

$$A_m^{GS} = A^d, \tag{3.18}$$

where A^d is the desired amplitude.

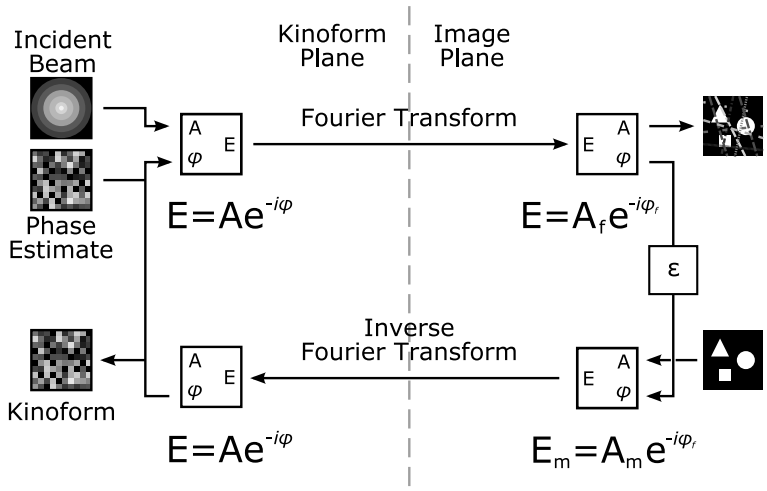

Figure 3.10: The Gerchberg-Saxton algorithm. First an estimate is taken at the correct kinoform. A Fourier transform is taken to find the field in the back focal (image) plane. The error is calculated, then a function of the desired amplitude is mixed back in. Next, the inverse Fourier transform is found, the amplitude discarded and the phase replaces the phase estimate. The process is repeated until the error function, ϵ, reaches a predetermined value. A_m is the mixing formula and its exact form is important as described in the text.

Generalised Adaptive Additive

The Gerchberg-Saxton algorithm is a limiting result of the more general adaptive additive algorithm[161] in which the mixing formula is

$$A_m^{GAA} = \left((1-\zeta) + \zeta \frac{A^d}{A_n^f} \right) A^d, \tag{3.19}$$

where ζ is a constant between 0 and 1 that governs the balance between uniformity and efficiency, A^d is the desired amplitude and A_n^f is the amplitude from the Fourier transform of the current estimate. Here the desired and resulting amplitudes are mixed in a manner that can preferentially optimise efficiency or uniformity, with $\zeta \simeq 0.5$ giving a nice balance between the two[41].

Weighted Gerchberg Saxton

Again, this is largely similar to the Gerchberg Saxton algorithm except rather than replacing the amplitude in each iteration with the desired amplitude, it is first weighted. This effectively places more emphasis on improving the incorrect points of light for the

next iteration. The mixing formula now becomes

$$A_m^{WGS} = \frac{1}{A_n^f} w^m, \tag{3.20}$$

where w_m also changes iteratively following

$$w_{n+1}^m = \frac{w_n^m}{\langle w_n^m \rangle_m} \quad \text{and} \quad w_0^m = 1. \tag{3.21}$$

3.3.3 Algorithm performance

The choice of algorithm to obtain the optimum performance is based on several factors; which of the three performance metrics is most highly desired, the speed with which I want to perform the calculation, and the type of pattern. The algorithms perform differently when trying to create either highly symmetric or random patterns of foci. Table 3.1 shows the relevant quantities for each algorithm having been performed on both symmetric and asymmetric patterns of foci.

Algorithm	Pattern	ϵ	u	σ	Speed (secs)
Superposition	Sym	0.18	0.32	57.4	52
	Asym	< 0.01	< 0.01	142	50
Random Superposition	Sym	0.50	0.24	48.7	52
	Asym	< 0.01	0.02	94.0	50
Random Phase Mask	Sym	0.04	0.14	46.7	50
	Asym	< 0.01	0.07	87.1	52
Gerchberg-Saxton	Sym	0.92	0.54	33.1	122
	Asym	0.79	0.99	0.51	121
Generalised Adaptive Additive	Sym	0.93	0.84	10.9	129
	Asym	0.79	0.99	0.63	128
Weighted Gerchberg-Saxton	Sym	0.93	1.00	0.14	127
	Asym	0.79	1.00	< 0.01	126

Table 3.1: The results were obtained from running the generation software in figure 3.15 on a Intel Pentium M 1.73 GHz processor with 1 GB of 795 MHz RAM. The symmetric pattern (Sym) consisted of 16 individual foci equidistantly spaced around the origin covering an area of 30×30 μm. The asymmetric pattern (Asym) was found by adding a random step of 8 μm to the x and y position to each focus. The iterative algorithms were run for $n = 40$ iterations and all algorithms calculated a kinoform with a resolution of 768×768 pixels. The Direct Search algorithm does not appear as the time for computation on such a system for the size of hologram was unfeasible.

As seen in table 3.1 the choice of algorithm is dependent on the task at hand. One must decide which parameter is most important, the speed with which it needs to be performed and the pattern type required. The optimum algorithm to use, if computation time is available, is Weighted Gerchberg-Saxton because of its superior uniformity for both symmetric and asymmetric patterns of foci.

One may assume SLM devices have a relatively large minimum step limit regarding the precision with which optical tweezers can be placed due to their pixellated nature and large pixel pitch in the device ($\sim 19\ \mu m$). However, this is not the case and it has been shown that 'virtually continuous placement' of optical tweezers is possible with the limit $(\lambda f/D)\,(2/Ng)$, where λ is the wavelength of light, f is the focal length of the lens, D is the diameter of the back aperture, N is the resolution of the device, and g is the number of discrete phase levels possible[100]. For an average SLM optical tweezers setup this gives a theoretical minimum step size of ~ 2 pm.

3.3.4 More complex tweezers and continuous patterns

Should one wish to create an arbitrary beam mode at the tweezers location, such as Laguerre-Gaussian, Bessel or an aberration, the process is straightforward when using the first three non-iterative algorithms. The required phase profile, φ^{addi}, is simply included so equation 3.12 becomes

$$\varphi^{3D} = \left(\varphi^{prism} + \varphi^{lens} + \varphi^{addi}\right) \bmod 2\pi. \tag{3.22}$$

and the remaining equations adopt this new φ^{3D}.

I have discussed how one can displace multiple foci axially along the beam propagation direction for the simple algorithms of superposition and random phase mask. However, should one want to use an iterative method to calculate the kinoforms for a three dimensional pattern of foci then the process is slightly more complex. There are two methods that are somewhat equivalent. In the first one a Fourier transform into the image plane is performed as usual but then the field is propagated to the axial plane at which the foci of interest lies. The process is reversed and the computation carries on as normal[163]. The second method follows equation 3.6, as before, except it includes a kernel that defines the axial displacement required[41]. Equation 3.6 now reads

$$E\left(\mathbf{r}\right) = \frac{A}{i\lambda f}\int\int u(\boldsymbol{\rho})e^{i\varphi(\boldsymbol{\rho})}K(\boldsymbol{r}_m,\boldsymbol{\rho})e^{-i\frac{2\pi \boldsymbol{r}_m\cdot\boldsymbol{\rho}}{\lambda f}}d^2\boldsymbol{\rho}, \tag{3.23}$$

where $\boldsymbol{r}_m$ is the position of the individual foci in image space. The kernel can also define

beams such as Laguerre-Gaussian, Bessel or other novel implementations.

In chapter 4 I will demonstrate the application of continuous patterns of light which differ from the multiple foci previously discussed because they no longer exist as discrete points and are thus more complex to compute. In order to create continuous patterns of light one treats the sample plane as a pixellated image space. I immediately discretise the desired image so its resolution matches that of the output kinoform thus giving a direct relationship between sample plane and input image. The iterative algorithms work in the same manner except rather than determining the field at multiple individual points in space and using the relevant mixing formula, the process is performed on the whole field.

3.4 How to implement SLMs in optical manipulation systems

Having covered optical tweezers, SLMs, beam shaping, and holography they can be combined to build a holographic optical tweezers (HOTs). Re-considering the conjugate planes in figure 3.5 where angular deviation is created by the SLM, it is this that forms the basis of a HOTs system, shown in figure 3.11. Note the SLM is placed one Fourier transform lens focal length away from the transform lens to ensure that the quadratic phase factor in equation 3.6 vanishes to become equation 3.17.

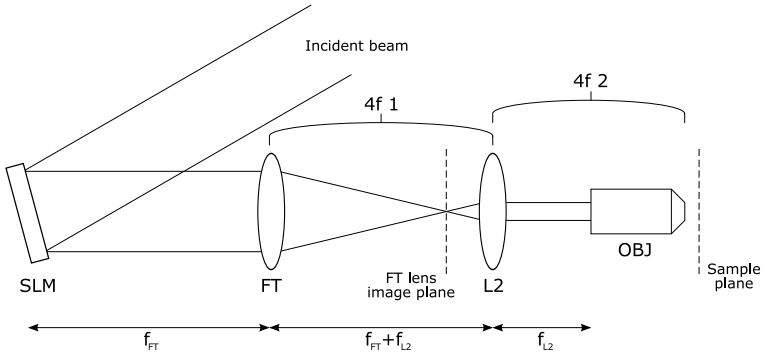

Figure 3.11: The basic setup for any holographic optical tweezers. The beam is incident on the SLM at as smaller angle as possible. Lenses FT and L2 form one $4f$ imaging system while lenses L2 and OBJ form another. These lenses allow the conversion of angular to lateral displacement, demagnification of the beam to ensure it still slightly overfills the back aperture, and also keeps the relationship between image and hologram space a simple Fourier transform.

The reasons for the $4f$ systems in figure 3.11 are three-fold. It allows the conversion of angular to lateral displacement (without introduction of aberration), the demagnification of the beam reflected by the SLM to ensure it slightly overfills the back aperture, and also

keeps the relationship between image and hologram space a simple Fourier transform.

The three lenses in figure 3.11 can be thought of as two interconnected $4f$ imaging systems. The first uses lenses FT and L2 to image the SLM onto the back aperture of the objective (its conjugate plane). The second uses lenses L2 and OBJ to image the FT lens image plane into the sample plane (its conjugate plane). Thinking of it in these terms allows one to understand and predict what effect changing something in one plane will have.

In reality the system uses five lenses after the SLM to obtain the required demagnification and relay particular conjugate planes through the system while keeping their Fourier relationship. The system used in experimental investigations is illustrated in figure 3.12

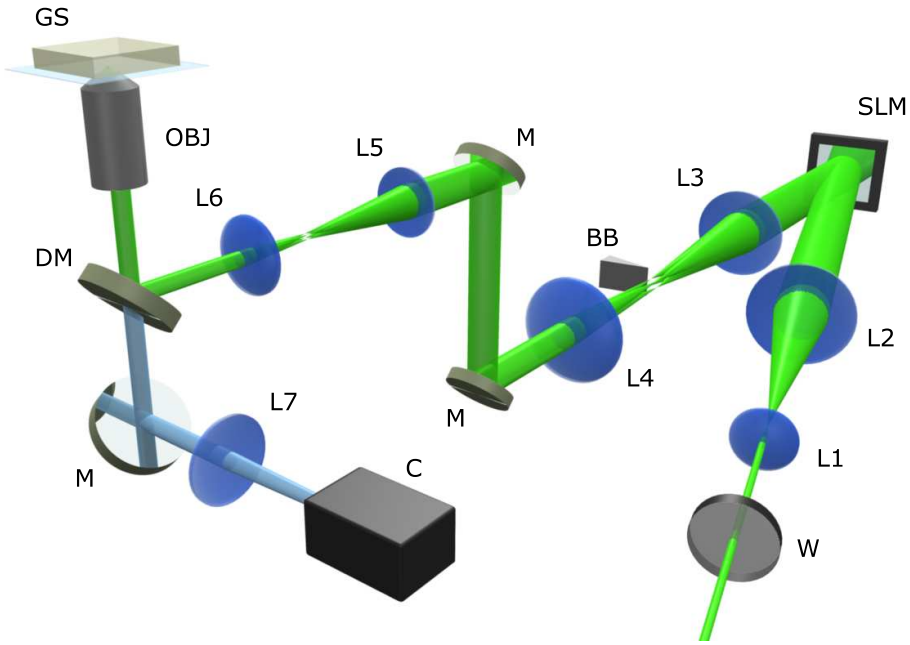

Figure 3.12: Experimental setup. W is a half-wave plate to control the polarisation incident on the SLM. Lenses L1 (100 mm) and L2 (750 mm) are a Keplarian telescope (lenses separated by the sum of their focal lengths) to expand the laser source to slightly overfill the short axis of the spatial light modulator (SLM). Lenses L3 (400 mm) and L4 (250 mm), and, L5 (175 mm) and L6 (100 mm) form two 4f imaging systems (lenses separated by the sum of their focal lengths) to image the SLM onto the back aperture of the objective (OBJ). Lens L7 is a the tube lens used in conjunction with OBJ to form an image on the camera (C). The mirrors (M) are broadband dielectric mirrors and a green dichroic mirror (DM) is used to reflect the trapping beam and transmit illumination and image light. A beam block, BB, is used to remove the SLMs zeroth diffraction order. The cream coloured block represents the 'generic sample' (GS) into which the light is focussed. Lenses L4 and L5, and, L6 and OBJ can also be thought of as imaging the first Fourier transform plane into the sample plane at the focus of OBJ.

A 532 nm beam from a continuous wave Laser Quantum Finesse laser (beam diamter 2.2 mm with 0.4 mrad divergence) is controlled in power by using a half-wave plate and

polarising beam splitter cube so plate rotation results in power variation. A second half-wave plate is used to rotate the output plane polarised light to optimise the diffraction efficiency of the SLM because as noted earlier (section 3.2.1) it is polarisation sensitive. The beam is then expanded with lenses L1 and L2 so that it completely overfills the active area of the short axis of the Holoeye LCR-2500 SLM. The reflected beam is demagnified by two $4f$ imaging systems using lenses L3 and L4, and L5 and L6, to image the SLM onto, and slightly overfill, the back aperture (5 mm in diameter) of the microscope objective. As mentioned earlier lens L3 acts as the Fourier transform lens and lenses L4, L5, L6, and the objective act to image the Fourier or image plane into the sample plane. Köhler illumination is used for observation in conjunction with the dichroic mirror, DM, that allows the transmission of a large fraction of the visible light that is then imaged with an objective and tube lens, L7, onto the Firewire CMOS camera. The illumination system is not shown here, but remains the same as described in figure 2.3.

As noted earlier the SLM creates an undiffracted order due to specular reflection. As this light can dominate the desired pattern it is usual to remove it. The simplest method is to block the zeroth order from passing through the first image plane. I have mainly used a sharp edge of metal placed on a translation stage (at the focal plane), BB in figure 3.12, but one could equivalently paint or lithographically deposit a metallic spot on a thin sheet of glass placed in the image plane to transmit the desired light pattern but block the unwanted zeroth order. This technique can be further improved by making the beam incident on the SLM convergent to allow efficient blocking of the undiffracted light[88].

There are many ways to align optical systems with personal preference playing a major role. To align my optical systems I generally follow a few simple procedures. First I remove all lenses and mirrors, then use two pinholes to align the laser beam using the mirrors from laser to sample. Taking a reference of the focussed beam location in the sample plane I introduce each lens in turn starting nearest the sample. For each lens I ensure the focus returns to the original reference location with no asymmetry.

Having set the experiment up it must be noted that the system can only be aligned perfectly for a single on-axis beam and all others will undergo some aberration. Thus during system set up the usual image plane 'origin' (zeroth order) must be replaced with one chosen by the user through tipping and tilting the SLM. In this way the +1st order occupies the ideal path through the optical train.

3.4.1 Generating software

There are few commercially available software packages for producing and displaying kinoforms on SLMs, and those that do exist are rather poor in terms of user interactivity, speed, and quality. The choice was made to develop my own software that can deal with the specific challenges I would encounter but also lay down a basic foundation of software to be shared amongst fellow researchers that do not necessarily have the physics background to develop such a system.

There are many programming languages that can be chosen from, all with the usual advantages and disadvantages. My choice was National Instruments LabVIEW which has superb user interactivity, instrument communication capabilities and can be very modular. This modular nature lends itself well to creating interactive programs to calculate holograms as once the basics have been understood and programmed they can easily be included in further programs.

The re-mit was to develop software that was able to calculate and display, in as close to real time as possible, phase-only kinoforms for both three dimensional distributions of individual foci and continuous patterns of light. The developed software constitutes three programs that perform these duties and that can be used either independently or jointly. Many other programs have been developed, including firewire camera interfaces, Zernike aberration correction programs and video editing software but here I shall only briefly outline my end product hologram generation software.

The first piece of software utilises the adaptive-additive algorithm to calculate kinoforms from two different starting points. The user can either input the parameters of a grid of spots that can be displaced, expanded and rotated or the user can input an 8-bit greyscale bitmap representing either a pattern of foci or a continuous field of light. In figure 3.13 a photo is chosen as the input image with a theoretical estimate of the optical reconstruction of the calculated kinoform shown.

It is this program that discretises the hologram and image planes to enable fast and simple computation of continuous light fields. The light field desired is simply created as an 8-bit bitmap image with intensity represented as greyscale values. The image is fed in as the desired amplitude distribution and the program iteratively calculates the kinoform required.

Next, I have also written software that allows user interactivity with the sample plane (figure 3.14). Through the superposition and random superposition algorithms this program allows the user to simply click on the sample image and place a tweezers at that location.

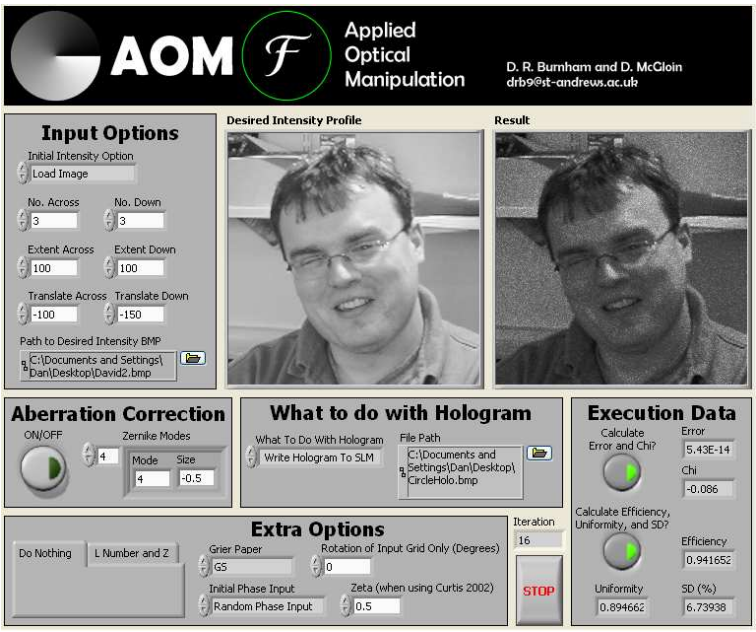

Figure 3.13: Screen shot of the adaptive additive algorithm program that allows calculation of symmetrical grid points of tweezers or any arbitrary greyscale image, which can either be an arrangement of tweezers locations or a continuous field. The input image shown here is a photograph (left) and the program calculates the theoretical optical reconstruction (right) of the calculated kinoform.

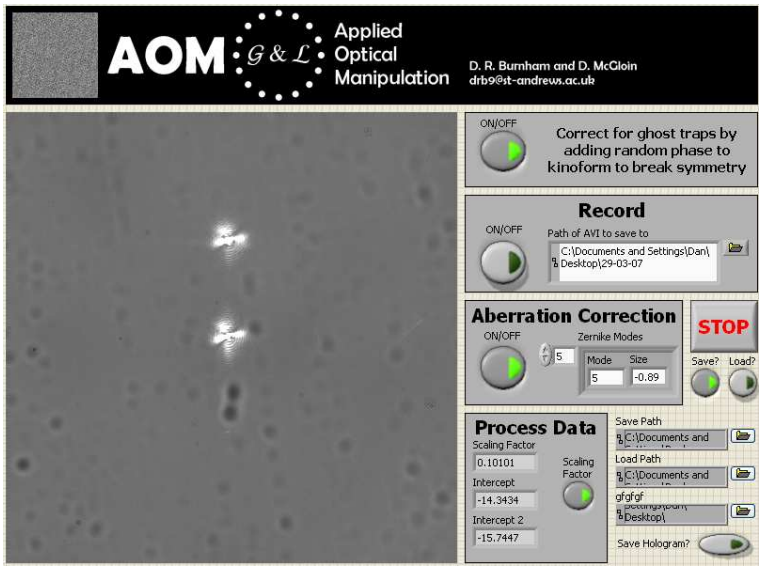

Figure 3.14: Screenshot of user interactive software that allows a simple point and click method of optical tweezing using the superposition algorithm. Multiple tweezers can be created and manipulated by simply clicking on the sample image and deleted as desired. The program can correct for ghost images by applying the random superposition algorithm, apply specific aberrations and trap locations can be imported and exported.

Multiple tweezers can be added and moved from location to location and deleted as necessary. Trap locations chosen using this program can be exported for refinement through the next, final, program described.

In the final program all the previous algorithms are implemented. The input into the program is a spreadsheet where the columns represent trap locations and the rows their evolution through time. The program performs an initial kinoform estimate using either random superposition or random phase mask and then feeds the estimate into one of the iterative algorithms which refine the three performance metrics, efficiency, uniformity, and standard deviation (figure 3.15). The resulting kinoforms, after the required number of iterations can be saved to files for later use or displayed as calculated on the SLM.

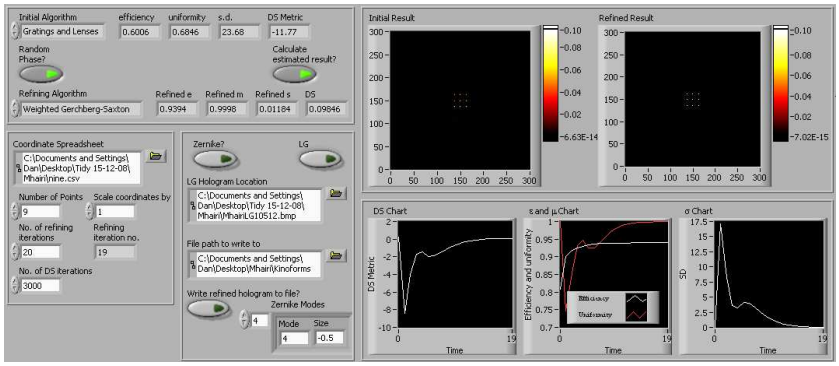

Figure 3.15: Screenshot of the software that can perform all the algorithms discussed. Using a simple spreadsheet input the user only has to decide on the location of the tweezers required and how they evolve over time.

Figure 3.16 shows, as a few examples, desired intensity patterns, calculated kinoforms, their theoretical Fourier transforms, and images of their true reconstruction.

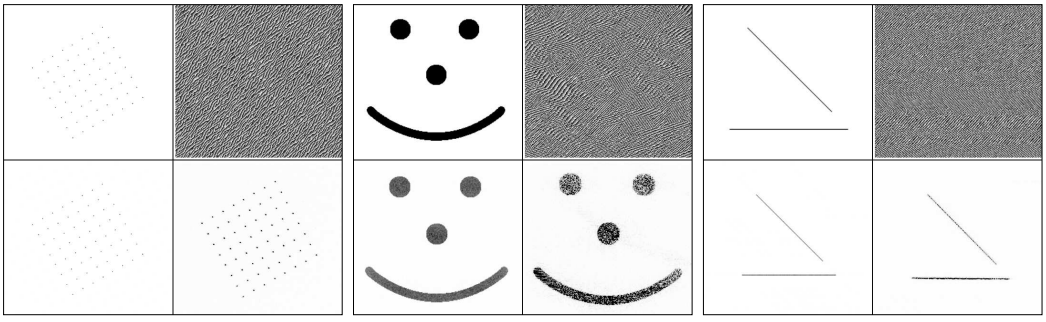

(a) (b) (c)

Figure 3.16: In clockwise order from the top left image for (a), (b) and (c) are the desired input intensity pattern, the calculated kinoform, its true optical reconstruction and its theoretical reconstruction. All images, except for kinoforms, are negatives of the true images for clarity.

Of interest in figure 3.16(c) is the relative intensity of the diagonal and horizontal lines of light which, even though the same length, have differing diffraction efficiencies and hence intensity. This highlights the complex nature of how SLMs operate and also one difficulty in measuring the trapping power at the sample plane.

The current state of the art for holographic optical tweezers comprises many different interaction methods and is nicely exemplified in the work of Gibson *et al.*[96]. Knowing how to build HOTs and how kinoforms can be generated it is worth the effort to optimise the system to obtain as close to diffraction limited resolution, high efficiency and ideal phase to true phase retardation conversion. These are the topics I turn to next.

3.5 Optimisation

3.5.1 Phase characterisation

As with most phase retardation based optical devices SLMs have a wavelength sensitive refractive index and hence diffraction of white light would create chromatic dispersion. For example, if a 2π phase change is applied to 700 nm light using the SLM, it is likely 400 nm incident light would undergo more than a 2π phase change. Another consideration is the non-linear response of phase retardation against voltage signal applied, occurring due to the complex energy change associated with balance between electric and elastic energy densities[148], mentioned earlier. For these two reasons the system must be optimised for a single wavelength. Fortunately, the wavelength has stayed constant throughout this thesis so I have only had to perform the wavelength optimisation once. This process is simple to perform when required as I will now explain.

Clearly, with 256 discrete phase levels, represented by 256 greyscale values, an individual pixel can change the phase by $2\pi/256$ or for 532 nm light a distance of 532 nm/256 $\simeq$ 2.1 nm. The voltage that would give rise to these increments in retardation over the full 2π range needs to be determined. The only way to measure such small values is using interferometry, such as placing the SLM as one mirror in a Mach-Zehnder interferometer[143,164] and varying its retardation instead of moving a mirror. However, for simplicity and using the addressability of SLMs to my advantage I followed the method given by Kohler *et al.*[165]. I simply illuminated the whole SLM with an expanded Gaussian laser beam of the desired wavelength and then masked the incident beam to create two spatially separate beams that arrive on separate halves of the SLM. The two reflected beams from the SLM are then passed through a lens, interfering with each other at the focus. They are then projected via a microscope objective lens on to a camera as shown in figure 3.17.

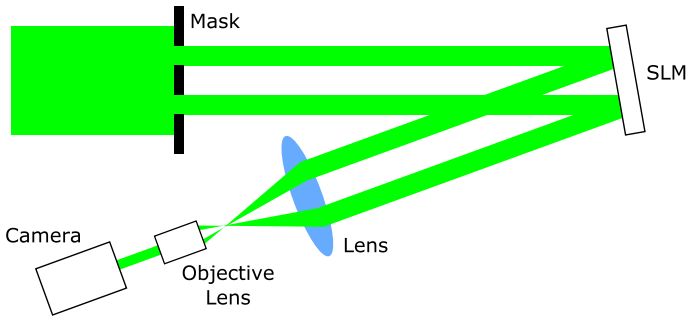

Figure 3.17: An input Gaussian beam is apertured by a mask with two $\simeq 5$ mm holes to produce two separate beams incident onto two separate halves of the SLM. By changing the retardation of one half of the SLM the interference fringes produced at the focal plane of the lens shifts laterally. This fringe is imaged onto a CCD camera and images taken for later analysis.

To create the effect of an interferometer the phase retardation level requested on one half of the SLM is varied in uniform increments while keeping the other half constant. In this way with each new increment the interference fringe pattern at the focus of the lens laterally displaces a fraction of the full 2π range.

Extracting a single line from the same place in each interference pattern and stacking them vertically gives figure 3.18(a). Analysing this allows determination of what fraction of 2π a given grey level can retard enabling the plotting of figure 3.18(b), phase retardation against grey level.

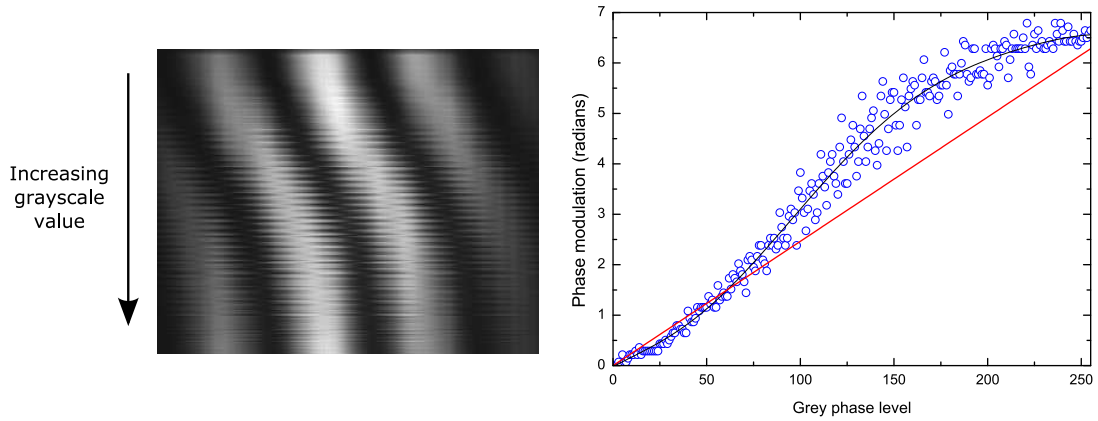

(a) (b)

Figure 3.18: (a) Each line in this image, one pixel in height, is taken from the interferometer image for a given grey level displayed. As is clear the interferometer pattern shifts to the right with each new grey level, hence image line. Extracting the phase retardation per grey level allows a plot of phase modulation against grey level, shown in (b).

Clearly the function is non-linear so a correction must be applied to either alter the voltage addressed for a given phase level or to manipulate the desired grey level to obtain the correct voltage. The former can be performed within the hardware of the Holoeye LCR-2500 SLM using a Look Up Table (LUT) transferred via parallel port and the latter can be performed in software when the kinoform is calculated. An example correction applied in our case is shown in figure 3.19.

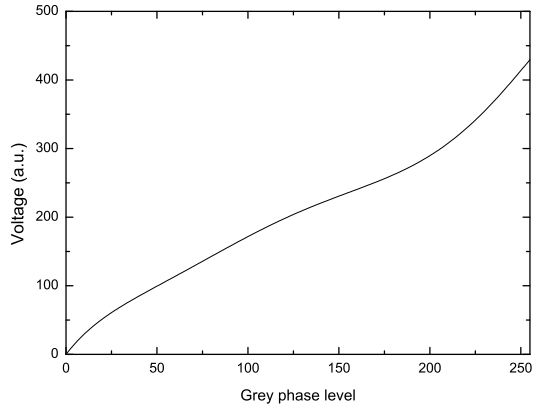

Figure 3.19: Correction to the voltage versus grey level value that should be placed on the SLM hardware to act as the LUT.

Placing this correction on the hardware of the SLM driver and re-running the experiment gives the corrected phase retardation as a function of grey level, shown in figure 3.20, which is reasonably linear and significantly superior to before correction.

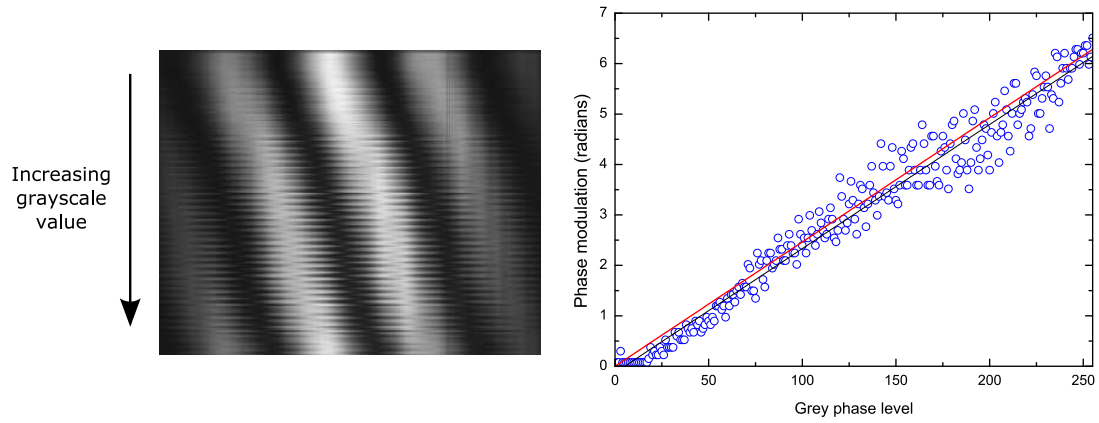

(a) (b)

Figure 3.20: Having placed the correction LUT of figure 3.19 on the SLM driver the experiment is repeated to find (a), a line of amplitude from each interference image, one pixel in height. Extracting the phase retardation per grey level from this image the corrected phase modulation against grey level is plotted in (b).

3.5.2 Aberration correction

To optimise the focussing of beams and to also remove any additional experimental errors it would be ideal to approach, as closely as possible, a diffraction limited focus. A measure of how well this is achieved is the Strehl ratio, S, defined as the ratio of the peak intensity measured at the aberrated focus to the theoretical maximum or[166]

$$S \simeq e^{-(2\pi\sigma)^2}, \tag{3.24}$$

where σ is the wavefront standard deviation. The Marèchal criterion[166] states that the focus is well corrected if $S > 0.8$ which corresponds to a standard deviation in the wavefront deformation of $\lambda/14$.

It is well known that liquid crystal over silicon (LCoS) SLMs can have very non-flat back planes. Any beam incident on the SLM will take on the non-flatness as an additional phase distribution, or aberration. When transmitted by a lens this wavefront is no longer focussed to a diffraction limited Gaussian waist but takes on a deformed shape governed by its aberration.

Further aberrations can be induced by mis-alignment in the optical train, such as off-axis lenses and tilted mirrors. Borrowing techniques from adaptive optics in astronomical observation helps combat these problems. Zernike[167,168] developed a set of orthogonal polynomials that when combined can describe any aberration. The SLM, hence phase retardation, can be used to place a phase correction on the wavefront that will remove the aberration and return the focus to the diffraction limit. To do this I precalculate kinoforms representing each mode of aberration, from -2λ to 2λ in uniform increments, and display them on the SLM in order. For each one a measure of the quality of a focussed diffracted beam is taken using the method outlined by Wulff *et al.*[169] where the beam is focussed on a coverslip and an image taken with the camera through the microscope. This image is then analysed and the metric

$$M_s = \frac{\left(\sum_{ij} I_{ij}\right)^2}{\sum_{ij} I_{ij}^2}, \tag{3.25}$$

calculated, where I_{ij} is the intensity of the ij^{th} pixel. Repeating the procedure 20 times and finding the mean, I obtain figure 3.21 showing the metric performance as the correction passes through from -2λ to 2λ in magnitude for each orthogonal polynomial.

Clearly a minimum exists for one component and using the corresponding magnitude of aberration this is easily converted into a phase profile using the polynomials. Finally this

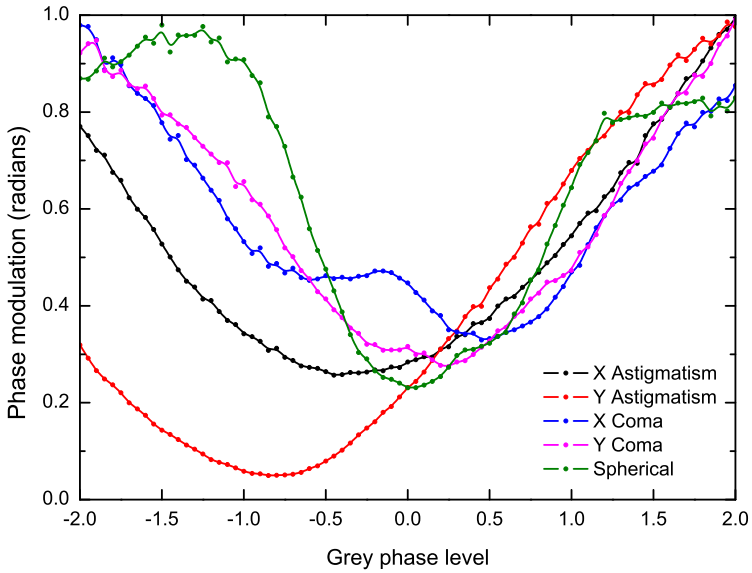

Figure 3.21: Plot of the metric in equation 3.25 as a function of the magnitude of aberration for the first five non-trivial Zernike polynomials. The lower the metric the more closely the reflection of the focussed beam resembles a Gaussian. There is a clear offset to the Y astigmatism curve indicating that placing a kinoform on the SLM for this aberration mode of magnitude $\simeq 0.9\lambda$ will make the beam significantly more Gaussian.

is added modulo 2π to each kinoform before being displayed on the SLM. An example of the 8-bit correction kinoform displayed on the SLM in addition to the normal kinoform is shown in figure 3.22.

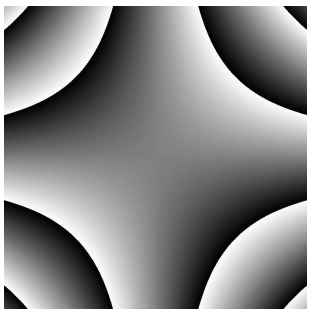

Figure 3.22: Correction kinoform calculated from determining which Zernike polynomials describe the aberration in the system and with what magnitude. If more than one is in error then they are summed modulo 2π.

Using this correction kinoform and repeating the previous experiment gives figure 3.23 showing full correction for the SLM non-flatness and mis-alignments in the optical train.

Measuring the Strehl ratio of a system is difficult as it requires knowledge of the theoretical point spread function or maximum intensity so usually an increase is quoted[170]. In my

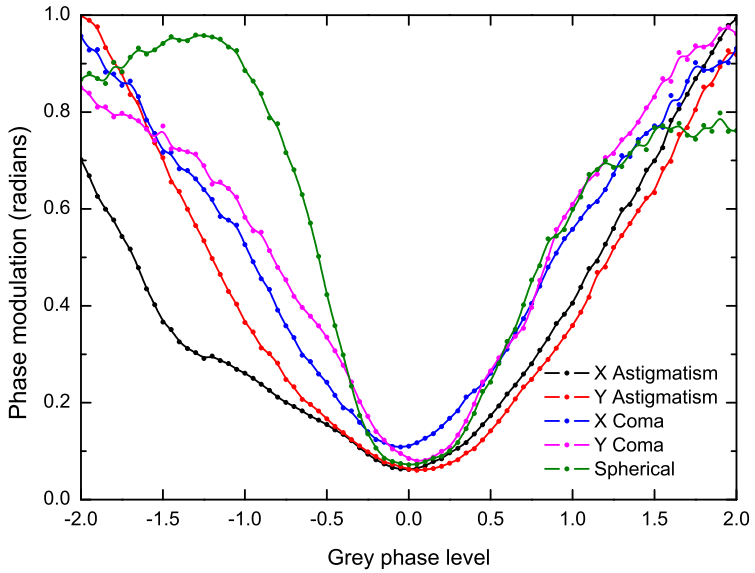

Figure 3.23: Plot of the metric in equation 3.25 as a function of the magnitude of aberration for the first five non-trivial Zernike polynomials with the correction kinoform of figure 3.22 included with each kinoform displayed on the SLM.

system I measured a six fold increase in Strehl ratio.

The method of Wulff *et al.*[169] is chosen as it is simple to implement in current optical tweezers; no apparatus needs to be moved and the aberration correction is performed for the whole instrument not just the SLM. Since this experiment and subsequent correction was performed another method has been described. It uses optical vortex beams to infer information about the aberration[171] which is more precise due to the susceptibility of such beams to aberrations in the optical train.

3.5.3 Problems

Larger lateral and axial displacements from the zeroth order require higher spatial frequencies to be displayed on the SLM with a resulting loss in diffraction efficiency[172]. Also as the spatial frequencies required become higher and higher, due to increased displacement or complexity, aliasing can occur from the pixellation of the SLMs. Their finite resolution means that when discretising sufficiently complex kinoforms the true phase profile is not sampled at twice the maximum spatial frequency (as required by Nyquist sampling) resulting in aliasing and again a lowered diffraction efficiency[172].

The usual dual objective method[173] is performed to quantify the amount of light transmitted to the sample plane relative to a given point at the start of the optical train. However, difficulties appear when trying to measure the power in a holographically generated light

field. Clearly, it is unreasonable to assume the efficiency will always be the same if the same algorithm is used as the hologram generation can start form different points. A good place to measure the power would be in the Fourier transform plane of the kinoform but it is not advisable to focus light onto photodetectors and any light unwanted in the measurement would need to be masked out.

The approach taken was to mask out, as much as feasible, the unwanted light in the Fourier transform plane, then allowing the beam to propagate into an area of collimation where the power could be measured. This still poses a problem when dynamically altering the kinoform as masking becomes a great hinderence. In this case the measurement was made after completion of the time sensitive experiment.

3.6 Conclusion

Although other methods have been described, holographic beam shaping with an SLM is the instrument of choice due to the ease with which it can be set up, relative low cost, its ability to convert between different beam modes and the axial shaping possibilities.

I have described how one should design kinoforms for the efficient generation of the desired light pattern and also how to optimise the SLM to perform correctly.

In the next chapter I will describe how the work of this chapter can be implemented into three new applications for microscopic systems.

Chapter 4

Applications of Holographic Beam Shaping

The state of the art in optical manipulation using holographic beam shaping was discussed in chapter 1. The main body of literature describes improvements in techniques, algorithms and their understanding with few true applications to be found.

In this chapter the application of holographic optical manipulation to three fields of research that have not previously been considered is described, which cover two orders of magnitude in dimension.

Firstly, I apply the techniques to micron sized airborne particles, specifically liquid aerosols. Normally, the liquid medium surrounding biological and colloidal samples acts to damp out the motion of microscopic particles. Combined with their buoyancy trapping such samples is relatively straightforward. To trap particles in the absence of such a highly damping medium (such as air) is more difficult, as will be demonstrated, and less relevant for studies to date. Secondly, I will move to a size regime of ~ 10 μm and into a kingdom of biology rarely investigated with optical tweezers; fungi. Most biological applications of optical tweezers lie within the animalia kingdom but here the methods will be shown to be of use to mycologists. Finally, I move into the ~ 100 μm regime and look at applications in digital droplet microfluidics where my methods provide a versatile non-contact multi beam and pattern extension of optically induced thermocapillary forces[174]. These have allowed the manipulation of objects far larger in size than optical forces alone would permit.

Each subject area in this chapter has its own commonly associated figures of merit which I will briefly review next. Some of the quantities remain relevant for further chapters also.

4.1 Quantities relevant to experiments

When studying processes of microscopic dimension, common sense no longer applies and new parameters must be defined that can indicate how such systems will behave. For example, taking the behaviour of a microfluidic system and applying it to water running off a table, these parameters would indicate that water does not run off but would rather travel around and underneath still 'attached' to the table.

The first parameter of interest relates the ratio of inertial and viscous forces within the fluid flow[59]. This ***Reynolds' number***, Re, is given as

$$Re = \frac{vL}{\nu}, \tag{4.1}$$

where v is the velocity of fluid or particle, L is the characteristic length scale and $\nu = \mu/\rho_{fluid}$, the kinematic viscosity where μ is the dynamic viscosity and ρ_{fluid} is the density of the fluid. The characteristic length is a parameter of the particular system, for example the radius of a microsphere or the width of a microfluidic channel. The value of the dimensionless Reynolds' number indicates whether the system will exhibit turbulent or laminar flow[175]. If $Re < 500$ then it is generally considered the flow will be laminar[175], as is the case in most microfluidic systems. If $Re \ll 1$ then Stokes' flow occurs and viscous forces dominate over inertial forces. In this case the drag on a sphere is given by Stokes' law,

$$F_{stokes} = -6\pi\rho_{fluid}\nu R v, \tag{4.2}$$

where R is the particle radius, v is the relative velocity of particle and fluid, and the remaining symbols retain their meaning.

Next the behaviour of a particle in fluid relative to the fluid molecules is considered. The average distance travelled by a molecule before collision with another is called the *mean free path*, λ, of the fluid. If the particle is much larger than the mean free path of its surrounding fluid than it will 'experience' a continuous fluid. If the particle is much smaller than the mean free path then it can be treated as another fluid molecule. An adimensional number representing this is the ***Knudsen number*** defined as

$$Kn = \frac{\lambda}{R}, \tag{4.3}$$

For $Kn \ll 1$ the fluid is said to behave as a continuum, for $Kn \gg 1$ the fluid resides in the kinetic regime and the region in between is the transition regime. In terms of microspheres in fluids, as the Knudsen number increases towards unity, the drag force on the particle decreases to less than that predicted by Stokes' law. These noncontinuum effects can be

corrected by including the empirical *slip correction factor*, C_c, so Stokes' law becomes

$$F_{stokes} = -\frac{6\pi\nu\rho_{fluid}Rv}{C_c}, \tag{4.4}$$

where

$$C_c = 1 + \frac{\lambda}{R}\left(1.257 + 0.4e^{\left(-\frac{1.1R}{\lambda}\right)}\right). \tag{4.5}$$

giving $\simeq 5.5\% - 1.6\%$ reduction in drag for $3 - 10$ μm diameter droplets, respectively[59].

In relation to aerosols I will need to consider the ***relative humidity*** (RH) of the environment surrounding the liquid droplet being trapped. This is defined as the ratio of the actual vapour pressure of the liquid's vapour, p, to the saturation vapour pressure of the liquid, p^*, at the given temperature and is normally expressed as a percentage[59,176]:

$$RH = \frac{p}{p^*} \times 100\%. \tag{4.6}$$

The saturation ratio, S, is defined as (%RH/100). $S < 1$ for subsaturated vapour, $S = 1$ for saturated vapour, and $S > 1$ for supersaturated vapour. The Kelvin equation shows that "the vapour pressure over a curved interface always exceeds that of the same substance over a flat surface" thus $p > p^*$[59]. Therefore for equilibrium of a *pure* water droplet, a curved surface, in air the surrounding environment must be supersaturated. However, this equilibrium is unstable[59] and droplets in the atmosphere never consist solely of water.

To create a stable equilibrium dissolved impurities, namely sodium chloride, NaCl, are introduced which decreases the equilibrium vapour pressure over a water surface[176]. Now, imagine a droplet made from an aqueous solution of sodium chloride, as it increases in size two processes occur;

- the curvature of the surface decreases, hence the vapour pressure over the curved water surface also decreases.
- the NaCl concentration decreases, hence the vapour pressure increases.

These two competing effects determine the saturation ratio ($\propto$ RH) at which an equilibrium size of droplet is achieved and is more quantitatively described using Köhler theory[59]. The result is demonstrated nicely in figure 4.1 where the equilibrium curves for pure water and three masses of sodium chloride are plotted as a function of radius and saturation ratio. As discussed it is not possible for pure water to reach an equilibrium size in a non-supersaturated environment. Including salt allows the droplets to exist in a subsaturated environment which is possible to create in the laboratory. Of importance to the investigations here is that for larger dry particle masses of salt larger liquid droplets can

exist.

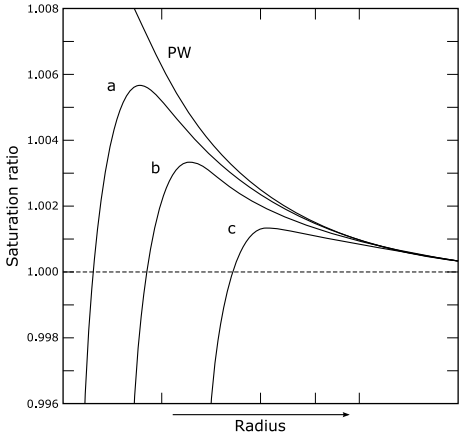

Figure 4.1: Change in droplet radius for varying salt concentration as a function of saturation ratio. The radius scale here extends from ~ 0.1 to 10 μm. Examples of the mass of salt in the droplet for curve (c) is $\sim 10^{-15}$ g, for (b) is $\sim 10^{-16}$ g and $\sim 4 \times 10^{-17}$ g for (a). (Adapted from Monteith and Unsworth[176]).

Figure 4.2 displays the evolution of particle radius as a function of relative humidity allowing an appreciation of the physical chemistry at work. My studies exist on the far right curve of the plot above crystalisation and below $RH \simeq 95\%$.

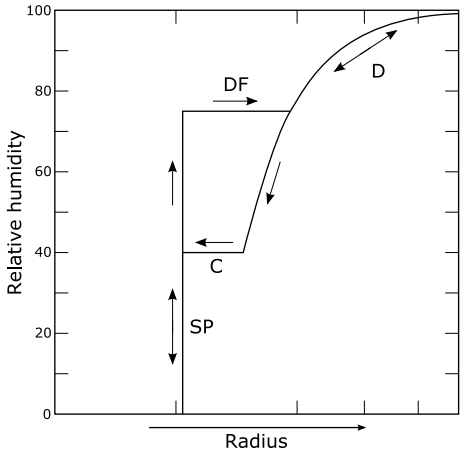

Figure 4.2: An example plot for a specific salt mass of the radius of a droplet as a function of relative humidity showing the hysteresis in the crystalisation (C) and droplet formation (DF) processes. In the regions SP and D only solid and liquid particles exist respectively. I work on droplets that exist on the far right curve of the plot above crystalisation and below $RH \simeq 95\%$. (Adapted from Monteith and Unsworth[176]).

4.2 Aerosols

The ability to trap and interrogate multiple airborne particles in a controlled manner offers much to those who wish to study aerosol properties, composition and dynamics.

In this section I describe the first use of the holographic methods discussed earlier to optically trap and manipulate airborne particles, in this case liquid droplets. Making use of such devices allows for arrays of particles to be trapped simultaneously, as well as allowing their controlled x, y and z translation and thus coagulation. Coupling HOTs with cavity enhanced Raman spectroscopy (CERS) to create micro total analysis systems (μTAS) is also discussed.

4.2.1 Apparatus specific to the manipulation of aerosols

As with all subsequent experiments in this thesis the experiment is performed in a specific type of chamber above a glass cover slip or microscope slide. The apparatus and techniques are described in chapter 3, the only differences here are the microscope objectives used and the application specific sample. For the holographic optical trapping of aerosols I use a 100× Nikon microscope objective (CFI E Plan Achromat 100× oil, NA 1.25) and use the sample chamber pictured in figure 4.3 which takes the position of 'generic sample' in figure 3.12.

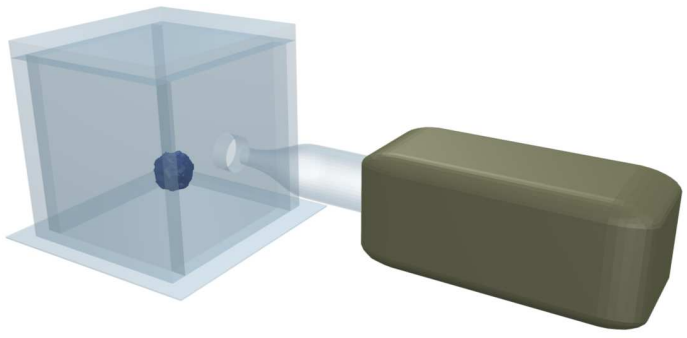

Figure 4.3: Representation of the chamber into which nebulised salt solution is inserted. The nebuliser uses a vibrating mesh driven by piezoelectrics and the resulting aerosol is passed into the chamber via a custom made glass nozzle. In one corner of the chamber distilled water soaked tissue paper is placed to assist in creating a humid environment.

The glass cube is placed on a type one coverslip through which the trapping light is focussed. A piece of blue tissue paper is saturated with distilled water and placed inside the chamber to increase the relative humidity. The liquid aerosol is produced by nebulising a salt solution with an Omron MicroAir NE-U22 vibrating mesh nebuliser which produces a polydisperse sample of liquid droplets with a mass median aerodynamic diameter of 4.9 μm[177,178]. The aerosol is transferred through a hole in the chamber side via a custom made tapered glass nozzle[81].

The chambers are not perfectly sealed so achieving 100% relative humidity is unrealistic but, as explained, the addition of sodium chloride to water allows droplets to reach stable equilibrium at lower relative humidity. So I use the addition of impurities to the aerosol to my advantage by creating salt solutions of varying concentrations. Within this section the salt concentration was set to be 20 gL^{-1} and kept constant throughout. However, in chapter 5, variations in concentration are used to coarsely adjust droplet size.

The insertion of nebulised salt solution into a closed chamber creates a cloud of aerosol that, unless trapped, will inevitably settle on the coverslip surface. The 'puddles' of water created, 10s of microns across, are problematic. They can aberrate the trapping beam to such an extent that not only do droplets fall from traps but also imaging is distorted preventing video microscopy sizing, unless they are sited directly over the puddles centre where curvature is at a minimum and symmetric. The solution is to treat the coverslips by placing them in a 50% distilled water dilution of 'Decon 90' for longer than one week and rinsing them with distilled water before use. This increases the hydrophilicity of the surface and provides a thin and uniform layer of water, above which, aerosol can be trapped.

4.2.2 Holographic optical trapping of aerosol droplets

Arrays of aerosol droplets, shown in figure 4.4, can be trapped[179] although the images also illustrate one of the difficulties of trapping in air. In a liquid medium colloidal particles are relatively slow moving and one can actively seek them out without too much trouble. Alternatively the trap can be static with particles flown in to try and fill the sites, but this can lead to multiple particles in a single trap, jamming, or particles knocking each other out.

In air the aerosols move far more quickly than colloids in water, and at times it is difficult to discern individual particles until they are stationary in traps. So, there is no choice but to place the trap sites in the desired locations and wait for the particles to 'fall' into the traps.

In the current experimental geometry trap loading is far from optimised. The images shown illustrate that although the trap pattern is relatively simple, and would be easy to fill in liquid, it may be that no sites at all are filled if no aerosol passes through the trapping region of any site. Possible reasons for this difficulty of capture will be discussed in more detail in chapter 6.

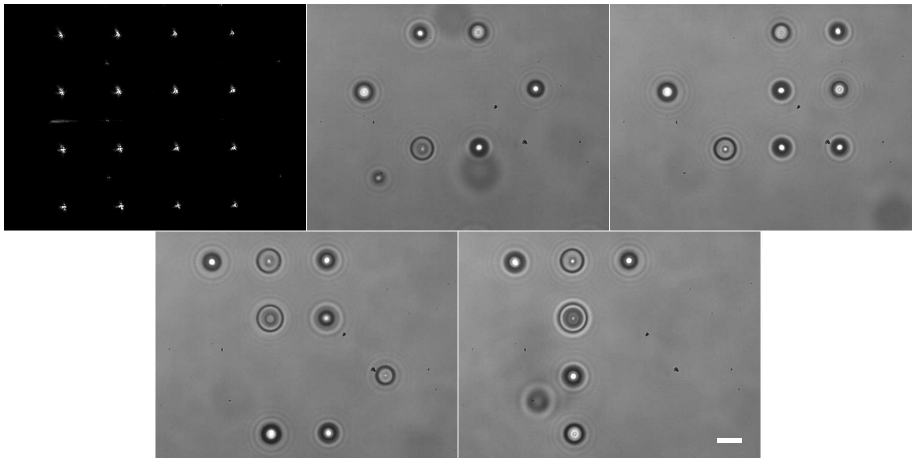

Figure 4.4: Top left image shows the backscattered light from the bottom of the microscope slide revealing the holographic trapping pattern. The remaining images show the resulting trapped water droplets after multiple uses of the nebuliser in attempts to fill all trap sites. As indicated in the text, although the trapping pattern is relatively simple, it is hard to fill all the sites at once. Scale bar is 5 μm.

In chapter 3 it was shown that near continuous resolution of movement is possible if the correct algorithm is used to calculate the kinoforms. The experiment's speed has two limiting factors, firstly the refresh rate of the SLM, ~ 75 Hz, and secondly the diffusivity of the particles given by

$$\langle x \rangle^2 = \frac{k_B T C_c t}{3\pi\mu R}, \tag{4.7}$$

where k_B is Boltzmann's constant, T is temperature, C_c is the slip correction factor, μ is the dynamic viscosity of the surrounding fluid, R is the droplet radius, and t is time. When tweezing in liquid the movement of a trap site cannot be too large an increment because the particle motion is so heavily over-damped it may not follow the trap quickly enough and in effect 'lag' behind. When trapping in air the converse problem occurs; if the trap site is not re-positioned quickly enough the Brownian diffusivity may be too great and the droplets will have diffused too far away to be affected by the trap in its new position. Figure 4.5 plots the Brownian diffusivity of particles in water and air media against radius, illustrating the need for careful thought before choosing the manipulation scheme.

The apparatus is able to trap a range of droplet sizes from $\simeq 2.5$ to 12 μm in diameter

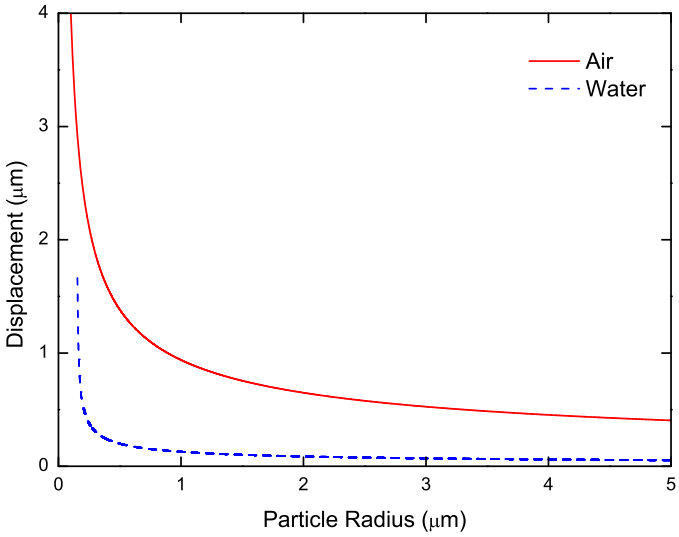

Figure 4.5: Theoretical curves showing displacement after 16 ms (SLM response time) due to Brownian diffusion as a function of particle radius when suspended in water (dashed blue curve) or air (solid red curve).

with the minimum power required to trap an aerosol being 380 ± 20 μW giving an axial efficiency, Q_{axial}, of 0.22 ± 0.01, comparable to results in conventional tweezers[121].

It is common knowledge when working with optical tweezers that a lower limit on the power needed to trap exists, with an increase in power improving trap stiffness and the ease with which a nearby particle is 'captured'. Some things entirely unintuitive occur when trapping objects in air; there is a linear dependence of 'captured' droplet size as a function of trapping power no overall change in ease of capture and small droplets cannot be 'captured' at large powers. This is shown in figure 4.6

In liquid based tweezers nearly all studies are reliant upon using microspheres with a highly calibrated radius to ensure the same conditions throughout repeated experiments. The situation in aerosol trapping is vastly different with the nebulised aerosol having a large polydispersity and no robust method of selecting size, although figure 4.6 suggests some size selectivity may be possible.

The size distribution within the sample chamber is dependent upon the water's salt concentration, the nebuliser used, flow conditioning[81] and perhaps chamber geometry. It is also possible that the duration between nebulisation and trapping can influence coagulation and settling. It is therefore a reasonable assumption that the gradient and intercept of figure 4.6 will vary between experiments[79].

The stable trapping and precise manipulation of water droplets allow not only their individual control but also the ability to coagulate multiple droplets, as demonstrated in

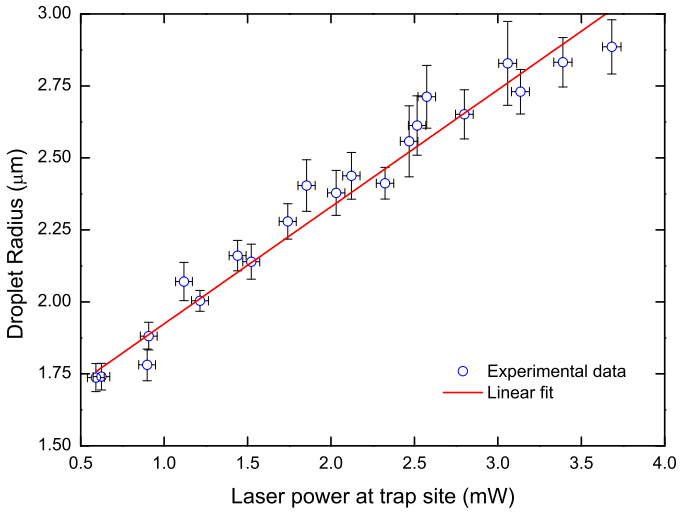

Figure 4.6: Graph showing the variation of droplet size as a function of power. The vertical standard error bars increase in size with power indicating that not only can higher powers trap, on average, larger droplets but also a greater distribution of sizes. The horizontal error bars mostly arise from the non-perfect intensity uniformity of the trapping sites.

figure 4.7. Axial control is also achievable (figure 4.8) using algorithms described in section 3.3.2.

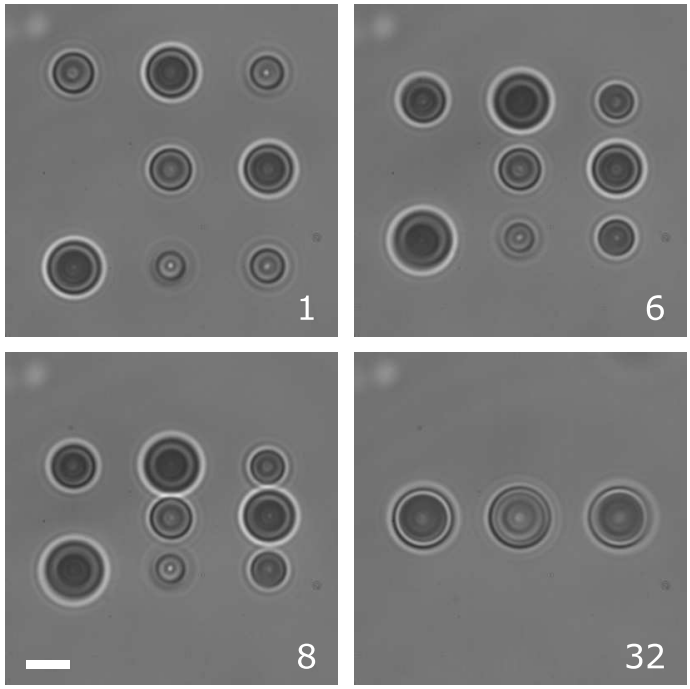

Figure 4.7: A series of four images showing the coagulation of eight water droplets into three by altering the kinoforms displayed on the SLM. The numbers indicate the video frame with the time between frames being $1/30^{\text{th}}$ of a second. The scale bar is 5 μm.

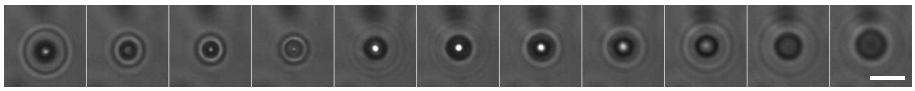

Figure 4.8: A series of microscope images demonstrating the axial control of water droplets from −10 to +10 μm. The white bar indicates a scale of 5 μm.

The system is not limited to homogeneous species, for example, figure 4.9 shows the coagulation of aqueous NaCl and dodecane droplets.

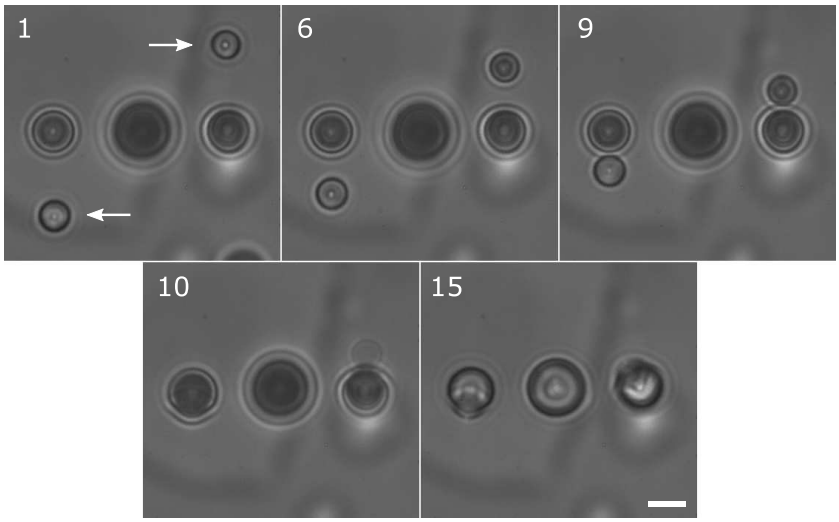

Figure 4.9: Still images taken from a video showing the coagulation of two dodecane droplets with two separate aqueous sodium chloride droplets. The white arrows in the first frame indicate the two dodecane droplets before movement. The numbers indicate the frame number where the time between single frames is $1/30^{\text{th}}$ of a second. Scale bar is 5 μm.

The problems with trap loading are exacerbated when dealing with two different species of chemical. There is no easy way to load each different one into a predetermined trap site or indeed to prevent them from coagulating accidentally as they become trapped. Again, it is a matter of patience and fortune as to whether the desired species are trapped at the desired locations.

The figures with images of trapped droplets highlight a major hurdle in quantitative analysis with the inability to precisely size droplets from video images alone. This is due not only to their dynamic nature but also to the poor definition of their circumference on the video output. Far more precise techniques are already in frequent use[12] and when coupled with the holographic manipulation outlined here enable a robust airborne micro total analysis system (μTAS) which will be described shortly. I have also developed a new simple and quick method of sizing aerosols, as will be discussed in section 5.4.2. One difficulty is how to extend this technique to size multiple droplets simultaneously but I

will also present some ideas to solve this problem.

The quantitative results given here are specific to a single concentration of sodium chloride, with any alteration in the aerosol composition significantly altering the droplet's properties (figures 4.1 and 4.2). This obviously increases the complexity compared to simple monodispersed or even polydispersed microspheres with fixed dimensions and properties because droplets can condense, evaporate, absorb, and constantly interact with their surroundings. These challenges can be overcome by designing better chambers[180] and using multiple particles as controls[181] and will hopefully allow for interesting and useful science not just in atmospheric chemistry but also in fundamental physics as will be discussed in chapter 7.

The experiments described here were the first demonstration of optically trapped arrays of aerosols with controlled manipulation and coagulation. It has been shown that, perhaps counter-intuitively, SLMs can reposition traps fast enough so the aerosols will not be out of the trap's capture range. Published at approximately the same time the second type of popular beam shaping method, AODs, were also used to trap arrays of aerosols[181], but this technique cannot displace the trap in the axial direction and may also present further problems by the nature in which they operate. The time-sharing of the beam between trap sites causes an oscillation in power, going from zero to maximum (with a specific response time), at a specified frequency. I will show later in section 5.6 that this oscillation can completely and catastrophically change the trapping properties of the system if the frequency is not selected correctly.

Since the work was carried out improved kinoform generation algorithms have been developed[87]. When trapping aerosols the efficiency with which HOTs operate is not of paramount concern as only very small powers are required. However, these algorithms can vastly improve the uniformity of the trap intensities which, given the linear dependence of captured droplet size on power, is essential for more controlled experiments.

Issues remain with holographic optical trapping. The input of an aerosol sample mimics that of atmospheric aerosols to some extent but for 'in the field' applications more robust methods of trapping must be developed[82]. For airborne microfluidic applications, where specific chemical reactions wish to be carried out, improved loading strategies must be investigated. Piezoelectric driven micro droplet generators have been tried but due to the bulk of the device and the high velocities upon exit these have proved difficult to use. I feel there is potential in optically guiding the airborne particles to the trap sites using either free[80] or enclosed[182,183] beams. A more recent device which creates micron size droplets in liquid-liquid phase microfluidics[184] may be adapted in future to suit the airborne situation allowing the precise creation and placement of airborne droplets.

I have established that holographic optical tweezers can be repositioned quickly enough to prevent the loss of optically trapped droplets. However, I made the assumption that the beam to be relocated is simply turned off instantly, moved, and switched back on instantly. This is likely to be a bad assumption with the finite response time of the SLM, therefore, it is worth noting how the repositioning of traps really occurs. In order to do this I recorded at high speed, and display in figure 4.10, the translation of a single focus through a microscope objective reflected at a coverslip to water interface.

Figure 4.10: Images of the translation of a single focus reflected from a coverslip to water interface taken at high speed. The time between start and end is $\simeq$ 100 ms. The light does not simply disappear and reappear within the response time of the SLM as may have been expected but rather seems to spread out between original and new foci.

One's first, naïve, assumption would be that the light completely disappears from the focus but as can be seen the original focus extinguishes as the new focus appears with the intensity not only split but also spread out between the two. Perhaps this helps to 'guide' the aerosol between the traps.

Having established the technique of holographic manipulation of aerosols it is interesting to explore the technique's power. A crucial parameter of a liquid-gas phase droplet system is the relative humidity (RH) but there is difficulty in measuring it for the gas phase accurately. It has been shown that using multiple droplets enables the use of one as a local probe of RH enabling comparative measurements between droplet species[180]. By implementing HOTs with spectroscopic techniques, collaborators and I have shown that multiple aerosols can be simultaneously manipulated, sized with CERS, and coagulated. Using one droplet as a RH probe enables the prediction of the size evolution of those remaining and using coagulation allows the upper limit on droplet size to be pushed[185].

In conclusion I have established the use of HOTs in aerosol studies to manipulate homogeneous and inhomogeneous species of aerosol in three dimensions with the ability of coagulation, thus improving the toolbox at the disposal of atmospheric chemists.

4.3 Orbital Angular Momentum (OAM)

One application of beam shaping is the ability for mode conversion. Creating a Laguerre-Gaussian beam with the SLM allows the creation of beams carrying orbital angular momentum[186], which is closely related to spin angular momentum[9]. A famous experiment was carried out by Beth[187] that showed a torque could be produced by the refraction of circularly polarised light through a waveplate suspended on a torsional pendulum due to spin angular momentum. The magnitude of what he observed was tiny because of the small angular forces imparted, $\sigma\hbar$ per photon, and the relatively large mass of the object.

The use of optical tweezers has allowed the study of the fundamental properties of light, such as its momentum, to be more accessible. Construction of experiments to study the beam properties with optical tweezers is far simpler as no vacuum equipment or careful manufacture and setup of torsional pendulums is needed. It has also allowed the detailed study of orbital angular momentum with several classic experiments[9,32,33]. Based on the same principles as Beth's original, these experiments allow the focussing of light onto microscopic objects and hence the effect is hugely magnified.

Although the transfer of SAM and OAM has been shown successfully, angular acceleration has not been observed in microscopic experiments but only macroscopically with SAM by Delannoy *et al.*[188]. Is there improved potential for observing microscopic angular acceleration in an air medium due to its lower dynamic viscosity?

Focussing a Laguerre-Gaussian beam[189], created with the HOTs apparatus, with azimuthal index $l = 80$, into the aerosol chamber it is possible to trap multiple droplets around its circumference. The rotation rates are far more rapid than for colloidal particles in water due to both the increased momentum transfer and the higher terminal velocity in air. An example is shown in figure 4.11, although a full rotation is not illustrated, multiple orbits can be achieved.

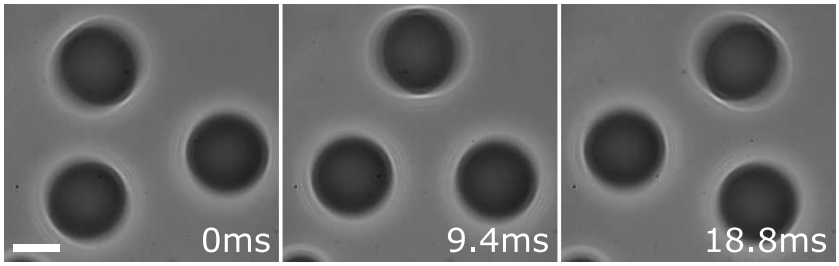

Figure 4.11: Rotation of water aerosol using a Laguerre-Gaussian beam. The three droplets are trapped in a single $l = 80$ beam with the upper one staying in the upper half of each image. The clockwise rotation is clearly seen as a function of time. Full rotation of complete circuits is possible but not shown. Scale bar is 5 μm.

Although there are clear increases in rotation speed due to the reduced dynamic viscosity the system still reaches terminal velocity too quickly to observe angular acceleration. If the power was lowered to reduce acceleration then droplets are unlikely to be trapped. The angular acceleration is given by

$$\alpha = \frac{3Pl\lambda}{8\pi^2 R^3 \left(\frac{2}{5}R^2 + r^2\right)\rho c}, \tag{4.8}$$

giving the time to reach terminal velocity to be

$$t_{term} = \frac{16\pi^2}{27}\frac{R^5 g \left(\frac{2}{5}R^2 + r^2\right)\rho^2 c}{3rPl\lambda\eta}. \tag{4.9}$$

where P is the laser power, l is the azimuthal index, λ is the wavelength, R is the particle radius, r is the beam radius at waist, ρ is the density of the sphere, η is the fluid's dynamic viscosity, c is the speed of light and g is the acceleration due to gravity.

An order of magnitude estimate for a reasonably large aerosol ($R = 5\ \mu m$) gives $t_{term} = 0.25$ ms. This is below the frame rate of even relatively fast cameras capable of 1000 frames per second and to obtain enough data the exposure time would need to be approaching 100 μs. Therefore to observe acceleration either the detection technique needs to be faster or the experiment parameters changed. Decreasing the dynamic viscosity would help but to do this a vacuum greater than one thousandth of an atmosphere would need to be created before the viscosity starts to change[190]. At this pressure water would boil and we can see that this experiment begins to become increasingly complex; solid aerosol will be needed in a high quality vacuum chamber which presents its own challenges, not least how to get the aerosol in the sealed chamber.

The other option is to use a faster detection method such as a very high speed camera that tracks particle position in hardware[191] to sample at well below the time to reach terminal velocity.

In conclusion more work is necessary but it is hoped the advantage of microscopic orbital angular momentum experiments in air can be brought to bear on angular acceleration due to orbital angular momentum.

4.4 Fungi

The second new field of application that I apply HOTs to, is in the manipulation of the filamentous fungi *Neurospora Crassa*, a common fungus also known as bread mould. In this section I step up an order of magnitude and start to look at objects that are $\sim 10\ \mu$m

in width, and begin to move away from direct manipulation with optical forces and look at indirect methods using the light as the initiating tool. The ability of optical tweezers to precisely position a highly localised intensity gradient of light is the reason for its choice here. Here I provide evidence to support that it is not direct optical manipulation of fungus that causes the effects observed but that the effect must be mediated by some other method.

This section describes work that was carried out as a collaboration with the Fungcal Cell Biology group from the University of Edinburgh. The project was caried out jointly by myself and Graham Wright and lead my Nick Read and David McGloin.

Light is well known to affect many biological processes and can be used to experimentally manipulate growth at both organismal[192] and cellular levels[193]. The focussing of light through a microscope is ideal for manipulation at the cellular level and optical tweezers have proved themselves useful in many areas of biology.

In recent years optical tweezers have been used extensively as tools for micromanipulating biological systems. The techniques of Ashkin quickly found use in manipulating individual cells, viruses, and bacteria[46,194]. They have been used in a wide range of applications including micromanipulating cells to redirect their growth[195–199], micromanipulating organelles within cells[195,200,201], isolating individual cells, organelles and chromosomes[202,203], measuring the forces produced by motor proteins and RNA polymerases[204–207], measuring the biophysical properties of DNA[26,208–212], fusing cells[213], providing localised mechanostimulation to cells[214] and automated cell sorting[215].

Whilst optical tweezers have been widely used in biological investigations, their use with filamentous fungi has been largely unexplored. The filamentous fungi are an extremely important group of organisms. They cause human and crop diseases, spoil food, recycle nutrients in the biosphere, promote the growth of plants with which they have symbiotic associations, and are used in food production, brewing, and as a source of pharmaceutical drugs[216]. The colony of a filamentous fungus develops into a complex interconnected network of multinucleate, tubular cellular elements called hyphae (figure 4.12a)[217]. These hyphae grow at their tips and penetrate with force and by digestion through the microenvironments which they inhabit. Hyphae exhibit tip growth as the result of the activity of a multi-component structure called the Spitzenkörper. The Spitzenkörper secrete vesicles in a localised region (the extension zone) to allow for 'wall-building' exclusively at hyphae tips (4.12b)[218,219]. *Neurospora crassa*, the species used throughout this investigation, is commonly used as a model system for experimental studies[220,221] and was the first filamentous fungus to have its complete genome sequenced[216,222]. It produces large, fast growing hyphae making it an excellent system for combining live-cell microscopic imaging

with experimental micromanipulation using optical tweezers[223,224]. After initial inoculation from a parent colony the hyphae can grow into a new colony covering $\sim$ 15 mm in diameter in less than one day if left in a non-regulated environment, making it ideal for investigation outside a specialised fungal cell biology laboratory.

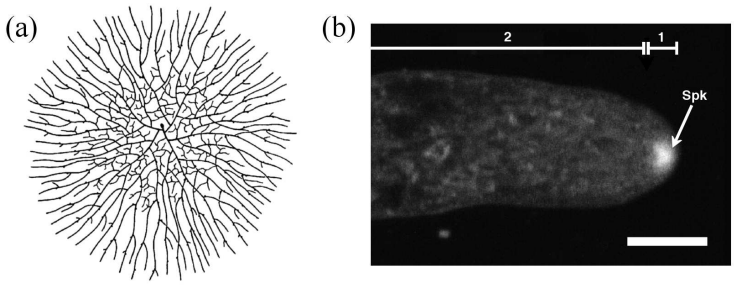

Figure 4.12: (a) The colony of a filamentous fungus composed of a network of hyphae. The hyphae studied in the present investigation are those located at the colony periphery. (b) A confocal image of a growing hyphal tip of *Neurospora crassa* at the colony periphery after staining with the membrane-selective fluorescent dye, FM4-64[225]. Note the concentration of stained secretory vesicles within the Spitzenkörper (Spk), the region of hyphal extension (1), and the non-extending region (2) (adapted from Wright *et al.*[226]). Scale bar is 5 μm.

The first use of optical tweezers with filamentous fungi showed that organelles could be manipulated inside living hyphae without causing damage[200]. Later single beam optical tweezers were used to change the direction of hyphal growth, concentrate secretory vesicles and induce branching[196]. The most significant observation in this work was that the Spitzenkörper seemed to be repelled by the laser rather than being trapped, which was confirmed and investigated more recently[223,224,226]. The refractive index of the Spitzenkörper is predominately higher than the adjacent cytoplasm[227], so one would expect it to become trapped[196]. Wright*et al.*[226] used optical tweezers to measure the growth forces generated by hyphae at the colony periphery of *N. crassa* (figure 4.12). Calibrated optical traps placed beads in the path of growing hyphal tips to study the forces induced upon contact from particle displacement. It was found the hyphae were able to generate growth forces in excess of the forces achievable with the optical trap used (i.e. $>$ 19 pN). It was later shown that specialized hyphae, namely germ tubes, produced during spore germination and which are involved in colony establishment, are not able to completely displace the optically trapped beads, suggesting that they produce growth forces $<$ 19 pN. The germ tubes responded to the trapped beads by undergoing apical swelling until the beads were removed whereupon their growth extension resumed[223,224]. In contrast, the fast growing hyphae at the colony periphery when mechanically stimulated with beads only underwent a slight redirection in growth and their rate of extension was unaffected[223].

Fungi possess a variety of photoreceptors and a range of responses to light but little is

known about light-mediated responses of fungal hyphae, except that hyphal tips have been shown to avoid 785 nm[223,224,226] and 830 nm[196] light. Whether these are photoreceptor-mediated responses or some sort of physical repulsion of the Spitzenkörper by the tweezers is unknown.

Previously, alterations in the pattern of hyphal tip growth have been induced by what can be termed active methods; single or dual beam conventional Gaussian tweezers have been actively moved to interfere with the hyphal tips[196,223,224]. However, this work aims to use passive methods, in which the hyphae are allowed to grow towards and through stationary optical tweezers. Of significant interest would be the possibility to not only briefly redirect the hyphal tips but to manipulate hyphal growth over significant distances, and possibly into complex patterns allowing controlled studies of inter-hyphae signalling.

In chapter 3, I discussed how optical beam shaping proves to be a useful technique that allows light to be 'sculpted' into more complex structures than single or dual beam Gaussian tweezers. Although yeast cells and ungerminated spores have previously been manipulated with multiple optical traps[228–230], fungal hyphae, and hyphal tip growth, have not. Here I describe the first use of holographic optical tweezers, and more generally holographic beam shaping, to create both multiple single beam tweezers and extended patterns of light to manipulate filamentous fungi.

By borrowing the light sculpting techniques of optical tweezers, but without the sole purpose of trapping, the main aims of this study were to further assess what processes give rise to the redirection of hyphal growth by light, and to determine how the pattern of hyphal growth and branching can be manipulated over extended distances with HOTs.

4.4.1 Apparatus and experimental procedure specific to fungi

Three different wavelengths of light were investigated, 532 nm, 785 nm, and 1064 nm produced using a Laser Quantum finesse, a Blue Sky Research laser diode (VPSL-0785-070-x-5-A) and a IPG Photonics YLM series lasers respectively. Each wavelength used a separate piece of apparatus, but all are based upon the systems described in the preceding chapters. In particular the 785 nm apparatus is a basic tweezers as described in chapter 2 and has been used in previous fungi studies[224]. The 532 nm system was the same HOTs apparatus shown in figure 3.12 and to create a comparable single beam tweezers the SLM was replaced by a mirror.

The holographic apparatus remains the same except for the sample into which the light is focussed and the microscope objectives used. In this the objective was either a Nikon Plan (objective A) or a Nikon E Plan (objective B), 100× 1.25 NA oil microscope objective.

The objective used for the results presented here is indicated in each figure.

The continuous light patterns produced through holography only exist with a reasonable fidelity in a relatively shallow axial plane. Experiments with axially extended light fields, or 'pseudowalls' of light were also performed, as discussed later. These walls consisted of multiple, two dimensional, continuous light patterns displaced above and below the normal focus. Figure 4.13 illustrates the clear difference between these pseudowalls and the simple, axially compact, structures normally produced. The kinoform to be placed on the SLM is created simply by calculating those required to produce particular patterns at desired axial planes and then finding the argument of their complex sum, in a similar manner to equation 3.13. The result is a single kinoform producing patterns in multiple, spatially separated, axial planes.

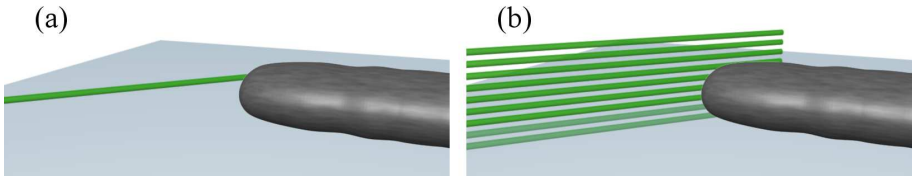

Figure 4.13: Representation of a hyphal tip approaching (a) a single line of light, as shown in the results of figures 4.16-4.19, or (b) nine, axially stacked, single lines of light, or a pseudowall as shown in the result of 4.20.

Fungal strains, culture conditions and sample preparation

The *Neurospora crassa* wild-type strain 74-OR23-1VA (# 2489, FGSC, Kansas City, KS, USA) was used. It was grown and maintained on solid Vogel's minimal medium[220] at room temperature. An agar plug was used to inoculate a plate at one edge, allowing growth for ∼17 hours before experimentation. To image and manipulate hyphal tips, the inverted agar block culture method was used[225] and replaced the generic sample in figure 3.12. Hyphal tips were given > 30 minutes to recover and resume normal growth once sample preparation was completed.

4.4.2 Results

Each experiment was carried out between 2 and 15 times.

Gaussian Beams

It has been established that both 785 nm and 830 nm simple optical traps can be used to manipulate hyphal growth and branching[196,223,224,226]. Here I examined the effects of 532 nm and 1064 nm light and included further experiments with 785 nm light for comparison.

The range of powers needed to cause a change in the pattern of hyphal growth varied largely with wavelength; for 1064 nm light $150 - 500$ mW, for 785 nm $40 - 70$ mW, and for 532 nm light $1.9 - 14$ mW. For each range stated the minimum power was the lowest to cause an observable effect and the maximum was the highest to cause an effect without producing irreparable damage to the hyphae. The laser powers quoted are those incident on the back aperture of the microscope objective with the focus approaching the diffraction limit for each wavelength.

Examples of changed growth patterns for each wavelength, are shown in figure 4.14. The altered growth effect in each case was clearly associated with the proximity of the hyphal tip (and thus Spitzenkörper) to the optical trap. Once the hyphal tips had passed the trap, normal growth resumed back along its original direction, unless growth was stopped because a hyphal tip was exposed to too high a laser power. In all experiments it was important to judiciously use the minimum laser power necessary to cause a change in hyphal growth patterns otherwise it would commonly be stopped.

Unfortunately, the alteration of direction is short lived, both in time and distance, for all wavelengths studied. The usefulness of optical manipulation here would be greatly increased if the hyphae could be controlled over extended distances. To combat this the holographic methods are introduced.

Multiple Gaussian Beams

Figure 4.15 shows the result of allowing a hyphal tip to grow into a curve made from nine individual tweezers, produced using the holographic techniques already described.

The results were wildly inconsistent, rarely ending in a hyphal tip following the full pattern of multiple tweezers. These unsuccessful results generally occurred for one of two reasons. Firstly, the spacing of the tweezers often allowed hyphal tips to grow through the gaps between them without causing redirection. Secondly, if the hyphae grew through a tweezers their growth could cease from overexposure to the laser beam.

To minimise these factors the light needs to be evenly distributed along the desired alter-

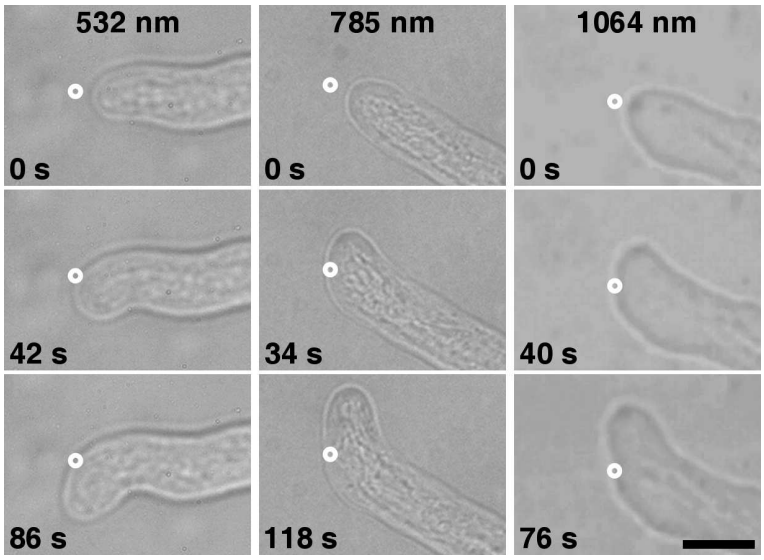

Figure 4.14: Examples of redirecting growth using 532 nm, 785 nm, and 1064 nm single Gaussian beam traps. The power required to cause the effect is between $1.9 - 14$ mW at 532 nm, $40 - 70$ mW at 785 nm and $150 - 500$ mW at 1064 nm. The white circle indicates the position of the optical trap. Scale bar is 10 μm.

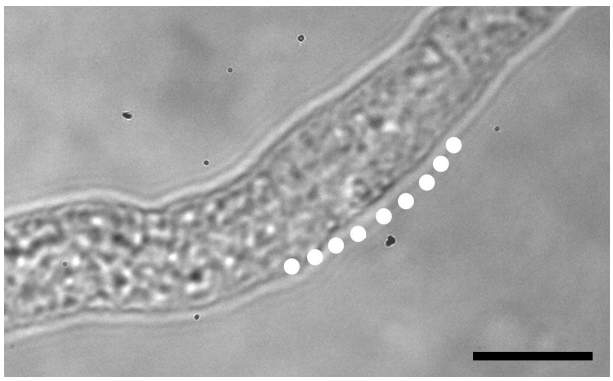

Figure 4.15: Continuous redirection using nine 532 nm Gaussian traps produced with HOTs and objective A. The hyphal tip grew from bottom left to top right. White dots represent the position of each focussed trap. The laser power per tweezer focus was $\simeq 2 - 3$ mW. Scale bar is 10 μm.

ation pattern. This even distribution is again possible through the use of holography to create continuous light patterns.

Continuous Light Patterns

Generating single, continuous, 30 μm long lines of light at an angle $\geq 50°$ to the direction of growth consistently caused hyphal redirection as demonstrated in figure 4.16. The time stamps on subsequent figures are displayed in minutes:seconds.

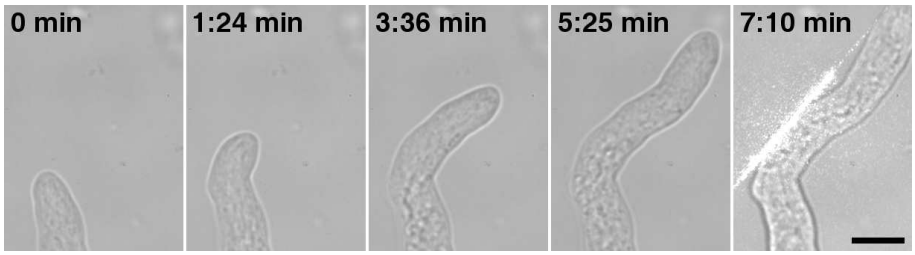

Figure 4.16: Extended redirection using a single continuous line of 532 nm light produced with objective A and introduced at 57° to the original axis of hyphal growth at time 0 min. The final image in the sequence was captured after the laser filter was removed from its location in front of the camera, allowing visualisation of the laser pattern and position. The total laser power spread over the whole pattern was 8.1 ± 0.1 mW. Scale bar is 10 μm.

Producing a 'channel' of light made the hyphae 'bounce' down it to be guided along as shown in figure 4.17.

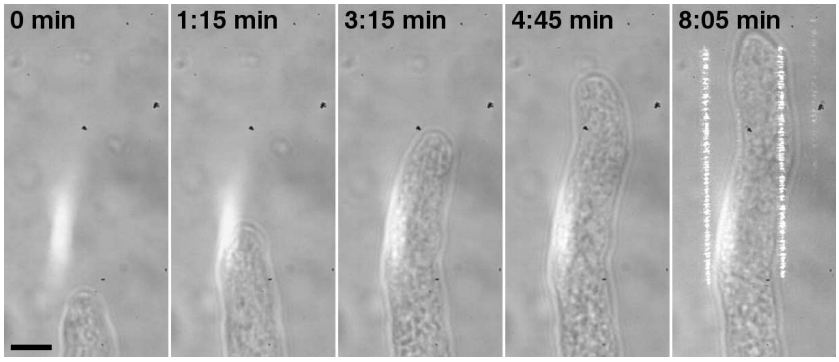

Figure 4.17: Guiding a hyphal tip through a 17 μm wide channel bordered by 60 μm long lines of light produced with objective B. The final image in the sequence was captured after the laser filter was removed to show the laser pattern and position. The white 'smudge' appearing in each image is an optical artifact. The total laser power spread over the whole pattern was 16.0 ± 0.3 mW. Scale bar is 10 μm.

Instances where the hypha was wider than the light channel resulted in width constriction as it entered the channel as exemplified in figure 4.18.

Additionally the first point of interaction between the hyphal tip and the light induced branch formation. In figure 4.18 this causes a hyphal branch to form at the lower left of the image and in figure 4.19 at the centre right of the last image. Hyphal branching never occurred within a channel bordered by light or from a hypha growing up against a line of light.

Switching between pre-calculated kinoforms on the SLM, hence optical fields in the sample plane, two sharp continuous redirections in hyphal growth can be produced as shown in figure 4.19. Having redirected the hyphae at an angle of 45° by time 4:44 minutes, the

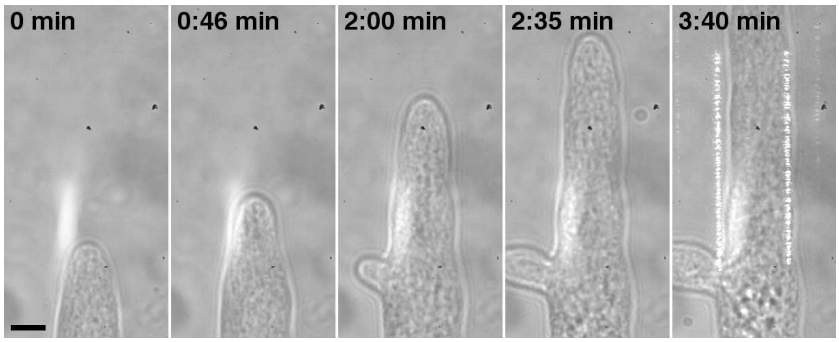

Figure 4.18: Constriction and branching caused by a relatively thin channel (17 μm wide) bordered by 60 μm long lines of light produced with objective B. The final image in the sequence was captured after the laser filter was removed to show laser pattern and position. The white 'smudge' appearing in each image is an optical artifact. The total laser power spread over the whole pattern was 9.0 ± 0.2 mW. Scale bar is 10 μm.

kinoform was changed to produce a second line of light redirecting the hyphae by another 53° by time 10:27 minutes.

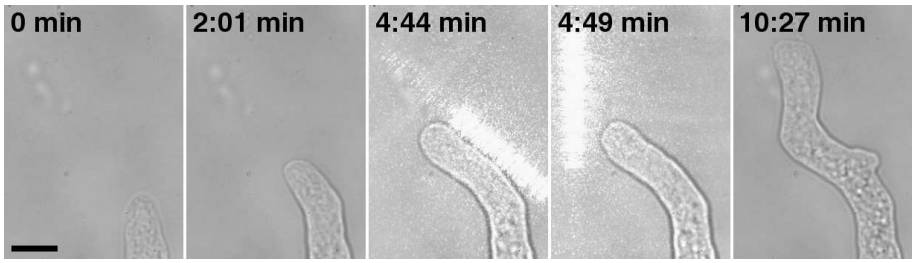

Figure 4.19: Multiple redirections of hyphal growth caused by switching between different kinoforms produced with objective A. The switch in light patterns took place between 4:44 minutes and 4:49 minutes at which time the laser filter was removed to show laser pattern and position. The total laser power spread over each light pattern was 8.1 ± 0.1 mW. Scale bar is 10 μm.

As discussed in section 3.5.3 it is difficult to accurately measure laser power in holographically generated beams. Here, the laser power input into the system was carefully selected by following a simple procedure. First, an estimate of the power required was made and then hyphal manipulation was attempted. If unsuccessful the power was either increased or decreased depending on whether the hyphae had been unaffected or overly affected respectively. It was also at times necessary to search and find a new hyphal tip to experiment on had the power needed been overestimated and caused damage.

A pseudowall of light, as described in section 4.4.1, improved the precision of growth redirection, an example of which is shown in figure 4.20. To produce the pseudowall of light the hologram used for figure 4.16 was axially stacked to produce nine axial planes of light, four each side of the normal focus, each separated by 0.5 μm. This axial extension over 4μm makes the pattern more comparable in height to the hyphal tips (< 18 μm).

The hyphae consistently followed the edge of the pattern more closely with light sculpted in this way than with those used in the previous experiments.

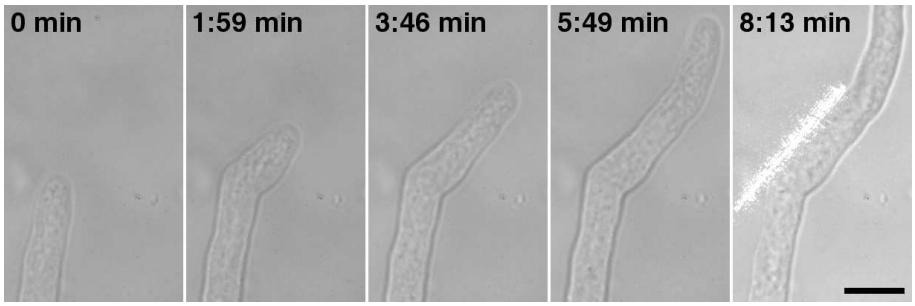

Figure 4.20: Extended growth redirection using a pseudo 3D wall of 532 nm light produced with objective A. The final image in the sequence was captured after the laser filter was removed to show laser pattern and position. The total laser power spread over the whole pattern was 8.1 ± 0.1 mW. Scale bar is 10 μm.

4.4.3 Discussion

It has been shown hyphal tip growth in *N. crassa* can be redirected using optical tweezers with three different wavelengths of light (532 nm, 785 nm and 1064 nm), and the lower the wavelength used, the lower the laser power required to produce the changes.

Ranges, rather than average powers with associated errors have been quoted, at which hyphal growth alteration occurs for each wavelength. This is because, as is well known, biological systems have a large amount of variability and hence the resulting values are largely dependent on the size of the hyphal tips being studied and the patterns being produced. For a given run of experiments an effective power can quickly be found using trial and error with the aim of minimising the level of irradiation whilst still eliciting a response in the pattern of hyphal growth.

Assuming a diffraction limited focus, the range of laser intensities required at the focal plane of the tweezers to ellicite a response is lower for lower wavelengths, indicating a wavelength dependence. The cause of this is unknown. Possibilities include photoreceptors more sensitive to certain ranges of wavelength, preferential absorption of light by the medium and subsequent heating, or perhaps an optical repulsion, in the opposite sense to optical tweezers.

The results demonstrate that holographic beam shaping enables production of fixed patterns of light that can redirect or constrict hyphal growth over extended distances or initiate hyphal branching.

With all the optical methods employed to alter growth it is possible to use either too little or too much power. If too little power was used then hyphal tip growth was unaffected and the hyphae grew through the light. If the laser power was too high, then hyphal growth ceased, a response common in filamentous fungi exposed to stress. In the particular case of single optical tweezers, too high a power could cause hyphae to burst resulting in the cytoplasm leaking from the hyphal tip. A number of papers have assessed the damage caused to a variety of biological specimens by optical tweezers[231–233]. Potential sources for photodamage were cited as the generation of reactive oxygen species, two-photon absorption and transient local heating. It would be interesting to analyse the possible influence of these factors in future work.

It has previously been proposed that repulsion of the Spitzenkörper organelle complex by the optical trap is responsible for the variety of growth responses observed[196,223,224]. The work presented here provides further evidence to support this. It is only when the optical tweezers or light patterns were positioned at the hyphal apex that redirection of tip growth took place. Repeatedly switching the irradiation of the growing hyphal apex from one side to the other resulted in a repeated redirection of the growth axis giving rise to a zig-zag pattern of filamentous growth[218,223]. Figure 4.15 shows that even though the gaps between multiple optical traps were much smaller than the width of the hyphal tip it was not smaller than the Spitzenkörper which could therefore fit through the gaps without being influenced by the laser. Lines and 'pseudowalls' of light were shown to be much more effective at redirecting hyphal growth and when sufficient power was used, the hyphal tips were unable to grow across the light barriers.

It is not possible to say whether the effects of light at the green, near infrared and infrared wavelengths are a physical phenomenon. Examples include optical repulsion of the Spitzenkörper[224] or aversion to localised heating. Other possible phenomena include local intracellular generation of reactive oxygen species[231] or a photoreceptor-mediated negative phototropism[224].

It is believed that the growth alteration for both discrete and continuous patterns of light cannot be explained simply by the physics, i.e. optical forces, but must involve some unknown biological phenomenon.

The reason why hyphal branches were induced when hyphae became constricted by growing into narrow channels bordered by light is unclear. It is possible that the initial perturbation of hyphae by laser irradiation resulted in branch formation. Hyphal branch induction is often observed at the point of initial exposure to a laser trap[223] and has also been initiated by using tweezers to apparently concentrate secretory vesicles within hyphae[196].

The axial extent of the two dimensional continuous light patterns produced was very small compared to the actual vertical extent of the hyphal tips (< 18 μm) so the alignment of the system and point of focus are thus highly critical. In order to increase the alignment tolerance, 'pseudowalls' of light were investigated and found to produce very consistent results in terms of redirecting hyphal growth. Also, the hyphae seemed less perturbed by the walls and followed the barriers much more closely than the single line of light. Two possible reasons for the improvement in results obtained with the three dimensional pseudowalls of light are as follows. Firstly, the same total power was used for both the pseudowalls and lines of light, but the pseudowall was spread between nine individual planes so at any one point the light was less intense, thus less damaging to cells. Secondly, because the pseudowalls were extended axially, given a misalignment in the system, there was a higher chance of the hyphal tip and Spitzenkörper being coplanar with the light field. It is foreseen that one of the main advantages of holographic beam shaping is its ability to produce light patterns with axial extent, unlike, for example, AODs. To increase the tolerance still further, the possibility of creating true three dimensional walls of light[234] could be explored in future.

4.4.4 Conclusion

Optical tweezers provide a useful tool to manipulate the pattern of growth in filamentous fungi. More advanced techniques offer the potential to create artificial networks of hyphae in three dimensions by growing these filamentous organisms through light mazes. Fungal hyphae within mycelial networks sense and respond to each other in complex ways which regulates the morphology of the colony. Being able to precisely manipulate the three dimensional nature of these networks with light mazes may provide a useful experimental technique to analyse cell-to-cell communication in these complex systems.

4.5 Thermocapillary digital microfluidics

This third application of beam shaping is in the manipulation of objects ~ 100 μm in size, sealed within microscopic channels. The objects are microscopic droplets of liquid water carried in a flow of oil and confined within microfluidic channels. Microfluidics is currently a very 'hot-topic' largely encompassed by the term 'lab-on-a-chip'. The aim of the majority of this research is to establish techniques that allow processes normally carried out in large laboratories to be performed on hand held chip sized devices. With many macroscopic experimental techniques it is the analysing, sorting, counting, mixing, assaying and labelling of liquids and their contents that is key.

The work described was carried out as a collaboration with Laboratoire d'Hydrodymanique at École Polytechnique in Paris. The project was caried out by myself, Maria-Luisa Cordero, David McGloin and Charles Baroud.

The essence of the field is to minimise the amount of analyte used, down to microscopic volumes, and to provide automation through the miniaturisation of fluid handling systems to enable efficient and highly parallel measurements of biological and chemical processes. The benefits are clear, for example, rather than taking a syringe of blood from patients a pin prick drop will suffice to perform a multitude of tests.

Many approaches are being explored towards this goal, of which the manipulation of droplets in microchannels is one of the most promising[235–237]. In this binary-like 'digital microfluidics' each droplet can be thought of as an independent vessel containing a reaction one may want to perform repeatedly, for example in the case of controlled chemical synthesis[236], or instead, vary the parameters of in order to explore a large number of combinations[237–239].

One major criticism of this area of research is that rather than the devices being lab on a chip they are more like chips in a lab, with the small devices requiring a large amount of surrounding apparatus for them to operate. The experiments here fall within this latter category with the large holographic apparatus described thus far being a crucial part. However, I see this investigation as a proof of principle with a clear direction to possible commercial designs because of its flexibility and isolation from the microfluidic channels.

To perform the basic operations required several integrated methods have previously been described, including electrical[240–242], direct optical manipulation[243,244] and indirect optical[245]. All these techniques require direct integration with, or modification of, the microfluidic channel. The holographic method requires no such modification or integration allowing for much greater versatility. Should specific processes, and those alone, be required it is not far fetched that truly lab on a chip devices could be made, especially when considering microscopic devices that already exist[246].

I introduced HOTs in chapter 1 as a versatile tool in standard colloidal and biological studies[247]. They are also providing increasingly complex possibilities in the control of droplets in the micrometer size range[179]. Currently manipulation through optical forces alone is limited to these micron size regimes but here I extend the idea that optics can induce a process, which itself creates far larger forces and hence can act affect larger objects[248].

4.5.1 How it works

Our technique varies the surface tension of the droplets locally, through the use of a focussed laser beam, thus inducing a thermocapillary force on the drop. For liquids without surfactant, local heating produces a reduction in surface tension at the interface and a Marangoni flow is set up from hot to cold regions (low to high surface tension). However, for liquids with surfactant, the surface tension increases with local heating so the flow is in the opposite direction, from cold to hot regions, opposite to what one may expect. This action can produce a net force that can block the formation of drops, carry out simple routing[174], fuse them, synchronise them or control their division[248].

Here I demonstrate that the combination of microfluidics with my holographic methods, that have formed the core of this chapter, extends the possibilities of droplet manipulation. The contactless nature of the holographic manipulation system allows the use of different laser patterns to implement complex operations that are not possible using the current electrical forcing and direct optical manipulation methods. The ability to vary the shape of the laser beyond a simple Gaussian beam provides an additional degree of freedom which can extend the limits of the technique. I investigate the effect of the laser beam's shape on the blockage of droplets then go on to demonstrate novel implementations which show conceptually new operations on drops in microchannels.

4.5.2 Apparatus and experimental specific to microfluidics

Again I employed the apparatus in figure 3.12 except with one key difference between our approach and standard optical tweezers. Here the forces are only indirectly produced by the application of the laser beam. Therefore, there is no need for high NA optics, as optical gradient forces will not affect droplets of the sizes used (~ 200 μm).

Two objectives were used over the course of the experiments; the first was a Nikon 10x (NA = 0.25) and the second a Mitutoyo 10x (NA = 0.26) both of which focus the beam into the prefabricated microfluidic channels positioned on the usual three axis translation stage above the objective taking the place of the 'generic sample'.

The microfluidic chips were fabricated with molded polydimethylsiloxane (PDMS) (Sylgard 184, Dow Corning) using standard soft lithography techniques and sealed against a glass microscope slide. The dimensions of the channels ranged from 75 to 200 μm in width and were 50 μm in height. Oil (Hexadecane + Span 80, 2% w/w) and an aqueous solution (water + ink 2% v/v) are injected into the channel using syringe pumps. Dark blue Parker pen ink was added to the water in order to absorb the 532 nm light to in-

duce heating. Were chemically, biologically, or physically sensitive material to be placed within the droplets it is possible to use other absorbing dyes depending on absorption requirements and the laser wavelength used[248].

In order to investigate the effect of different light patterns on drops, the minimum optical power, P_{min}, required to block the advance of a drop, was studied for three different shapes. These were a Gaussian focus with 0.5 μm radius beam waist, a straight line aligned along the flow direction, and a straight line orthogonal to the flow direction. Both lines were 2 μm in width and 200 μm in length. The PDMS microchannels had two oil inlets and one for aqueous solution. Droplet size is determined by the ratio between the first oil flow rate Q_{oil-1} and the water flow rate Q_{water}, which were both kept constant. The second oil flow rate Q_{oil-2} was used to tune the total flow rate $Q_{tot} = Q_{oil-1} + Q_{oil-2} + Q_{water}$. This enabled the size of the droplets to be kept constant while their velocity varied with Q_{tot}.

4.5.3 Results

The first observation, as the drops reach the laser beam, is that the water-oil interface adapts to the laser shape, as seen in figure 4.21. When the line is parallel to the direction of flow, the front interface is flattened and the drop stops after advancing through a significant portion of the line. In the case of a line perpendicular to the flow direction, the surface of the drop is even more flat than in the previous case, taking on the shape of the line. For a Gaussian beam the drop behaves similarly to the former case but not with as large a magnitude.

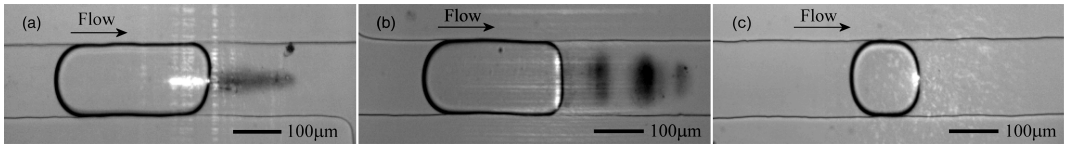

Figure 4.21: The effect of (a) a line parallel to the flow, (b) a line perpendicular to the flow, and (c) a Gaussian beam, upon the profile of a droplet. It is clear in image (b) that the droplet morphs to match the pattern. The black marks and the reason for their occurence are described in section 4.5.4.

For each optical pattern, the total flow rate was varied from $Q_{tot} \simeq 1 - 11$ nLs^{-1} in increments of 0.17 nLs^{-1} and for each rate the laser power was started at high values and reduced for successive drops, until the minimum power P_{min} that still held the drops was reached. The maximum flow rate attained was limited by the water in the drops boiling, not by the laser being unable to block the droplets.

The minimum laser power for each of the laser distributions is plotted against the total flow rate in figure 4.22. The minimum optical power scales approximately linearly with flow rate for each pattern with gradients and intercepts differing for all three cases. The use of a line perpendicular to the flow allows the blocking of drops at higher flow rates, up to more than 10 nLs^{-1}. Conversely, even though a lower laser power is necessary to hold the droplets in the case of a single Gaussian beam, it was not possible to hold droplets for flow rates higher than about 5 nLs^{-1}. This was also the case for the line parallel to the flow.

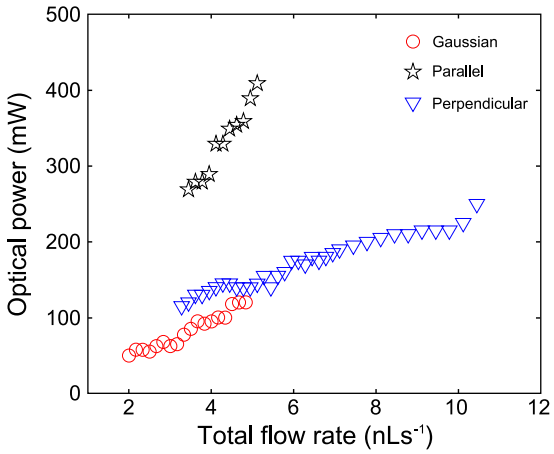

Figure 4.22: Minimum laser power required to block a drop at varying flow rates for a Gaussian beam and lines parallel and perpendicular to the direction of flow.

If the pattern intensity is calculated and plotted instead of power, the minimum intensity I_{min} necessary to block a droplet is found to be several times higher for a Gaussian beam than for a line distribution as shown in figure 4.23. The perpendicular line is found to block droplets for the lowest value of I_{min}.

I will now consider the advanced operations made possible by the use of holographic beam shaping and how single beam applications can be extended.

Routing (simple sorting)

Firstly I demonstrate the re-direction of droplets into different channels at a trifurcation. Making use of the ability to both dynamically switch the optical patterns projected into the microfluidic channel and the ability to create extended patterns (in this case four separate Gaussian beams), droplets can be deflected through large angles and sent into preferred channels. This is shown using a four way cross channel in figure 4.24 demonstrating the droplets being routed to the left, straight on or to the right. The switching time of the

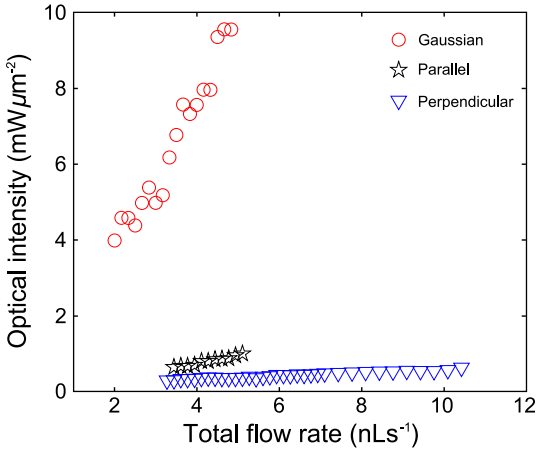

Figure 4.23: Minimum laser intensity required to block a drop at varying flow rates for a Gaussian beam and lines parallel and perpendicular to the direction of flow.

droplets into a given channel is limited only by the update speed of the SLM, $\sim$ 75Hz. With integration of simple image recognition software and hologram switching this could provide a robust method for sorting in digital microfluidics, one of its major applications. One could imagine the sorting being based on droplet size, chemical composition, fluorescence measurements or simply the contents of a drop.

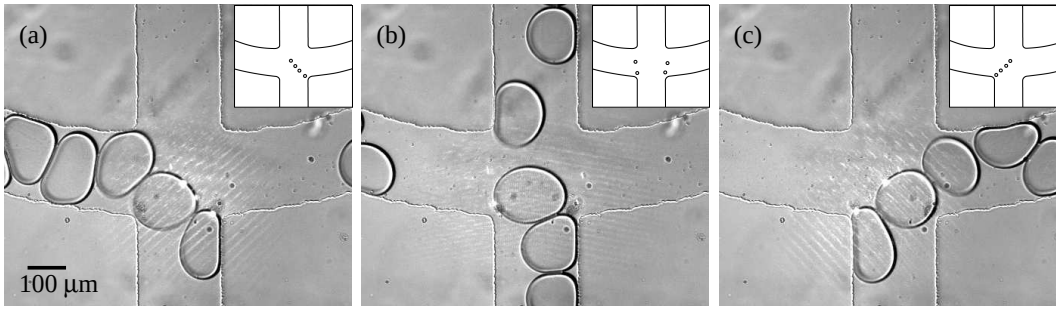

Figure 4.24: Four Gaussian beams are aligned to route droplets into either (a) the left-hand channel, (b) the center channel, or (c) the right channel. The flow is from image bottom to top. The insets show the positions of the holographically generated multiple Gaussian foci within the channel.

Storage and re-ordering

Next I show an example that goes beyond simple Gaussian beams by using continuous line patterns of light to store droplets at given points in the channel while rerouting other droplets to move past the stored droplet. The line patterns produced cannot be treated like a simple Gaussian beam and exist with relatively low fidelity over the same axial

distance but remain sufficiently intact to produce the desired effect. Snapshots from an example video using such lines are shown in figure 4.25. The first line upstream is set to move a droplet into one side of the larger channel. The droplet is then stored by the second, downstream, line further along the channel. The first line is then changed so as to move subsequent droplets in the flow past the first droplet. Thus droplets can be stored and could be interrogated without the need to stop the flow, which is important if one wishes to obtain longer interrogation times. Note that the ability to focus the laser to a small area on the drop, allows real droplet-level manipulation, contrary to electrical fields which produce a uniform forcing on a region of the microchannel. This is what allows the drop order to be inverted in this case.

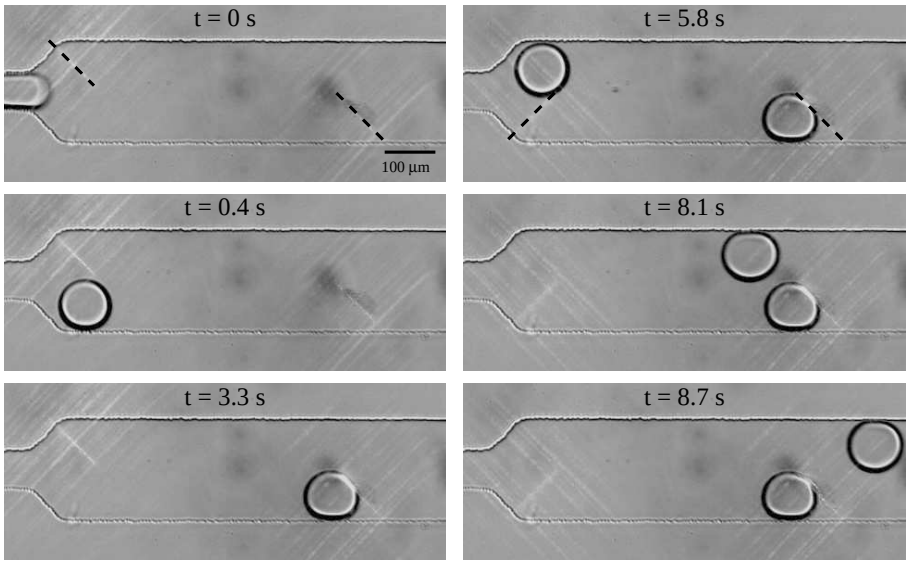

Figure 4.25: Image sequence (left column followed by right column) showing droplet storage and potential re-ordering. The initial drop is sent down and held stationary and droplets thereafter are sent up past the first. The flow is from left to right. Dashed lines overlay the position of the laser patterns.

Multiple Storage (Memory)

Extending the previous idea allows multiple droplet storage, shown in figure 4.26. Here several droplets are trapped at once, first one, then two and finally three using three lines of light. Again this is in the presence of droplets flowing through the channel. It is then possible to shuttle the droplets through the pattern, by turning the whole pattern on and off, so the first droplet is lost and the second droplet takes its place and so on. This allows large scale storage and controlled movement of many droplets simultaneously which may be useful for analysis of droplets, droplet re-ordering or droplet 'memory' applications.

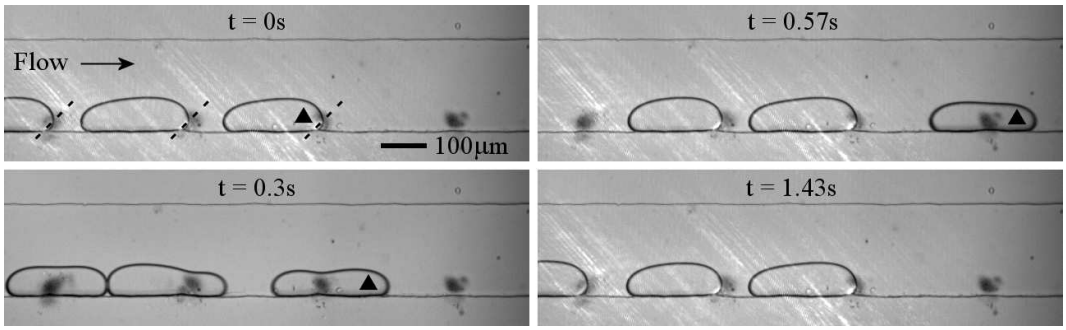

Figure 4.26: A drop treadmill holds up to three droplets and can function as a first-in-first-out buffer memory. The triangle marks the same droplet in the different images (sequenced left column followed by right column), indicating its movement. Dashed lines overlay position of the laser patterns. Total power in sample plane is $\sim$ 475 mW.

Finally I demonstrate, in figure 4.27, the forces produced are large enough to stop droplets filling the whole channel or touching the channel walls. It is hoped with further work it may be possible to design microfluidic channels and optical fields that would allow 'wall-less' microfluidics.

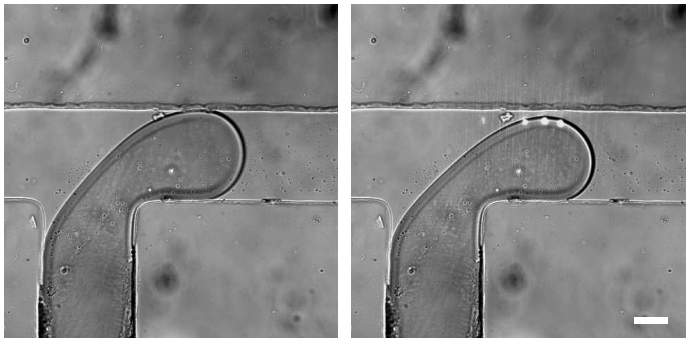

Figure 4.27: Five separate Gaussian beams are placed in a line parallel to one wall. In the left-hand image the laser is off and the droplet touches the top wall as it is formed. In the right-hand image the laser is on and the droplet is prevented from touching the upper wall. Three foci are clearly visible, due to droplet contact, with two more to their left. Scale bar is 100 μm.

4.5.4 Discussion

I have extended previous work that allows optical fields to induce the production of forces well above those possible from the scattering and gradient forces alone. The use of dynamic holography allows a system of microfluidic control whose purpose of operation can be altered in real time and allows microfluidic channels to be easily interchanged.

Outlined above are just a few simple examples providing some novel operations. The system is sufficiently simple and user friendly that if the desired operation for a particular

application does not exist, it can be created with relative ease.

The operations explored here are either controlled by the user manually choosing the kinoform to be displayed or by a simple timer between displayed kinoforms. This could be automated in several ways. Should the system be used in conjunction with spectroscopy or other forms of analysing system the results could be fed back into the kinoform software to produce the desired operation on the droplet under study. Using computer aided machine vision, particularly in LabVIEW, the automation could be quickly implemented and with training could recognise a plethora of shapes, colours or patterns with which to decide the outcome of the kinoform displayed.

The droplet throughput of the system is really limited by the speed at which the light patterns can be altered. In this setup it is calculated that the number of droplets which could be affected using the perpendicular line, hence the system's limiting throughput from the maximum force imparted, is $\simeq 2200\ s^{-1}$.

Quite obviously some results in this section show 'black marks', most noticeable in figures 4.21 and 4.26. These marks are believed to be a mixture of ink and surfactant that has been released from the surface of the droplets upon interaction with the laser focus that is then deposited on the upper PDMS surface. Their effect is negligible unless a large amount of power is left at a single location for prolonged periods of time.

The process of optically induced thermocapillary forces works due to a localised heating and subsequent temperature gradient. This temperature has been shown to rise by up to 55°C[249] which could both hinder and assist future applications. For example, many reaction rates increase with higher temperatures but should one study mammalian cells this heating of the surroundings can be detrimental. Temperatures greater than ~ 42°C cause denaturation of proteins and DNA ending in cell apoptosis[250,251], a known problem in optical manipulation[232]. There are mechanisms that could circumvent this problem by pre-stressing cells so subsequent stress is less damaging[252].

4.5.5 Conclusion

In conclusion this work demonstrates that holographic beam shaping has a number of advantages over conventional methods of inducing thermocapillary forces on droplets. Extended patterns of light offer significant additional functionality over techniques using a single optical tweezers, which can lead to enhanced control in digital droplet microfluidic devices.

This optically induced thermocapillary force technique is superior to electrical forcing

methods as no electrodes need to be built into the system with careful design. The method also outweighs manipulation through optical forces alone should one wish to manipulate mesoscopic scale objects.

4.6 Outlook

All the applications in this chapter have not only produced the results contained here but the principles continue to be used by colleagues and collaborators where the experiments have been developed further.

The Aerosol Dynamics group in Bristol, headed by Dr Jonathan Reid, uses the software and apparatus in combination with spectrometers, as discussed earlier, to further advance their understanding of atmospheric chemistry with the multiparticle abilities providing a unique tool. The Ritchie group in Oxford, headed by Dr Grant Ritchie, uses a HOT system with my software for applications in the probing and controlling of chemical processes.

4.7 Conclusion

In conclusion I have demonstrated three entirely new applications of holographic optical tweezers through two orders of magnitude in dimension. This is starting to show the versatility of optical manipulation in inter-disciplinary fields of research.

Without the application of SLMs the physics and effects observed could be greatly different. For aerosols this will be discussed in parts of the next chapter. For fungi the ability to make three dimensional 'walls' of light to increase the phenomenon efficacy would not have been possible. In microfluidics the timescales over which the different types of beam shaping work allows interaction with the hydrodynamics of the system due to similar timescales in this area of physics[253].

I have also shown a preliminary investigation using beam conversion to transfer orbital angular momentum to airborne droplets that has promise in tackling the problem of observing the orbital angular acceleration of objects due to the orbital angular momentum of light.

The first application of this chapter regards the optical manipulation of aerosols, the understanding of which is unclear. It is for this reason that the next two chapters are dedicated to the study of single beam gradient traps of liquid aerosols in the hope of gaining an understanding of how such experiments behave and operate.

Chapter 5

Single Beam Studies of Trapped Aerosol Dynamics

Most aerosol tweezing has been applied in the study of atmospheric chemistry with no detailed studies into the physics or limits of such experiments. This is understandable because the experiments often work well enough to provide precise results without questioning how it works. However, should one wish to push forward the boundaries of the technique, its understanding will clearly assist. For example the current size range of aerosol trapped is approximately $2-7$ μm in radius, within the coarse mode, but to move into the atmospherically important accumulation mode the physics will need to be pushed.

This chapter describes the investigation of the parameters affecting airborne tweezing, the limits these produce and the surprising physics arising. The information contained within has allowed a new method for sizing to be developed, will help to improve similar techniques and will assist future researchers.

5.1 Brownian motion

Anyone who has peered down a microscope at suspended microscopic objects will have noticed their 'random walk' through the sample. It is now well known that the factor dominating this 'walk' arises from the thermal motion of surrounding molecules. First noticed by Brown[254], it was not explained until Einstein[255] and subsequently by Smoluchowski[256] and Langevin[257] who realised the particle in motion would diffuse just like a molecule in the fluid, hence its diffusion could be calculated using the equipartition of energy theorem. Finally, Perrin[258] performed an experiment that agreed with their predictions and proved

the atomic nature of matter[259,260]. Since then Brownian motion has provided many opportunities for analogies in areas beyond microscopic diffusion, for example in the stock market[261], and over 100 years after its explanation[255] research continues into its further understanding and application[262].

The understanding of Brownian motion can be used in conjunction with optical detection to determine the size of microscopic colloidal suspensions[263,264] or to measure Avogadro's number[260]. Recently it has allowed optical traps to provide a useful tool in diverse research fields capable of acting as a force transducer for molecular biology[142], viscometry[265], microscopy[266], and fundamental physics[267]. These applications often use the power spectrum method[268] to detect position[269], measure forces[270], or investigate colloidal dynamics[271] and rely on the study of over-damped systems[272].

The investigation of over-damped systems via optical trapping has produced classic experiments with important physical results including tests of Kramer's theory[273], measurements of critical Casimir forces[267] and cross correlations between colloids[271]. The various optical potentials created through optical manipulation have, for example, been used to investigate colloidal crystals[274,275], with particle dynamics providing analogies in thermal ratchets[101] and freezing[276].

All experiments in optical tweezers in a water type environment behave as over-damped oscillators but there have been discussions that under-damped motions are reachable[277] and comments that this should not be possible[272,278]. Rarely have systems that are not over-damped been investigated[83,277] but as mentioned in the introduction, there is a resurgence in the original airborne particle experiments of Ashkin[14,58,79]. Due to the importance of inertia in such systems they provide a drastically different damping environment and hence experimental possibilities. This would allow the testing of whether under-damped motion in an optical trap is possible as expected theoretically.

Little thought has gone into the mechanical dynamics of airborne systems[279] but these need to be investigated with the realisation they could provide access to the little probed, under-damped regime[83]. To define the problem and construct the solution of describing a Brownian particle's motion I will use the approach taken by Langevin[257] due to its relative simplicity.

5.2 Theory

Throughout this work I assume the particle velocity is well below the speed of sound and the propagations of interactions in the fluid are instantaneous, hence the fluid is treated

as incompressible[280]. It has been established the frictional viscous drag force on a sphere, with vanishing Reynolds' number, immersed in a fluid is governed by Stokes' law, and with corrections due to the finite Knudsen number is

$$F_{stokes} = -\frac{6\pi\nu\rho_{fluid}Rv}{C_c} = -\gamma_0\dot{x}, \tag{5.1}$$

so the equation of motion for such a particle is

$$m\ddot{x} + \gamma_0\dot{x} = 0, \tag{5.2}$$

or equally

$$\ddot{x} + \Gamma\dot{x} = 0, \tag{5.3}$$

where x is position, $\Gamma = \gamma_0/m = 1/\tau$, τ is the velocity relaxation time, m is the particle's mass and all other symbols retain their previous meaning.

Equation 5.2 is only valid when the particle mass is large enough that its velocity due to thermal fluctuations is negligible. For sufficiently small particles one must consider their thermal energy which, from the equipartition theorem, is

$$\frac{1}{2}m\left\langle\dot{x}^2\right\rangle = \frac{1}{2}k_BT, \tag{5.4}$$

where k_B is Boltzmann's constant and T is temperature. If the particle mass is still large compared to that of the molecules equation 5.3 can be modified to include the effect of thermal motions becoming[281]

$$\ddot{x} + \Gamma\dot{x} = \Lambda(t), \tag{5.5}$$

where the time fluctuating force per unit mass $\Lambda = \lambda(t)/m$ and λ is a stochastic force. $\Lambda(t)$ has the properties that its average over an ensemble (of measurements for example) is zero;

$$\langle\Lambda(t)\rangle = 0. \tag{5.6}$$

Given that the duration of a collision between molecule and particle, τ_0, is shorter than the time difference $t' - t$ then

$$\left\langle\Lambda(t)\Lambda(t')\right\rangle = 0, \tag{5.7}$$

but usually the collision time is so brief compared to the relaxation time, $\tau = 1/\Gamma$, that the limit $\tau_0 \to 0$ can be used and hence

$$\left\langle\Lambda(t)\Lambda(t')\right\rangle = q\delta(t - t'). \tag{5.8}$$

The spectral density of $\Lambda(t)$ is, by the Wiener-Khintchine theorem[281], the Fourier trans-

form of the correlation function in equation 5.8;

$$S_\Lambda = \int_{-\infty}^{\infty} e^{-i\omega\tau} \left\langle \Lambda(t)\Lambda(t') \right\rangle d\tau = \int_{-\infty}^{\infty} e^{-i\omega\tau} q\delta(\tau) d\tau = q, \tag{5.9}$$

and is hence independent of frequency, ω. With some maths (pages 32-34 in Risken[281]) equation 5.5 can be used to find the velocity correlation function to be

$$\langle \dot{x}(t_1)\dot{x}(t_2) \rangle = \frac{q}{2\Gamma} e^{-\Gamma|t_1 - t_2|}, \tag{5.10}$$

thus the average energy of the particle is

$$\langle E \rangle = \frac{1}{2} m \left\langle \dot{x}^2 \right\rangle = \frac{1}{2} m \frac{q}{2\Gamma}. \tag{5.11}$$

Combining this with equation 5.4 gives

$$q = \frac{2\Gamma k_B T}{m} \tag{5.12}$$

therefore the equation of motion for a particle undergoing thermal fluctuations, or Brownian motion, is[281]

$$\ddot{x} + \Gamma\dot{x} = \left(\frac{2\Gamma k_B T}{m} \right)^{\frac{1}{2}} \eta(t). \tag{5.13}$$

where $\langle \eta(t) \rangle = 0$ and $\langle \eta(t)\eta(t') \rangle = \delta(t - t')$. When studying the behaviour of particles in traps, the physics is modified slightly by placing the particle under motion in an external potential. Traditionally this is said to be a harmonic potential well arising from the focussed laser and to within a good degree of accuracy this picture is correct[282].

Previously I defined the Reynolds' number as equation 4.1 involving a velocity term. Unfortunately only the frequency of oscillation is known in our case, but knowing the approximate amplitude of oscillation, a, the velocity of the sphere is of the order $a\omega$ hence I redefine the Reynolds' number to be[280]

$$Re = \frac{a\omega R}{\nu}, \tag{5.14}$$

where the symbols retain their same meaning. The oscillation of the sphere generates waves which are damped by the surrounding viscous fluid as they propagate away from the sphere surface. Therefore, introduced is the term *depth of penetration*,

$$\delta = \sqrt{\frac{2\nu}{\omega}}, \tag{5.15}$$

such that the wave amplitude falls off by a factor of e in a distance δ.

In order to simplify the Navier-Stokes[280] equation, such that the drag on a sphere simplifies to Stokes' law, there are the two conditions

$$\delta \gg R \quad \text{hence} \quad R^2\omega \ll \nu \tag{5.16}$$

and

$$\frac{\omega a R}{\nu} \ll 1. \tag{5.17}$$

Using equation 5.13 multiplied by m and assuming the fulfillment of the criteria in equations 5.16 and 5.17 the Langevin equation describing the motion of a microsphere of radius R, mass m, in a fluid of temperature T, kinematic viscosity ν, density ρ_{fluid} and trapped in a harmonic potential of stiffness κ is[280,283]

$$m\ddot{x}\left(t\right) + \gamma_0\dot{x}(t) + \kappa x\left(t\right) = \lambda\eta\left(t\right), \tag{5.18}$$

where $\gamma_0 = 6\pi\rho_{fluid}\nu R$ is the viscous damping of the medium, $\lambda = \sqrt{2k_BT\gamma_0}$ is the Brownian stochastic force[281,284] and k_B is the Boltzmann constant. This equation describes the motion of an optically trapped particle residing in a harmonic potential well that experiences a Hookean restoring force when displaced by Brownian stochastic forces.

Generally the two unknown quantities are κ and γ_0, as these system properties are complex to ascertain without direct experimental observation. By studying the Brownian motion of particles in harmonic potentials these parameters can be deduced and hence the properties of the tweezers or surrounding environment. It is possible to obtain the particle mass, or radius, from studying their Brownian motion but there are several complications that make this difficult as will be explained in section 5.4.2.

The third term in equation 5.18 arises as the optical forces are treated as a Hookean spring such that given the trap stiffness κ (normally in units of pNμm^{-1}) the force, F, can be obtained from

$$F = -\kappa x. \tag{5.19}$$

This simple formula in the right instrument can yield incredible results. It is the displacement calibration of instruments that allows precise displacement measurements, far beyond the diffraction limit of the light being used to tweeze. This in combination with trap stiffness calibration allows calculation of the forces being exerted on trapped objects. Optical tweezers can measure a range of forces from $\sim$ 10's fN to $\sim$ 100's pN[27,285]. These forces and associated displacements are in the realm of those that occur at the biomolecular level so provide a wonderful tool for their study, for example it enables displacement measurements reaching down to the Angström level[142], and force measurements of 25 fN[285].

The advent of numerical models enable precise calculation of theoretical forces, stiffnesses, and other parameters when tweezing objects within a specific system. Comparing these to experimental data governed by equation 5.18 allows the determination of the viscosity of environments, the viscoelastic properties of complex fluids[286] or measurements of particle refractive index[287].

5.2.1 How can the parameters be measured experimentally?

Optical tweezers have been coupled with advanced position detection systems providing incredibly precise measurements of force[285], displacement[142], and, in conjunction with complex numerical simulations, physical properties of microscopic systems[287] in the liquid phase. Position and force measurement relies on calibration of the detection system or measurement of trap stiffness, respectively, through position sensitive detectors, video tracking or quadrant photodiodes (QPDs) to detect particle position[288,289].

I will give a brief overview of how the instruments can be calibrated and the trap stiffness determined. The escape force method was described in section 2.3 as an introduction to measuring lateral efficiency, Q_ρ, and so I will begin with the next most complicated method.

Drag force method

This is the first method that really needs precise position measurement. Taking equation 5.19 and knowing the displacement for a given force allows calculation of trap stiffness[38,290]; $\kappa = -F/x$. This known force can be created by relative flow between fluid and particle but the position sensor must be calibrated to give κ in the correct units. As with the escape force method the viscous drag must also be known, which unless for a spherical particle, can be complex to determine.

Equipartition method

Using the equipartition theorem of energy, equation 5.4, for a particle bound in a harmonic potential;

$$\frac{1}{2}k_B T = \frac{1}{2}\kappa \left\langle x^2 \right\rangle , \tag{5.20}$$

κ can be determined. No knowledge of the medium viscosity is needed but the position detection system must be well calibrated to provide precise true positions with the detector having a high bandwidth[38,291]. A disadvantage is the susceptibility of the technique to

noise which will increase the average squared displacement.

Power spectrum method

The power spectrum method[269,270,290,291] is considered the most reliable[292] and works through the equipartition theorem at non-zero frequency. By measuring and calculating the power spectrum of position fluctuations one can obtain the trap stiffness, κ, independently of the detector calibration. If an absolute detector calibration is known then the viscous damping can be extracted which, if the radius is known, can give the viscosity of the fluid. There are subtle differences in analysis when studying a system where inertia is and is not a significant contributor to the motion. The manner in which parameters can be extracted and the pre- and co-requisites required, vary between the two situations and I will discuss this in section 5.4.2.

Step response method

An extension of the drag force method, the response of a trapped particle to a stepwise translation of the trap allows calculation of the stiffness. For a small step, x_t, the response in displacement, after time t, is[293,294]

$$x_b = x_t \left(1 - e^{-\kappa t/\gamma_0}\right), \tag{5.21}$$

where again the viscous drag, γ_0, must be known but the detector calibration is not required.

Combining the latter two methods, the viscous drag on the particle does not need to be known in order to find the trap stiffness[295]. The particle can be oscillated with AODs or a sample stage allowing determination of both trap stiffness and viscosity independently from experimentally measured parameters alone.

To measure the power spectrum of harmonically confined Brownian motion the ideal method would be both highly precise and fast. Interferometry allows high precision measurements of particle position through the interference of scattered light from an optically trapped object. Coupled with detection on a photodiode, with bandwidths in the MHz regime, these ideal goals are achieved.

In this investigation, to characterise the Brownian motion of droplets within optical traps, a QPD was employed and the power spectrum method used as it is considered the most reliable[292]. Although I am mainly concerned with observing the dynamics of trapped

aerosols, it is feasible to use this method to measure precise forces and position. Normally the method is used for calculation of trap stiffness with prior knowledge of the surrounding medium's viscosity and the particle radius[28], but, it will be shown that when in air, only the radius is needed.

5.2.2 Why should the dynamics of optically trapped aerosols be studied?

The interest and benefits of aerosol tweezing was discussed in chapter 1 and the introduction to this chapter. The experiments described and those of colleagues throws up many questions relating to the physics of the system. With no real detailed study on airborne tweezing, beyond the most basic level[11], coupled with unusual behaviour it was felt it would be pertinent to investigate the system fully.

The unusual trapping behaviour in air, compared to trapping in liquid media, include the following. Varying trapping power alters the axial equilibrium position of droplets resulting in 'power gradients'[279] with further increases causing its loss, as shown in figure 5.1. Given a polydisperse nebulised sample the initial power used to capture a droplet gives a pronounced size selectivity[12,179] and once trapped the droplet can undergo vertical oscillations at frequencies of $\sim 0.1 - 10$ Hz.

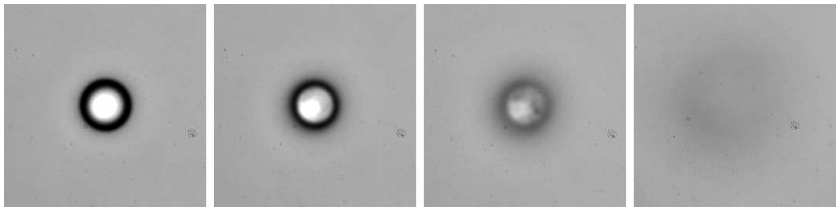

Figure 5.1: Images showing increasing defocus as a function of increasing power (left to right). The defocus is due to the increase in height at which the droplet sits above the coverslip, hence image plane. The droplet can be returned to its lower position by simply decreasing the power. At times it can be pushed so far it is no longer visible yet it can still be recovered.

So, the aim of this study is to develop an understanding of the process of aerosol trapping. This will be done by looking at the transition from over- to under-damped motion in detail, investigating whether the mechanical dynamics of the system cause the observed phenomena and exploring the parameter space by analysing dependence on power, size and depth into the sample.

5.2.3 Theory for power spectrum of harmonically trapped microspheres

I will begin by looking at the classical use of power spectra in optical trapping. For a colloidal system the characteristic time for loss of energy through friction, $t_{inert} = m/\gamma_0 \simeq 100$ ns, is far shorter than the experimental time resolution $\simeq 20$ μs, and so it is a reasonable approximation to follow Einstein[255] and neglect inertia. In this case the Langevin, equation 5.18, becomes

$$\dot{x}(t) + \omega_c x(t) = D\eta(t), \tag{5.22}$$

where $\omega_c = \kappa/\gamma_0$, the corner frequency and $D = k_B T/\gamma_0$, Einstein's diffusion coefficient. Fourier transforming equation 5.22 and finding the expectation value decomposes the motion into its frequency components to give the power spectrum of position fluctuations to be

$$S_x^{over}(\omega) = \frac{2k_B T}{\gamma_0}\frac{1}{\omega^2 + \omega_c^2}. \tag{5.23}$$

The corner frequency is defined as the frequency at which the power reaches half its low frequency asymptotic value. The power spectrum has a characteristic tail with gradient ω^{-2} and a low frequency plateau of amplitude $2k_B T\gamma_0/\kappa^2$.

When studying objects in air the time for loss of energy through friction, t_{inert}, is now, due to the lower dynamic viscosity, longer than the experimental time resolution and so inertial terms can no longer be neglected. Re-arranging equation 5.18 now gives

$$\ddot{x}(t) + \Gamma\dot{x}(t) + \Omega^2 x(t) = \Lambda\eta(t), \tag{5.24}$$

where $\Omega = \sqrt{(\kappa/m)}$ is the natural angular frequency of the droplet's position fluctuations, $\Gamma = 6\pi\eta R/mC_c$ is the viscous damping of the medium, and $\Lambda = \sqrt{(2k_B T\Gamma/m)}$ is the Brownian stochastic force per unit mass[281,284] where k_B is Boltzmann's constant.

Fourier transforming equation 5.24 and finding the expectation value gives the power spectrum of position fluctuations for a system including inertia to be

$$S_x^{inertia}(\omega) = \frac{2k_B T}{\kappa}\frac{\Omega^2\Gamma}{\left(\omega^2 - \Omega^2\right)^2 + \omega^2\Gamma^2}. \tag{5.25}$$

This spectrum has a characteristic high frequency tail with ω^{-4} gradient and a plateau value at low frequencies equal to $2k_B T\Gamma/\kappa\Omega^2$. As inertia is included there is an additional limiting case at the point of inflection equal to $2k_B T/\kappa\Gamma$. I also define the ratio of damping coefficient to natural frequency as the 'damping ratio', Γ/Ω. For over-damped systems this is always greater than unity, as is found for colloidal systems where it is usually greater

than ten. When trapping in air the system has the potential to become under-damped and hence $\Gamma/\Omega < 1$.

In figure 5.2, I plot the theoretical power spectrum of position fluctuations for two systems that include and exclude inertia.

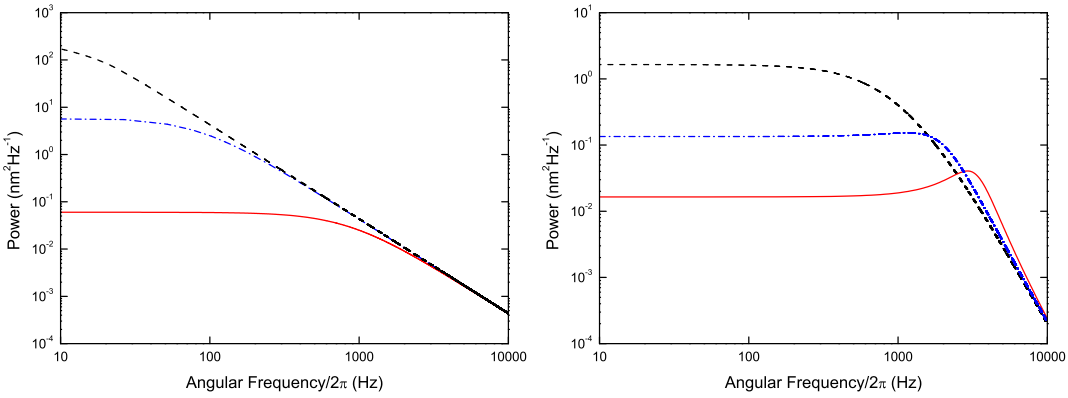

(a) (b)

Figure 5.2: Power spectrum examples for systems including and excluding inertia. (a) Neglecting inertia for a 1 μm sphere trapped in a water medium with trap stiffnesses 1 pNμm^{-1} (dashed black line), 10 pNμm^{-1} (dash-dotted blue line) and 100 pNμm^{-1} (solid red line). (b) Including inertia for a 6 μm water droplet trapped with stiffnesses 1 pNμm^{-1} (dashed black line), 3.5 pNμm^{-1} (dash-dotted blue line) and 10 pNμm^{-1} (solid red line).

Hydrodynamic corrections

For both cases when inertia is and is not included the Langevin equations assume the motion occurs in bulk fluid media with uniform velocity, far away from other objects and surfaces so Stokes' law only needs to be corrected for finite Knudsen number. However, in reality the objects here are undergoing linear harmonic motion within reasonable proximity ($\leq 10R$) of a coverslip so it is inappropriate to assume Stokes' law still applies. Analysing this problem it is seen there are two significant corrections that need to be applied to the 'in bulk' theory.

Firstly I will look at the 'true' behaviour due to linear oscillations within fluid. Although a limiting result of Stokes' original paper[296] was indeed the familiar law that bares his name, describing the drag on a sphere in uniform motion through a fluid, his paper was concerned with the oscillation of pendulums in fluid. This is similar to the processes occurring here but, rather than gravity driven, it is stochastic Brownian motion delivering

the energy. He showed that the friction on an oscillating sphere is[280,296,297];

$$F_{friction} = -\gamma_0 \left(1 + \sqrt{\frac{R^2\omega}{2\nu}}\right)\dot{x} - \frac{2}{3}\pi\rho_{fluid}R^3\left(1 + \frac{9}{2}\sqrt{\frac{2\nu}{R^2\omega}}\right)\ddot{x}. \tag{5.26}$$

The first term comprises the familiar Stokes' drag plus a frequency dependent correction. The second term arises from the inertia created by any fluid entrained due to the particle's past motion. This hydrodynamic correction is often neglected[83,142,277,298,299], at times with good cause, but needs to be applied when requiring precision $> 10\%$[297]. Here I will try to justify my exclusion of such terms in a little detail.

Using equation 5.26 and following Berg-Sørensen *et al.*[297] I derive the hydrodynamically correct power spectrum in angular frequency to be

$$S^{inert}_{x-hydro}(\omega) = \frac{2k_bT}{\kappa}\frac{\Omega^2\Gamma\left(1 + \left(\frac{\omega}{\omega_\nu}\right)^{1/2}\right)}{\left(\Omega^2 - \Gamma\left(\frac{\omega^{3/2}}{\omega_\nu^{1/2}}\right) - \frac{\omega^2\Gamma}{\omega_m}\right)^2 + \left(\omega\Gamma + \Gamma\left(\frac{\omega^{3/2}}{\omega_\nu^{1/2}}\right)\right)^2}, \tag{5.27}$$

where $\omega_m = \Gamma/(1 + \frac{2\pi\rho R^3}{3m})$ and $\omega_\nu = 2\nu/R^2$. For systems where inertia is included the definition of ω_c clearly can no longer apply so the dependence on corner frequency has been removed. The low density of air reduces ω_m's denominator close to unity, so effectively removing any effective mass considerations as the entrained fluid is negligible[300]. Decomposing equation 5.26 into frequency components via Fourier theory (equation 31 in Berg-Sørensen and Flyvbjerg[297]) shows air's larger kinematic viscosity, hence ω_ν, produces a reduction in any correction to Stokes' law compared to trapping in water. Considering these arguments, reviewing relevant and similar work, and understanding I am not attempting to make highly precise measurements, I believe I am justified in neglecting the frequency dependent friction correction. Also note that other sources of error inherent in the experiments, discussed later, will dominate over any induced by this exclusion.

The second correction to be considered is that given by Faxén regarding the force on a sphere in motion near a plane surface, exactly what occurs when trapping with high NA optical tweezers due to the proximity of coverslips. Here I only consider the correction in the lateral direction although both axial and rotational equivalents exist[301,302]. Faxén's law shows the viscous drag on a sphere increases as it approaches a plane surface according to[303]

$$\Gamma_{Faxen} = \frac{\Gamma}{1 - \left(\frac{9R}{16L}\right) + \frac{1}{8}\left(\frac{R}{L}\right)^3 - \frac{45}{256}\left(\frac{R}{L}\right)^4 - \frac{1}{16}\left(\frac{R}{L}\right)^5} \tag{5.28}$$

where L is the distance between sphere centre and surface. For the particle sizes studied here this can have a dramatic effect on the friction experienced; even when trapping at distances approaching 40 μm from coverslips there can be a 7% increase.

Calibration

The final theoretical consideration is that to compare power spectra in given data sets one must calculate the detection system sensitivity, β, given in volts output per unit displacement of the particle. This is because the sensitivty can alter between experiments due to variations in power or simply geometry at the focus. Finding β allows voltage power spectra, those directly from data, to be converted to physical spectra, $\mathrm{nm^2Hz^{-1}}$ versus Hz. Conventional methods rely on the relative simplicity of colloidal systems by using, for example, the drag force method[123], its extension to an oscillating sample stage[295] or moving a fixed bead over a known distance through the laser beam waist[304]. Clearly the former two would be difficult to implement in air and the latter is obviously not a good replica of experimental conditions[305]. The recent technique alluded to in section 5.2.1 combines two techniques to measure detector calibration from experimentally measured values alone[295]. It is hoped, even with the unique problems of airborne trapping, by using AODs or SLMs to oscillate the trap position this technique will be developed for future experiments.

There is a simple and quick method to calculate β from the voltage power spectrum alone but can be less precise than the other, previously mentioned, methods. Consider the high frequency limit, $\omega \gg \omega_c$, of equation 5.23;

$$S^V(\omega \gg \omega_c) = \beta^2 S_x^{over}(\omega \gg \omega_c) \tag{5.29}$$

$$S^V(\omega \gg \omega_c) = \beta^2 \frac{2k_BT}{\gamma_0}\frac{1}{\omega^2} \tag{5.30}$$

$$\omega^2 S^V(\omega \gg \omega_c) = \beta^2 \frac{2k_BT}{\gamma_0} \tag{5.31}$$

$$P^V = \beta^2 \frac{2k_BT}{\gamma_0}. \tag{5.32}$$

Multiplying the uncalibrated voltage power spectra S^V by ω^2 (the expected tail gradient) gives a constant plateau value at high frequencies, P^V, hence the detector sensitivity for a system neglecting inertia is

$$\beta_{over} = \sqrt{\frac{P^V\gamma_0}{2k_BT}}. \tag{5.33}$$

The equivalent can be calculated for power spectra where the inertial term is not neglected by multiplying with ω^4 to obtain the plateau at high frequencies, thus I find the detector sensitivity to be

$$\beta_{inertia} = \sqrt{\frac{P^V m}{2k_BT\Gamma}}. \tag{5.34}$$

5.3 Experimental

Droplets are trapped using the custom built inverted tweezers pictured in figure 5.3. The beam from a 532 nm Laser Quantum Finesse 4W continuous wave laser is expanded by a Keplerian telescope to slightly overfill[115] the back aperture of a Nikon Plan 100× (NA = 1.25[†]) oil immersion microscope objective. The beam is focussed through a type one coverslip into an aerosol chamber constructed from a cylindrical plastic enclosure 9 mm in height and 35 mm in diameter. This produces an enclosed environment where a high relative humidity can exist and also shields the trapping region from external air currents. The top of the chamber is made from a type zero coverslip to allow for transmission and then collection of the scattered trapping laser by a long working distance (LWD) Mitutoyo 100× (NA = 0.55) objective, whose back aperture is imaged[266] equally onto the four quadrants of a QPD (Hamamatsu Silicon Diode Array S5980) via a 4f imaging system. The Mitutoyo objective also acts as the condenser lens for Köhler illumination (not shown in figure 5.3 but remains the same as illustrated in figure 2.3). The Nikon objective and an appropriate tube lens image the sample through a laser filter onto a Basler A602f firewire camera.

The liquid aerosol is produced using the same nebuliser as for the holographic optical trapping of aerosols except the salt solution concentration was varied between 20 and 80 gL^{-1}.

The trapping beam is focussed $\simeq 15$ μm above the coverslip which is again soaked in the aqueous dilution of Decon 90 as described in section 4.2.1. Water saturated tissue paper is also placed in the chamber to increase the relative humidity, but I ensure it does not touch the cover slip as this can induce flows in the water layer. Figure 5.4 shows an enlarged view of the trapping region's geometry and also explains the relation between paraxial focus height, L, and objective displacement, X.

Control over droplet size was required to fully investigate observed phenomena. Firstly, this was achieved imprecisely by varying the concentration of the nebulised salt solution because as discussed earlier a higher concentration decreases the droplets vapour pressure allowing them to equilibrate with their surroundings at larger sizes (chapter 4.1). Secondly, more precise size selectivity can be induced with the, on average, positive linear dependence of captured droplet size on laser power[12,179] as mentioned in the previous chapter.

[†]It is important to note that the NA clearly cannot be larger than unity in the focal region and in fact due to total internal reflection at the glass:water:air boundary the NA is effectively reduced to $\simeq 0.67$. See chapter 6 for more detail.

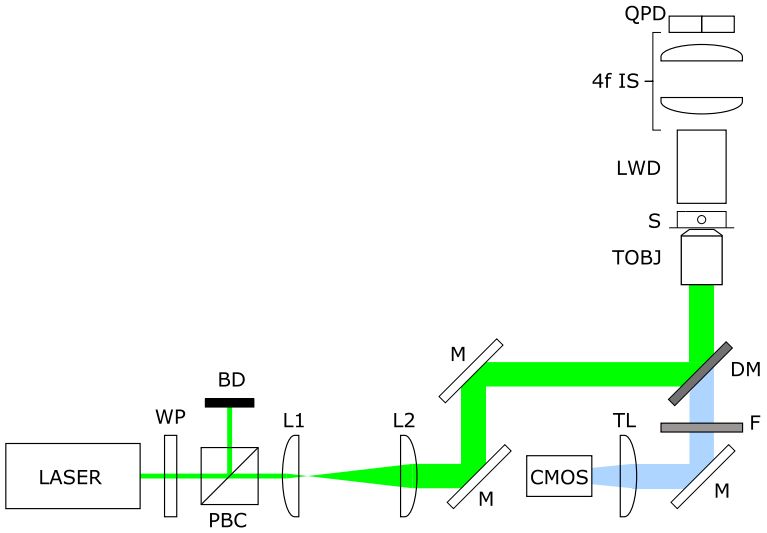

Figure 5.3: Apparatus diagram. A Gaussian beam is expanded by lenses L1 and L2 and directed to slightly overfill the back aperture of the Nikon objective (TOBJ) with mirrors M and DM. The long working distance objective (LWD) collects the droplet's scattered light and its back aperture is imaged onto the QPD via a 4f lens system. Power is controlled using a polarising beam cube (PBC) and half wave plate (WP). The same Nikon objective with an appropriate tube lens (TL) is used to image the sample (S) through a dichroic mirror (DM) and filter (F) onto the firewire camera (CMOS). The QPD, COBJ, and TOBJ are each mounted on three axis translation stages with TOBJ's axial axis controlled either manually or by digital micrometer. BD is a beam dump.

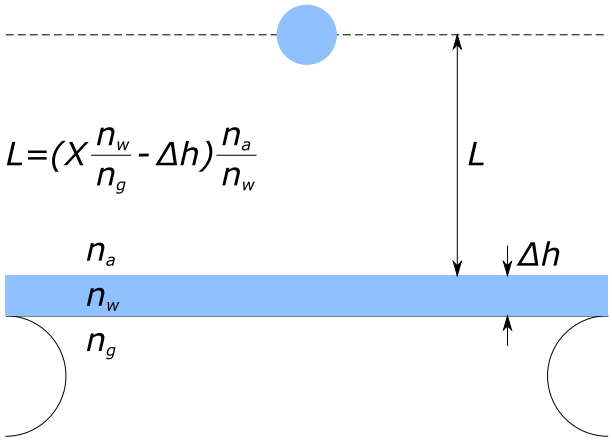

Figure 5.4: Enlarged view of the trapping region in the sample of figure 5.3. The refractive indices of the coverslip and index matched oil, water, and air are n_g, n_w and n_a respectively. Δh is the thickness of the water layer. Displacing the objective X microns from being focussed on the first interface displaces the particle a distance L, given in the figure.

Having trapped a droplet the nebuliser is turned off. Once the droplet has reached equilibrium with its surrounding environment, and the remaining aerosol settled, the current produced by the detection of light on the QPD is sent, via shielded cables, to amplification electronics[306] containing a 50 kHz anti-aliasing filter. Data was acquired at a sampling

frequency of 50 kHz for four seconds with a National Instruments PCI-6014E DAQ card, in differential mode. The voltage difference between left and right pairs of quadrants on the QPD represents the x position and the difference between the top and bottom pairs represents the y position. Summing all quadrants represents the axial position. The voltage versus time data was Fourier transformed using LabVIEW and all remaining data analysis was performed offline at a later time. In order to minimise any parameter variation over time the experiments were carried out as quickly as possible with raw voltage versus time data not saved to increase speed still further. The detailed analysis of the data obtained for a colloidal case is extensively described in Berg-Sørensen and Flyvbjerg[297], and much remains the same here. An image of the trapped droplet was also taken with each power spectrum for later analysis.

It is an initially difficult process to obtain a sufficiently noise free signal from the amplification electronics to enable accurate analysis. Plotted in figure 5.5 are the power spectra of position fluctuations of the laser alone, with no particle trapped both with good and bad noise, with a clear distinction between the two.

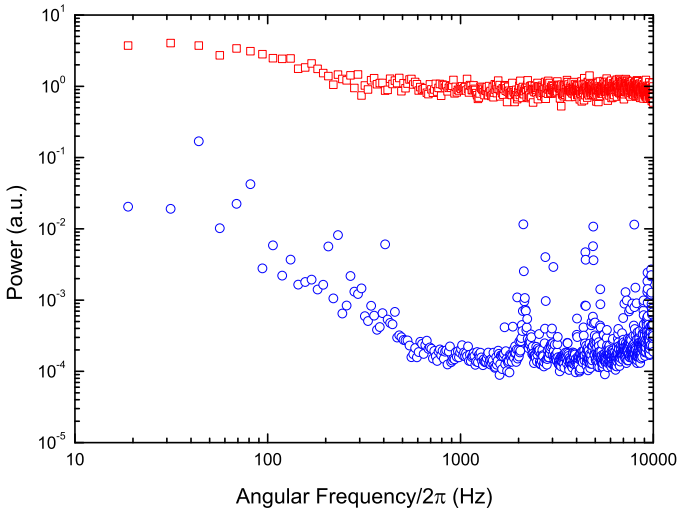

Figure 5.5: Power spectra of position fluctuations for the focussed laser alone, with no particle trapped. The red squares are from voltage data with what is considered bad noise and the blue circles plot data with good noise.

It is essential to ensure the background noise level is as low as possible so the fluctuations due to Brownian motion will be observed. There are several reasons unwanted noise can occur; the current signals produced from the QPD are small so very susceptible to interference and care must be taken to ensure the signal reaches the amplification electronics without additional signal being induced. Also the Poynting stability of the laser and any mechanical vibration contributes by effectively increasing the non-Brownian noise.

Ideally removing interference can be achieved by placing the QPD directly next to the amplification circuit but in my case it is ensured that the cable used to transfer the signal from the QPD to amplifier is fully shielded. To reduce mechanical noise work was always carried out, where possible, solitarily in the laboratory and to improve the stability of the laser it was always used at $> 30\%$ capacity and power control achieved by using a pair of half wave plates coupled with polarizing beam cubes. The first split the beam for two different experiments and the second controlled power for this experiment alone. The power was varied between a minimum of 0.702 ± 0.009 mW and a maximum of 510 ± 6 mW. Using these simple noise reduction schemes reduces my experimental noise spectrum by two to three orders of magnitude, as shown in figure 5.5, and is essential to its success.

Unfortunately no matter the extent of the noise reduction schemes some cannot be removed from the axial position signal. This is particularly true of noise inherent in the laser. When analysing the lateral motion the voltage difference between the halves of the diode allows cancellation of symmetric noise, i.e. noise that appears equal on each half. However, due to the summation of quadrant voltages for axial position the noise remains, rather than being cancelled, with sufficient strength that further data analysis cannot be attempted. It is for this reason I consider only lateral motion.

To investigate whether droplets are becoming unstable at any point in parameter space I investigated over a range of radii how power and height vary the damping ratio and observed the behaviour around the point of critical damping, the most likely place for instability.

As alluded to in section 4.2.2 unlike tweezing in water, simply increasing the trapping power does not assist in capturing an aerosol droplet from the nebulised cloud, so initial laser power must be carefully selected. Each droplet trapped was subject to an increase in laser power in uniform steps with power spectra measurements taken at each. The minimum attainable damping ratio for each droplet was taken from the last power spectrum measured before it fell from the trap upon increasing the power (i.e. the highest power). This represents an upper limit on the ratio for that size.

To study how the water-air interface to droplet height may affect the dynamics, the laser power was kept constant and the height of the sample stage varied, controlled and measured by a micrometer. The water layer thickness was measured by observing when a reflection of the trapping beam focus is obtained at both the water-air and glass-water interfaces. Having been focussed through two refractive index mismatched interfaces (glass to water and water to air) there is an associated focal shift[307] of which a rigorous description is complex[308,309] and not discussed here but rather in chapter 6. A simple paraxial approximation is used to calculate the droplets position inside the chamber given a vertical

displacement of the sample stage around a fixed objective.

5.3.1 Data analysis

To optimise the accuracy and precision of results both pre- and post-experimental statistical analysis can be used. Measurements are taken in the time domain during the experiment for which there is an optimum timescale to reduce overall noise, hence increase precision. The factors affecting the exact timescale are combinations of electrical, mechanical, temperature, laser power and particle size and will obviously be different from experiment to experiment. One can imagine measuring particle position for 30 seconds and the expectation would be of thermal noise around a fixed origin. However, the system may drift over time with a shift of origin as illustrated in figure 5.6. Ideally the data would be binned into time periods, t, over which there is negligible drift from the local origin yet enough data to obtain an accurate result once all periods have been averaged. The best way of determining this timescale is through using Allan variance[310].

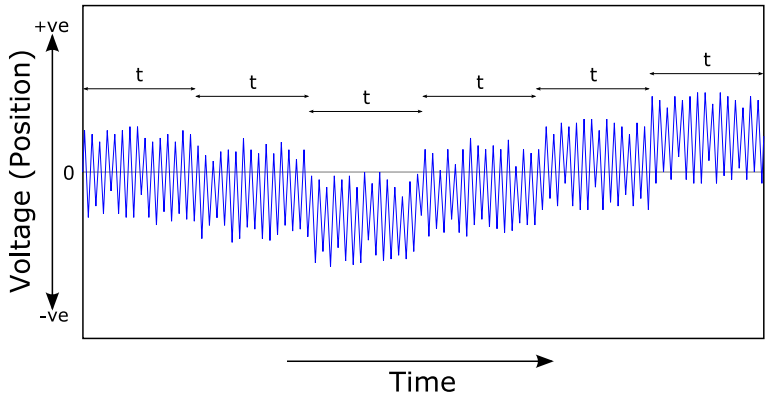

Figure 5.6: Representation of the voltage output from a QPD as a function of time to illustrate that although one would expect oscillation around the zero point there is an additional overall drift. However, there are periods of time, t, over which the drift is negligible and the data should be binned into these.

The data is also analysed in the frequency domain and so one must be careful in its analysis too. The data obtained by Fourier transforming the particle position versus time output from the experiment is exponentially distributed[297] and I would like to perform a non linear least squares fitting algorithm to find the parameters that define the best fit. To do this the data must be Gaussian in distribution with associated uncertainties, so, each power spectrum is binned into predetermined frequency windows replacing the frequency range with the average frequency over the bin and the power value with their mean and associated standard deviation.

Performing the analysis in frequency space for each period of data in time space and averaging over all of them gives the final set of data to be fit to. We use a built-in software Levenberg-Marquardt algorithm that performs a nonlinear least squares fit to the data by reducing chi squared weighted with the uncertainties (standard deviation);

$$\chi^2 = \frac{(O_i - E_i)^2}{\sigma_i^2}. \tag{5.35}$$

Here O_i is the observed data point, E_i is the expected data point from the fit and σ_i is the associated standard deviation.

5.4 Results

5.4.1 Langevin dynamics

Typical power spectra of position fluctuations from optically trapped droplets are shown in figure 5.7, illustrating, for a 3.7 ± 0.2 μm radius droplet, the ease with which the system can be transferred between over- and under-damped dynamics by varying laser power. The tail falls off with ω^{-4} as expected for $\omega \gg \Omega$ from equation 5.25 and a clear resonance peak begins to establish itself, indicative of the droplet moving through the critical and into the under-damped regime.

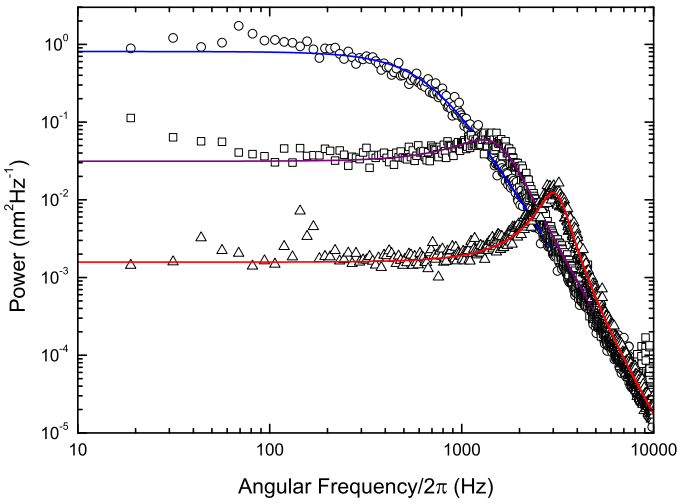

Figure 5.7: Power spectra of a droplet of radius 3.7 ± 0.2 μm trapped at powers 40.9 ± 0.5 (circles), 130 ± 2 (squares), and 356 ± 4 (triangles) mW resulting in damping ratios of 1.69 ± 0.04, 0.794 ± 0.01, and 0.364 ± 0.001 respectively. As the power increases the appearance of a resonance peak is clear indicating the move into an under-damped regime, along with a decrease in area and hence position variance. The natural frequency increases with laser power because of the associated increase in lateral trap stiffness, κ.

For completeness, a plot of the autocorrelation function[271] of a single droplet in an under- and over-damped state is shown in figure 5.8. It shows the classic exponential decay for over-damped motion and sinusoidal oscillation enveloped by exponential decay for under-damped oscillators as expected.

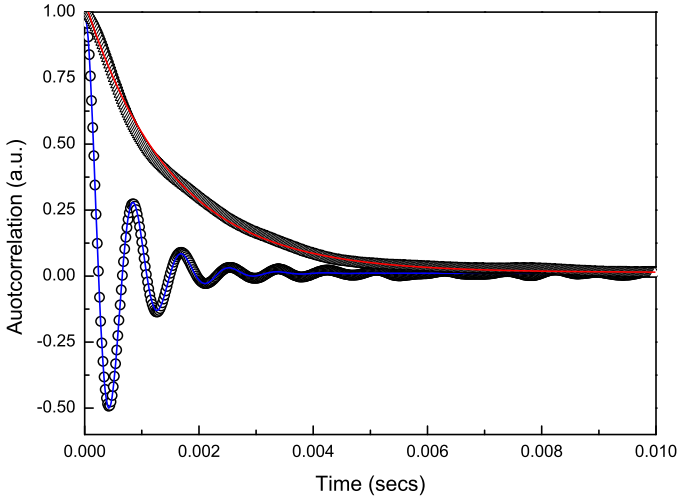

Figure 5.8: Plot of experimental autocorrelation data with associated fits for a 5.2 ± 0.2 μm optically trapped aerosol in an over- (triangles) and under-damped (circles) state trapped with powers 74 ± 1 and 442 ± 7 mW respectively. Both traces clearly follow the classic exponential decay except in the under-damped case there is also the sinusoidal oscillation expected.

The trend seen in figure 5.7 remains for all droplets; an increase in power increases lateral trap stiffness and moves the system towards or into the under-damped regime. A range of damping ratios has been observed from 3.57 ± 0.07 down to 0.260 ± 0.006 over the 4.7 ± 0.5 μm radius range studied. There is also an associated decrease in area under the power spectrum curve with increasing laser power, indicating a reduction in the position variance of the droplet.

The inclusion of inertial terms in the Brownian theory means only the particle's mass is needed to calculate trap stiffness. Using the radius from video microscopy I obtain lateral trap stiffness values ranging from 0.12 ± 0.10 to 98 ± 17 pNμm^{-1} for 1.0 ± 0.3 to 5.7 ± 0.4 μm radius droplets.

One would expect the natural frequency of trapped droplets to vary as the square root of laser power, assuming the trap stiffness is linearly proportional to trapping power. This is confirmed in figure 5.9 for a 1.8 ± 0.2 μm radius droplet. For the range of radii and powers studied here I observe natural frequencies between $2\pi(328 \pm 12)$ Hz and $2\pi(3433 \pm 15)$ Hz, falling close to and well above the corner frequencies measured by tweezers in liquid based systems, although obviously not directly comparable.

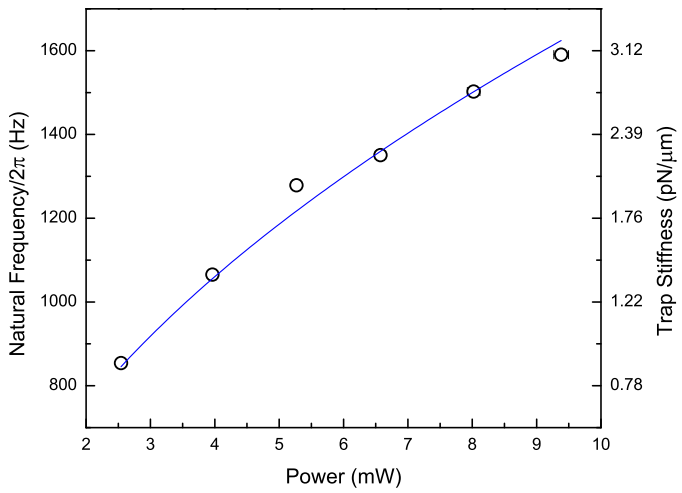

Figure 5.9: An example of how natural frequency for a 1.8 ± 0.2 μm radius droplet increases with the square root of laser power as expected from $\Omega = \sqrt{\kappa/m}$. The lateral trap stiffness axis is displayed for interest and is non linear. The error bars are standard error of the mean for the natural frequency rather than the trap stiffness (although they are smaller than the points themselves).

As mentioned a curiosity of airborne trapping is an upper limit on laser power above which particles fall from their trap. To ascertain the cause of this clear instability I plot, in figure 5.10, the upper limit on the minimum damping ratio attainable against droplet radius.

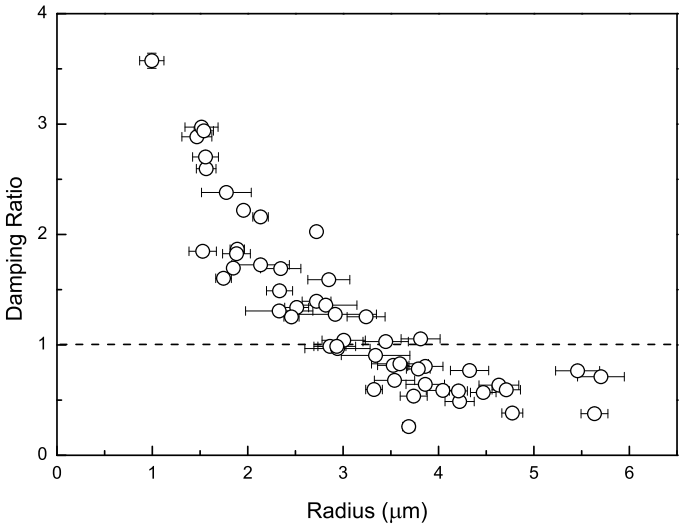

Figure 5.10: Upper limit on the minimum attainable damping ratio against droplet radius. It is an upper limit as we increase the laser power in finite increments. The dashed horizontal line represents a critically damped system. The error bars are standard error of the mean.

Figure 5.10 illustrates there is no problem in transferring from over- to under-damped

dynamics with no instability induced, suggesting this is not the reason for the odd phenomena seen. There is clear size dependence but one must be careful to note this does not lead to the conclusion that small droplets cannot exist in the under-damped regime; this cannot be excluded for certain as they fall from the optical traps before they reach it.

The above results produce a downward shift in damping ratio by increasing lateral trap stiffness with larger laser powers. A decrease in friction felt by the droplet could likewise shift the ratio by varying the damping and as stated earlier Faxén's correction predicts that the proximity of a surface to our microscopic object heavily influences this. Utilising this surface to droplet height dependence figure 5.11 demonstrates that lowering the sample stage, hence increasing the distance, reduces the damping and transfers the system from over- to under-damped. Note the resonance peak remains approximately at the same frequency for each spectrum as only the damping is changing, not the trap stiffness, contrary to figure 5.7.

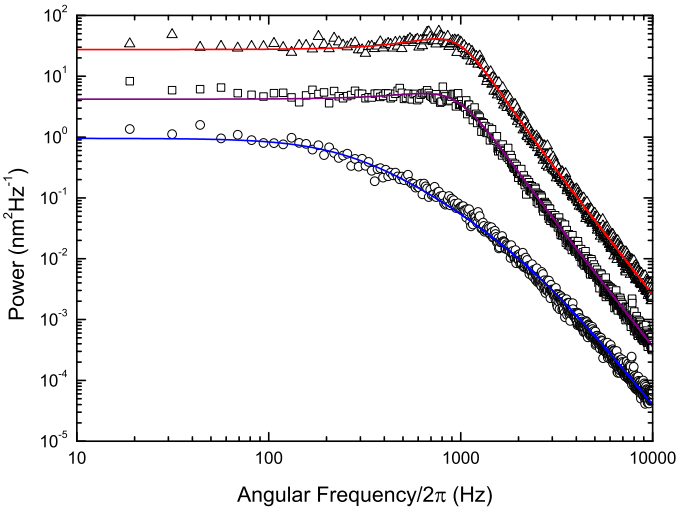

Figure 5.11: Power spectra demonstrating changes in damping as a function of surface-droplet distance for a 3.8 ± 0.2 μm radius droplet trapped with 46.3 ± 0.6 mW. The droplet was moved to heights of 4 ± 1 μm (circles), 9 ± 1 μm (squares), and 14 ± 1 μm (triangles) above the water layer resulting in damping ratios of 3.40 ± 0.06, 1.06 ± 0.01, and 0.92 ± 0.01 respectively. The middle and top spectra are multiplied by 25 and 200 respectively to displace the data on the y-axis for clarity.

The majority of previous work using the power spectrum method is based on tweezing solid microspheres, with precisely known radii, in the liquid phase allowing very high precision studies; indeed, the ability to detect sphere non-uniformity is possible[295]. In the studies here a large source of error is measuring the radius using video microscopy with the likely errors propagating heavily into some of the systems calculated properties ($\kappa \propto m \propto R^3$). Trapping of solid aerosols, with known radii would remove this problem[81] but due to their high refractive index compared to air this idea poses significant problems as one

will understand from the next chapter. In addition, highly precise radius measurements are possible via CERS[180] but require sensitive spectrometers. In the following section I demonstrate a new method to size aerosols in optical tweezers.

5.4.2 Sizing

Many fundamental properties of individual droplets are governed by their radius and hence its measurement is of great importance. In the context of optical manipulation the main sizing methods are light scattering analysis with lasers[311,312] or broadband sources[313] along wih a few methods using the physical dynamics of their motion[63,279,314]. Using CERS and fitting to the excited whispering gallery modes is the most precise technique to size trapped aerosols to date enabling very detailed studies, with precisions of ± 1 nm[180]. These studies have mostly concentrated on the coarse mode of atmospheric aerosols ($>$ 1 μm in radius) but have not extended into the accumulation or nucleation modes ($<$ 1 μm). For studies of the smaller aerosols CERS fails in measuring their radii because the quality factor, Q, diminishes and the modes become too widely spaced to observe more than a single peak in measured spectra[315]. The study of accumulation mode aerosol is very important as it constitutes the largest proportion of atmospheric aerosol in terms of surface area to volume ratio and so dominates atmospheric chemistry[54]. As optical trapping moves into this region CERS will become redundant and must be replaced by a new method of radius measurement.

Methods to obtain the properties of objects and their surroundings in conventional optical tweezers have relied on trap stiffness or position detector calibration and normally require more than one independent experiment. In the monodisperse colloid area of optical tweezers the particle size is usually known, through use of size calibrated microspheres, and so techniques are aimed at obtaining those parameters that remain, for example viscosity, trap stiffness, displacement and forces.

However, the size of optically trapped aerosols is not precisely known before the experiment because the nebulised sample is highly polydispersed. I propose to determine their radius by studying their confined Brownian motion and show that being airborne presents unique challenges and solutions, specifically that the calibration techniques important in water need not be applied due to the significant contribution to the motion from inertia.

The literature shows one could study the low frequency plateau in the power spectrum of force fluctuations, which is proportional to particle size, to give an indirect measure of radius[48,316] but I would like an absolute measurement. It is possible to measure the absolute size of colloidal particles suspended in a water environment from their position

fluctuations in free Brownian motion by using detection instruments with absolute position calibration. Einstein's diffusion coefficient can be extracted from the position data and the particle radius determined assuming knowledge of viscosity. Through this method Viana *et al.*[317] determined the radius of spheres by measuring position in a 'switched' optical trap using a camera, however, this method of detection has limits on its precision[28]. Furthermore, the distance a given particle can diffuse in a set time is approximately an order of magnitude greater when suspended in air rather than water, which means the droplet quickly disappears from the focal plane disabling the possibility of video tracking. Additionally, the laser modulation to take the object in and out of free Brownian motion could cause failure of the airborne optical trap as I shall describe in section 5.6. So, for these reasons the particle must remain localised within the optical tweezers.

Our experiment is ideally suited to the problem at hand as the position information of the trapped droplet is not undersampled and I obtain a clear representative set of position data by imaging the scattered laser light, related to its position, onto a high speed photodiode via a condenser lens[269]. The signal to position calibration here is a little more complex than for cameras. I have shown that the high frequency tail in the power spectrum of position fluctuations of the particle can be used to calculate the detector calibration[81,268]. However, for suspensions in both water and air equations 5.33 and 5.34 show this method cannot be used as the particle radius is needed *a priori*.

As mentioned when discussing detector position calibration Tólic-Nørrelykke *et al.*[295] coupled the power spectrum method with analysing the response of a trapped particle to a given flow. This enables the viscous damping, trap stiffness and detector calibration to be determined from experimentally measured parameters alone enabling, for example, the determination of local viscosity[318]. This technique could equally work for determining the radius of spheres if the medium's viscosity is known. In the context of airborne tweezers it is unknown what effect lateral trap oscillation will have on particle dynamics and also whether sample stage oscillation will indeed induce the required flow in the current chamber environment.

In air it is possible to analyse the power spectrum of the particle's position fluctuations to extract the radius without calibrating the detection system *a priori* or using the method of Tolic-Norrelykke *et al. in situ*, as I shall now discuss. Furthermore, the same data and extracted parameters then allow detector system and trap stiffness calibration *a posteriori*[81,268].

To summarise, measuring Γ, with units of Hz, allows determination of the aerosol droplet radius with no pre-calibration or measure of trap stiffness necessary. However, these can be calculated from the data and fitting parameters as a result of the radius determination.

Therefore, in air, the system for radius determination is fairly simple with cheap diodes, electronics and a method of altering the droplet to surface height being the only additions to normal optical tweezers.

There are slight changes to the experimental method but much remains the same as previously. The droplet to water surface height is now controlled by a digital micrometer (Newport NSA12). I first focus the beam $\simeq 15$ μm above the coverslip for ease of trapping; once caught the sample stage is lowered, hence the droplet is moved away from the water surface. The micrometer has a large amount of hysteresis so to begin, the droplet is moved to approximately twice the distance from where the first measurement is made. The sample stage is now raised in 1 μm increments until the position desired for the first measurement is reached, by which time any hysteresis has been removed and motion is as expected. The height was recorded and a power spectrum taken before moving the sample stage up, hence droplet down, by the desired increment where the next spectrum is taken. This procedure was repeated until the droplet falls from the trap, probably due to coagulation with the underlying water layer.

Extracting damping values from data similar to figure 5.11 the dependence of friction upon droplet to surface distance can be plotted to obtain figure 5.12. Here the micrometer raised the sample stage in increments of 1 μm, decreasing to 0.5 μm as the surface was approached due to the high gradient of Faxén's correction in this region. Fitting to such data using equation 5.28 with R as a variable and $\eta = 1.8 \times 10^{-5}$ allows the droplet radius to be extracted. Clearly the fit to Faxén's correction is critical upon knowing the distance to the surface and as such I include an offset, h, so that $L \rightarrow L + h$ in equation 5.28 to compensate for any errors in the trap position-paraxial focus assumption, or measurements on the relative positions of the interfaces[305,317].

The measurements made for figure 5.12 are repeated for different droplets to obtain figure 5.13, a comparison between radius measurements through video microscopy and from studying their Brownian motion.

Figure 5.13 demonstrates droplets can be sized with good precision, better than video microscopy, by only studying the damping they experience. There is a significant shift from the radius measured by microscopy which I believe highlights the ambiguity in sizing aerosols from microscope images. Figure 5.14 shows four images of the same droplet taken at various stages of a sizing experiment, exemplifying the difficulty in video imaging. I believe it is caused through several reasons; the trapping objective is not designed to image through air, the condenser lens is optimised for collection of scattered light not illumination, and there is a high refractive index mismatch between water and air. These contribute to increased diffraction and decreased resolution, hence the ambiguity in deter-

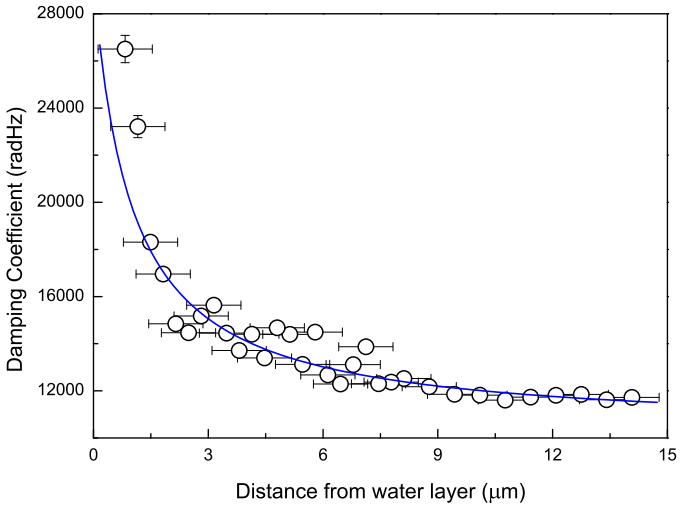

Figure 5.12: Variation of viscous damping experienced by a droplet, trapped with 6.2 ± 0.1 mW, as a function of surface-droplet height. The droplet radius is measured by video microscopy to be 2.80±0.16 μm and 3.28±0.02 μm from the fit to experimental damping data. For this case the height offset $h = -2.84 \pm 0.19$ μm.

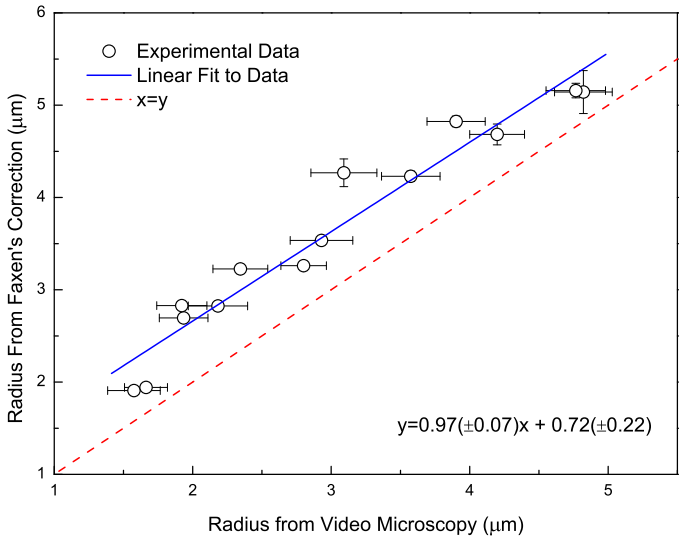

Figure 5.13: Comparison of radius measurements made by video microscopy and through fitting to variations in viscous damping as the droplet approaches a surface. x and y error bars are standard errors of the mean.

mining the perimeter of the droplet images. Finally, for completeness I plot in figure 5.15 the natural frequency as a function of height from the water layer. There is a steady fall off with distance indicating the spherical aberration induced is degrading the trap stiffness. Unlike the data in Vermeulen *et al.*[305] the fit is approximately linear as the trap stiffness is independent of the viscous damping.

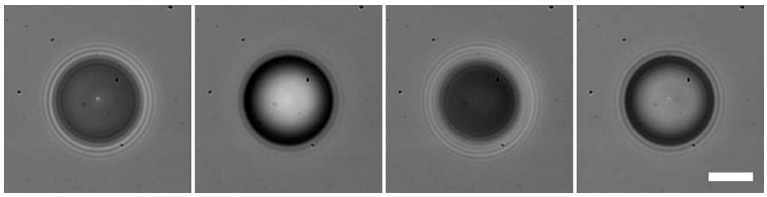

Figure 5.14: Images taken during the sizing process showing the variation in droplet appearance and indicating the ambiguous nature of determining the perimeter. By studying the damping experienced during Brownian motion this ambiguity is removed. This droplet is measured to be 4.77±0.21 μm from video microscopy and 5.19±0.08 μm from fitting to Faxén's correction. Scale bar 5 μm.

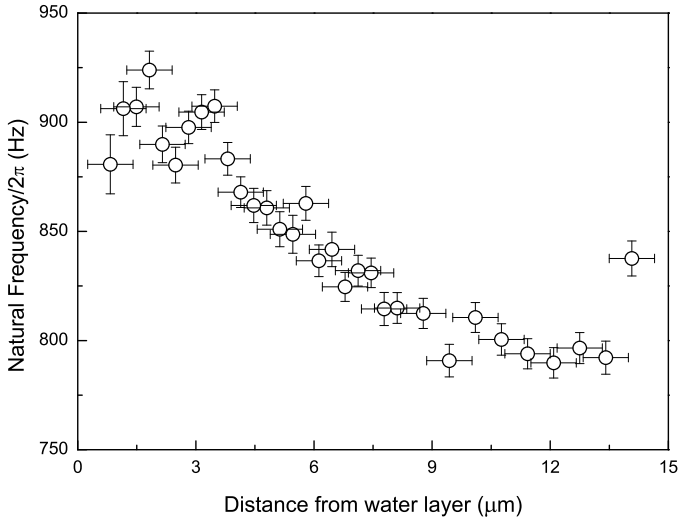

Figure 5.15: Natural frequency as a function of distance from the water layer for the droplet in figure 5.12.

5.5 Discussion

The reader may notice significantly more scatter in this investigation's results compared to experiments using similar techniques in liquid. The reasons will now be discussed briefly showing the complex nature of the experiment and the engineering challenges faced to improve future precision.

It is difficult to determine which individual factor, trap stiffness or damping, contributes to the variation in damping ratio for any given experiment. For an individual droplet the surrounding conditions can remain relatively constant over the time of a single experiment as, with no additional aerosol flow from the nebuliser, the droplet quickly reaches equilibrium with its surroundings. To trap another droplet nebulisation must resume where upon the chamber conditions can alter. Additional aerosol can settle on the coverslip changing the water layer's thickness and hence the optical potential[309,317,319] at the trap site together with the proximity of the particle to the surface[297,303,319]. As mentioned variation

in trapping power between droplets alters the droplet's height[279] and hence distance from the underlying water layer, thus again altering the optical potential and damping. These factors contribute to the system's rather complex and difficult analysis.

The difficult nature (relative to colloidal tweezers) of trapping in air imposes several important experimental methods. A long working distance condenser must be used due to the aerosol chamber height, but a higher NA lens may have been desirable to improve detector sensitivity[320]. Most colloidal experiments use monodisperse suspensions of solid particles thus allowing an arbitrary number of measurement repetitions; often up to 100 power spectra are averaged. However, with the dynamic system investigated here (the droplets are continuously finding an equilibrium with the surrounding environment) the conditions of the experiment may not remain constant long enough for repeated measurements to improve precision, hence the choice of sampling and no averaging over multiple power spectra. Also, I am looking at an inherently unstable region with the aim, at times, of losing the trapped droplet so, clearly, another particle of the exact same size and composition cannot be found. With the current iteration of apparatus there is a clear trade off between speed and precision.

Some studies have used a secondary, independent probe beam to monitor position fluctuations as this allows greater flexibility and perhaps improved accuracy[321]. I employ only a single beam because a very small amount of power is needed to tweeze in air[179] and a second beam would significantly alter the potential at the trap site.

In future studies I suggest that a system including a 'science chamber' be developed where many variables can be controlled. A particle could be trapped and transferred to such a chamber with relative humidity control, with or without a water layer, and with a lower physical profile to enable the use of higher NA condenser optics. Also the mechanical stability of our system is not fully optimised so the precision seen could be improved.

The precision to which aerosols can be sized through studying their Brownian motion is currently limited by the apparatus iteration. With the outstanding precision possible in more refined experiments[301] it is believed this method can compete with CERS and will supersede it when studying aerosols < 2 μm in radius.

For improvements in precision and accuracy of the sizing technique several problems must be combated; firstly, the water layer on the surface of the cover slip creates a relative humidity gradient and as the droplet approaches this layer its size can increase[322]. Secondly, mathematical modelling (see chapter 6) shows airborne droplets are trapped significantly, $\sim R$, below the paraxial focus of the beam and hence my simple paraxial approximation for the droplet position will be slightly offset. This potential error can be absorbed into the offset h, mentioned above, but with further work I believe much could be inferred

about both the relative humidity gradient and the axial position offset while providing a more accurate technique. It is also proposed that with the incredible precision of optical tweezers and by using spheres of known radius a verification or perhaps improvement of the empirical slip correction factor, C_c, could be performed.

The sizing technique through Brownian motion removes any subjectivity or ambiguity and as such these results are considered to be more accurate and reliable than those from video microscopy. An appealing experiment would be to compare this method with CERS and will hopefully be performed in future. Unfortunately, without the necessary equipment to obtain CERS measurements it is difficult to obtain or state an absolute accuracy for the experiment.

Another problem is the axial stability of the droplets. Low frequency axial oscillations can occur which in a mis-aligned system causes the droplet to, or appear to, displace laterally. Furthermore the oscillations mean the particle position is sampled at many heights rather than a single one. It is believed removing the central core of the trapping beam, by using Laguerre-Gaussian beams for example, would improve the stability and hence accuracy.

For both the Langevin dynamics and the sizing experiments I have neglected any hydrodynamic corrections, specifically effective mass due to entrained fluid[300] and the frequency dependent Stokes' friction[296], and as such it would be pertinent to discuss the effects here. Figure 5.16 plots the ratio of the power spectrum in equation 5.25 to the hydrodynamically correct version in equation 5.27. Clearly for a given particle type and size the correction is significantly smaller when studying aerosols. However, the solid line shows the error begins to become significant for aerosols with a radius that would be considered relatively large for particles normally used in power spectrum based studies in liquid. Should further studies be performed the hydrodynamic correction must be investigated to improve accuracy and precision.

Not discussed in detail here is that Faxén derived his correction for a sphere moving with constant velocity which is not the case, so for a complete solution the frequency dependent friction should be combined with Faxén's correction [295,297].

When dealing with solid in fluid systems no slipping occurs at the boundary between the two materials upon translation. However, the physics involved becomes more complicated when studying fluid in fluid systems; slip can occur. Due to the possibility of slip at the fluid sphere's surface, flow can be induced inside the sphere, as illustrated in figure 5.17. This flow causes reduction in the well known pre-factor of Stokes' Law according to[303,323]

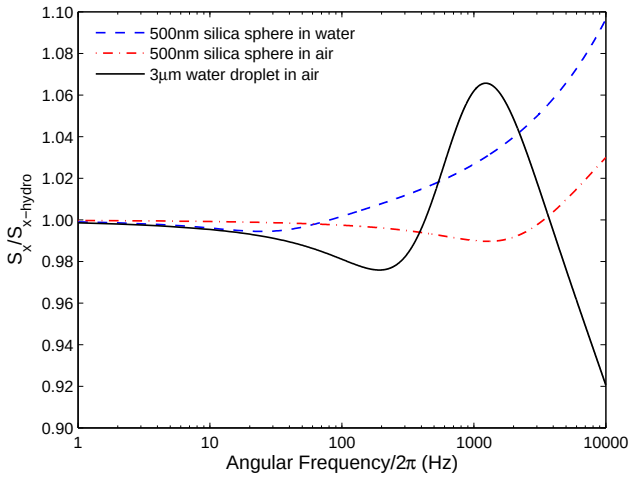

Figure 5.16: Theoretical plot of $S_x/S_{x-hydro}$ as a function of angular frequency. For a given particle radius the hydrodynamic correction is smaller in air (red dot dashed) than in water (blue dashed), but, for the large liquid aerosols (black solid) the effect starts to become significant. Trap stiffness, $\kappa = 2$ pNμm^{-1}.

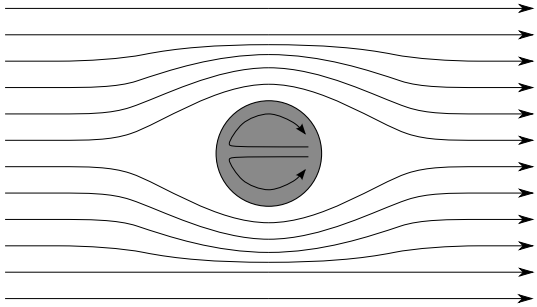

Figure 5.17: A fluid sphere immersed in a laminar fluid flow will have slip occurring at the boundary between the two materials hence a flow will be induced within the liquid sphere. This internal flow reduces the viscous drag force on the sphere.

$$F_{stokes} = -\frac{6\pi\nu\rho Rv}{C_c}\frac{1+\frac{2}{3}\sigma}{1+\sigma}, \tag{5.36}$$

where σ is the ratio of the medium to the droplet's dynamic viscosity, μ_m and μ_p respectively, giving Stokes' law for a water droplet in air, to be

$$F_{stokes} = -\frac{5.96\pi\nu\rho Rv}{C_c}, \tag{5.37}$$

which has been taken into account in the data analysis for this chapter.

Exploration of these discrepancies for optically trapped aerosols could not only provide improved particle sizing but also insights into interesting physics which I shall discuss in the final chapter.

5.6 Parametric oscillation

The work described next was carried out as a collaboration with the Optics group at the University of Glasgow and Roberto Di Leonardo at thr Universitá di Roma "La Sapienza".

It has been shown in this chapter that water droplets trapped in air have significant contributions from the inertial terms in their equation of motion (equation 5.18). This can lead to the appearance of a resonance peak in their power spectrum of position fluctuations.

If the resonance peak of an oscillator, in our case a harmonically trapped aerosol droplet, is dependent upon a number of parameters, then modulating any of them at twice the natural oscillation frequency ($\Omega_p = 2\Omega$) parametrically excites the resonance.

Parametric resonance provides an efficient and straightforward way to pump energy into an under-damped harmonic oscillator as it is far easier to modulate a system parameter rather than applying an oscillating driving force. Such behavior leads to surprising phenomena in the macroscopic world such as pumping a swing, the stability of vessels and surface waves in vibrated fluids[324]. In my microscopic scale system, the particle is driven by Brownian stochastic forces[325], the parametric driving of which has been shown to be at the origin of some peculiar behaviour such as the squeezing of thermal noise in Paul traps[326].

I have demonstrated that optically trapped microparticles are beautiful examples of a Brownian damped harmonic oscillator, and it has been reported that modulating the trap's laser power in a colloidal system at its resonant frequency increases the amplitude of fluctuations[277,327]. However, these results have been difficult to reproduce and are in contrast to the predictions of the Langevin equation[272,278,328], due to the heavy damping objects experience in water.

The ability of our airborne trapping experiments to exist in the under-damped regime allows the excitation of resonances through parametric oscillation. The laser power is easy to modulate and is therefore chosen as the parameter to vary. Taking equation 5.24 but including a term that modulates the trap stiffness as a function of time gives the Langevin with a parametrically modulated potential to be

$$\ddot{x}(t) + \Gamma\dot{x}(t) + \Omega^2\left(1 + gf(t)\right)x(t) = \Lambda\eta(t), \tag{5.38}$$

where $f(t+\tau) = f(t)$, $-1 < (t) < 1$, and $0 < g < 1$ is the strength of modulation. Fourier transforming equation 5.38 gives

$$\left(-\omega^2 - i\omega\Gamma + \Omega^2\right)\hat{X}(\omega) + g\Omega^2\sum_{k=-\infty}^{\infty} a_k\hat{X}(\omega + k\Omega_p) = \Lambda\eta(t), \tag{5.39}$$

where Ω_p is the modulation frequency and a_k is the coefficient of the $2\pi k/\tau = k\Omega_p$ frequency component of the Fourier series expansion of $f(t)$. One can see the coupling between all frequencies that are an integer multiple of Ω_p that contribute to the excitation of the natural frequency. Following di Leonardo *et al.*[83] the power spectrum of position fluctuations for a particle in a power modulated optical trap is found to be

$$S_x(\omega) = \frac{2\Gamma k_B T \kappa}{\Omega^2} \sum_{k=-N}^{N} |G_{0k}(\omega)|^2 . \tag{5.40}$$

Plotted in figure 5.18 is the power spectrum of a water droplet in an under-damped regime (white circles). Fitting the power spectrum of equation 5.25 gives $\Omega/2\pi = 2.0$ kHz. Knowing this a square wave modulation of the trapping power with $g = 0.4$ and $\Omega_p/2\pi \simeq 2\Omega/2\pi \simeq 3.9$ kHz can be applied whilst retaining the same average power as previously. Measurements from the experiment with these system conditions yield the data shown in black circles. The expected resonance excitement is found and predicted well (black line) using the known parameters Ω, Γ, Ω_p and g.

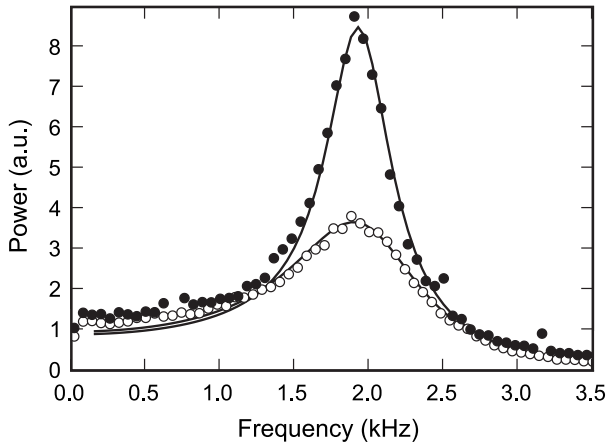

Figure 5.18: The measured power spectrum of a trapped water droplet for no modulation of the laser power (white circles) and modulation at $\Omega_p/2\pi \simeq 2\Omega/2\pi \simeq 3.9$ kHz (black circles). The peak is higher and narrower on the resonant condition, thus indicating parametric excitation. The solid line below the black circles is the predicted spectrum from equation 5.40.

To understand the implications of this experiment re-consider the beam shaping techniques of chapter 3 and the diffusivity of Brownian particles in section 4.2.2. In the context of optical tweezers sharing the beam with AODs or scanning mirrors obviously removes the potential felt by the particle for a significant portion of time, in which it could diffuse (due to Brownian motion) out of the tweezers' influence once the trap returns. So such systems must be carefully designed depending on the number of trap sites, size of particles, and optical power used. When splitting the beam this problem does not arise due to the

constant potential, but the peak power at each individual trap site is reduced.

Now consider the optical tweezing of aerosols which have been shown to behave as under-damped oscillators, with the potential to be parametrically excited. In such a system if the laser is modulated with an amplitude greater than twice the damping ratio, $g > 2\Gamma/\Omega$, then the system becomes unstable. One immediately realises that should the beam shaping method not be carefully considered, the optical trap can catastrophically fail.

5.7 Conclusion

The parameters governing the dynamics of optically trapped aerosols have successfully been described and experimentally investigated. It has been shown that there is no instability induced by crossing through the critically damped regime leading to the conclusion that the phenomena seen are due to the optical potential of the trapping laser. The investigation has provided results extending the boundaries of precise studies of Brownian motion in optical tweezers into a new damping regime.

The science has already been applied to demonstrate the possibility of using Brownian motion to precisely size aerosol droplets with relatively inexpensive apparatus. The apparatus allows sizing to a greater precision than through video microscopy, works at smaller size regimes than CERS does, and should work for arbitrarily small particles as long as they can be trapped. The low dynamic viscosity of air, the inclusion of inertial terms in the Langevin, and measuring the viscous damping in frequency space negate the need for *a priori* system calibration, making the process simple. I have not perfected the technique so there is potential for further increases in precision by using the more advanced techniques and apparatus.

It is hoped these results will provide researchers with a new understanding of an old tool for studies in both fundamental and applied science, providing a rich playground of study in the under-damped regime.

From the Langevin equation it is seen that there are only four processes providing forces that give rise to droplet position fluctuations. There is Brownian white noise, friction, inertia, and the optical force. Transferring from over- to under-damped dynamics does not inhibit the stability of the system yet there is clear size dependence with which the droplets fall from the trap. The logical conclusion is that the optical force must determine whether the droplet remains trapped or not and this will be discussed next, in chapter 6.

Chapter 6

Optical Trap Modelling

As mentioned at the end of the previous chapter I would like to answer a specific question regarding the optical force on an optically tweezed liquid droplet. This is a very difficult task to carry out experimentally[316] and the standard technique is to computational model momentum transfer from focussed beam to particle.

From a purely scientific viewpoint modelling can increase the understanding of an experiment thus giving a more complete picture of the process. Practically, numerical simulations allow the interested party to explore many parameters sometimes faster than, or not possible through, experimentation. This way the technique's perimeters can be probed to see if the boundaries of the current experiment can be extended. Accurate modelling, when compared to experimental data, can also lead to the extraction of physical parameters not otherwise obtainable[287].

The modelling of optical forces is used extensively in the field of optical manipulation to understand, for example, force mapping[329] and optical binding[330]. In some cases the behaviour of colloids is so complex and counter-intuitive that the only way to explain what is observed is through highly complex simulations[331]. One of the best examples is the understanding of how optical forces affect the cellular matrix. Changes in the elasticity of this matrix are directly related to stages of cancer within individual cells[332]. As shown the optical trapping of aerosols pushes the technology to its limits so the modelling of the optical forces involved may act as a method for testing the theories at their limits.

As with most modelling, symmetry within the system simplifies the mathematics. A sphere in an axially symmetric beam is probably the simplest of formulations, with a large amount of the constituent work already available. Should one like to model the trapping of non-spherical objects then the computation becomes more complex with the

T-matrix approach the most favoured method. Once the T-matrix has been calculated for a given object it need not be calculated again for every orientation of the object in the beam, thus making it rather advantageous. Nieminen *et al.*[333] have used this approach to code an 'optical tweezers computational toolbox' freely available for use[334].

The principle problems with many of the approaches available are the over-complexity (mine is a relatively simple problem), their inappropriateness for the size scale I am looking at, and the lack of a description of the true trapping beam profile, as I will explain later. A nice introduction to the inadequacies are given by Viana *et al.*[317]. The microdroplets I am studying are ≥ 1 μm in radius so the force calculation lies above the Rayleigh regime and to a first approximation I will approach the description of the modelling by using the geometrical optics (GO) model. It will show that by studying airborne objects the physics is really being pushed and that simple models, and indeed some of the more complex ones, cannot deal with the system under study.

I shall show how and where geometrical optics breaks down before moving onto a model that uses an integral representation of focussed light crossing refractive index interfaces and an exact form of plane wave scattering from spheres.

The principle aim of my numerical modelling investigation is to see if the isolated physics of optical forces leads to the phenomena observed in experiments and to see how far the boundaries of my techniques can be pushed. I will begin by restating the experimental observations already discussed;

1. As trapping laser power increases so does the height above the water layer or coverslip that the droplet is trapped.

2. With further increases of power the droplet is lost from the trap. This does not always occur and is more pronounced for smaller droplets.

3. After first capture, the droplet can undergo significant growth or evaporation coupled with large axial oscillations. These oscillations can occur well after capture but are far slower.

4. There is a linear dependence of 'captured' droplet radius with trapping power.

The boundaries I would like to determine and push are

- the range of particle refractive indices it is possible to trap,

- the limits on radii of particles that can be trapped with the current apparatus.

Fortunately my system is highly symmetric and almost complete solutions already exist in the literature. I will test both GO and a more rigorous full wave approach. Although the more rigorous theory is already described in literature no computer code is readily available and modifications must be made to suit my problem.

As noted earlier the forces exerted on spheres are decomposed into two directions, lateral and axial (figure 2.1). That is the direction perpendicular to and crossing the beam propagation axis, and the direction lying on the beam propagation axis respectively. To fully understand and interpret the results of this chapter one must familiarise oneself with the type of results output from the simulations and so I shall briefly discuss the topic here.

The simulations programmed in MATLAB calculate, for a given point on one of the two axes described above, the efficiency with which momentum is transferred to the object, Q, and hence, through equation 2.5, the force, F, that is exerted on it. I am interested in observing how force varies with position along the axis and as such output force curves that are either a function of lateral, or axial displacement. From these force curves several parameters can be taken or calculated that describe the system under study and are illustrated in figure 6.1.

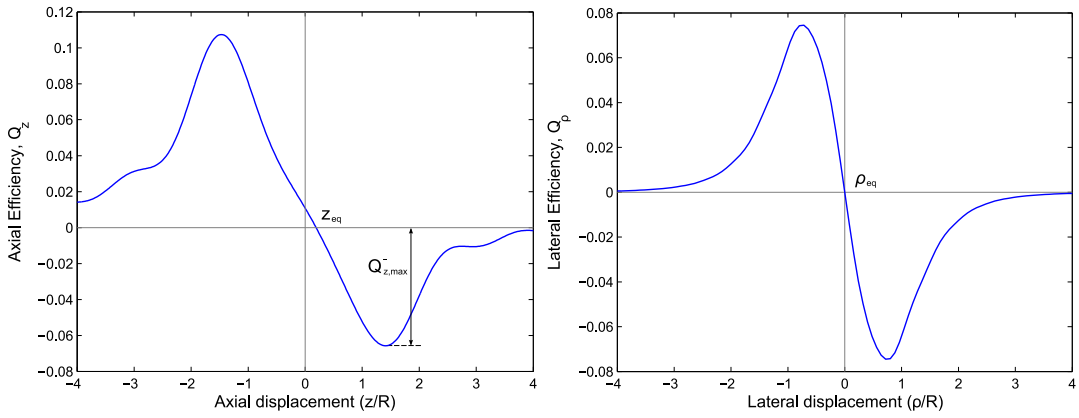

(a) (b)

Figure 6.1: (a) Axial efficiency, Q_z, as a function of axial displacement. The axial equilibrium position, z_{eq}, occurs where the curve crosses y = 0 with negative gradient, $Q^{-}_{z,max}$ quantifies the traps axial strength. (b) Lateral efficiency, Q_ρ, as a function of lateral position. The lateral equilibrium position, ρ_{eq}, occurs where the curve crosses y = 0 with negative gradient. For (a) and (b) the gradient of the curve at z_{eq} and ρ_{eq} are proportional to the axial and lateral trap stiffness, κ_z and κ_ρ respectively.

An object placed at a point where it experiences zero total force and is surrounded (within a certain proximity) by a negative gradient is said to be in *equilibrium*. Should the object be displaced the local gradient will produce a restoring force back toward this equilibrium position. In figures 6.1(a) and 6.1(b) these positions, z_{eq} and ρ_{eq}, are the axial and lateral

equilibrium positions respectively.

Now consider solely the axial force, as outlined in chapter 2 to achieve a single beam gradient force trap the force in the negative axial direction must overcome that along the beam propagation direction. If this is accomplished then the force curve will at some position become negative, hence allowing a point of zero force and negative gradient to exist. The maximum magnitude of this negative force, $Q^{-}_{z,max}$, is a good measure of the optical trap's axial strength[335], with its sign indicating whether a stable equilibrium position exists or not.

A quantity of interest to calculate would be the volume which a particle needs to enter before it becomes trapped. This volume extends between the maximum and minimum force points in the axial and lateral directions simultaneously. Its calculation, however, is complex and will be discussed in section 6.3.5.

Finally the trap's axial and lateral stiffness is proportional to the gradient of the force curves at their equilibrium position, which for the lateral case, assuming symmetry, is at zero. The trap stiffness, κ, is related to the efficiency, Q, by

$$\kappa = -\frac{n_m P}{c}\frac{\partial Q}{\partial s}. \tag{6.1}$$

where P is the trapping power, n_m is the medium's refractive index, c is the speed of light and s is either z or ρ for axial and lateral respectively.

During the discussion I shall look at the force curves alone and also results that are determined from many such curves where the parameters have been varied.

Ideally I want to model the forces on a microdroplet trapped near the focus of a beam given only the properties readily known. In figure 6.2 a laser beam of wavelength λ, waist w, is incident upon the back aperture of an objective lens of focal length f, aperture ρ and focussed to the diffraction limit at a converging angle of θ_0, normally quantified in terms of numerical aperture, $\mathrm{NA} = n_m \sin\theta_0$.

With this problem in mind I will now describe the theories behind a rigorous approach to geometrical optics, an integral representation of a focussed beam, and the scattering of light by spheres for radii approximately equal to the wavelength.

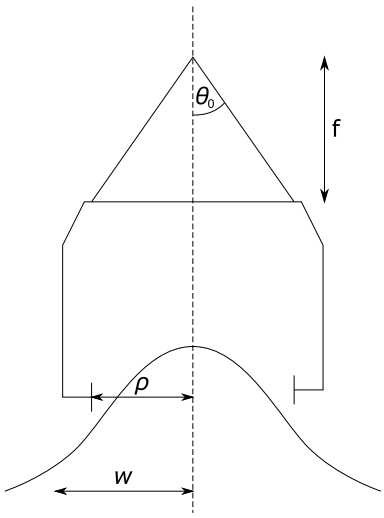

Figure 6.2: System setup for focussing a beam of waist w through a lens of focal length f, and back aperture of radius ρ and NA $= n_m \sin\theta_0$.

6.1 More rigorous Geometrical Optics (GO)

In chapter 2 I reviewed a hand-waving definition of geometrical optics but here I will be slightly more rigorous. Figure 6.3 shows the conventions used in the geometrical optics approach of the interaction of a single ray of light with a sphere.

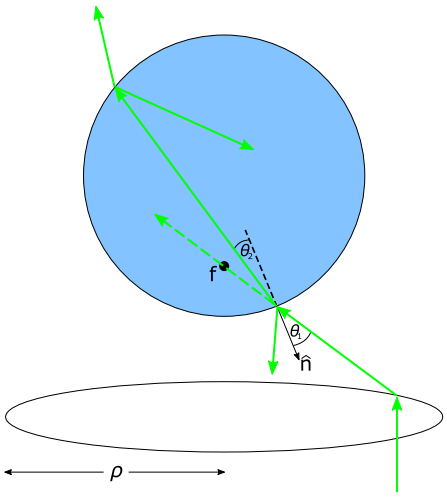

Figure 6.3: Geometry of the system considered when calculating the force on a dielectric sphere in the ray optic regime. θ_1 is the angle of incidence, θ_2 is the angle of refraction, $\hat{\boldsymbol{n}}$ is the unit normal vector, f is the focal point and ρ is the radius of the objective back aperture (adapted from Svoboda and Block[24]).

A beam with converging rays from $0 \rightarrow \theta_0$ will have rays entering the sphere with an angle

of incidence, θ_1, and resulting angle of refraction, θ_2, given by

$$\theta_1 = \arcsin \frac{d_\perp}{R} \quad \text{and} \quad \theta_2 = \arcsin \frac{\sin \theta_1}{m}. \tag{6.2}$$

where R is the sphere radius, $m = n_p/n_m$, the ratio of particle and medium refractive indices, and $\boldsymbol{d}_\perp$ is a vector defined to be the projection of the sphere position along the direction perpendicular to a given ray, $\hat{\boldsymbol{r}}(\theta, \phi)$ such that,

$$\boldsymbol{d}_\perp = \boldsymbol{d} - (\hat{\boldsymbol{r}} \cdot \boldsymbol{d})\, \hat{\boldsymbol{r}}, \tag{6.3}$$

where $\boldsymbol{d}$ is the position of the sphere and $d_\perp$ has magnitude

$$d_\perp(\theta, \phi) = \sqrt{\left(1 - \sin^2\theta \sin^2\phi\right) \rho_d^2 + \sin^2\theta z_d^2 - \sin 2\theta \sin\phi \rho_d z_d}. \tag{6.4}$$

where z_d and ρ_d are the sphere position in cylindrical coordinates.

In equation 2.3, I defined the force on a sphere due to a single ray. This force was directed perpendicular and parallel to the direction of the ray's propagation, $\hat{\boldsymbol{r}}$ and now needs to be summed over all rays, taking into account the beams Gaussian nature and the Abbe sine condition. The Abbe sine condition is best defined with the aid of figure 6.4

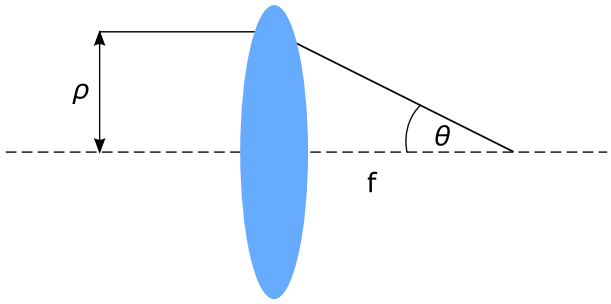

Figure 6.4: Definition of parameters in an aplanatic imaging system. ρ is the hieght at which a ray enters the system, θ is its converging angle from a lens of focal length f. Adapted from Richards and Wolf[336].

According to the sine condition the emergent ray exits the imaging system at the same height the corresponding ray entered the system such that

$$\rho = f \sin\theta, \tag{6.5}$$

with f being the focal length of the system[336].

Now consider an infinitesimally thin annulus of beam has been focussed by the objective.

The power, dP, contained in the solid angle, $d\Omega$, subtended by the beam is

$$dP = I_0 e^{\frac{-2\rho^2}{w^2}} \rho d\rho d\phi, \tag{6.6}$$

where I_0 is the on-axis beam intensity. Combining this with the Abbe sine condition, the power contained in a thin annulus of beam focussed by an aplanatic imaging system with incident intensity I_0 is

$$dP = I_0 e^{\frac{-2f^2}{w^2}\sin^2\theta} f^2 \cos\theta \sin\theta d\theta d\phi. \tag{6.7}$$

As mentioned, equation 2.3 gives the force components due to a single ray, but more accurately the components are $\Lambda^{\parallel,\perp} = \frac{1}{2}\left(\Lambda^{\parallel,\perp}_{TE} + \Lambda^{\parallel,\perp}_{TM}\right)$, where

$$\Lambda^{\parallel}_{\alpha} = 1 + r_\alpha \cos 2\theta_1 - t^2_\alpha \frac{r_\alpha \cos 2\theta_1 + \cos(2\theta_1 - 2\theta_2)}{1 + r^2_\alpha + 2r_\alpha \cos 2\theta_2}, \tag{6.8}$$

and

$$\Lambda^{\perp}_{\alpha} = r_\alpha \sin 2\theta_1 - t^2_\alpha \frac{r_\alpha \sin 2\theta_1 + \sin(2\theta_1 - 2\theta_2)}{1 + r^2_\alpha + 2r_\alpha \cos 2\theta_2}. \tag{6.9}$$

Here r_α and t_α are the Fresnel reflection and transmission coefficients[309] for both $\alpha = TE$ and $\alpha = TM$ modes.

Finally, the efficiency with which momentum is transferred by a ray of power dP and direction $\hat{\boldsymbol{r}}(\theta, \phi)$, first determined by Roosen[117], is;

$$dQ = \left(\Lambda^{\parallel}\hat{\boldsymbol{r}} + \Lambda^{\perp}\frac{\boldsymbol{d}_\perp}{d_\perp}\right)\frac{dP}{P}. \tag{6.10}$$

Integrating 6.10 over $d\Omega$ gives the overall efficiency for the whole beam which is a sum of two components $\boldsymbol{Q} = \boldsymbol{Q}_\parallel + \boldsymbol{Q}_\perp$ and can be easily converted to the force, $\boldsymbol{F}$, using equation 2.5. The force will be broken into the axial and lateral components from the beams perspective, so the axial component is given by[337]

$$Q^{\parallel}_z = \frac{2\gamma^2}{\pi A}\int_0^{\theta_0} \sin\theta\cos^2\theta e^{\frac{-2\rho^2}{w^2}} d\theta \int_0^{2\pi} \Lambda^{\parallel}(d_\perp) H(R - d_\perp) d\phi, \tag{6.11}$$

and

$$Q^{\perp}_z = \frac{2\gamma^2}{\pi A}\int_0^{\theta_0} \sin\theta\cos\theta e^{\frac{-2\rho^2}{w^2}} d\theta \times \int_0^{2\pi} \frac{\Lambda^{\perp}(d_\perp)}{d_\perp}\left(z_d \sin^2\theta - \frac{1}{2}\rho_d \sin 2\theta \sin\phi\right) H(R - d_\perp) d\phi. \tag{6.12}$$

Similarly the lateral efficiency is given by

$$Q_{\rho}^{\parallel} = \frac{2\gamma^2}{\pi A}\int_0^{\theta_0} \sin^2\theta\cos\theta e^{\frac{-2\rho^2}{w^2}}d\theta \int_0^{2\pi} \sin\phi\Lambda_{\parallel}(d_{\perp})H(R-d_{\perp})d\phi, \tag{6.13}$$

and

$$Q_{\rho}^{\perp} = \frac{2\gamma^2}{\pi A}\int_0^{\theta_0} \sin\theta\cos\theta e^{\frac{-2\rho^2}{w^2}}d\theta \times \int_0^{2\pi} \frac{\Lambda_{\perp}(d_{\perp})}{d_{\perp}}\left[\rho_d\left(1-\sin^2\theta\sin^2\phi\right) - \frac{1}{2}z_d\sin 2\theta\sin\phi\right]H(R-d_{\perp})d\phi. \tag{6.14}$$

where H is the Heaviside step function. Before calculating the forces predicted by geometrical optics I need to discuss its shortcomings.

Figure 6.2 does not accurately describe the trap I wish to model nor does geomertical optics accurately describe the interaction of the light and sphere, for several reasons. Firstly, the NA, hence the opening angle θ_0, of optical tweezers is large and the paraxial assumption ($\sin\theta \simeq \theta$) is no longer applicable. For highly convergent beams the focus is not Gaussian but rather governed by an integral representation due to the electromagnetic diffraction within the optical system[336,338]. Also, as the beam is focussed into a chamber it must pass through a coverslip. The interface created by this glass slide and trapping medium (usually water) creates a mismatch in refractive index through which the beam is focussed. This discontinuity introduces spherical aberration into the focussed beam and so can only be fully described using a full wave analysis.

Secondly, the interaction of a plane wave with a sphere where $R \simeq \lambda$ is more challenging to describe than by constructing the problem as a beam of many single rays passing through a sphere acting as a lens, as in geometrical optics. The description really must take into account diffraction. There is an analytical solution to Maxwell's equations for the scattering of a plane light wave by a single sphere for any ratio of radius to wavelength. The solution was independently developed by Mie, Debye, and Lorenz around the turn of the 20th century but has been historically referred to as 'Mie theory' or 'Mie scattering' since and shall be done so here[339].

Thirdly, there is something intuitively wrong with the wavelength independence of geometrical optics. The focal waist and scattering of light by colloidal particles is known experimentally to be wavelength dependent so surely a theory of optical tweezers should also be wavelength dependent. An additional complexity arises from the proximity of reflecting surfaces which can cause 'reverberations'[317] of light that significantly change the interaction. Finally, a true description of the physics at play must traverse the full range of applicability from Rayleigh scattering to geometrical optics.

6.2 Mie scattering and Richards and Wolf theory

I will first describe the tight focussing of a beam using the integral representation developed by Richards and Wolf[336,338] and then give a solution that describes light scattering from spheres.

6.2.1 Richards and Wolf theory

A Gaussian laser beam with plane wavefronts entering the back aperture of a lens is described by

$$\boldsymbol{E}_{\text{obj}}(\rho, z) = E_{\text{obj}} e^{ik_0 z} e^{-\rho^2/w^2} \hat{\boldsymbol{\epsilon}}, \tag{6.15}$$

where $k_0 = 2\pi/\lambda_0$, z is the axial direction, ρ is the lateral direction, and $\hat{\boldsymbol{\epsilon}}$ is a unit vector along the wave propagation direction.

When focussed into a medium of refractive index n_g, in my case glass, the beam will occupy a conical region in space governed by the angle of convergence θ_0, and the azimuthal angle φ. This beam can be thought of as a superposition of plane waves and given by an integral representation of electromagnetic diffraction described by Richards and Wolf[336]. The electric field in glass is therefore

$$\boldsymbol{E}_{\text{glass}} = E_0 \int_0^{2\pi} \int_0^{\theta_0} \sin\theta_g \sqrt{\cos\theta_g} e^{-\gamma^2 \sin^2\theta_g} e^{-i\boldsymbol{k}\cdot\boldsymbol{r}_f} e^{i\boldsymbol{k}\cdot\boldsymbol{r}} \hat{\boldsymbol{\epsilon}}'(\theta, \varphi) d\theta d\varphi, \tag{6.16}$$

where

$$E_0 = -i \frac{n_g f}{\lambda_0} T_{\text{obj}} E_{\text{obj}}, \tag{6.17}$$

and θ_0 is the opening angle of the focussed beam given by the NA of a lens, $\theta_0 = \arcsin(\text{NA}/n_g)$, n_g is the refractive index of glass, θ_g is the half-cone angle in glass, T_{obj} is the transmission of the objective, E_{obj} is the electric field magnitude at the objective lens back aperture, $\gamma = f/w$ and f, ω and r_f are defined in figure 6.5. $\hat{\boldsymbol{\epsilon}}'(\theta, \varphi)$ rotates the plane waves to occupy all angles from 0 to θ_0 and all φ using a rotation by Euler angles[308,309] $(\varphi, \theta_g, -\varphi)$. It should be noted that within this chapter the NA of a lens infers information about the opening angle of the cone of focus exterior to and immediately before any interfaces only.

This is the classic representation of a beam focussed to a point, $\boldsymbol{r}_f$, however, my system differs with two interfaces between exit from the lens and reaching the focal point as shown in figure 6.5. So, the plane wave components of equation 6.16 each refract at the interfaces at $z_1 = -h$ and $z_2 = -h + \Delta h$. From Snell's law the angle of refraction in the water layer $\theta_w = \arcsin(\sin\theta_g / N_1)$ and the angle of refraction in air $\theta_a = \arcsin(\sin\theta_a / N_w)$ where

$N_1 = n_w/n_g$ and $N_2 = n_a/n_w$ are the relative refractive indices of the glass-water and water-air interfaces respectively.

When the opening angle of the converging beam is larger than the critical angle for the ratio of the glass to air refractive indices, the NA of the beam is effectively reduced to $\theta_0 = \arcsin(N_1 N_2)$.

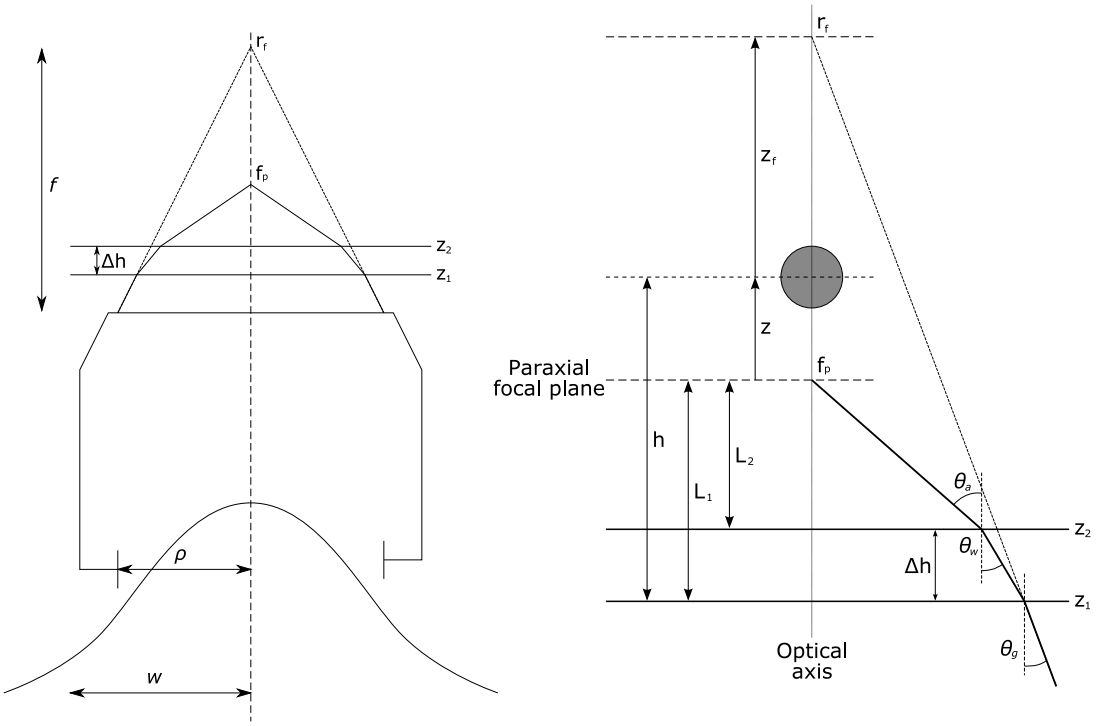

Figure 6.5: Illustration of the optical system and its parameters for my experiments and computational modelling. Left) A beam of wasit w enters an objective lens of focal length f with a back aperture of radius ρ. It is focussed to a point f_p having propagated through two mismatched refractive index interfaces, z_1 and z_2, such that the thickness of the middle medium is Δh. If neither interface existed then the light would be focussed to point r_f. Right) Expanded view of the focal region of the microscope objective to the left. Light is incident on the first interface, z_1, at an angle θ_g and refracted to an angle θ_w. It is then incident on the second interface z_2, a distance Δh away, at an angle θ_w where it is refracted to an angle θ_a and focussed to its paraxial focus point f_p. The height of the paraxial focus above the second and first interfaces is L_2 and L_1 respectively. The droplet is trapped a distance h above the first interface, z above the paraxial focus and z_f below the point r_f. In my experimental system of chapter 5 and the airborne system I model in this chapter the first interface is between glass and water, and the second interface is between water and air.

The beam representation must therefore include the effects of propagation through media of stratified refractive index[309]. In this way the focussed beam in the third medium, air,

is described by

$$\boldsymbol{E}_{\text{air}} = E_0 \int_0^{2\pi} \int_0^{\theta_0} T(\theta_g) \sin\theta_g \sqrt{\cos\theta_g} e^{-\gamma^2 \sin^2\theta_g} e^{-i(k_{gz}-k_{wz})h} e^{-i\boldsymbol{k}\cdot\boldsymbol{r}_f} e^{i\boldsymbol{k}_a\cdot\boldsymbol{r}} \hat{\boldsymbol{\epsilon}}'(\theta_a, \varphi_a) d\theta d\varphi, \tag{6.18}$$

where $(k_{gz} - k_{wz})\, h$ takes into account beam propagation in the glass slide up to the first interface and $k_a = n_a k_0$ is the wavenumber in air and each plane wave amplitude is multiplied by its respective Fresnel transmission coefficient

$$T(\theta_g) = T_1(\theta_g) T_2(\theta_g) = \frac{2\cos\theta_g}{\cos\theta_g + N_1 \cos\theta_w} \frac{2\cos\theta_w}{\cos\theta_w + N_2 \cos\theta_a}. \tag{6.19}$$

The effect of the additional factors in equation 6.18 over equation 6.16 and the geometry of figure 6.5 introduces a spherical aberration that deforms the wavefront preventing the diffraction limited focussing to the point $\boldsymbol{r}_f$. This aberration is quantified in terms of an aberration function as will be shown later in section 6.2.3.

Having focussed the beam through two mismatched refractive index interfaces, the height of the paraxial focal plane above the water layer is found from the objective displacement, X, through

$$L = \left(X \frac{n_w}{n_g} - \Delta h \right) \frac{n_a}{n_w}. \tag{6.20}$$

as mentioned in figure 5.4.

Using the work of Török and Varga[309] on beam propagation through stratified media and equation 6.18 I can calculate the profiles of beams focussed in my system and compare them to the ideal beam assumed in most cases, hopefully giving some insight into the physics.

Figure 6.6 displays the yz-plane beam profiles for beam focussing in water, through a glass-water interface, and through glass-water-air interfaces. The axial displacement zero point is the position that the paraxial focus, $\boldsymbol{r}_f$, would exist at when no refractive index interfaces are in the system.

The beam focussed in water with no preceding interfaces varies smoothly at the focus compared to those focussed in water and air having first travelled through glass coverslips. In particular the beam focussed to a point in air has a large number of oscillations in intensity along the axial plane. Could this interact with the particles in a non-trivial manner?[340] Particles that are large relative to this may not 'see' the oscillations while small particles could be trapped at more than one of the 'hot-spots'. The colour scale remains the same for all plots so the maximum intensity is less in an airborne tweezers than for others given the same input power.

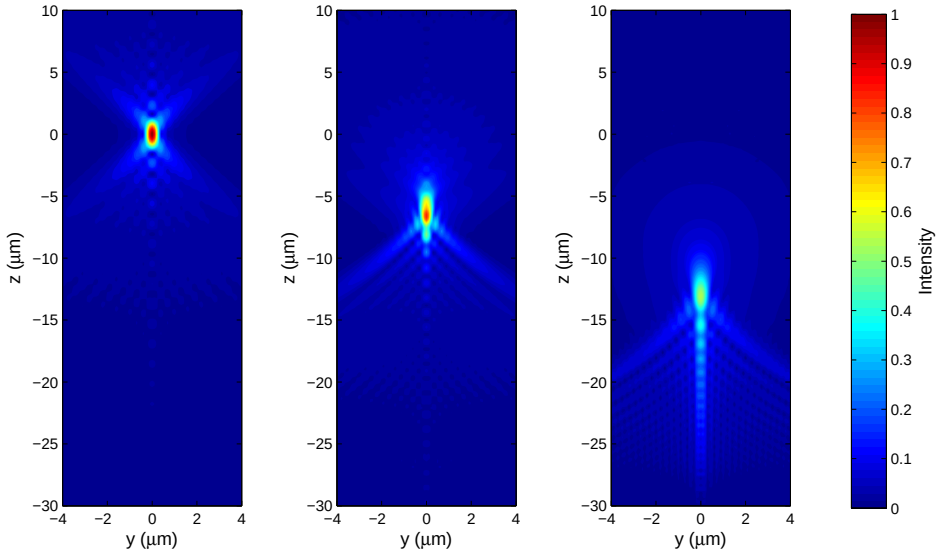

Figure 6.6: Profile of a focussed 532 nm Gaussian beamstaken from a y-z slice through the beam axis. (a) The beam is focussed into water ($n_w = 1.33$). (b) The beam is focussed into water having crossed a glass ($n_g = 1.517$) to water ($n_w = 1.33$) interface after the lens. (c) The beam is focussed into air ($n_a = 1.00$) across glass ($n_g = 1.517$) to water ($n_w = 1.342$) and water to air interfaces. The objective displacement $X = 40$ μm, the water layer is 10 μm thick, $\gamma = 1$ and $\theta_0 = 41.23°$. Zero on the axial axis is the position of the paraxial focus had there been no interfaces.

Having described beam focussing more realistically, specifically for stratified media, I will move onto the scattering of light by the particles I wish to model in these beams.

6.2.2 Mie scattering

The development of the Mie theory of scattering was a means to an ends of understanding one of the classic questions of science: Why is the sky blue? I will not attempt to delve into the history of this period as a far more complete one is included in Kerker[339]. Mie approached the problem from a slightly different perspective in the hope of explaining the colours of scattering from gold colloidal particles in a water suspension. I will not attempt to derive the Mie theory from first principles as a lovely version is found in Bohren and Huffman[341] but I will include the results that are important to my needs.

A plane wave incident on a spherical particle results in a scattered electric field that is dependent on the Mie scattering coefficients a_n and b_n[341] where n appears because of the Legendre polynomials in the solution which have n degrees. To simplify the following the

Riccati-Bessel functions are introduced as;

$$\psi_n(kr_s\xi) = kr_s J_n(kr_s) \quad \text{and} \quad \xi_n(kr_s) = kr_s h_n^{(1)}(kr_s), \tag{6.21}$$

where k is the wavenumber, r_s is from the spherical coordinates system and $h_n^{(1)} = J_n + iy_n$ is the spherical Hankel function with the spherical Bessel functions J_n and y_n. Using these the scattering coefficients are

$$a_n = \frac{m\psi_n(m\xi)\psi_n^{'}(\xi) - \psi_n(\xi)\psi_n^{'}(m\xi)}{m\psi_n(m\xi)\xi_n^{'}(\xi) - \xi_n(\xi)\psi_n^{'}(m\xi)} \tag{6.22}$$

and

$$b_n = \frac{\psi_n(m\xi)\psi_n^{'}(\xi) - m\psi_n(\xi)\psi_n^{'}(m\xi)}{\psi_n(m\xi)\xi_n^{'}(\xi) - m\xi_n(\xi)\psi_n^{'}(m\xi)} \tag{6.23}$$

where $\xi = n_m k_0 R$ is the size parameter and $m = n_p/n_m$, the relative refractive index of particle to medium.

The previous two sections have given all the necessary background to allow me to move onto how the force in optical tweezers is calculated.

6.2.3 Force calculation

To calculate the force I follow the full electromagnetic approach where the Maxwell stress tensor is integrated over the surface of the object;

$$\langle F \rangle = \left\langle \oint_S \hat{\boldsymbol{n}} \cdot \boldsymbol{T} dS \right\rangle, \tag{6.24}$$

where $\hat{\boldsymbol{n}}$ is the surface normal and $\boldsymbol{T}$ is the electromagnetic stress tensor. Due to system symmetry and also momentum conservation the force simplifies so the surface is at infinity, thus giving

$$F = \lim_{r\to\infty} \left(-\frac{r}{2} \int_{S_r} \boldsymbol{r} \left(\epsilon E^2 + \mu_0 H^2 \right) \right), \tag{6.25}$$

where $\boldsymbol{E} = \boldsymbol{E}_{inc} + \boldsymbol{E}_{scat}$ with equivalents for the magnetic field[337].

An analytical solution to this can be complicated, even for spheres, as can be seen in Barton *et al.*[342]. An exact partial wave approach must be taken so the effects of the refractive index interfaces can be taken into account which cause the field of the beam to behave as described by equation 6.18 rather than equation 6.16 (i.e. with spherical aberration). I will take the simpler approach described by Mazolli *et al.*[337] where the vector electric and magnetic fields are given in terms of scalar Debye potentials, also known as Hertz vectors[168]. The optical forces are calculated by following Farsund and Felderhof[343], who

derive force, torque and absorbed energy for an object of arbitrary shape and material given the Debye potentials for the incident and scattered fields. The results of Farsund and Felderhof[343] also match those of Barton *et al.*[342] with slight notation changes.

Debye, as early as 1909, calculated the force on a sphere due to an incident plane wave, and here the result is generalised to a focussed beam. First, the Debye potential for a single plane wave is[337]

$$\Pi^E_{\boldsymbol{k}(r,\theta,\varphi)} = \frac{E_0}{k}\sum_{j=1}^{\infty} i^{j-1} J_j(kr)\sqrt{\frac{4\pi\,(2j+1)}{j\,(j+1)}}\sum_{m=-j}^{j} e^{-i(m-1)\varphi_k} d^j_{m,1}(\theta_k) Y_{jm}(\theta,\varphi). \quad (6.26)$$

where J_j are the spherical Bessel function and Y_{jm} are the spherical harmonics. Using the matrix elements of finite rotations, also known as Wigner d functions[344,345], for rotation in the basis of spherical harmonics, the Debye potential for a focussed Gaussian beam made from a superposition of plane waves, whose field is represented by equation 6.18, is

$$\begin{aligned}\Pi^E_{inc}(r,\theta,\varphi) = \frac{E_0}{k}\int_0^{\theta_0} \sin\theta_k\sqrt{\cos\theta_k}\, e^{-\gamma^2\sin^2\theta_k}\sum_{j=1}^{\infty} i^{j-1} J_j(kr)\sqrt{\frac{4\pi\,(2j+1)}{j\,(j+1)}} \\ \times\sum_{M=-j}^{j} d^j_{m,1}(\theta_k) Y_{jm}(\theta,\varphi)\int_0^{2\pi} e^{-i\boldsymbol{k}\cdot\boldsymbol{r}_{\mathrm{f}}} e^{-i(k_{gz}-k_{wz})h} e^{-i(m-1)\varphi_k} d\varphi_k. \quad (6.27)\end{aligned}$$

Evaluating the integral over the azimuthal angle the incident Debye potential becomes

$$\begin{aligned}\Pi^E_{inc}(r,\theta,\varphi) = \frac{E_0}{k}\int_0^{\theta_0} \sin\theta_k\sqrt{\cos\theta_k}\, e^{-\gamma^2\sin^2\theta_k}\sum_{j=1}^{\infty} i^{j-1} J_j(kr)\sqrt{\frac{4\pi\,(2j+1)}{j\,(j+1)}} \\ \times\sum_{m=-j}^{j} d^j_{m,1}(\theta_k) Y_{jm}(\theta,\varphi) 2\pi\,(-i)^{m-1}\, e^{-ikz_f\cos\theta_k} e^{-i(k_{gz}-k_{wz})h} \\ \times J_{m-1}(k\rho_R\sin\theta_k) e^{-(m-1)\varphi_f}. \quad (6.28)\end{aligned}$$

From figure 6.5 the relative locations of the planes gives $z_f = \frac{1}{N_1}\left(\Delta h + \frac{L_2}{N_2}\right) - L_1 - z$. Substituting this into the middle two exponents of equation 6.28 I derive the aberration function[308,309,317,346], Ψ, of my system to be

$$\Psi = k_0\left(-\left(\frac{n_g}{N_1}\Delta h + \frac{n_g}{N_1 N_2}L_2\right)\cos\theta_g + n_w\Delta h\cos\theta_w + n_a\,(L_2+z)\cos\theta_a\right). \quad (6.29)$$

The Debye potential for the scattered field is found through the incident fields interaction with a sphere and hence is dependent on Mie coefficient a_j and Hankel function $h^{(1)}_j$ of section 6.2.2 to be

$$\Pi^E_{inc}(r,\theta,\varphi) = -2\pi\frac{E_0}{k}\sum_{j=1}^{\infty}\sum_{m=-j}^{j} i^{j-m}G_{jm}(\rho_f,z_f)e^{-(m-1)\varphi_f}\sqrt{\frac{4\pi\,(2j+1)}{j\,(j+1)}} \times a_j h_j^{(1)}(kr)Y_{jm}(\theta,\varphi), \quad (6.30)$$

where

$$G_{jm} = \int_0^{\theta_0} T(\theta)\sin\theta\sqrt{\cos\theta}e^{-\gamma^2\sin^2\theta}d^j_{m,1}(\theta_a)J_{m-1}(k\rho\sin\theta_a)e^{i\Psi(z,\theta)}d\theta. \quad (6.31)$$

Similar expressions can be found for the magnetic field, H, using the Mie coefficient b_n.

The efficiencies are given for the lateral and axial components each with two separate contributions, one for the rate of removal of momentum from the incident beam, Q_e, and the other for minus the rate of momentum transfer to the scattered field, Q_s, so $Q^{\rho,z}_{tot} = Q^{\rho,z}_s + Q^{\rho,z}_e$. The forces are calculated for circularly polarised light but can equally but done for linear polarisations[346]. I will start with the axial component of the trapping efficiency given by[317,337,346,347];

$$Q^z_e = \frac{4\gamma^2}{AN_1N_2}\mathcal{R}\sum_{j=1}^{\infty}\sum_{m=-j}^{j}(2j+1)\,(a_j+b_j)\,G_{j,m}G'^*_{j,m} \quad (6.32)$$

and

$$Q^z_s = \frac{8\gamma^2}{AN_1N_2}\mathcal{R}\sum_{j=1}^{\infty}\sum_{m=-j}^{j}\left(\frac{\sqrt{j\,(j+2)\,(j-m+1)\,(j+m+1)}}{j+1}\left(a_ja^*_{j+1}+b_jb^*_{j+1}\right)\right. \times G_{j,m}G^*_{j+1,m} + \left.\frac{2j+1}{j\,(j+1)}ma_jb^*_j\left|G_{j,m}\right|^2\right). \quad (6.33)$$

The lateral efficiencies are

$$Q^\rho_e = \frac{2\gamma^2}{AN_1N_2}\mathcal{I}\sum_{j=1}^{\infty}\sum_{m=-j}^{j}(2j+1)\,(a_j+b_j)\,G_{j,m}\left(G^-_{j,m+1}-G^+_{j,m-1}\right)^* \quad (6.34)$$

and

$$Q^\rho_s = \frac{8\gamma^2}{AN_1N_2}\mathcal{I}\sum_{j=1}^{\infty}\sum_{m=-j}^{j}\frac{\sqrt{j\,(j+2)\,(j-m+1)\,(j+m+1)}}{j+1}\left(a_ja^*_{j+1}+b_jb^*_{j+1}\right) \times\left(G_{j,m}G^*_{j+1,m+1}+G_{j,-m}G^*_{j+1,-m-1}\right), \quad (6.35)$$

where A is the fraction of the beam power that enters the objective back aperture, to

account for overfilling, and the functions $G'_{j,m}$ and $G^{\pm}_{j,m}$ are defined as

$$G'_{jm} = \int_0^{\theta_0} T(\theta) \sin\theta \sqrt{\cos\theta} \cos\theta_a e^{-\gamma^2 \sin^2\theta} d^j_{m,1}(\theta_a) J_{m-1}(k\rho \sin\theta_a) e^{i\Psi(z,\theta)} d\theta. \quad (6.36)$$

and

$$G^{\pm}_{jm} = \int_0^{\theta_0} T(\theta) \sin\theta \sqrt{\cos\theta} \sin\theta_a e^{-\gamma^2 \sin^2\theta} d^j_{m\pm1,1}(\theta_a) J_{m-1}(k\rho \sin\theta_a) e^{i\Psi(z,\theta)} d\theta. \quad (6.37)$$

The analytical solutions for force found through Farsund and Felderhof[343] are converted to trapping efficiency, again through equation 2.5.

In the limiting case where $\Delta h = 0$ and $n_w = n_g$ the results return to those of Viana *et al.*[317] for a glass to water interface without an intermediate water layer. For $\Delta h = 0$ and $n_g = n_a = n_w$ and $X = 0$, I find the results of Mazolli *et al.*[337], and Neto and Nussenzveig[347] are matched.

The final crucial point concerns the computation of these equations. Rather than completing the sums in equations 6.32 to 6.35 to infinity it is useful to know that it is sufficient to sum over j up to $\xi_s + 4\xi_s^{1/3} + 2$, or its nearest integer, due to the convergence of the Mie scattering coefficients (Appendix A in Bohren and Huffman[341]).

Having introduced the theory and visualised the focussed beams I will move onto examining the outcome of applying the theories to 'normal' optical tweezers and then to my application.

6.3 Results and discussion

Ashkin observed that even with relatively loose focussing of a Gaussian beam, particles (with $m > 1$) always had the tendency to move toward the beam centre where they would reach a lateral equilibrium position. In exactly the same manner this occurs in airborne tweezing so its modelling is not of great importance. It is the axial efficiency and force curves, and the associated balance between gradient and scattering forces, that governs whether a particle is trapped or not. Although thw far more complex code has been written to calculate lateral efficiencies, it will be the axial direction I consider as it determines the unusual phenomena observed.

The results I present must be considered to be a set of typical examples that can be produced using my code and is by no means exhaustive. Now written, many questions can be asked and large areas of parameter space explored. This has already started with

collaborators in the Aerosol Dynamics group, headed by Dr Jonathan Reid. I also note that I have included several results pertaining to the optical tweezing of spheres in water, not a topic of my thesis, but as a means of comparison to indicate the large difference between these experiments and those in air.

6.3.1 Comparison of geometrical optics and Mie scattering

First I will make a comparison between the theoretical predictions of geometrical optics (GO) against those from Mie scattering. In this first instance I will neglect the effects of spherical aberration and show in figure 6.7 the axial trapping efficiency calculated through both theories when a 250 nm, 1 μm, and 5 μm silica sphere is trapped with 532 nm light in water. As described in the theory section there is a limit to the opening angle of the focussed light and hence NA of the system under study. For a beam focussed through a coverslip-water interface this limit $\theta_0 = \theta_c \simeq 62°$, thus NA $= 1.33 \sin\theta_c = 1.17$, and is the value used for this first test.

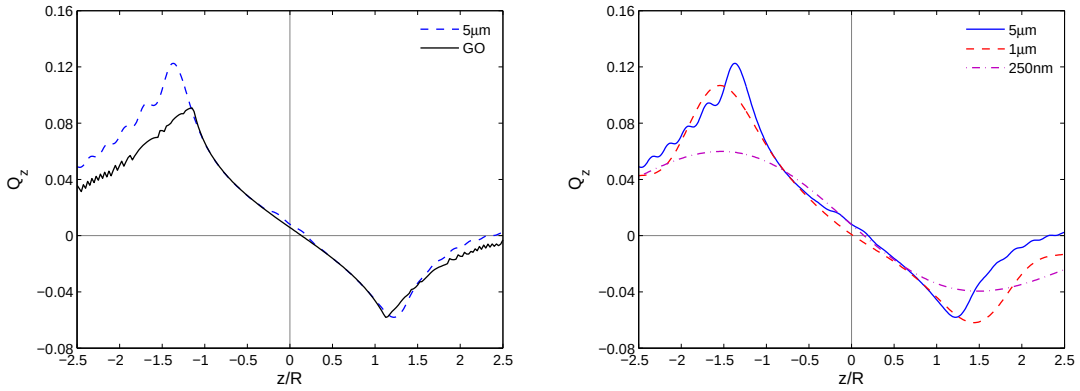

(a) (b)

Figure 6.7: Axial trapping efficiency calculated through GO and Mie theories when 250 nm, 1 μm, and 5 μm silica spheres ($n_p = 1.445$) are trapped with 532 nm light in a water medium ($n_m = 1.33$) with $\gamma = 1$ and $\theta_0 = 61.25°$ in a system like figure 6.2 with no refractive index interfaces. The four curves are plotted on two separate graphs for clarity. In (a) the black solid line is calculated through GO and the blue dashed line is calculated through Mie scattering. In (b) all curves are calculated with Mie scattering.

Clearly the prediction of geometrical optics disagrees with those of Mie scattering. However, GO stands up surprisingly well even for spheres with radii similar to the wavelength of trapping light. Testing the theory on a 5 μm sphere which is approaching the regime where GO should become applicable it is indeed a reasonable approximation except for the area closest to the paraxial focus and at the extremities.

The inaccuracies are hardly surprising considering the discussion of GO's limits made earlier. For the small spheres Mie scattering plays a dominant role that differs to simple ray optics and for the larger sphere the non-Gaussian beam focus plays the important role that GO cannot account for.

I will now test how applicable geometrical optics is when trapping objects in air. Here the NA's upper limit is reduced ($\theta_0 = \theta_c \simeq 41.2°$ therefore $NA \simeq 0.66$) and lends itself toward the paraxial approximation, hence GO. Yet the ratio of particle to medium refractive index is higher than in colloidal systems thus moving further into the applicability of Mie scattering. Figure 6.8 plots the axial efficiency for the same particles as figure 6.7 except the medium is now air ($n_m = 1.00$) and the particle is a water droplet ($n_p = 1.33$).

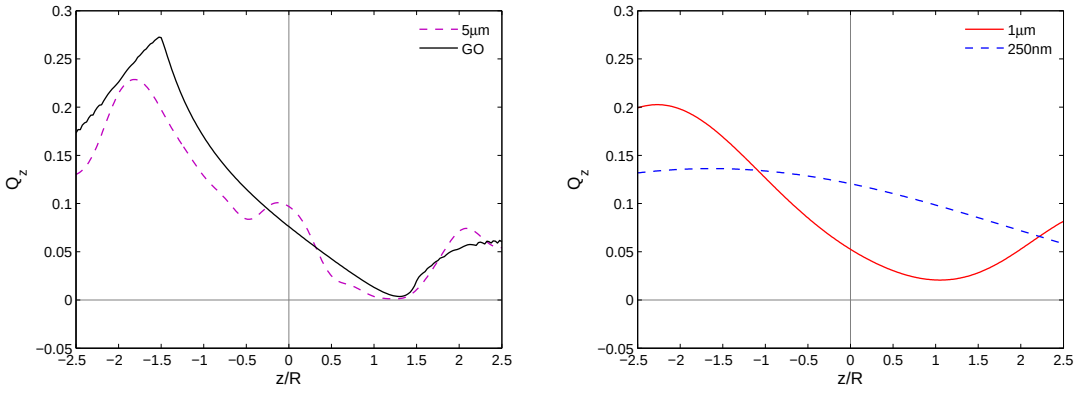

(a) (b)

Figure 6.8: Axial trapping efficiency calculated through GO and Mie theories for 250 nm, 1 μm, and 5 μm water droplets ($n_p = 1.342$) trapped with 532 nm light in air ($n_m = 1.000$) with $\gamma = 1$ and $\theta_0 = 41.23°$ in a system like figure 6.2 with no refractive index interfaces. The four curves are plotted on two separate graphs for clarity. In (a) the black solid line is calculated through GO and the purple dashed line is calculated through Mie theory. In (b) both curves are calculated with Mie theory.

The form of the geometrical curve remains similar to the previous example except with an absolute increase in efficiency. This is probably due to an increased scattering force component from the larger particle-medium refractive index contrast and reduction in NA. Clearly, GO predicts the droplet will 'just' not obtain an axial equilibrium position allowing it a brief reprieve in matching the more rigorous Mie theory. However, this disappears quite quickly when noting the drastic curve change as the forces on three sizes of spheres are computed using Mie scattering. The largest sphere, 5 μm, enters the beginning of the GO regime ($R \gg \lambda$), yet the theory completely fails to indicate the occurrence of a second minima, predicted by Mie theory.

It has been shown geometrical optics, although not highly accurate, can provide reasonable

predictions of the efficiencies of trapping colloidal particles in water, giving indications of what one would expect in real world systems. However, in the same manner it has been shown that GO is not an appropriate description of airborne tweezing with the wild variation as a function of size not predicted, and the inability to predict important features.

My next extension is where the GO description falls down, namely in the consideration of the relevance of spherical aberration for both colloidal and airborne systems. Only Mie theory can accommodate variations in phase wavefront profile so only this will be considered from now on.

Figure 6.9 plots the axial efficiency curves for 1 μm and 5 μm silica spheres trapped in a water medium when the aberration due to a single coverslip-water interface is and is not neglected.

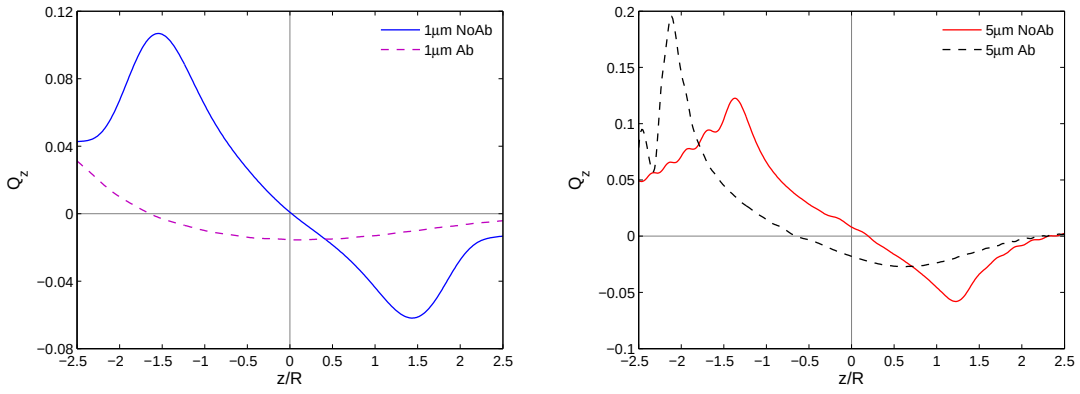

(a) (b)

Figure 6.9: Axial efficiency curves for 1 μm and 5 μm silica spheres ($n_p = 1.445$) trapped in water above a glass coverslip with and without the aberration induced by the refractive index interface of glass ($n_g = 1.517$) to water ($n_w = 1.33$) taken into account. The objective axial displacement $X = 35$ μm, $\gamma = 1$ and $\theta_0 = 61.25°$. (a) For a 1 μm sphere the blue solid line is without aberration and the purple dashed line with aberration. (b) For a 5 μm sphere the red solid line is without aberration and the black dashed line with aberration.

Spherical aberration clearly has a significant effect on optical trapping efficiency curves as expected[348,349]. There is a drastic difference between the axial efficiencies from aberrated and non-aberrated beams. The two main effects are a reduction in $Q^{-}_{z,max}$, reducing the trap's axial strength, and a decrease in axial equilibrium position, z_{eq}, so the spheres 'sit' lower in the trap relative to the beam's respective paraxial focal point.

It has been established that spherical aberration plays a major role in the physics describing optical tweezing, so it must be considered in my system (figure 6.5) where there

are two interfaces with mismatched refractive indices. The airborne tweezing geometry is especially interesting as the intermediate thin layer of water may smooth out the abrupt refractive index change that would otherwise exist. So, let us first repeat the previous figure for water droplets trapped in air above a coverslip and thin water layer; figure 6.10.

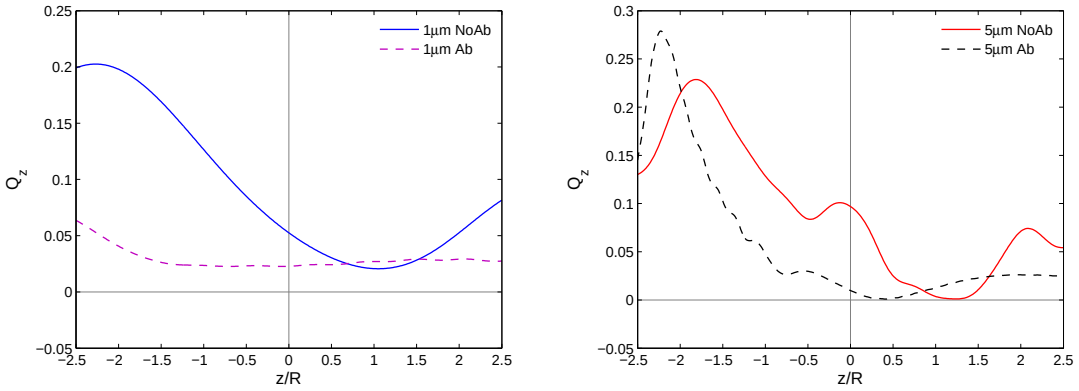

(a) (b)

Figure 6.10: Axial efficiency curves for 1 μm and 5 μm water droplets ($n_p = 1.342$) trapped in air ($n_a = 1.000$) above a glass coverslip ($n_g = 1.517$) and thin water layer ($n_w = 1.342$) as depicted in figure 6.5. The objective axial displacement $X = 40$ μm, the water layer is 10 μm thick, $\gamma = 1$ and $\theta_0 = 41.23°$. (a) For a 1 μm sphere the blue solid line is without aberration and the purple dashed line with aberration. (b) For a 5 μm sphere the red solid line is without aberration and the black dashed line with aberration.

The inclusion of spherical aberration in the description greatly affects the efficiency curves for airborne water droplets. There is a reduction in $Q^{-}_{z,max}$, reducing the trap's axial strength and for the large droplet a general 'smoothing' of the curve occurs with smaller local minima created. Figure 6.11, for the same system and objective displacement but with and without the water layer, shows a change in the axial curves indicating its significance and its necessary inclusion in the theory.

Hopefully the reader will now feel more comfortable with the optical forces and their effects. Having established the most appropriate model to use and the physics to include, I will now move on to trying to explain the phenomena observed, as recalled in the introduction to this chapter.

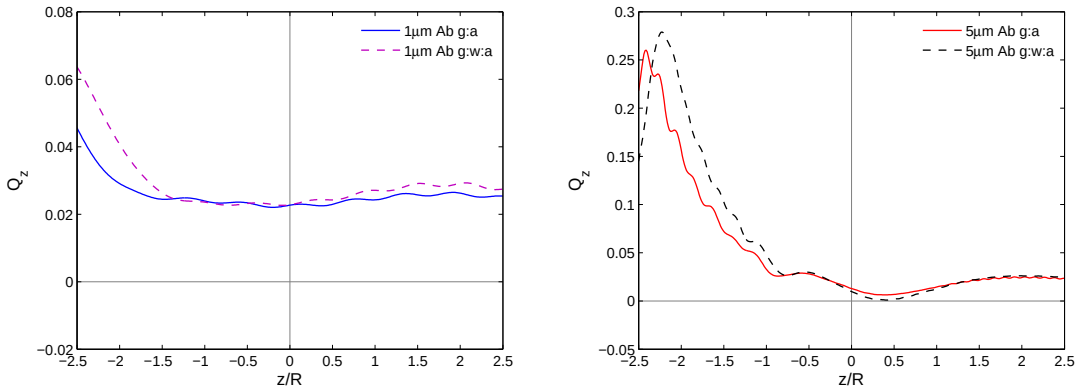

(a) (b)

Figure 6.11: Axial efficiency curves for 1 μm and 5 μm water droplets ($n_p = 1.342$) trapped in air ($n_a = 1.000$) above a glass coverslip ($n_g = 1.517$) with and without a thin water layer ($n_w = 1.342$). The objective axial displacement, $X = 40$ μm, $\gamma = 1$, $\theta_0 = 41.23°$ and when the thin water layer exists it is 10 μm thick. In (a) the blue solid and purple dashed curves are calculated without and with the thin water layer respectively. In (b) the red solid and black dashed curves are calculated without and with the thin water layer respectively.

6.3.2 Predicting experimental observations

All the previous theoretical results shown have neglected any particle buoyancy. For colloidal systems this is a reasonable approximation with the density of the trapped objects approximately that of the medium. Thus, there is only a multiplicative factor between efficiency and force graphs via equation 2.5 which allows the axial Q curves to be treated as scaled force curves. However, this is a very poor assumption when considering objects suspended in air with the large density contrast; for water droplets $\rho_{fluid} \simeq 1000\rho_{air}$. In order to fully appreciate what the theory predicts I must calculate the force experienced by the microsphere using equation 2.5 and subtract its weight. The droplet and system parameters from figure 6.10 including aberration is replicated with a trapping power of 10 mW to calculate the corresponding force curves in figure 6.12.

For the 1 μm, unlike the 5 μm droplet, the force plot has no significant effect on the properties deduced from the efficiency plot. The weight of the 5 μm droplet is comparable to the optical force so that an equilibrium position, z_{eq}, exists which was not deduced from the optical efficiency curve. I also note that $F^{-}_{z,max}$, the force equivalent of $Q^{-}_{z,max}$, is large, in fact comparable to $F^{+}_{z,max}$, making the trap far more axially symmetric.

The basics above have hopefully established an understanding of the physics in the system and how the results should be interpreted correctly. Now I will see if the theory can predict some of the behaviour observed during aerosol trapping experiments starting with points

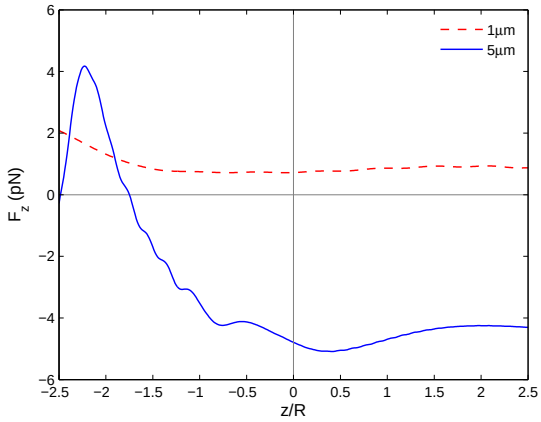

Figure 6.12: Axial force curves for 1 μm and 5 μm water droplets ($n_p = 1.342$) trapped in air ($n_a = 1.000$) above a glass coverslip ($n_g = 1.517$) and thin water layer ($n_w = 1.342$). The objective axial displacement, $X = 40$ μm, the water layer is 10 μm thick, $\gamma = 1$, $\theta_0 = 41.23°$. The red dashed line is for a 1 μm droplet and the blue solid line is for a 5 μm droplet.

one and two at the beginning of this chapter. In figure 6.13(a) I plot for a 4 μm water droplet, trapped in the experimental system depicted in figure 6.5, the predicted axial force curves for increasing trapping powers. Repeating for several droplet radii the height above the water layer a droplet is trapped, obtained from z_{eq}, can be plotted as a function of power as shown in figure 6.13(b).

Figure 6.13(a) successfully predicts two physical observations from experiments. As the trapping power increases the droplet's equilibrium position, z_{eq}, hence height above the underlying water layer, increases and with enough power eventually falls from the trap. The 2 μm, 3 μm and 4 μm droplets in figure 6.13(b) do not continue for higher powers as the droplet has no equilibrium position in its axial efficiency curve but the 5.5 μm droplet continues indefinitely. It is easy to understand that if an equilibrium position exists in the efficiency curves alone, then the droplet will always remain trapped. If no such position exists then the force may eventually lose its equilibrium position with power. This qualitatively explains my own results, figure 5.1, and by extension the power gradients of Knox *et al.*[279]. My results indicate that their measured gradients[279] are tangents to one area of the larger curves. With this enhanced understanding their suggestion of using power gradients as a tool for aerosol sizing applications could benefit.

Figure 6.13(b) may also explain why there is a linear dependence on captured droplet size as a function of power and why small droplets cannot be trapped at high powers (figure 4.6). The power gradients show that above certain powers, depending on droplet radius, no equilibrium position exists. Therefore, although a 'large' droplet may be trapped at relatively large powers, smaller droplets cannot be for the same power.

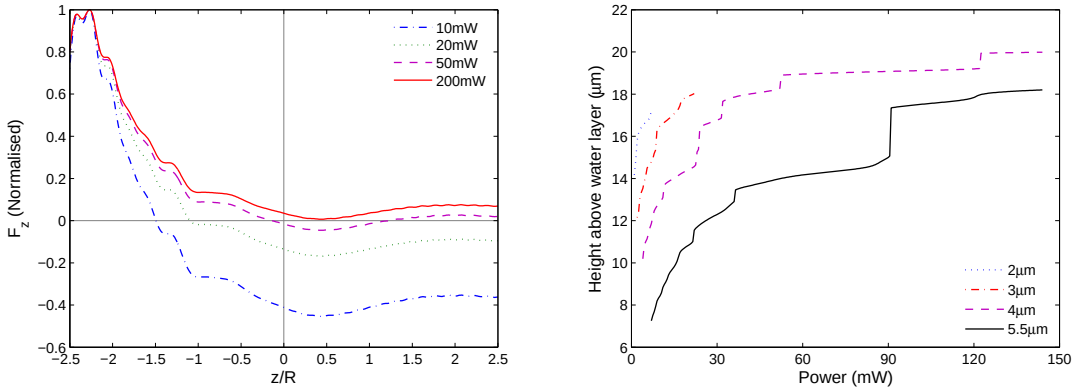

(a) (b)

Figure 6.13: (a) Variation of axial force for a 4 μm water droplet ($n_p = 1.342$) trapped in air ($n_a = 1.000$) at trapping powers of 10 mW (blue dot-dashed line), 20 mW (green dotted line), 50 mW (purple dashed line) and 200 mW (red solid line). The force for each power has been normalised to unity for clarity, as it is only the axial equilibrium position, z_{eq}, that is of conern. (b) Variation in height above the water layer droplets of radius 2 μm (blue dotted line), 3 μm (red dot-dashed line), 4 μm (purple dashed line) and 5.5 μm (black solid line) are trapped as a function of trapping power (power gradients of Knox *et al.*[279]). All but the 5.5 μm droplet's curve stop due to the loss of axial equilibrium position at high powers as in (a). The objective axial displacement, $X = 40$ μm, the water layer ($n_w = 1.342$) is 10 μm thick, $\gamma = 1$, $\theta_0 = 41.23°$ and the coverslip refractive index $n_g = 1.517$ for both (a) and (b).

A large parameter that governs the magnitude of the spherical aberration induced by the interfaces is the depth into the sample which the beam is focussed. For example, a lower focus has less aberration. In figure 6.14 the beam is focussed at several depths into the sample chamber and the force curve calculated again for a 4 μm water droplet.

The decrease in aberration not only shifts z_{eq} closer to the paraxial focus but also increases the strength of the optical trap with an increasing $F^{-}_{z,max}$ and overall deepening of the potential well.

Now consider point 3 from this chapters introduction. This work investigates the interaction between light and droplets of dimensions similar to the wavelength in a wave nature context, so it is reasonable to expect the particle to exhibit some sort of interferometric properties with reflections from the inside of the droplet interfering with themselves. This can be demonstrated by simplifying the model and treating it as an interferometer which performs reasonably well at estimating the axial efficiency at the paraxial focus[347]. In section 4.1 it was discussed that liquid aerosols will establish a stable size once in equilibrium with their surrounding environment, namely the relative humidity. Although the process of growth and evaporation is relatively fast it is at times clear one of these is occurring just after the droplet becomes trapped. The obvious step is to explore the parameter

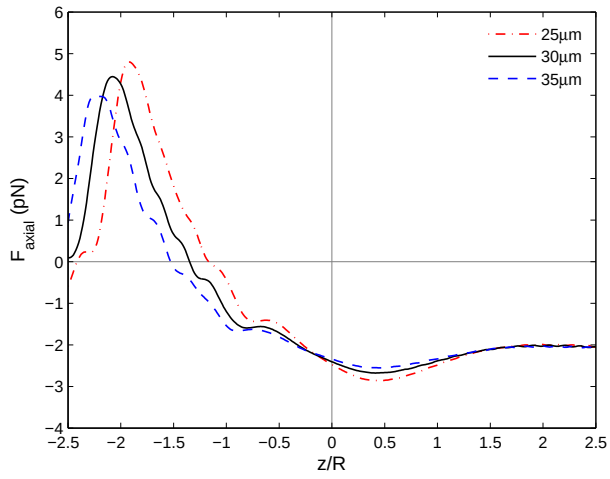

Figure 6.14: Variation of axial force for a 4 μm water droplet ($n_p = 1.342$) trapped in air ($n_a = 1.000$) with 8 mW of power for microscope objective displacements of 25 μm (red dot-dashed line), 30 μm (solid black line) and 35 μm (dashed blue line). The water layer ($n_w = 1.342$) is 10 μm thick, $\gamma = 1$, $\theta_0 = 41.23°$ and the coverslip refractive index $n_g = 1.517$.

space further by investigating how the height at which the droplet is trapped varies with droplet radius. This is plot in figure 6.15

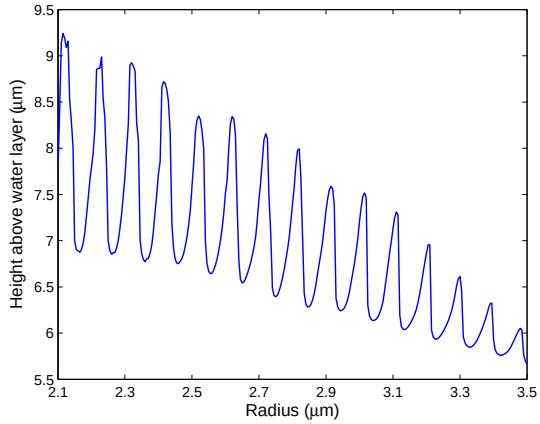

Figure 6.15: Plot of the height a water droplet ($n_p = 1.342$) in air ($n_a = 1.000$) is trapped above the underlying water layer ($n_w = 1.342$) as a function of radius. The objective axial displacement, $X = 25$ μm, the water layer is 10 μm thick, $\gamma = 1$, $\theta_0 = 41.23°$, the coverslip refractive index $n_g = 1.517$ and the trap power is 10 mW

There is a clear, near sinusoidal, oscillation in droplet height as a function of its radius. A single oscillation in height occurs over a change in droplet radius of $\sim$ 100 nm, going from a local minima to maxima in half this, $\sim$ 50 nm. So, a change in trap height of ~ 2 μm occurs due to only a 50 nm change in droplet radius. When observing a particle

just after capture the change in size is clear, far above the limit of resolution, so must be greater than 50 nm. Knowing that the oscillations are most frequent just after capture I conclude the multiple oscillations that occur in experiments are due to changing particle radius and hence equilibrium position z_{eq}.

To measure this oscillation would be a challenging experiment. The droplets would need to be imaged from the side to measure their height and also coupled with a high precision sizing technique such as CERS. With such instruments in place the droplet radius would have to be varied by altering ambient relative humidity or varying droplet temperature, but both would also change the droplet's salt concentration hence refractive index. This refractive index change should be possible to include in the model should such an experiment be performed.

6.3.3 Limits of techniques

I have managed to qualitatively explain the three unique phenomena observed when trapping airborne water droplets by modelling the optical forces created by the focussing of a high NA beam through two refractive index mismatched interfaces. How far can the boundaries of optical trapping in air be pushed? Can smaller particles (< 1 μm) be trapped? Can the axial trap strength and capture volume be increased? What are the limits on the particle refractive index that can be trapped? To explore these questions $Q^{-}_{z,max}$ is calculated as a function of both particle radius and relative refractive index[335], first for particles suspended in water, figure 6.16, as means of comparison, and then for airborne particles; figure 6.17.

The white areas on the plots represent parameter space where a negative Q_{axial} value does not exist and hence no stable trap position is possible[†]. Of immediate note are the 'spikes' in the contour plots indicating resonance in the force experienced by the particles. The effect is more pronounced as a function of radius although at the high refractive index end of the spikes there are rapid resonances in force as a function of refractive index, creating tiny islands of parameter space where traps can exist.

These resonances can be explained by interference effects due to spheres high refelctivity at high relative refractive index and its associated variation with radius[335]. The decreased frequency of the resonances in air is due to the lower medium refractive index ($n_a = 1.00$ and $n_w = 1.33$).

As the plots are functions of relative refractive index it is noted that for a given particle

[†]This is not completely accurate as there is a very small value of $Q^{-}_{z,max}$ in the white areas but it is negligible[350,351].

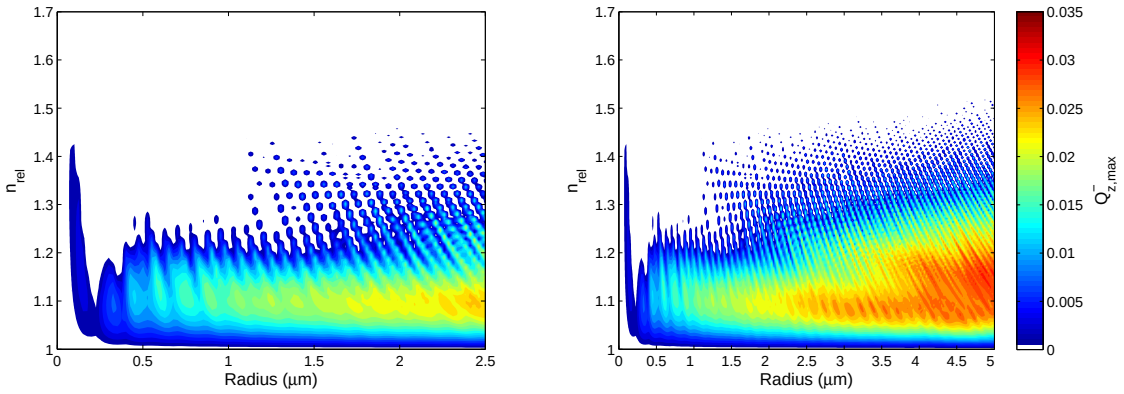

(a) (b)

Figure 6.16: $Q^{-}_{z,max}$ as a function of relative refractive index and radius for spheres trapped in a water medium ($n_w = 1.33$). The objective axial displacement, $X = 40$ μm, $\gamma = 1$, $\theta_0 = 61.25°$ and the coverslip refractive index $n_g = 1.517$. The colour bar in (b) is representative for both plots. (a) is an expanded view of the first 2.5 μm of (b) as this is the region where the boundaries would really like to be pushed.

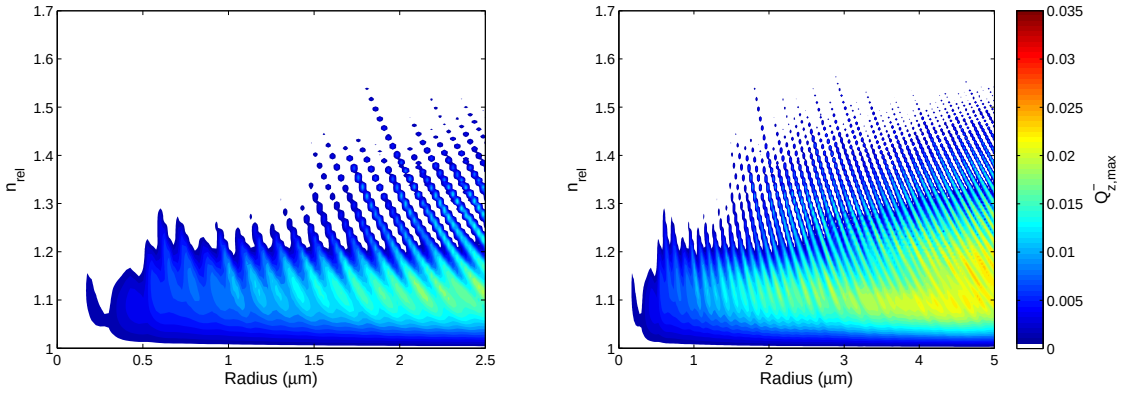

(a) (b)

Figure 6.17: $Q^{-}_{z,max}$ as a function of relative refractive index and radius for spheres trapped in an air medium ($n_a = 1.000$). The objective axial displacement, $X = 40$ μm, the water layer ($n_w = 1.342$) is 10 μm thick, $\gamma = 1$, $\theta_0 = 41.23°$ and the coverslip refractive index $n_g = 1.517$. The colour bar in (b) is representative for both plots. (a) Is an expanded view of the first 2.5 μm of (b) as this is the region where the boundaries would really like to be pushed.

refractive index the horizontal line of interest is higher up the refractive index axis in air than water. Looking at the sorts of particles normally trapped in both media gives a 'feel' for the plots. For example, a silica sphere in water exists along the line defined by $n_{rel} \simeq 1.09$ in figure 6.16 and for a water droplet in air the line is at $n_{rel} \simeq 1.34$ in figure 6.17.

The continuous region of stability for optical tweezers in air is over a smaller range of

refractive indices ($\Delta n_{rel} \simeq 1 - 1.25$) than when trapping in water ($\Delta n_{rel} \simeq 1.33 - 1.65$) and also, the maximum negative axial efficiency values, $Q^{-}_{z,max}$, are smaller overall for trapping in air than in water. This is understandable because the larger relative refractive index between particle and medium in air increases the Fresnel reflection coefficients, hence increases scattering forces which probably overcome the gradient forces. The minimum radius trappable is smaller in water than air probably due to the focussed beam's increased spherical aberration, induced by the coverslip interface, which has a larger refractive index contrast in airborne traps. As seen in figure 6.6 this increased aberration produces larger period oscillations in intensity allowing more 'room' for particles to 'fall' between.

These plots are deceptive; the true range of particles that would theoretically obtain an axial equilibrium position in air has been misquoted because, as previously mentioned, the weight of the particle is significant. $F^{-}_{z,max}$ is the truly relevant quantity that will allow the determination of whether the spheres are isolated in three dimensions or not. Unfortunately, this poses a problem as the force from equation 2.5 is dependent on laser power and with this additional variable not all parameter space can be easily plotted. Instead $F^{-}_{z,max}$ is plotted for a single power, $P = 10$ mW, in figure 6.18.

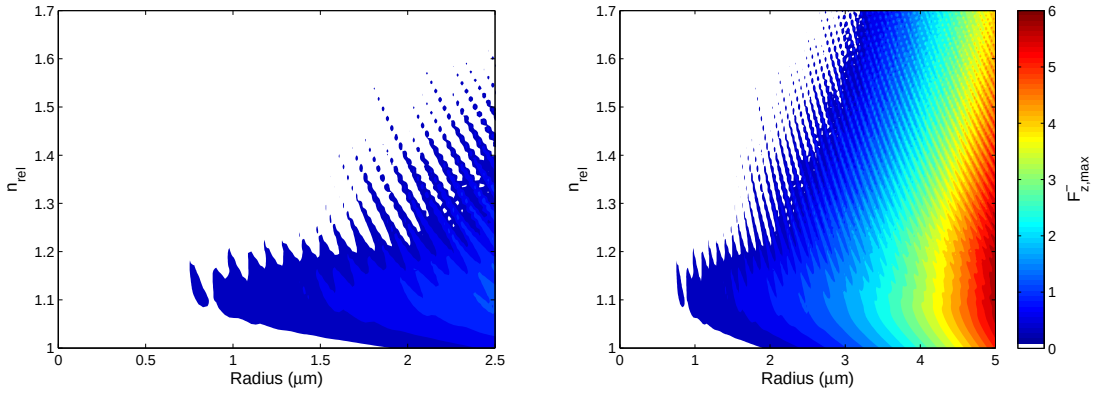

(a) (b)

Figure 6.18: $F^{-}_{z,max}$ as a function of relative refractive index and radius for spheres trapped in an air medium ($n_a = 1.000$). The objective axial displacement, $X = 40$ μm, the water layer ($n_w = 1.342$) is 10 μm thick, $\gamma = 1$, $\theta_0 = 41.23°$ and the coverslip refractive index $n_g = 1.517$. The colour bar in (b) is representative for both plots. (a) is an expanded view of the first 2.5 μm of (b).

Comparing figures 6.17 and 6.18 I come to an interesting conclusion. For droplets with certain particle parameters, indicated in figure 6.17, traps are created through the transfer of optical momentum alone (single beam gradient force trap or optical tweezers). However, figure 6.18 indicates that with the assistance of gravity a larger range of droplets can be 'trapped', although not with momentum transfer alone. Consider a droplet that evolves

in size (it will also evolve slightly in refractive index due to salt concentration changes); as the radius varies the particle's 'path' in the parameter space of figure 6.17 may cross through a non-tweezing region but due to its weight remains trapped (figure 6.18). This difficulty in deciding whether a droplet is tweezed or levitated leads to the conclusion that as a general name for the experimental tool being used I really have a *quasi-optical tweezers*.

In figure 6.19 I superimpose the tweezing and trapping areas of figures 6.17 and 6.18. Areas of parameter space truly optically tweezed are coloured grey, areas that are only trapped because of the assistance of gravity are coloured red and the area that would be truly tweezed if the droplets had neutral buoyancy is coloured blue. White areas retain the same meaning of neither tweezing nor levitation.

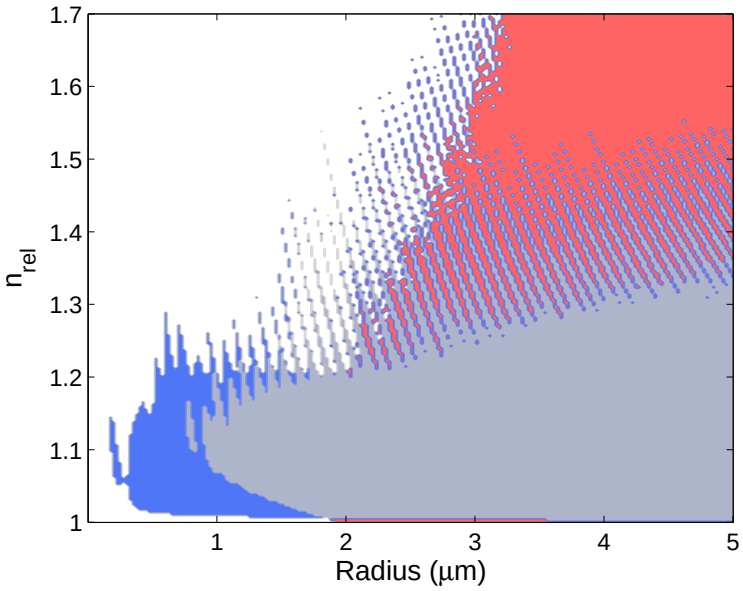

Figure 6.19: Superposition of figures 6.17(b) and 6.18(b) highlighting the areas of parameter space, as a function of relative refractive index and radius, where water droplets are truly optically tweezed (grey), only trapped with the assistance of gravity (red), and optically tweezed if the droplet had neutral buoyancy (blue). The white area represents areas where neither optical tweezing nor levitation occurs. The parameters for these plots are the same as the respective figures.

It is clear now that the choice of inverted or non-inverted tweezers is critical in the success of optically trapping a large range of aerosol sizes. Having established the true nature of the technique I am using, is it possible to move more of parameter space into the tweezing regime?

6.3.4 Optimisation and extension of limits

I have demonstrated several points of physics that stop airborne tweezers from reaching their optimum performance. These include spherical aberration created in the beam, a high refractive index contrast between particle and medium causing large scattering forces, and a lack of high converging angles (reduced NA) due to total internal reflection at the coverslip interface.

Total internal reflection is not easily circumvented but it could be possible to correct for spherical aberration or possibly remove the large scattering forces and I shall explore the effects of attempting to fix these next.

Spherical aberration correction

The largest aberration that occurs in an airborne tweezing system is spherical aberration with the results in the beam profile shown in figure 6.6. In section 3.5.2 I showed aberrations on the SLM and in the optical system can be removed with ease. It is feasible, therefore, that the aberration induced by the mismatched refractive index interfaces could be corrected for by using the SLM to display additional correction kinoforms. Any correction would clearly be advantageous creating better localisation of aerosols and hopefully moving into the important accumulation mode size regime. In figure 6.20 I plot for the same parameters as figure 6.17 but an additional spherical aberration is placed on the objective's input beam of magnitude 0.08λ.

Figure 6.20 shows an improvement in the axial strength of the optical tweezers, an increase in the overall range of parameter space that can be tweezed but unfortunately also an increase in the minimum particle radius that can be tweezed.

Removal of beam centre intensity

In chapter 2, I discussed that Ashkin used geometrical optics to predict an increase in $Q^{-}_{z,max}$ if a 'doughnut' mode beam (TEM_{01}) fills the back aperture of an objective. As increasing $Q^{-}_{z,max}$ is by far the most difficult problem in airborne tweezers, as shown and discussed, it is of clear interest to predict the effects of removing the central portion of a Gaussian beam using Mie theory. In figure 6.21 I plot $Q^{-}_{z,max}$ against both radius and relative refractive index for a Gaussian beam where $\sim 57\%$ of the beam area is removed leaving an annulus, yet the total power remains the same.

The figure shows that the area in parameter space over which a true optical tweezer can

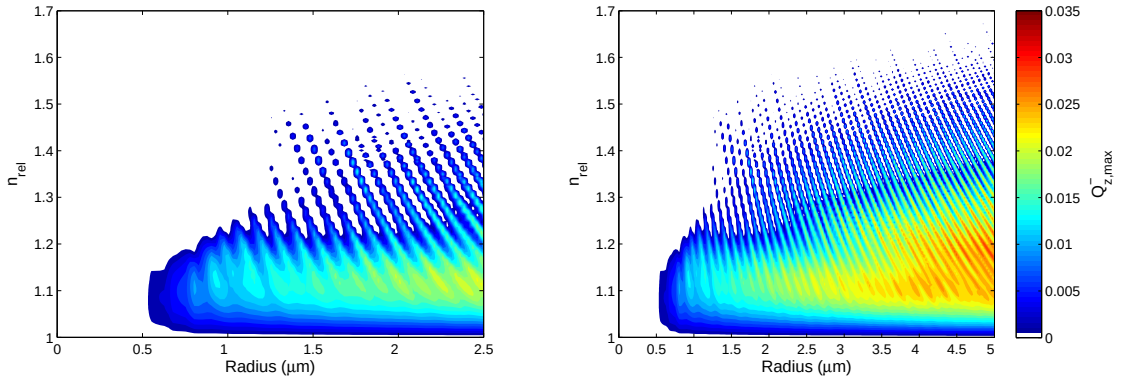

Figure 6.20: $Q^{-}_{z,max}$ as a function of relative refractive index and radius for spheres trapped in an air medium ($n_a = 1.00$) with a Gaussian beam entering the back aperture of the microscope objective with an additional spherical aberration placed on the beam at the entrance to the objective back aperture of magnitude 0.08λ. The objective axial displacement, $X = 40$ μm, the water layer is 10 μm ($n_w = 1.342$) thick, $\gamma = 1$, $\theta_0 = 41.23^\circ$ and the coverslip refractive index $n_g = 1.517$. (a) is an expanded view of the first 2.5 μm of (b).

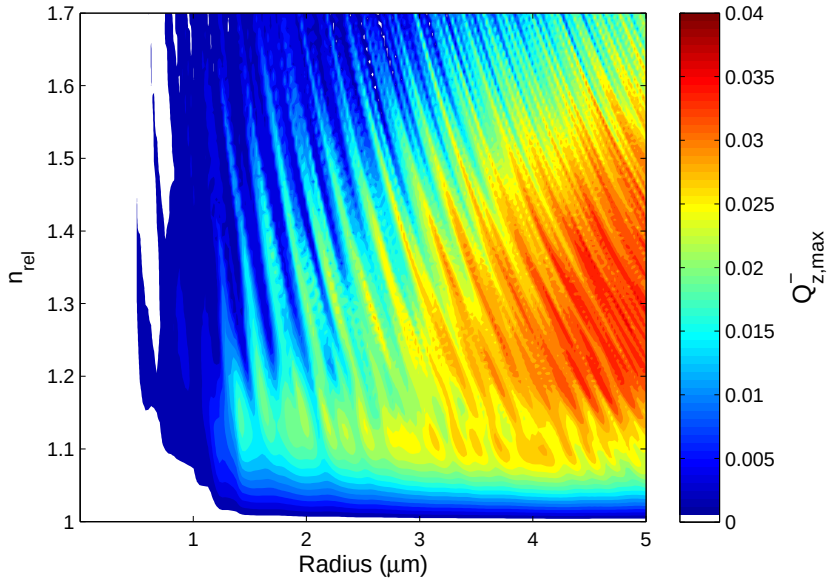

Figure 6.21: $Q^{-}_{z,max}$ as a function of relative refractive index and radius for spheres trapped in an air medium ($n_a = 1.000$) with a Gaussian beam entering the back aperture of the microscope objective with 57% of its central area removed. The objective axial displacement, $X = 40$ μm, the water layer ($n_w = 1.342$) is 10 μm thick, $\gamma = 1$, $\theta_0 = 41.23^\circ$ and the coverslip refractive index $n_g = 1.517$.

be created is greatly increased by removing the central core of a Gaussian beam, although the minimum sphere radius tweezable has increased. The minimum radius increase could

be due to the zero intensity that may now exist in the focal plane of the tweezers into which a small enough sphere could sit, experiencing no forces from the surrounding light.

The predicted increase in parameter space over which aerosols can be tweezed is of great promise to the field of aerosol optical manipulation. It is difficult to trap high refractive index aerosols, specifically solid microspheres, yet they are of great importance to the fields of medicinal drug lung delivery and atmospheric chemistry. It is hoped that a definitive experiment can be performed in future to verify this huge increase in optical tweezer parameter space.

6.3.5 Capture volume

I have demonstrated that power gradients may explain the linear dependence of captured droplet size on trapping power but there may be more interactions occurring than thought. In order for the droplets to become trapped they must enter the capture volume mentioned in the introduction to this chapter, so it would be pertinent to calculate how this volume varies with trapping power and droplet radius. Unfortunately, evaluation of this volume requires calculation of forces for locations away from the optical axis. At these locations there is a complex interplay between axial and lateral efficiencies[317,337]. This will require more study to ascertain a suitable description and answer to the question of whether the capture volume plays a significant role in the linear dependence of droplet size on trapping power.

6.4 Shortcomings of theory

Within the Mie scattering theory outlined above I make the assumption that the Fresnel transmission coefficients, t_s and t_p, for TE and TM modes of polarisation respectively are equal and take $t_s = t_p$. Plotted in figure 6.22 are both modes of the transmission coefficients as a function of incident angle on a glass to air interface to highlight the inaccuracy in this assumption.

The discrepancy in figure 6.22 is significant. I propose that in future work both TE and TM modes should be attempted to be placed into the theory.

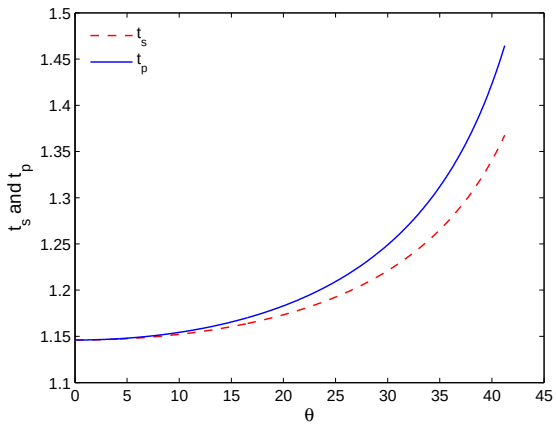

Figure 6.22: Fresnel transmission coefficients t_s and t_p for TE and TM modes of polarisation respectively as a function of incident angle θ up to the critical angle $\simeq 41.5^\circ$ for a glass ($n_g = 1.517$) to air ($n_a = 1.000$) refractive index interface.

6.5 Conclusion

The resonance type plots in this chapter go some way to explaining what the experimenter observes although it is difficult to make anything more than hand-waving conclusions. For example, it has been shown in this thesis that water droplets ($n_{rel} \simeq 1.342$) are easily trapped for a wide range of sizes as observed experimentally, but I can say from experience that it is difficult to trap small water aerosols (≤ 1 μm) even though they are produced from the nebuliser. Having worked closely with the main author of Summers *et al.*[81] where solid aerosols ($n_{rel} \simeq 1.445$) are trapped, I can say that the expected range of particles he could trap was odd. In colloidal systems, if two particle sizes can be trapped, almost certainly a size between these two will also be trapped. However, in air, spheres with certain radii could not be trapped yet sizes both above and below could.

Looking at figure 6.18 both these phenomena can be qualitatively explained with the existence of the resonances as a function of radius and the lack of $Q^{-}_{z,max}$ for small spheres (≤ 1 μm). Obviously, it is not easy to prove the non-result of being unable to trap certain objects, but the results here give some indication as to why it is so hard to trap small spheres, with a relatively high refractive index, that are so easily trapped in water.

The work of this chapter has lead to many new insights into how aerosols are trapped in single beam gradient force traps. It has given some qualitative predictions that explain physical phenomena observed experimentally helping to define the parameters of the current tools at our disposal. The challenge for the future is to produce quantitative agreement between experiment and theory.

Chapter 7

Conclusion and Outlook

The work carried out within this thesis has opened areas of research not previously considered, so there are many experiments that could still be performed and questions that should be investigated. In this chapter I highlight the most important and interesting outstanding experiments and questions and discuss how they should progress, before finally concluding.

7.1 Outlook

7.1.1 Single beam studies

In the future I would like to investigate the colour of thermal noise in Brownian motion. Equation 5.9 shows that the fluctuating force per unit mass is independent of ω and hence has a white noise spectrum. In reality, due to the frequency dependent friction, this spectrum may be coloured[262]. Measuring this coloured Brownian noise is a challenging experiment with measurement times in water needing to be approximately nine hours in duration. Increasing the kinematic viscosity of the surrounding fluid should help to simplify things; changing to airborne tweezing decreases the measurement time three-fold from its difference in viscosity alone. With careful investigation further improvements may be found due to simply trapping in air.

Another clear next step is to vary the type of trapping beam and to measure the effect. I have already shown in section 4.3 that Laguerre-Gaussian beams can impart orbital angular momentum to aerosol droplets. However, would the use of lower azimuthal index, l, to trap droplets improve their performance due to the lack of intensity in the core of the

beam? This is partially answered in chapter 6 where the theoretical effect of a core-less beam is calculated and has already been shown to work in a colloidal system[121].

Finally, for single beam aerosol studies, as discussed in chapter 5, work by Tólic-Nørrelykke *et al.*[295] showed that in an over-damped system it is possible to extract the trap stiffness, detector calibration and viscous damping from a single experiment *in situ*. The derivations in the work are carried out for a system that cannot exist in the critical or under-damped regime. I would find it interesting to carry out this work for an airborne based optical trap to see if the same parameters can be extracted or if extra information can be gained.

7.1.2 Fungi

A good follow-up experiment would be to test the photoreceptor-mediated negative phototropism hypothesis by repeating the experiments using strains in which the genes encoding different photoreceptors have been mutated[216]. Also it would be interesting to test a greater range of wavelengths and attempt to image the behaviour of the Spitzenkörper during redirection.

7.1.3 Sizing

At the moment the ability to size aerosol droplets from the friction they experience is restricted to a single particle at a time. CCDs can be used to detect multiple particles simultaneously but usually do not run at high enough frame rates to sample the motion correctly. However, with the advent of high speed multiple particle video tracking[191], it is feasible that holographic trapping of multiple aerosols (chapter 4) can be combined with the sizing technique (section 5.4.2) enabling simultaneous multiple aerosol sizing.

7.1.4 Hydrodynamics

I have realised, as the work in this thesis has progressed, that the physics needed to describe the motion of optically trapped aerosols is rather complex. I have derived the hydrodynamically correct power spectrum of position fluctuations for a sphere with oscillatory motion in a bulk medium, i.e. far away from surfaces. I have also demonstrated that as a droplet approaches a surface, Faxén's correction to Stokes' law must be used. However, I have not included a description of the hydrodynamic correction to Faxén's correction arising from oscillatory motion near a plane surface. This has not been solved for particles trapped in air, unlike in water[295]. The solution in air should be determined

if improvements in accuracy and precision are required.

Circulation frequency dependence

There is a correction to Stokes' law when dealing with fluid in fluid systems as I discussed for liquid droplets in air in section 5.5. This correction can reduce the viscous damping which I have included in my analysis. However, what is not clear is whether or not this correction also has a significant frequency dependence and is a question to be answered in the future.

Colloidal crystals

Optically trapped microparticles are a useful tool in the study of hydrodynamic interactions in colloidal suspensions[109,271,275] and it has been shown that microparticles localised in optical traps form hydrodynamically coupled arrays. Polin *et al.*[275] predicted that trapping larger spheres with higher trap stiffness in a lower viscosity medium would display the crossover from over-damped dynamics to a regime of under-damped propagating elastic waves with uniformly negative group velocities (see figure 3 of Polin *et al.*[275]).

The optical trapping of aerosol experiments described in this thesis provide a route to observing these under-damped propagating waves due to the low dynamic viscosity of air. The difficulty is the high speed detection of more than one particle simultaneously; in water this is not a problem as the slow frequencies of oscillation allow normal video tracking to be used. Alternatively in a time shared beam system the laser modulation can be synchronised with the position detection system to circumvent this problem[352], but becomes difficult for more than two objects. The recent development of high speed cameras that track multiple particles simultaneously 'on chip' at greater than 10 kHz allows studies at frequencies above the natural frequency of objects in airborne optical traps[353], providing a solution to tracking multiple (> 2) objects at high speed.

Preliminary experiments with one such high speed camera have shown that observation of the desired under-damped waves is possible.

7.1.5 Spherical aberration correction

As suggested in chapter 6 it may be possible to correct for the spherical aberration induced at the refractive index interfaces by using the SLM to alter the wavefront. However, the problem is the difficulty in measuring and quantifying the amount of spherical aberration

induced. One option would be to place a mirror a set distance above the interface and then use the same method as explained in section 3.5.2 to measure the aberration. This will only give the aberration for a very specific point in space with particular system properties that are liable to variation, so realistically, a different method would need to be developed.

Assuming trap stiffness is representative of the amount of aberration induced in the beam, a feedback system could be implemented that measures stiffness as different correction kinoforms are displayed on the SLM. This would iterate towards the correct kinoform for removal of spherical aberration artefacts.

7.2 Conclusion

I have provided an introduction to the field of optical manipulation that should be useful for novices. Starting with the basic apparatus and physical explanations in chapter 2, the ideas have evolved to provide complex experimental instruments and theoretical models that demonstrate several original results.

In chapter 3 I discussed the application of beam shaping methods in optical manipulation, specifically spatial light modulators. I described the apparatus needed and its correct construction before overviewing the software I have written to generate kinoforms through several different algorithms all implemented in LabVIEW. I also examined the optimisation of the system.

In chapter 4 I used the holographic optical tweezers from chapter 3 to demonstrate three novel applications of holographic optical tweezers that cover two orders of magnitude in dimension. These include the trapping and coagulation of multiple aerosols, the manipulation of filamentous fungi hyphal tips over extended distances and novel digital microfluidic operations using thermocapillary forces. These experiments move holographic optical tweezers away from direct optical manipulation, improving their versatility and the range of other disciplines for which they can be used[179,354,355]. I also laid down preliminary results for observing orbital angular acceleration using beams carrying orbital angular momentum.

In chapter 5 I described experiments that investigated the Brownian dynamics of optically trapped airborne liquid droplets. Exploration of the parameter space gives unique results in optical tweezers, showing that the trapped object is able to behave as an under-damped Brownian oscillator, that in turn can be parametrically excited. The ability for optical tweezers to access this regime has lead to several novel results[83,356], and will continue to

do so[357]. The results also show that when using beam shaping methods to study objects in air, one must be careful in its design to ensure the system does not fail. Perhaps the most useful result is the ability to determine the radius of optically trapped aerosols from studying the damping they experience. This technique requires no calibration *a priori*, thus making it simple to perform with little additional equipment over basic optical tweezers.

In chapter 6, I used a theoretical model to describe the forces imparted to a sphere trapped in a beam with spherical aberration, I qualitatively explain the phenomena observed in airborne optical traps. Specifically, potential reasons for the linear dependence of captured droplet size on laser power are given. Also, the reason droplets change in height as a function of laser power ('power gradients') and why with sufficiently large powers some droplets leave the trap, is explained. Finally, a likely mechanism for the axial oscillations of droplets is given. A major test of these explanations will be the future quantitative comparison to experimental results.

The work on holographic optical tweezers is already being used by three collaborating groups to enhance their toolbox of techniques[185]. Also the theoretical modelling is being used by collaborators to enhance their understanding of experiments with airborne traps[358].

As described in this chapter there still remains much scope for interesting experiments to be performed and physics to be probed, with my thesis providing the background.

References

[1] M. Padgett, "On diffraction within a dielectric medium as an example of the Minkowski formulation of optical momentum," Optics Express **16**, 20864–20868 (2008).

[2] A. Ashkin, "Acceleration and trapping of particles by radiation pressure," Physical Review Letters **24**, 156–159 (1970).

[3] A. Ashkin, J. M. Dziedzic, J. E. Bjorkholm, and S. Chu, "Observation of a single-beam gradient force optical trap for dielectric particles," Optics Letters **11**, 288–290 (1986).

[4] E. A. Abbondanzieri, W. J. Greenleaf, J. W. Shaevitz, R. Landick, and S. M. Block, "Direct observation of base-pair stepping by RNA polymerase," Nature **438**, 460–465 (2005).

[5] S. Dumont, W. Cheng, V. Serebrov, R. K. Beran, I. Tinoco, A. M. Pyle, and C. Bustamante, "RNA translocation and unwinding mechanism of HCVNS3 helicase and its coordination by ATP," Nature **439**, 105–108 (2006).

[6] P. T. Korda, G. C. Spalding, and D. G. Grier, "Evolution of a colloidal critical state in an optical pinning potential landscape," Physical Review B **66**, 024504 (2002).

[7] P. M. Hansen, J. K. Dreyer, J. Ferkinghoff-Borg, and L. Oddershede, "Novel optical and statistical methods reveal colloid-wall interactions inconsistent with DLVO and Lifshitz theories," Journal of Colloid and Interface Science **287**, 561–571 (2005).

[8] V. Garcés-Chávez, D. McGloin, M. J. Padgett, W. Dultz, H. Schmitzer, and K. Dholakia, "Observation of the transfer of the local angular momentum density of a multiringed light beam to an optically trapped particle," Physical Review Letters **91**, 093602 (2003).

[9] N. B. Simpson, K. Dholakia, L. Allen, and M. J. Padgett, "Mechanical equivalence of spin and orbital angular momentum of light: An optical spanner," Optics Letters **22**, 52–54 (1997).

[10] A. Constable, J. Kim, J. Mervis, F. Zarinetchi, and M. Prentiss, "Demonstration of a fiberoptic light-force trap," Optics Letters **18**, 1867–1869 (1993).

[11] R. Omori, T. Kobayashi, and A. Suzuki, "Observation of a single-beam gradient-force optical trap for dielectric particles in air," Optics Letters **22**, 816–818 (1997).

[12] R. J. Hopkins, L. Mitchem, A. D. Ward, and J. P. Reid, "Control and characterisation of a single aerosol droplet in a single-beam gradient-force optical trap," Physical Chemistry Chemical Physics **6**, 4924–4927 (2004).

[13] A. Ashkin, "History of optical trapping and manipulation of small-neutral particle, atoms, and molecules," IEEE Journal Of Selected Topics In Quantum Electronics **6**, 841–856 (2000).

[14] A. Ashkin and J. M. Dziedzic, "Optical levitation by radiation pressure," Applied Physics Letters **19**, 283–& (1971).

[15] P. T. Korda, M. B. Taylor, and D. G. Grier, "Kinetically locked-in colloidal transport in an array of optical tweezers," Physical Review Letters **89**, 128301 (2002).

[16] M. Pelton, K. Ladavac, and D. G. Grier, "Transport and fractionation in periodic potential-energy landscapes," Physical Review E **70**, 031108 (2004).

[17] M. P. MacDonald, G. C. Spalding, and K. Dholakia, "Microfluidic sorting in an optical lattice," Nature **426**, 421–424 (2003).

[18] N. K. Metzger, E. M. Wright, W. Sibbett, and K. Dholakia, "Visualization of optical binding of microparticles using a femtosecond fiber optical trap," Optics Express **14**, 3677–3687 (2006).

[19] K. Dholakia, G. Spalding, and M. MacDonald, "Optical tweezers: the next generation," Physics World **15**, 31 (2002).

[20] D. G. Grier, "A revolution in optical manipulation," Nature **424**, 810–816 (2003).

[21] D. J. Stevenson, T. K. Lake, B. Agate, V. Garcés-Chávez, K. Dholakia, and F. Gunn-Moore, "Optically guided neuronal growth at near infrared wavelengths," Optics Express **14**, 9786–9793 (2006).

[22] L. Paterson, E. Papagiakoumou, G. Milne, V. Garces-Chavez, S. A. Tatarkova, W. Sibbett, F. J. Gunn-Moore, P. E. Bryant, A. C. Riches, and K. Dholakia, "Light-induced cell separation in a tailored optical landscape," Applied Physics Letters **87**, 123901 (2005).

[23] P. R. T. Jess, V. Garcés-Chávez, D. Smith, M. Mazilu, L. Paterson, A. Riches, C. S. Herrington, W. Sibbett, and K. Dholakia, "Dual beam fibre trap for raman microspectroscopy of single cells," Optics Express **14**, 5779–5791 (2006).

[24] K. Svoboda and S. M. Block, "Biological applications of optical forces," Annual Review of Biophysics and Biomolecular Structure **23**, 247–285 (1994).

[25] S. C. Kuo, "Using optics to measure biological forces and mechanics," Traffic **2**, 757–763 (2001).

[26] M. J. Lang and S. M. Block, "Resource letter: Lbot-1: Laser-based optical tweezers,"

American Journal of Physics **71**, 201–215 (2003).

[27] J. Molloy and M. Padgett, "Lights, action: optical tweezers," Contemporary Physics **43**, 241–258 (2002).

[28] K. C. Neuman and S. M. Block, "Optical trapping," Review of Scientific Instruments **75**, 2787–2809 (2004).

[29] G. C. Spalding, J. Courtial, and R. Di Leonardo, *Structured Light and its Applications: An Introduction to Phase-Structured Beams and Nanoscale Optical Forces* (Elsevier Press, 2008), chap. Holographic Optical Trapping, pp. 139–168.

[30] K. Franze, J. Grosche, S. N. Skatchkov, S. Schinkinger, C. Foja, D. Schlid, O. Uckermann, K. Travis, A. Reichenbach, and J. Guck, "Muller cells are living optical fibers in the vertebrate retina," Proceedings of the National Academy of Sciences of the United States of America **104**, 8287–8292 (2007).

[31] K. Volke-Sepulveda, V. Garces-Chavez, S. Chavez-Cerda, J. Arlt, and K. Dholakia, "Orbital angular momentum of a high-order bessel light beam," Journal of Optics B - Quantum and Semiclassical Optics **4**, S82–S89 (2002).

[32] J. Courtial and M. J. Padgett, "Limit to the orbital angular momentum per unit energy in a lightbeam that can be focussed onto a small particle," Optics Communications **173**, 269274 (2000).

[33] A. T. O'Neil, I. MacVicar, L. Allen, and M. J. Padgett, "Intrinsic and extrinsic nature of the orbital angular momentum of a light beam," Physical Review Letters **88**, 053601 (2002).

[34] M. M. Burns, J. M. Fournier, and J. A. Golovchenko, "Optical matter - crystallization and binding in intense optical-fields," Science **249**, 749–754 (1990).

[35] N. K. Metzger, R. F. Marchington, M. Mazilu, R. L. Smith, K. Dholakia, and E. M. Wright, "Measurement of the restoring forces acting on two optically bound particles from normal mode correlations," Physical Review Letters **98**, 068102 (2007).

[36] C. López-Mariscal, J. C. Gutiérrez-Vega, D. McGloin, and K. Dholakia, "Direct detection of optical phase conjugation in a colloidal medium," Optics Express **15**, 6330–6335 (2007).

[37] P. Y. Chiou, A. T. Ohta, and M. C. Wu, "Massively parallel manipulation of single cells and microparticles using optical images," Nature **436**, 370–372 (2005).

[38] K. Visscher, S. P. Gross, and S. M. Block, "Construction of multiple-beam optical traps with nanometer-resolution position sensing," IEEE Journal of Selected Topics in Quantum Electronics **2**, 1066–1076 (1996).

[39] S. Kawata and T. Sugiura, "Movement of micrometer-sized particles in the evanescent field of a laser beam," Optics Letters **11**, 772 (1992).

[40] V. Garcés-Chávez, K. Dholakia, and G. C. Spalding, "Extended-area optically in-

duced organization of microparticies on a surface," Applied Physics Letters **86**, 031106 (2005).

[41] J. E. Curtis, B. A. Koss, and D. G. Grier, "Dynamic holographic optical tweezers," Optics Communications **207**, 169–175 (2002).

[42] J. Plewa, "Biotechnology applications for holographic optical trapping," Tech. rep., Arryx.

[43] J. S. Plewa, T. Del Sol, R. W. Lancelot, W. A. Lopes, D. M. Mueth, K. F. Bradley, and L. S. Gruber, "Prospects for holographic optical tweezers," Tech. rep., Arryx.

[44] G. Milne, D. Rhodes, M. MacDonald, and K. Dholakia, "Fractionation of polydisperse colloid with acousto-optically generated potential energy landscapes," Optics Letters **32**, 1144–1146 (2007).

[45] T. Cizmar, V. Kollarova, X. Tsampoula, F. Gunn-Moore, W. Sibbett, Z. Bouchal, and K. Dholakia, "Generation of multiple bessel beams for a biophotonics workstation," Optics Express **16**, 14024–14035 (2008).

[46] A. Ashkin and J. M. Dziedzic, "Optical trapping and manipulation of viruses and bacteria," Science **235**, 1517–1520 (1987).

[47] H. Zhang and K. K. Liu, "Optical tweezers for single cells," Journal Of The Royal Society Interface **5**, 671–690 (2008).

[48] P. Luchette, N. Abiy, and H. B. Mao, "Microanalysis of clouding process at the single droplet level," Sensors and Actuators B - Chemical **128**, 154–160 (2007).

[49] L. Mitchem, R. J. Hopkins, J. Buajarern, A. D. Ward, and J. P. Reid, "Comparative measurements of aerosol droplet growth," Chemical Physics Letters **432**, 362–366 (2006).

[50] K. J. Knox and J. P. Reid, "Ultrasensitive absorption spectroscopy of optically-trapped aerosol droplets," The journal of physical chemistry A **112**, 1043910441 (2008).

[51] J. Reid, Aerosol Dynamics Group.

[52] M. Z. Jacobson, *Atmospheric Pollution: History, Science, and Regulation* (Cambridge University Press, 2002).

[53] N. R. Labiris and M. B. Dolovich, "Pulmonary drug delivery. part i: Physiological factors affecting therapeutic effectiveness of aerosolized medications," British Journal of Clinical Pharmacology **56**, 588–599 (2003).

[54] Reid, "Aerosols," in "Colloid Science: Principles, Methods and Applications," , vol. 10, T. Cosgrove, ed. (Wiley-Blackwell, 2005).

[55] NERC, "Aerosol properties, processes and influences on the earth's climate (appraise)," (2006).

[56] S. Solomon, D. Qin, M. Manning, Z. Chen, M. M. Marquis, K. B. Averyt, M. Tig-

nor, and H. L. Miller, *IPCC: Climate Change 2007: The Physical Science Basis. Contribution of Working Group I to the Fourth Assessment Report of the Intergovernmental Panel on Climate Change* (Cambridge University Press, 2007), chap. Summary for Policymakers.

[57] R. Watson and the Core Writing Team (eds.), *IPCC: Climate Change 2001: Synthesis Report. A Report of Working Group I of the Intergovernmental Panel on Climate Change* (Cambridge University Press, 2001), chap. Summary for Policymakers.

[58] L. Mitchem and J. P. Reid, "Optical manipulation and characterisation of aerosol particles using a single-beam gradient force optical trap," Chemical Society Reviews **37**, 756–769 (2008).

[59] J. H. Seinfeld and S. N. Pandis, *Atmospheric chemistry and physics: Air pollution to climate change* (John Wiley and Sons Inc., 1998).

[60] F. Priego-Capote and L. de Castro, "Ultrasound-assisted levitation: Lab-on-a-drop," Trends in Analytical Chemistry **25**, 856–867 (2006).

[61] S. Holler, M. Surbek, R. K. Chang, and Y. L. Pan, "Two-dimensional angular optical scattering patterns as droplets evolve into clusters," Optics Letters **24**, 1185–1187 (1999).

[62] H. Azzouz, L. Alkhafadiji, S. Balslev, J. Johansson, N. A. Mortensen, S. Nilsson, and A. Kristensen, "Levitated droplet dye laser," Optics Express **14**, 4374–4379 (2006).

[63] G. Hars and Z. Tass, "Application of quadrupole ion-trap for the accurate mass determination of submicron size charged-particles," Journal Of Applied Physics **77**, 4245–4250 (1995).

[64] A. Ashkin and J. M. Dziedzic, "Optical levitation of liquid drops by radiation pressure," Science **187**, 1073–1075 (1975).

[65] A. Ashkin and J. M. Dziedzic, "Observation of light-scattering from nonspherical particles using optical levitation," Applied Optics **19**, 660–668 (1980).

[66] R. Thurn and W. Kiefer, "Raman-microsampling technique applying optical levitation by radiation pressure," Applied Spectroscopy **38**, 78–83 (1984).

[67] J. Musick, J. Popp, M. Trunk, and W. Kiefer, "Investigations of radical polymerization and copolymerization reactions in optically levitated microdroplets by simultaneous Raman spectroscopy, Mie scattering, and radiation pressure measurements," Applied Spectroscopy **52**, 692–701 (1998).

[68] W. Kiefer, J. Popp, M. Lankers, M. Trunk, I. Hartmann, E. Urlaub, and J. Musick, "Raman-Mie scattering from single laser trapped microdroplets," Journal of Molecular Structure **408**, 113–120 (1997).

[69] C. Mund and R. Zellner, "Optical levitation of single microdroplets at temperatures

down to 180 K," ChemPhysChem **4**, 630–638 (2003).

[70] N. Roth and A. Frohn, "Size and polarization behaviour of optically levitated frozen water droplets," Atmospheric Environment **32**, 3139–3143 (1998).

[71] M. Guillon, O. Moine, and B. Stout, "Longitudinal optical binding of high optical contrast microdroplets in air," Physical Review Letters **96**, 143902 (2006).

[72] M. Guillon, O. Moine, and B. Stout, "Longitudinal optical binding of high optical contrast microdroplets in air (vol 96, art no 143902, 2006)," Physical Review Letters **99**, 079901 (2007).

[73] A. Ashkin and J. M. Dziedzic, "Feedback stabilization of optically levitated particles," Applied Physics Letters **30**, 202–204 (1977).

[74] N. Magome, M. I. Kohira, E. Hayata, S. Mukai, and K. Yoshikawa, "Optical trapping of a growing water droplet in air," Journal of Physical Chemistry B **107**, 3988–3990 (2003).

[75] A. A. Ambardekar and Y. Q. Li, "Optical levitation and manipulation of stuck particles with pulsed optical tweezers," Optics Letters **30**, 1797–1799 (2005).

[76] M. D. King, K. C. Thompson, and A. D. Ward, "Laser tweezers raman study of optically trapped aerosol droplets of seawater and oleic acid reacting with ozone: implications for cloud-droplet properties," Journal of the American Chemical Society **126**, 16710–16711 (2004).

[77] R. Symes, R. M. Sayer, and J. P. Reid, "Cavity enhanced droplet spectroscopy: Principles, perspectives and prospects," Physical Chemistry Chemical Physics **6**, 474–487 (2004).

[78] J. Buajarern, L. Mitchem, and J. P. Reid, "Characterizing the formation of organic layers on the surface of inorganic/aqueous aerosols by raman spectroscopy," Journal of Physical Chemistry A **111**, 11852–11859 (2007).

[79] D. McGloin, D. R. Burnham, M. D. Summers, D. Rudd, N. Dewar, and S. Anand, "Optical manipulation of airborne particles: techniques and applications," Faraday Discussions **137**, 335–350 (2008).

[80] M. D. Summers, J. P. Reid, and D. McGloin, "Optical guiding of aerosol droplets," Optics Express **14**, 6373–6380 (2006).

[81] M. D. Summers, D. R. Burnham, and D. McGloin, "Trapping solid aerosols with optical tweezers: A comparison between gas and liquid phase optical traps," Optics Express **16**, 7739–7747 (2008).

[82] D. Rudd, C. López-Mariscal, M. Summers, A. Shahvisi, J. C. Gutiérrez-Vega, and D. McGloin, "Fiber based optical trapping of aerosols," Optics Express **16**, 14550–14560 (2008).

[83] R. Di Leonardo, G. Ruocco, J. Leach, M. J. Padgett, A. J. Wright, J. M. Girkin,

D. R. Burnham, and D. McGloin, "Parametric resonance of optically trapped aerosols," Physical Review Letters **99**, 010601 (2007).

[84] H. He, N. R. Heckenberg, and H. Rubinsztеindunlop, "Optical-particle trapping with higher-order doughnut beams produced using high-efficiency computer-generated holograms," Journal of Modern Optics **42**, 217–223 (1995).

[85] E. R. Dufresne, G. C. Spalding, M. T. Dearing, S. A. Sheets, and D. G. Grier, "Computer-generated holographic optical tweezer arrays," Review of Scientific Instruments **72**, 1810–1816 (2001).

[86] J. Courtial, G. Whyte, Z. Bouchal, and J. Wagner, "Iterative algorithms for holographic shaping of non-diffracting and self-imaging light beams," Optics Express **14**, 2108–2116 (2006).

[87] R. Di Leonardo, F. Ianni, and G. Ruocco, "Computer generation of optimal holograms for optical trap arrays," Optics Express **15**, 1913–1922 (2007).

[88] M. Polin, K. Ladavac, S. H. Lee, Y. Roichman, and D. G. Grier, "Optimized holographic optical traps," Optics Express **13**, 5831–5845 (2005).

[89] F. Belloni and S. Monneret, "Quadrant kinoform: an approach to multiplane dynamic three-dimensional holographic trapping," Applied Optics **46**, 4587–4593 (2007).

[90] W. J. Hossack, E. Theofanidou, J. Crain, K. Heggarty, and M. Birch, "High-speed holographic optical tweezers using a ferroelectric liquid crystal microdisplay," Optics Express **11**, 2053–2059 (2003).

[91] A. Jesacher, S. Furhapter, S. Bernet, and M. Ritsch-Marte, "Diffractive optical tweezers in the Fresnel regime," Optics Express **12**, 2243–2250 (2004).

[92] E. Schonbrun, R. Piestun, P. Jordan, J. Cooper, K. D. Wulff, J. Courtial, and M. Padgett, "3D interferometric optical tweezers using a single spatial light modulator," Optics Express **13**, 3777–3786 (2005).

[93] P. J. Rodrigo, R. L. Eriksen, V. R. Daria, and J. Glückstad, "Interactive light-driven and parallel manipulation of inhomogeneous particles," Optics Express **10**, 1550–1556 (2002).

[94] T. Shimobaba and T. Ito, "An efficient computational method suitable for hardware of computer-generated hologram with phase computation by addition," Computer Physics Communications **138**, 44–52 (2001).

[95] M. Reicherter, S. Zwick, T. Haist, C. Kohler, H. Tiziani, and W. Osten, "Fast digital hologram generation and adaptive force measurement in liquid-crystal-display-based holographic tweezers," Applied Optics **45**, 888–896 (2006).

[96] G. Gibson, D. M. Carberry, G. Whyte, J. Leach, J. Courtial, J. C. Jackson, D. Robert, M. Miles, and M. Padgett, "Holographic assembly workstation for optical

manipulation," Journal of Optics A - Pure and Applied Optics **10**, 044009 (2008).

[97] C. Basdogan, A. Kiraz, I. Bukusoglu, A. Varol, and S. Doganay, "Haptic guidance for improved task performance in steering microparticles with optical tweezers," Optics Express **15**, 11616–11621 (2007).

[98] J. A. Grieve, A. Ulcinas, S. Subramanian, G. M. Gibson, M. J. Padgett, D. M. Carberry, and M. J. Miles, "Hands-on with optical tweezers: a multitouch interface for holographic optical trapping," Optics Express **17**, 3595–3602 (2009).

[99] J. E. Curtis, C. H. J. Schmitz, and J. P. Spatz, "Symmetry dependence of holograms for optical trapping," Optics Letters **30**, 2086–2088 (2005).

[100] C. H. J. Schmitz, J. P. Spatz, and J. E. Curtis, "High-precision steering of multiple holographic optical traps," Optics Express **13**, 8678–8685 (2005).

[101] S. H. Lee and D. G. Grier, "Robustness of holographic optical traps against phase scaling errors," Optics Express **13**, 7458–7465 (2005).

[102] R. Agarwal, K. Ladavac, Y. Roichman, G. H. Yu, C. M. Lieber, and D. G. Grier, "Manipulation and assembly of nanowires with holographic optical traps," Optics Express **13**, 8906–8912 (2005).

[103] J. Leach, G. Sinclair, P. Jordan, J. Courtial, M. J. Padgett, J. Cooper, and Z. J. Laczik, "3D manipulation of particles into crystal structures using holographic optical tweezers," Optics Express **12**, 220–226 (2004).

[104] G. Sinclair, P. Jordan, J. Courtial, M. Padgett, J. Cooper, and Z. J. Laczik, "Assembly of 3-dimensional structures using programmable holographic optical tweezers," Optics Express **12**, 5475–5480 (2004).

[105] H. Melville, G. F. Milne, G. C. Spalding, W. Sibbett, K. Dholakia, and D. McGloin, "Optical trapping of three-dimensional structures using dynamic holograms," Optics Express **11**, 3562–3567 (2003).

[106] V. Emiliani, D. Cojoc, E. Ferrari, V. Garbin, C. Durieux, M. Coppey-Moisan, and E. Di Fabrizio, "Wave front engineering for microscopy of living cells," Optics Express **13**, 1395–1405 (2005).

[107] A. Jesacher, S. Furhapter, C. Maurer, S. Bernet, and M. Ritsch-Marte, "Holographic optical tweezers for object manipulations at an air-liquid surface," Optics Express **14**, 6342–6352 (2006).

[108] H. Mushfique, J. Leach, R. Di Leonardo, M. J. Padgett, and J. M. Cooper, "Optically driven pumps and flow sensors for microfluidic systems," Proceedings of the Institution of Mechanical Engineers Part C - Journal of Mechanical Engineering Science **222**, 829–837 (2008).

[109] R. Di Leonardo, S. Keen, F. Ianni, J. Leach, M. J. Padgett, and G. Ruocco, "Hydrodynamic interactions in two dimensions," Physical Review E **78**, 031406 (2008).

[110] R. Di Leonardo, F. Saglimbeni, and G. Ruocco, "Very-long-range nature of capillary interactions in liquid films," Physical Review Letters **100**, 106103 (2008).

[111] A. van der Horst and N. R. Forde, "Calibration of dynamic holographic optical tweezers for force measurements on biomaterials," Optics Express **16**, 20987–21003 (2008).

[112] L. I. McCann and S. Murphy, "Hysteretic axial motion of optically-trapped aerosol droplets," in "SPIE Vol. 7038," (2008).

[113] D. McGloin, "Optical tweezers: 20 years on," Philosophical Transactions Of The Royal Society A - Mathematical Physical And Engineering Sciences **364**, 3521–3537 (2006).

[114] J. W. Goodman, *Introduction to Fourier Optics* (Roberts and Company Publishers, 2005), 3rd ed.

[115] A. Ashkin, "Forces of a single-beam gradient laser trap on a dielectric sphere in the ray optics regime," Biophysical Journal **61**, 569–582 (1992).

[116] P. A. Tipler, *Physics for Scientists and Engineers* (W. H. Freeman and Co., 1999), 4th ed.

[117] G. Roosen, "Optical levitation of spheres," Canadian Journal Of Physics **57**, 1260–1279 (1979).

[118] G. Roosen and C. Imbert, "Optical levitation by means of 2 horizontal laser-beams - theoretical and experimental-study," Physics Letters A **59**, 6–8 (1976).

[119] G. Roosen, "Theoretical and experimental-study of stable equilibrium positions of spheres levitated by 2 horizontal laser-beams," Optics Communications **21**, 189–194 (1977).

[120] G. Roosen, B. Delaunay, and C. Imbert, "Radiation pressure exerted by a light-beam on refractive spheres - theoretical and experimental-study," Journal Of Optics-Nouvelle Revue D Optique **8**, 181–187 (1977).

[121] N. B. Simpson, D. McGloin, K. Dholakia, L. Allen, and M. J. Padgett, "Optical tweezers with increased axial trapping efficiency," Journal of Modern Optics **45**, 1943–1949 (1998).

[122] Z. Gong, Z. Wang, Y. M. Li, L. R. Lou, and S. H. Xu, "Axial deviation of an optically trapped particle in trapping force calibration using the drag force method," Optics Communications **273**, 37–42 (2007).

[123] N. Malagnino, G. Pesce, A. Sasso, and E. Arimondo, "Measurements of trapping efficiency and stiffness in optical tweezers," Optics Communications **214**, 15–24 (2002).

[124] F. Belloni, S. Monneret, F. Monduc, and M. Scordia, "Multiple holographic optical tweezers parallel calibration with optical potential well characterization," Optics

Express **16**, 9011 (2008).

[125] C. López-Mariscal, J. C. Gutiérrez-Vega, G. Milne, and K. Dholakia, "Orbital angular momentum transfer in helical mathieu beams," Optics Express **14**, 4182–4187 (2006).

[126] P. Feng, X. Wen, and R. Lu, "Long-working-distance synthetic aperture Fresnel off-axis digital holography," Optics Express **17**, 5473–5479 (2009).

[127] N. Al-Ababneh and M. Testorf, "Analysis of free space optical interconnects based on non-diffracting beams," Optics Communications **242**, 393–400 (2004).

[128] V. Arrizon, G. Mendez, and D. Sanchez-de La-Llave, "Accurate encoding of arbitrary complex fields with amplitude-only liquid crystal spatial light modulators," Optics Express **13**, 7913–7927 (2005).

[129] B. R. Brown and A. W. Lohmann, "Complex spatial filtering with binary masks," Applied Opitcs **5**, 967–969 (1966).

[130] B. R. Brown and A. W. Lohmann, "Computer-generated binary holograms," IBM Journal of Research and Development pp. 160–168 (1969).

[131] E. R. Dufresne and D. G. Grier, "Optical tweezer arrays and optical substrates created with diffractive optics," Review of Scientific Instruments **69**, 1974–1977 (1998).

[132] V. Garcés-Chávez, R. Quidant, P. J. Reece, G. Badenes, L. Torner, and K. Dholakia, "Extended organization of colloidal microparticles by surface plasmon polariton excitation," Physical Review E **73**, 085417 (2006).

[133] R. K. Tyson, M. Scipioni, and J. Viegas, "Generation of an optical vortex with a segmented deformable mirror," Applied Optics **47**, 6300–6306 (2008).

[134] Flexible Optical B. V., http://www.okotech.com/ (March 2009).

[135] E. Theofanidou, L. Wilson, W. J. Hossack, and J. Arlt, "Spherical aberration correction for optical tweezers," Optics Communications **236**, 145–150 (2004).

[136] K. Sasaki, M. Koshioka, H. Misawa, N. Kitamura, and H. Masuhara, "Laser-scanning micromanipulation and spatial patterning of fine particles," Japanese Journal Of Applied Physics Part 2-Letters **30**, L907–L909 (1991).

[137] C. Mio and D. W. M. Marr, "Tailored surfaces using optically manipulated colloidal particles," Langmuir **15**, 8565–8568 (1999).

[138] C. Mio, T. Gong, A. Terray, and D. W. M. Marr, "Design of a scanning laser optical trap for multiparticle manipulation," Review of Scientific Instruments **71**, 2196–2200 (2000).

[139] K. Sasaki, M. Koshioka, H. Misawa, N. Kitamura, and H. Masuhara, "Optical trapping of a metal-particle and a water droplet by a scanning laser-beam," Applied Physics Letters **60**, 807–809 (1992).

[140] P. H. Jones, E. Stride, and N. Saffari, "Trapping and manipulation of microscopic bubbles with a scanning optical tweezer," Applied Physics Letters **89**, 081113 (2006).

[141] M. T. Valentine, N. R. Guydosh, B. Gutierrez-Medina, A. N. Fehr, J. O. Andreasson, and S. M. Block, "Precision steering of an optical trap by electro-optic deflection," Optics Letters **33**, 599–601 (2008).

[142] M. J. Lang, C. L. Asbury, J. W. Shaevitz, and S. M. Block, "An automated two-dimensional optical force clamp for single molecule studies," Biophysical Journal **83**, 491–501 (2002).

[143] E. Martin-Badosa, M. Montes-Usategui, A. Carnicer, J. Andilla, E. Pleguezuelos, and I. Juvells, "Design strategies for optimizing holographic optical tweezers set-ups," Journal of Optics A - Pure and Applied Optics **9**, S267–S277 (2007).

[144] G. Milne, "Optical sorting and manipulation of microscopic particles," Ph.D. thesis, University of St Andrews (2007).

[145] P. C. Mogensen and J. Glückstad, "Dynamic away generation and pattern formation for optical tweezers," Optics Communications **175**, 75–81 (2000).

[146] P. J. Rodrigo, V. R. Daria, and J. Glückstad, "Four-dimensional optical manipulation of colloidal particles," Applied Physics Letters **86**, 074103 (2005).

[147] J. Gourlay, S. Samus, P. Mcowan, D. G. Vass, I. Underwood, and M. Worboys, "Real-time binary phase holograms on a reflective ferroelectric liquid-crystal spatial light-modulator," Applied Optics **33**, 8251–8254 (1994).

[148] S. M. Kelly, *Flat Panel Displays: Advanced Organic Materials* (Royal Society of Chemistry, 2000).

[149] E. Fällman and O. Axner, "Design for fully steerable dual-trap optical tweezers," Applied Optics **36**, 2107–2113 (1997).

[150] *Inverse Problems* (Institute of Physics).

[151] G. Tricoles, "Computer generated holograms an historical review," Applied Optics **26**, 4351–4360 (1987).

[152] D. Gabor, "Microscopy by reconstructed wave-fronts," Proceedings of the Royal Society of London. Series A, Mathematical and Physical Sciences **197**, 454–487 (1949).

[153] L. B. Lesem, P. M. Hirsch, and J. A. Jordon, Jr, "The kinoform: A new wavefront reconstruction device," IBM Journal of Research and Development **13**, 150–155 (1969).

[154] W. H. Lee, "Sampled fourier transform hologram generated by computer," Applied Optics **9**, 639–643 (1970).

[155] R. W. Gerchberg and W. O. Saxton, "A practical algorithm for the determination of phase from image and diffraction plane pictures," Optik **35**, 227246 (1972).

[156] F. Wyrowski and O. Bryngdahl, "Iterative fourier-transform algorithm applied to computer holography," Journal of the Optical Society of America A - Optics Image Science and Vision **5**, 1058–1065 (1988).

[157] M. Clark and R. Smith, "A direct-search method for the computer design of holograms," Optics Communications **124**, 150–164 (1996).

[158] M. Clark, "Two-dimensional, three-dimensional, and gray-scale images reconstructed from computer-generated holograms designed by use of a direct-search method," Applied Optics **38**, 5331–5337 (1999).

[159] M. Reicherter, T. Haist, E. U. Wagemann, and H. J. Tiziani, "Optical particle trapping with computer-generated holograms written on a liquid-crystal display," Optics Letters **24**, 608–610 (1999).

[160] J. Liesener, M. Reicherter, T. Haist, and H. J. Tiziani, "Multi-functional optical tweezers using computer-generated holograms," Optics Communications **185**, 77–82 (2000).

[161] V. Soifer, V. Kotlyar, and L. Doskolovich, *Iterative Methods for Diffractive Optical Elements Computation* (Taylor and Francis, 1997).

[162] M. Montes-Usategui, E. Pleguezuelos, J. Andilla, and E. Martin-Badosa, "Fast generation of holographic optical tweezers by random mask encoding of fourier components," Optics Express **14**, 2101–2107 (2006).

[163] G. Sinclair, J. Leach, P. Jordan, G. Gibson, E. Yao, Z. J. Laczik, M. J. Padgett, and J. Courtial, "Interactive application in holographic optical tweezers of a multi-plane Gerchberg-Saxton algorithm for three-dimensional light shaping," Optics Express **12**, 1665–1670 (2004).

[164] E. Martin-Badosa, A. Carnicer, I. Juvells, and S. Vallmitjana, "Complex modulation characterization of liquid crystal devices by interferometric data correlation," Measurement Science and Technology **8**, 764772 (1997).

[165] C. Kohler, X. Schwab, and W. Osten, "Optimally tuned spatial light modulators for digital holography," Applied Optics **45**, 960–967 (2006).

[166] V. N. Mahajan, *Optical Imaging and Aberrations, Part II. Wave Diffraction Optics* (SPIE Publications, 2001).

[167] F. Zernike, "Beugungstheorie des schneidenverfahrens und seiner verbesserten form, der phasenkontrastmethode."," Physica **1**, 689–704 (1934).

[168] M. Born and E. Wolf, *Principles of Optics* (1980).

[169] K. D. Wulff, D. G. Cole, R. L. Clark, R. Di Leonardo, J. Leach, J. Cooper, G. Gibson, and M. J. Padgett, "Aberration correction in holographic optical tweezers," Optics Express **14**, 4169–4174 (2006).

[170] G. Love, Personal Communication (2007).

[171] A. Jesacher, A. Schwaighofer, S. Fürhapter, C. Maurer, S. Bernet, and M. Ritsch-Marte, "Wavefront correction of spatial light modulators using an optical vortex image," Optics Express **15**, 5801–5808 (2007).

[172] G. Sinclair, P. Jordan, J. Leach, M. J. Padgett, and J. Cooper, "Defining the trapping limits of holographical optical tweezers," Journal of Modern Optics **51**, 409–414 (2004).

[173] N. B. Viana, M. S. Rocha, O. N. Mesquita, A. Mazolli, and P. A. M. Neto, "Characterization of objective transmittance for optical tweezers," Applied Optics **45**, 4263–4269 (2006).

[174] C. N. Baroud, J. P. Delville, F. Gallaire, and R. Wunenburger, "Thermocapillary valve for droplet production and sorting," Physical Review E **75**, 046302 (2007).

[175] R. J. Chorley and M. A. Carson, *Introduction to fluvial processes* (Barnes and Noble, 1971).

[176] J. Monteith and M. Unsworth, *Principles of Environmental Physics* (Academic Press, 2008).

[177] J. H. Dennis, C. A. Pieron, and K. Asai, "Aerosol output and size from Omron NE-U22 nebulizer," (2003).

[178] Omron, "Omron MicroAir NE-U22 nebuliser," Accompanying datasheet.

[179] D. R. Burnham and D. McGloin, "Holographic optical trapping of aerosol droplets," Optics Express **14**, 4175–4181 (2006).

[180] L. Mitchem, J. Buajarern, R. J. Hopkins, A. D. Ward, R. J. J. Gilham, R. L. Johnston, and J. P. Reid, "Spectroscopy of growing and evaporating water droplets: Exploring the variation in equilibrium droplet size with relative humidity," Journal of Physical Chemistry A **110**, 8116–8125 (2006).

[181] J. Buajarern, L. Mitchem, A. D. Ward, N. H. Nahler, D. McGloin, and J. P. Reid, "Controlling and characterizing the coagulation of liquid aerosol droplets," Journal of Chemical Physics **125**, 114506 (2006).

[182] F. Benabid, J. C. Knight, and P. S. Russell, "Particle levitation and guidance in hollow-core photonic crystal fiber," Optics Express **10**, 1195–1203 (2002).

[183] M. J. Renn, R. Pastel, and H. J. Lewandowski, "Laser guidance and trapping of mesoscale particles in hollow-core optical fibers," Physical Review Letters **82**, 1574–1577 (1999).

[184] M. He, J. S. Kuo, and D. T. Chiu, "Electro-generation of single femtoliter- and picoliter-volume aqueous droplets in microfluidic systems," Applied Physics Letters **87**, 031916 (2005).

[185] J. R. Butler, J. B. Wills, L. Mitchem, D. R. Burnham, D. McGloin, and J. P. Reid, "Spectroscopic characterisation and manipulation of arrays of sub-picolitre aerosol

droplets," Lab on a Chip **9**, 521–528 (2009).

[186] J. Leach, S. Keen, M. J. Padgett, C. Saunter, and G. D. Love, "Direct measurement of the skew angle of the Poynting vector in a helically phased beam," Optics Express **14**, 11919–11924 (2006).

[187] R. A. Beth, "Mechanical detection and measurement of the angular momentum of light," Physicl Review **50**, 115–125 (1936).

[188] G. Delannoy, O. Emile, and A. Le Floch, "Direct observation of a photon spin-induced constant acceleration in macroscopic systems," Applied Physics Letters **86**, 081109 (2005).

[189] H. He, M. E. J. Friese, N. R. Heckenberg, and H. Rubinszteindunlop, "Direct observation of transfer of angular-momentum to absorptive particles from a laser-beam with a phase singularity," Physical Review Letters **75**, 826–829 (1995).

[190] A. Ashkin and J. M. Dziedzic, "Optical levitation in high-vacuum," Applied Physics Letters **28**, 333–335 (1976).

[191] R. Di Leonardo, S. Keen, J. Leach, C. D. Saunter, G. D. Love, G. Ruocco, and M. J. Padgett, "Eigenmodes of a hydrodynamically coupled micron-size multiple-particle ring," Physical Review E **76**, 061402 (2007).

[192] D. B. Weibel, P. Garstecki, D. Ryan, W. R. Diluzio, M. Mayer, J. E. Seto, and G. M. Whitesides, "Microoxen: Microorganisms to move microscale loads," Proceedings of the National Academy of Sciences of the United States of America **102**, 11963–11967 (2005).

[193] D. Stevenson, B. Agate, X. Tsampoula, P. Fischer, C. T. A. Brown, W. Sibbett, A. Riches, F. Gunn-Moore, and K. Dholakia, "Femtosecond optical transfection of cells: viability and efficiency," Optics Express **14**, 7125–7133 (2006).

[194] A. Ashkin, J. M. Dziedzic, and T. Yamane, "Optical trapping and manipulation of single cells using infrared-laser beams," Nature **330**, 769–771 (1987).

[195] G. Leitz, E. Schnepf, and K. O. Greulich, "Micromanipulation of statoliths in gravity-sensing chara rhizoids by optical tweezers," Planta **197**, 278–288 (1995).

[196] C. E. Bracker, D. J. Murphy, and R. Lopez-Francp, "Laser microbeam manipulation of cell morphogenesis in growing fungal hyphae," in "SPIE Vol. 2983," (1997).

[197] G. Albrecht-Buehler, "Surface extensions of 3t3 cells towards distant infrared light-sources," Journal of Cell Biology **114**, 493–502 (1991).

[198] A. Ehrlicher, T. Betz, B. Stuhrmann, D. Koch, V. Milner, M. G. Raizen, and J. Kas, "Guiding neuronal growth with light," Proceedings of the National Academy of Sciences of the United States of America **99**, 16024–16028 (2002).

[199] B. Stuhrmann, M. Gogler, T. Betz, A. Ehrlicher, D. Koch, and J. Kas, "Automated tracking and laser micromanipulation of motile cells," Review of Scientific

Instruments **76**, 035105 (2005).

[200] M. W. Berns, J. R. Aist, W. H. Wright, and H. Liang, "Optical trapping in animal and fungal cells using a tunable, near-infrared titanium-sapphire laser," Experimental Cell Research **198**, 375–378 (1992).

[201] I. M. Tólic-Nørrelykke, L. Sacconi, C. Stringari, I. Raabe, and F. S. Pavone, "Nuclear and division-plane positioning revealed by optical micromanipulation," Current Biology **15**, 1212–1216 (2005).

[202] G. Leitz, C. Lundberg, E. Fallman, O. Axner, and A. Sellstedt, "Laser-based micromanipulation for separation and identification of individual frankia vesicles," FEMS Microbiology Letters **224**, 97–100 (2003).

[203] X. H. Liu, H. W. Wang, Y. M. Li, Y. S. Tang, Y. L. Liu, X. Hu, P. X. Jia, K. Ying, Q. Feng, J. P. Guan, C. Q. Jin, L. Zhang, L. R. Lou, Z. A. Zhou, and B. Han, "Preparation of single rice chromosome for construction of a DNA library using a laser microbeam trap," Journal of Biotechnology **109**, 217–226 (2004).

[204] S. M. Block, D. F. Blair, and H. C. Berg, "Compliance of bacterial flagella measured with optical tweezers," Nature **338**, 514–518 (1989).

[205] J. T. Finer, R. M. Simmons, and J. A. Spudich, "Single myosin molecule mechanics - piconewton forces and nanometer steps," Nature **368**, 113–119 (1994).

[206] K. O. Greulich, "Fluoresence spectroscopy on single biomolecules," ChemPhysChem **6**, 2458–2471 (2005).

[207] S. C. Kuo and M. P. Sheetz, "Force of single kinesin molecules measured with optical tweezers," Science **260**, 232–234 (1993).

[208] P. Cluzel, A. Lebrun, C. Heller, R. Lavery, J. L. Viovy, D. Chatenay, and F. Caron, "DNA: An extensible molecule," Science **271**, 792–794 (1996).

[209] M. D. Wang, H. Yin, R. Landick, J. Gelles, and S. M. Block, "Stretching DNA with optical tweezers," Biophysical Journal **72**, 1335–1346 (1997).

[210] K. O. Greulich and G. Pilarczyk, "Laser tweezers and optical microsurgery in cellular and molecular biology. working principles and selected applications," Cellular And Molecular Biology **44**, 701–710 (1998).

[211] C. G. Baumann, V. A. Bloomfield, S. B. Smith, C. Bustamante, M. D. Wang, and S. M. Block, "Stretching of single collapsed DNA molecules," Biophysical Journal **78**, 1965–1978 (2000).

[212] K. O. Greulich, G. Pilarczyk, A. Hoffmann, G. M. Z. Horste, B. Schafer, V. Uhl, and S. Monajembashi, "Micromanipulation by laser microbeam and optical tweezers: from plant cells to single molecules," Journal of Microscopy **198**, 182–187 (2000).

[213] S. M. Block, "Making light work with optical tweezers," Nature **360**, 493–495 (1992).

[214] Y. X. Wang, E. L. Botvinick, Y. H. Zhao, M. W. Berns, S. Usami, R. Y. Tsien, and

S. Chien, "Visualizing the mechanical activation of Src," Nature **434**, 1040–1045 (2005).

[215] S. C. Kuo and M. P. Sheetz, "Optical tweezers in cell biology," Trends in Cell Biology **2**, 116–118 (1992).

[216] K. A. Borkovich, L. A. Alex, O. Yarden, M. Freitag, G. E. Turner, N. D. Read, S. Seiler, D. Bell-Pedersen, J. Paietta, N. Plesofsky, M. Plamann, M. Goodrich-Tanrikulu, U. Schulte, G. Mannhaupt, F. E. Nargang, A. Radford, C. Selitrennikoff, J. E. Galagan, J. C. Dunlap, J. J. Loros, D. Catcheside, H. Inoue, R. Aramayo, M. Polymenis, E. U. Selker, M. S. Sachs, G. A. Marzluf, I. Paulsen, R. Davis, D. J. Ebbole, A. Zelter, E. R. Kalkman, R. O'Rourke, F. Bowring, J. Yeadon, C. Ishii, K. Suzuki, W. Sakai, and R. Pratt, "Lessons from the genome sequence of *Neurospora crassa*: Tracing the path from genomic blueprint to multicellular organism," Microbiology And Molecular Biology Reviews **68**, 1–108 (2004).

[217] N. D. Read, "Environmental sensing and the filamentous fungal lifestyle," in "Fungi in their Environment," , G. D. Gadd, S. C. Watkinson, and P. S. Dyer, eds. (Cambridge University Press, 2006), p. 38.

[218] S. Bartnicki-Garcia, "Hyphal tip growth: outstanding questions," in "Molecular Biology of Fungal Development," , H. D. Osiewacz, ed. (Marcel Dekker, 2002), p. 29.

[219] S. D. Harris, N. D. Read, R. W. Roberson, B. Shaw, S. Seiler, M. Plamann, and M. Momany, "Polarisome meets spitzenkorper: Microscopy, genetics, and genomics converge," Eukaryotic Cell **4**, 225–229 (2005).

[220] R. H. Davis, *Neurospora: Contributions of a model organism* (Oxford University Press, 2000).

[221] D. D. Perkins and R. H. Davis, "Neurospora at the millennium," Fungal Genetics And Biology **31**, 153–167 (2000).

[222] J. E. Galagan, S. E. Calvo, K. A. Borkovich, E. U. Selker, N. D. Read, D. Jaffe, W. FitzHugh, L. J. Ma, S. Smirnov, S. Purcell, B. Rehman, T. Elkins, R. Engels, S. G. Wang, C. B. Nielsen, J. Butler, M. Endrizzi, D. Y. Qui, P. Ianakiev, D. B. Pedersen, M. A. Nelson, M. Werner-Washburne, C. P. Selitrennikoff, J. A. Kinsey, E. L. Braun, A. Zelter, U. Schulte, G. O. Kothe, G. Jedd, W. Mewes, C. Staben, E. Marcotte, D. Greenberg, A. Roy, K. Foley, J. Naylor, N. Stabge-Thomann, R. Barrett, S. Gnerre, M. Kamal, M. Kamvysselis, E. Mauceli, C. Bielke, S. Rudd, D. Frishman, S. Krystofova, C. Rasmussen, R. L. Metzenberg, D. D. Perkins, S. Kroken, C. Cogoni, G. Macino, D. Catcheside, W. X. Li, R. J. Pratt, S. A. Osmani, C. P. C. DeSouza, L. Glass, M. J. Orbach, J. A. Berglund, R. Voelker, O. Yarden, M. Plamann, S. Seller, J. Dunlap, A. Radford, R. Aramayo, D. O. Natvig, L. A. Alex, G. Mannhaupt, D. J. Ebbole, M. Freitag, I. Paulsen, M. S. Sachs, E. S. Lander,

C. Nusbaum, and B. Birren, "The genome sequence of the filamentous fungus *Neurospora crassa*," Nature **422**, 859–868 (2003).

[223] G. D. Wright, J. Arlt, W. C. K. Poon, and N. D. Read, "Optical tweezer micromanipulation of filamentous fungi," Fungal Genetics and Biology **44**, 1–13 (2007).

[224] G. D. Wright, J. Arlt, W. C. K. Poon, and N. D. Read, "Experimentally manipulating fungi with optical tweezers," Mycoscience **48**, 15–19 (2007).

[225] P. C. Hickey, S. R. Swift, M. G. Roca, and N. D. Read, "Live-cell imaging of filamentous fungi using vital fluorescent dyes and confocal microscopy," Microbial Imaging **34**, 63–87 (2005).

[226] G. D. Wright, J. Arlt, W. C. K. Poon, and N. D. Read, "Measuring fungal growth forces with optical tweezers," in "Proceedings of SPIE," , vol. 5930 (2005), vol. 5930, pp. 101–107.

[227] R. Lopez-Franco and C. E. Bracker, "Diversity and dynamics of the spitzenkorper in growing hyphal tips of higher fungi," Protoplasma **195**, 90–111 (1996).

[228] N. Arneborg, H. Siegumfeldt, G. H. Andersen, P. Nissen, V. R. Daria, P. J. Rodrigo, and J. Glückstad, "Interactive optical trapping shows that confinement is a determinant of growth in a mixed yeast culture," FEMS Microbiology Letters **245**, 155–159 (2005).

[229] V. R. Daria, P. J. Rodrigo, and J. Glückstad, "Dynamic array of dark optical traps," Applied Physics Letters **84**, 323–325 (2004).

[230] A. Lafong, W. J. Hossack, J. Arlt, T. J. Nowakowski, and N. D. Read, "Time-multiplexed Laguerre-Gaussian holographic optical tweezers for biological applications," Optics Express **14**, 3065–3072 (2006).

[231] K. C. Neuman, E. H. Chadd, G. F. Liou, K. Bergman, and S. M. Block, "Characterization of photodamage to Escherichia coli in optical traps," Biophysical Journal **77**, 2856–2863 (1999).

[232] H. Liang, K. T. Vu, P. Krishnan, T. C. Trang, D. Shin, S. Kimel, and M. W. Berns, "Wavelength dependence of cell cloning efficiency after optical trapping," Biophysical Journal **70**, 1529–1533 (1996).

[233] L. Sacconi, I. M. Tólic-Nørrelykke, C. Stringari, R. Antolini, and F. S. Pavone, "Optical micromanipulations inside yeast cells," Applied Optics **44**, 2001–2007 (2005).

[234] G. Whyte and J. Courtial, "Experimental demonstration of holographic three-dimensional light shaping using a Gerchberg-Saxton algorithm," New Journal of Physics **7**, 117 (2005).

[235] H. Song, J. D. Tice, and R. F. Ismagilov, "A microfluidic system for controlling reaction networks in time," Angewandte Chemie - International Edition **42**, 768–772 (2003).

[236] H. Song, D. L. Chen, and R. F. Ismagilov, "Reactions in droplets in microflulidic channels," Angewandte Chemie - International Edition **45**, 7336–7356 (2006).

[237] S. Y. Teh, R. Lin, L. H. Hung, and A. P. Lee, "Droplet microfluidics," Lab on a Chip **8**, 198–220 (2008).

[238] A. Gunther and K. F. Jensen, "Multiphase microfluidics: from flow characteristics to chemical and materials synthesis," Lab on a Chip **6**, 1487–1503 (2006).

[239] P. Laval, N. Lisai, J. B. Salmon, and M. Joanicot, "A microfluidic device based on droplet storage for screening solubility diagrams," Lab on a Chip **7**, 829–834 (2007).

[240] K. Ahn, J. Agresti, H. Chong, M. Marquez, and D. A. Weitz, "Electrocoalescence of drops synchronized by size-dependent flow in microfluidic channels," Applied Physics Letters **88**, 264105 (2006).

[241] K. Ahn, C. Kerbage, T. P. Hunt, R. M. Westervelt, D. R. Link, and D. A. Weitz, "Dielectrophoretic manipulation of drops for high-speed microfluidic sorting devices," Applied Physics Letters **88**, 024104 (2006).

[242] C. Priest, S. Herminghaus, and R. Seemann, "Controlled electrocoalescence in microfluidics: Targeting a single lamella," Applied Physics Letters **89**, 134101 (2006).

[243] A. Terray, J. Oakey, and D. W. M. Marr, "Microfluidic control using colloidal devices," Science **296**, 1841–1844 (2002).

[244] A. Terray, J. Arnold, and S. J. Hart, "Enhanced optical chromatography in a pdms microfluidic system," Optics Express **13**, 10406–10415 (2005).

[245] K. T. Kotz, K. A. Noble, and G. W. Faris, "Optical microfluidics," Applied Physics Letters **85**, 2658–2660 (2004).

[246] V. Daria, J. Glückstad, P. C. Mogensen, E. R. L., and S. Sinzinger, "Implementing the generalized phase-contrast method in a planar-integrated micro-optics platform," Optics Letters **27**, 945–947 (2002).

[247] Y. Roichman, V. Wong, and D. G. Grier, "Colloidal transport through optical tweezer arrays," Physical Review E **75**, 011407 (2007).

[248] C. N. Baroud, M. R. de Saint Vincent, and J. P. Delville, "An optical toolbox for total control of droplet microfluidics," Lab on a Chip **7**, 1029–1033 (2007).

[249] M. Cordero, E. Verneuil, F. Gallaire, and C. N. Baroud, "Time-resolved temperature rise in a thin liquid film due to laser absorption," Physical Review E **79**, 011201 (2009).

[250] S. Y. A. Terry, Personal Communication (2009).

[251] D. Stevenson, Personal Communication (2009).

[252] K. Sahu, S. K. Mohanty, and P. K. Gupta, "HeNe laser (632.8 nm) pre-irradiation gives protection against DNA damage induced by a near-infrared trapping beam," Journal of Biophotonics **1**, 1–5 (2008).

[253] M. Cordero, H. O. Rolfsnes, D. R. Burnham, P. A. Campbell, D. McGloin, and C. N. Baroud, "Mixing via thermocapillary generation of flow patterns inside a microfluidic drop," Submitted (2009).

[254] R. Brown, "A brief account of microscopical observations made in the months of june, july and august, 1827, on the particles contained in the pollen of plants; and on the general existence of active molecules in organic and inorganic bodies," Philosophical Magazine **4**, 161–173 (1828).

[255] A. Einstein, *On the theory of the Brownian movement* (Dover Publications, 1956).

[256] M. von Smoluchowski, "Zur kinetischen theorie der brownschen molekularbewegung und der suspensionen," Annalen der Physik **326**, 756 – 780 (1906).

[257] D. S. Lemons and A. Gythiel, "Paul Langevin's 1908 paper 'On the theory of Brownian motion'," American Journal of Physics **65**, 1079–1081 (1997).

[258] J. Perrin, "Le mouvement brownien et la réalité moleculaire," Annales de chimie et de physique **18**, 5114 (1909).

[259] M. Haw, "Einstein's random walk," Physics World **18**, 19 (2005).

[260] R. Newburgh, J. Peidleb, and W. Ruecknerc, "Einstein, perrin, and the reality of atoms: 1905 revisited," American Journal of Physics **74**, 478–481 (2006).

[261] M. F. M. Osborne, "Brownian motion in the stock market," Operations Research **7**, 145–173 (1959).

[262] K. Berg-Sorensen and H. Flyvbjerg, "The colour of thermal noise in classical brownian motion: a feasibility study of direct experimental observation," New Journal of Physics **7**, 38 (2005).

[263] Z. G. Sun, C. D. Tomlin, and E. M. Sevick-Muraca, "Approach for particle sizing in dense polydisperse colloidal suspension using multiple scattered light," Langmuir **17**, 6142–6147 (2001).

[264] S. Sudo, Y. Miyasaka, and K. Otsuka, "Quick and easy measurement of particle size of brownian particles and plankton in water using a self-mixing laser," Optics Express **14**, 1044–1054 (2006).

[265] G. Pesce, A. Sasso, and S. Fusco, "Viscosity measurements on micron-size scale using optical tweezers," Review of Scientific Instruments **76**, 115105 (2005).

[266] A. Rohrbach, C. Tischer, D. Neumayer, E. L. Florin, and E. H. K. Stelzer, "Trapping and tracking a local probe with a photonic force microscope," Review of Scientific Instruments **75**, 2197–2210 (2004).

[267] C. Hertlein, L. Helden, A. Gambassi, S. Dietrich, and C. Bechinger, "Direct measurement of critical casimir forces," Nature **451**, 172–175 (2008).

[268] M. W. Allersma, F. Gittes, M. J. deCastro, R. J. Stewart, and C. F. Schmidt, "Two-dimensional tracking of NCD motility by back focal plane interferometry,"

Biophysical Journal **74**, 1074–1085 (1998).

[269] W. Denk and W. W. Webb, "Optical measurement of picometer displacements of transparent microscopic objects," Applied Optics **29**, 2382–2391 (1990).

[270] L. P. Ghislain, N. A. Switz, and W. W. Webb, "Measurement of small forces using an optical trap," Review of Scientific Instruments **65**, 2762–2768 (1994).

[271] J. C. Meiners and S. R. Quake, "Direct measurement of hydrodynamic cross correlations between two particles in an external potential," Physical Review Letters **82**, 2211–2214 (1999).

[272] Y. Deng, J. Bechhoefer, and N. R. Forde, "Brownian motion in a modulated optical trap," Journal of Optics A - Pure and Applied Optics **9**, S256–S263 (2007).

[273] L. I. McCann, M. Dykman, and B. Golding, "Thermally activated transitions in a bistable three-dimensional optical trap," Nature **402**, 785–787 (1999).

[274] A. Pertsinidis and X. S. Ling, "Diffusion of point defects in two-dimensional colloidal crystals," Nature **413**, 147–150 (2001).

[275] M. Polin, D. G. Grier, and S. R. Quake, "Anomalous vibrational dispersion in holographically trapped colloidal arrays," Physical Review Letters **96**, 088101 (2006).

[276] A. Chowdhury, B. J. Ackerson, and N. A. Clark, "Laser-induced freezing," Physical Review Letters **55**, 833–836 (1985).

[277] J. Joykutty, V. Mathur, V. Venkataraman, and V. Natarajan, "Direct measurement of the oscillation frequency in an optical-tweezers trap by parametric excitation," Physical Review Letters **95**, 193902 (2005).

[278] L. Pedersen and H. Flyvbjerg, "Comment on "Direct measurement of the oscillation frequency in an optical-tweezers trap by parametric excitation"," Physical Review Letters **98**, 189801 (2007).

[279] K. J. Knox, J. P. Reid, K. L. Hanford, A. J. Hudson, and L. Mitchem, "Direct measurements of the axial displacement and evolving size of optically trapped aerosol droplets," Journal of Optics A - Pure and Applied Optics **9**, S180–S188 (2007).

[280] L. D. Landau and E. M. Lifshitz, *Fluid Mechanics* (Pergamon Press, 1959).

[281] H. Risken, *The Fokker-Planck Equation: Methods of Solutions and Applications* (1989).

[282] A. Rohrbach, "Stiffness of optical traps: quantitative agreement between experiment and electromagnetic theory," Physical Review Letters **95**, 168102 (2005).

[283] M. C. Wang and G. E. Uhlenbeck, "On the thoery of the brownian motion ii," Reviews of Modern Physics **17**, 323–342 (1945).

[284] S. Chandrasekhar, "Stochastic problems in physics and astronomy," Reviews of Modern Physics **15**, 1–89 (1943).

[285] A. Rohrbach, "Switching and measuring a force of 25 femtonewtons with an optical

trap," Optics Express **13**, 9695–9701 (2005).

[286] M. Fischer and K. Berg-Sørensen, "Calibration of trapping force and response function of optical tweezers in viscoelastic media," Journal of Optics A: Pure and Applied Optics **9**, S239S250 (2007).

[287] G. Knoner, S. Parkin, T. A. Nieminen, N. R. Heckenberg, and H. Rubinsztein-Dunlop, "Measurement of the index of refraction of single microparticles," Physical Review Letters **97**, 157402 (2006).

[288] J. C. Crocker and D. G. Grier, "Methods of digital video microscopy for colloidal studies," Journal of Colloid and Interface Science **179**, 298–310 (1996).

[289] J. H. G. Huisstede, K. O. van der Werf, M. L. Bennink, and V. Subramaniam, "Force detection in optical tweezers using backscattered light," Optics Express **13**, 1113–1123 (2005).

[290] M. Capitanio, G. Romano, R. Ballerini, M. Giuntini, F. S. Pavone, D. Dunlap, and L. Finzi, "Calibration of optical tweezers with differential interference contrast signals," Review of Scientific Instruments **73**, 1687–1696 (2002).

[291] E. L. Florin, A. Pralle, E. H. K. Stelzer, and J. K. H. Horber, "Photonic force microscope calibration by thermal noise analysis," Applied Physics A - Materials Science and Processing **66**, S75–S78 (1998).

[292] G. Volpe, G. Volpe, and D. Petrov, "Brownian motion in a nonhomogeneous force field and photonic force microscope," Physical Review E **76**, 061118 (2007).

[293] W. Singer, S. Bernet, N. Hecker, and M. Ritsch-Marte, "Three-dimensional force calibration of optical tweezers," Journal of Modern Optics **47**, 2921–2931 (2000).

[294] R. M. Simmons, J. T. Finer, S. Chu, and J. A. Spudich, "Quantitative measurements of force and displacement using an optical trap," Biophysical Journal **70**, 1813–1822 (1996).

[295] S. F. Tólic-Nørrelykke, E. Schaffer, J. Howard, F. S. Pavone, F. Julicher, and H. Flyvbjerg, "Calibration of optical tweezers with positional detection in the back focal plane," Review of Scientific Instruments **77**, 103101 (2006).

[296] G. G. Stokes, "On the effect of the internal friction of fluids on the motion of pendulums," Transactions of the Cambridge Philosophical Society **IX** (1850).

[297] K. Berg-Sorensen and H. Flyvbjerg, "Power spectrum analysis for optical tweezers," Review of Scientific Instruments **75**, 594–612 (2004).

[298] S. Keen, J. Leach, G. Gibson, and M. J. Padgett, "Comparison of a high-speed camera and a quadrant detector for measuring displacements in optical tweezers," Journal of Optics A - Pure and Applied Optics **9**, S264–S266 (2007).

[299] M. Li and J. Arlt, "Trapping multiple particles in single optical tweezers," Optics Communications **281**, 135–140 (2008).

[300] A. Widom, "Velocity fluctuations of a hard-core brownian particle," Physical Review A **3**, 1394–1396 (1971).

[301] E. Schaffer, S. F. Norrelykke, and J. Howard, "Surface forces and drag coefficients of microspheres near a plane surface measured with optical tweezers," Langmuir **23**, 3654–3665 (2007).

[302] J. Leach, H. Mushfique, S. Keen, R. Di Leonardo, G. Ruocco, J. M. Cooper, and M. J. Padgett, "Comparison of Faxén's correction for a microsphere translating or rotating near a surface," Physical Review E **79**, 026301 (2009).

[303] J. Happel and H. Brenner, *Low Reynolds Number Hydrodynamics* (1965).

[304] A. Pralle, M. Prummer, E. L. Florin, E. H. K. Stelzer, and J. K. H. Hörber, "Three-dimensional high-resolution particle tracking for optical tweezers by forward scattered light," Microscopy Research and Techniques **44**, 378–386 (1999).

[305] K. C. Vermeulen, G. J. L. Wuite, G. J. M. Stienen, and C. F. Schmidt, "Optical trap stiffness in the presence and absence of spherical aberrations," Applied Optics **45**, 1812–1819 (2006).

[306] F. Pampaloni, "Force sensing and surface analysis with optically trapped microprobes," Ph.D. thesis, Universität Regensburg (2002).

[307] K. C. Neuman, E. A. Abbondanzieri, and S. M. Block, "Measurement of the effective focal shift in an optical trap," Optics Letters **30**, 1318–1320 (2005).

[308] P. Torok, P. Varga, Z. Laczik, and G. R. Booker, "Electromagnetic diffraction of light focused through a planar interface between materials of mismatched refractive-indexes - an integral-representation," Journal of the Optical Society of America A - Optics Image Science and Vision **12**, 325–332 (1995).

[309] P. Torok and P. Varga, "Electromagnetic diffraction of light focused through a stratified medium," Applied Optics **36**, 2305–2312 (1997).

[310] G. M. Gibson, S. Leach, J. Keen, A. J. Wright, and M. J. Padgett, "Measuring the accuracy of particle position and force in optical tweezers using high-speed video microscopy," Optics Express **16**, 14561–14570 (2008).

[311] T. R. Lettieri, W. D. Jenkins, and D. A. Swyt, "Sizing of individual optically levitated evaporating droplets by measurement of resonances in the polarization-ratio," Applied Optics **20**, 2799–2805 (1981).

[312] B. Steiner, B. Berge, R. Gausmann, J. Rohmann, and E. Ruhl, "Fast *in situ* sizing technique for single levitated liquid aerosols," Applied Optics **38**, 1523–1529 (1999).

[313] A. D. Ward, M. Zhang, and O. Hunt, "Broadband Mie scattering from optically levitated aerosol droplets using a white LED," Optics Express **16**, 16390–16403 (2008).

[314] G. Roll, T. Kaiser, and G. Schweiger, "Optical trap sedimentation cell: A new

technique for the sizing of microparticles," Journal Of Aerosol Science **27**, 105–117 (1996).

[315] J. P. Reid, Personal Communication (2008).

[316] S. B. Smith, Y. J. Cui, and C. Bustamante, "Optical-trap force transducer that operates by direct measurement of light momentum," Methods in Enzymology **361**, 134–162 (2003).

[317] N. B. Viana, M. S. Rocha, O. N. Mesquita, A. Mazolli, P. A. M. Neto, and H. M. Nussenzveig, "Towards absolute calibration of optical tweezers," Physical Review E **75**, 021914 (2007).

[318] C. Guzmán, H. Flyvbjerg, R. Köszalli, C. Ecoffet, F. L., and S. Jeney, "In situ viscometry by optical trapping interferometry," Applied Physics Letters **93**, 184102 (2008).

[319] D. R. Burnham and D. McGloin, "Modelling of airborne optical traps," in preparation .

[320] A. Rohrbach, H. Kress, and E. H. K. Stelzer, "Three-dimensional tracking of small spheres in focused laser beams: influence of the detection angular aperture," Optics Letters **28**, 411–413 (2003).

[321] E. Fällman, S. Schedin, J. Jass, M. Andersson, B. E. Uhlin, and O. Axner, "Optical tweezers based force measurement system for quantitating binding interactions: system design and application for the study of bacterial adhesion," Biosensors and Bioelectronics **19**, 1429–1437 (2004).

[322] J. R. Butler, L. Mitchem, K. L. Hanford, L. Treuel, and J. P. Reid, "*In situ* comparative measurements of the properties of aerosol droplets of different chemical composition," Faraday Discussions **137**, 351–366 (2008).

[323] H. Lamb, *Hydrodynamics* (Cambridge at the University Press, 1932), 6th ed.

[324] J. Bechhoefer and S. Wilson, "Faster, cheaper, safer optical tweezers for the undergraduate laboratory," American Journal of Physics **70**, 393–400 (2002).

[325] C. Zerbe, P. Jung, and P. Hanggi, "Brownian parametric oscillators," Physical Review E **49**, 3626–3635 (1994).

[326] A. F. Izmailov, S. Arnold, S. Holler, and A. S. Myerson, "Microparticle driven by parametric and random forces - theory and experiment," Physical Review E **52**, 1325–1332 (1995).

[327] V. Venkataraman, V. Natarajan, and N. Kumar, "Venkataraman, Natarajan, and Kumar reply," Physical Review Letters **98**, 189803 (2007).

[328] Y. Deng, N. R. Forde, and J. Bechhoefer, "Comment on "Direct measurement of the oscillation frequency in an optical-tweezers trap by parametric excitation"," Physical Review Letters **98**, 189802 (2007).

[329] Y. Zhao, G. Milne, J. S. Edgar, G. D. M. Jeffries, D. McGloin, and D. T. Chiu, "Quantitative force mapping of an optical vortex trap," Applied Physics Letters **92**, 161111 (2008).

[330] N. K. Metzger, E. M. Wright, and K. Dholakia, "Theory and simulation of the bistable behavior of optically bound particles in the mie size regime," New Journal of Physics **8**, 139 (2006).

[331] J. J. Taylor, L. Y. Wong, and G. D. Bain, C. Love, "Emergent behaviour of optically bound microparticles in laser beam traps," (2008). Photon.

[332] J. Guck, S. Schinkinger, B. Lincoln, F. Wottawah, S. Ebert, M. Romeyke, D. Lenz, H. M. Erickson, R. Ananthakrishnan, D. Mitchell, J. Kas, S. Ulvick, and C. Bilby, "Optical deformability as an inherent cell marker for testing malignant transformation and metastatic competence," Biophysical Journal **88**, 3689–3698 (2005).

[333] T. A. Nieminen, H. Rubinsztein-Dunlop, N. R. Heckenberg, and A. I. Bishop, "Numerical modelling of optical trapping," Computer Physics Communications **142**, 468–471 (2001).

[334] T. A. Nieminen, V. L. Y. Loke, A. B. Stilgoe, G. Knoner, A. M. Branczyk, N. R. Heckenberg, and H. Rubinsztein-Dunlop, "Optical tweezers computational toolbox," Journal of Optics A - Pure and Applied Optics **9**, S196–S203 (2007).

[335] A. B. Stilgoe, T. A. Nieminen, G. Knoner, N. R. Heckenberg, and H. Rubinsztein-Dunlop, "The effect of Mie resonances on trapping in optical tweezers," Optics Express **16**, 15039–15051 (2008).

[336] B. Richards and E. Wolf, "Electromagnetic diffraction in optical systems II. structure of the image field in an aplanatic system," Proceedings of the Royal Society of London. Series A, Mathematical and Physical Sciences **253**, 358–379 (1959).

[337] A. Mazolli, P. A. M. Neto, and H. M. Nussenzveig, "Theory of trapping forces in optical tweezers," Proceedings of the Royal Society of London. Series A - Mathematical, Physical and Engineering Sciences **459**, 3021–3041 (2003).

[338] E. Wolf, "Electromagnetic diffraction in optical systems I. an integral representation of the image field," Proceedings of the Royal Society of London. Series A, Mathematical and Physical Sciences **253**, 349–357 (1959).

[339] M. Kerker, *The scattering of light, and other electromagnetic radiation* (1969).

[340] G. Milne, K. Dholakia, D. McGloin, K. Volke-Sepulveda, and P. Zemanek, "Transverse particle dynamics in a bessel beam," Optics Express **15**, 13972–13987 (2007).

[341] C. F. Bohren and D. R. Huffman, *Absorption and scattering of light by small particles* (Wiley, 1983).

[342] J. P. Barton, D. R. Alexander, and S. A. Schaub, "Theoretical determination of net-radiation force and torque for a spherical-particle illuminated by a focused laser-

beam," Journal of Applied Physics **66**, 4594–4602 (1989).

[343] O. Farsund and B. U. Felderhof, "Force, torque, and absorbed energy for a body of arbitrary shape and constitution in an electromagnetic radiation field," Physica A **227**, 108–130 (1996).

[344] M. A. Blanco, M. Florez, and M. Bermejo, "Evaluation of the rotation matrices in the basis of real spherical harmonics," Journal of Molecular Structure: THEOCHEM **419**, 19–27 (1997).

[345] A. R. Edmonds, *Angular momentum in quantum mechanics* (Princeton University Press, 1957).

[346] R. S. Dutra, N. B. Viana, P. A. M. Neto, and H. M. Nussenzveig, "Polarization effects in optical tweezers," Journal of Optics A - Pure and Applied Optics **9**, S221–S227 (2007).

[347] P. A. M. Neto and H. M. Nussenzveig, "Theory of optical tweezers," Europhysics Letters **50**, 702–708 (2000).

[348] E. Fällman and O. Axner, "Influence of a glass-water interface on the on-axis trapping of micrometer-sized spherical objects by optical tweezers," Applied Optics **42**, 3915–3926 (2003).

[349] K. B. Im, H. I. Kim, I. J. Joo, C. H. Oh, S. H. Song, P. S. Kim, and B. C. Park, "Optical trapping forces by a focused beam through two media with different refractive indices," Optics Communications **226**, 25–31 (2003).

[350] B. Sun and D. G. Grier, "The effect of Mie resonances on trapping in optical tweezers: comment," Optics Express **17**, 2658–2660 (2009).

[351] T. A. Nieminen, A. B. Stilgoe, V. L. Y. Loke, N. R. Heckenberg, and H. Rubinsztein-Dunlop, "The effect of Mie resonances on trapping in optical tweezers: reply," Optics Express **17**, 2661–2662 (2009).

[352] W. H. Guilford, J. A. Tournas, D. Dascalu, and D. S. Watson, "Creating multiple time-shared laser traps with simultaneous displacement detection using digital signal processing hardware," Analytical Biochemistry **326**, 153166 (2004).

[353] Durham Smart Imaging, http://www.durhamsi.co.uk/ (March 2009).

[354] D. R. Burnham, G. D. Wright, N. D. Read, and D. McGloin, "Holographic and single beam optical manipulation of hyphal growth in filamentous fungi," Journal of Optics A - Pure and Applied Optics **9**, S172–S179 (2007).

[355] M. L. Cordero, D. R. Burnham, C. N. Baroud, and D. McGloin, "Thermocapillary manipulation of droplets using holographic beam shaping: Microfluidic pin ball," Applied Physics Letters **93**, 034107 (2008).

[356] D. R. Burnham and D. McGloin, "Radius measurements of optically trapped aerosols through brownian motion," Submitted (2008).

[357] A. M. Yao, S. A. J. Keen, D. R. Burnham, J. Leach, R. Di Leonardo, D. McGloin, and M. J. Padgett, "underdamped modes in a hydrodynamically coupled microparticle system,," Submitted (2009).

[358] K. J. Knox, Ph.D. thesis, University of Bristol (2009).